Single Epoch Analysis and Bi-hemisphere Study of Magnetoencephalographic (MEG) Signals using Vector Signal Transformation V3 and Magnetic Field Tomography (MFT)

Thesis

Single Epoch Analysis and Bi-hemisphere Study of Magnetoencephalographic (MEG) Signals using Vector Signal Transformation V3 and Magnetic Field Tomography (MFT)

LiChan Liu, B.Sc.(Hons)

Thesis submitted in partial fulfillment of the requirements
for the degree of Doctor of Philosophy in Biophysics

Department of Physics, The Open University,
Walton Hall, Milton Keynes MK7 6AA, U.K.

February, 1995

To my devoted mum and dad
with endless love
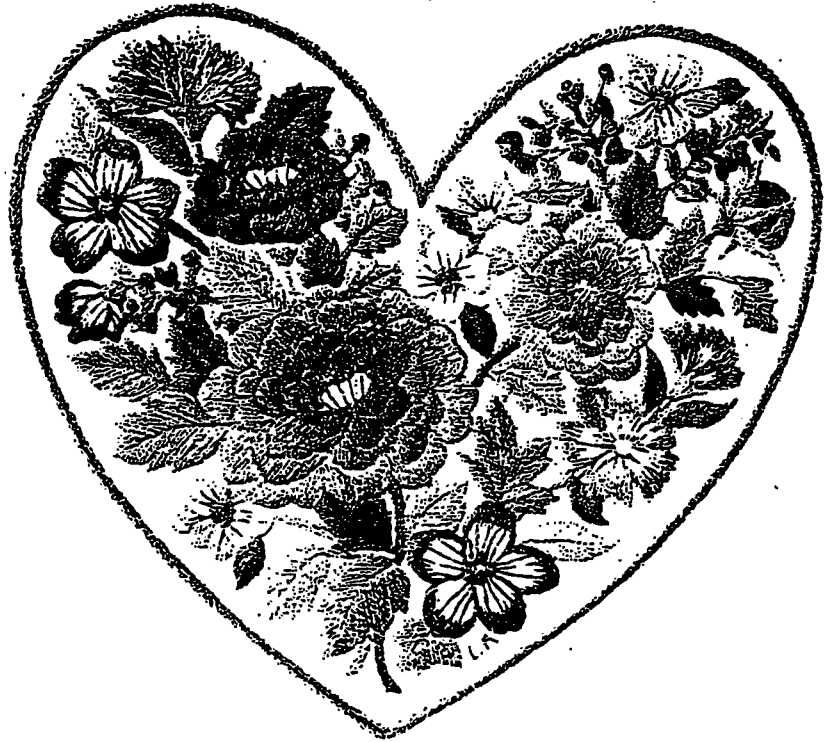
献 给 我 敬 爱 的 父 母 亲

踏 遍 心 田 的 每 一 角　采 透 心 灵 的 每 一 寸
满 是 对 你 们 的 敬 意　谢 谢 你 们 无 尽 的 爱

ABSTRACT

The biomagnetic inverse problem has no unique solution, nevertheless even a cursory look at the features shown in raw signal can often suffice to highlight strong superficial activity. To do a proper single epoch analysis is normally prohibitively expensive in terms of computing demands. Hence the original aim of this thesis was to use simple efficient signal transformations to characterize superficial generators and contrast the single epoch signature with that extracted from the average signal. The results have intrigued us sufficiently to go beyond the original goal and extract very preliminary estimates of activity across the cerebral hemisphere in single trials.

The original tool, and one that we have used for much of the work, is a simple vector signal transformation called V_3. This signal transformation highlights nearby sources; it is a crude but quick estimator of generators directly from the raw MEG signals. Together with Magnetic Field Tomography (MFT), which relies on distributed source analysis of the MEG signals, we have tackled the following specific problems relating to aspects of normal brain function: efficient estimation of generators of magnetic fields; relationship between the average signal and single trials; and interhemispheric differences and relationship between the activity in the left and right hemispheres of the brain.

During the project, we have used as examples auditory evoked MEG measurements obtained from two multichannel systems and applied the V_3 and MFT analysis to both the average and single trial signals. In particular, we chose the 40-Hz (or gamma band) auditory response as the study subject. We found that in single epochs similar patterns of high frequency activity are observed in the area around the auditory cortex well before, close to and well after stimulus onset; the sequence of events observed in the average can only represent the evolution of events in single trials in a statistical way; and deep and central areas of the brain may be the seeds for the main deflections observed in the auditory responses.

PREFACE

This thesis accounts for the project supported by a studentship from the Open University and carried out in the Physics Department, under the supervision of Dr. Andreas A. Ioannides between July 1991 and January 1995.

Accounts of part of this thesis have been published in the following papers:

1. L.C.Liu and A.A. Ioannides, "Single Epoch Analysis of MEG Signals", accepted for publication in the Proceedings of the BIOMAG'93 Conference in Vienna, Elsevier Science Publishers, Amsterdam, The Netherlands. In press.

2. L.C.Liu and A.A. Ioannides, "40-Hz Auditory Evoked Response in Single Epoch Analysis", in "5th International Congress on Brain Electromagnetic Topography, Book of Abstracts", p. 200-201 (1994).

3. L.C.Liu and A.A. Ioannides, "Comparison of Average and Single Trial MEG Signals using Bi-hemispheric Auditory Response to Monaural Stimuli", abstract submitted to *First International Conference on Functional Mapping of the Human Brain, June 1995, Paris* (1995).

4. A.A. Ioannides, M.J. Liu, L.C. Liu, P.D. Bamidis, E. Hellstrand and K.M. Stephan, "Magnetic Field Tomography of Cortical and Deep Processes: Examples of "Real-Time Mapping" of Averaged and Single Trial MEG Signals", submitted to *International Journal of Psychophysiology*.

I would like to take this opportunity to express my warmest thanks to my supervisor Dr. Andreas A. Ioannides for his support during my Ph.D study. For the past more than 3 years, he has been always there to advise and help me. Without his professional knowledge and guidance, this thesis would not have been possible. His continuous encouragement and patience helped me overcome the fluctuations during my study, and his friendship and sense of humour made my work much easier and more enjoyable. I cannot thank him enough.

CONTENTS

LIST OF FIGURES

LIST OF TABLES

CHAPTER 1.

INTRODUCTION

This thesis addresses three issues relating to MEG signals: crude but efficient estimation of generators of magnetic fields, the relationship between the average signal and single trials, the interhemispheric differences and relationship between the left and right hemispheres of the brain.

In this chapter, the non-unique inverse problem encountered in the MEG signal analyses is first introduced, followed by the proposed solutions. The main structure of the thesis is also briefly outlined at the end.

1.1. Statement of the Problem and Proposed Solution

Biomagnetism refers to the study of magnetic fields originating in biological systems. These may arise from several kinds of sources, namely,

1. Ionic displacement, inside and outside the membrane of excitable cells produce current flows which in turn generate both electric potentials and magnetic fields at the body surface.

2. Magnetic contaminants in the lungs of people exposed to pollution.

3. Excess or deficiency of paramagnetic substances revealed when the subject is exposed to an applied magnetic field, for example, in some organs (e.g., liver and spleen) as a consequence of genetic diseases, such as hemochromatosis and thalassemia.

This thesis is restricted to the study of the magnetic fields generated by the human brain.

The study of the human brain is one of the most fruitful and rapidly growing research areas in biomagnetism. An increasingly prominent way to study the brain is to measure a correlate of neural activity when a task is undertaken and then extract from the measurements estimates of the generators.

The electromagnetic field of the brain is a direct correlate of brain function; it varies slowly enough so that the electric and magnetic fields can be considered separately. The electric field is measured indirectly through the measurement of the electrical potential by electrodes and associated amplifiers. The magnetic field is measured with induction coils, coupled to superconducting quantum interference devices (SQUIDs), and associated circuits. Both sets of measurements vary with position on the head.

Images of brain activity are produced by positron emission tomography (PET) and functional magnetic resonance imaging (fMRI). At present, the temporal resolution of these two techniques is on the order of seconds; while some brain processes only last a few milliseconds, well within the ability of modern electronics to record. Only the electric and magnetic fields of the brain vary in step with the underlying activity. Electroencephalography (EEG) and magnetoencephalography (MEG) offer the dynamic topology or geography of brain activity millisecond by millisecond.

The inverse problem is to calculate the primary current distribution in the brain from the magnetic (or electric) field outside the head. The solution is not unique: an infinity of different current distributions can explain a given magnetic field. The main goal is to construct the best estimate for the primary current distribution [1]. With some prior knowledge and assumption about the form of the sources, the inverse problem can be tackled. To date, many models have been proposed and adopted to obtain the generators giving rise to magnetic measurements, which basically can be categorized into two models. The first one assumes that all primary activity is generated by one or few point sources, i.e., current dipoles, or at least that such a model can effectively summarize the measurement; while the second one allows for distributed source model, which is often expressed in terms of lead fields. Corresponding to these two models, several workable algorithms have been developed and applied successfully to MEG signals. The process is often demanding in terms of computing resources, particularly for fully distributed sources. With

this view, we have developed a simple vector signal transformation called V_3 to highlight nearby sources, that is, without running the inversion, a crude estimation of the (superficial) sources can be obtained by applying the V_3 to the raw signals and hence speed up the process dramatically.

To date, despite some obvious limitations, averaging has been widely used to improve signal-to-noise ratios. The traditional view is that the eliminated signal by averaging is background "brain noise", what remains after averaging is a small fraction of the original signal. Arguments against treating background brain activity as noise have been voiced many times, e.g. showing that the pre-stimulus EEG tends to attain a phase-order pattern prior to expected stimulation [2].

The averaging produces "clean" signals which at their peaks can often be described well by point sources, localized close to regions of the brain which are known to be associated with the processing of the stimulus used in the experiment. The use of one or few point sources as models for the generators does not produce good fits to single epoch data, and hence inferences about single epoch behaviour has relied on signal space descriptions. It is however difficult to relate the results of such analysis to what is happening in the brain.

With a single or few MEG channels, averaging is necessary if a map of signals is to be constructed outside the head. This map can only contain contributions from activity which repeats with a constant time delay in relation to the onset of a stimulus or other marker from trial to trial. In general such activity contributes to a small fraction of the signal (10% less). However, averaging is not necessary when MEG probes with a large number of channels are available to map single epochs in real time, and it is only history and inertia which makes its use still predominant with multichannel MEG probes [3]. In this thesis, V_3 was applied to both the average signal and the single epoch data obtained from two multichannel MEG systems. Tests with computer generated data shows that V_3 identifies correctly and efficiently the superficial sources. Despite this apparent success, in all that follows the V_3 must be viewed as a transformation of the signal, not an image of the (superficial) generators, although the correspondence can be excellent. The application of V_3 to single epochs reveals patterns observed in the average signal, and much more activity which is missing in the average signal. The results show that if the full spectrum of the

brain activity is to be understood, then the signal must be analysed epoch by epoch.

Going beyond the initial aim of this thesis, we have applied the MFT distributed source analysis to the auditory evoked MEG measurements recorded from both hemispheres at different placements and simultaneously, and provided the first study of single trial bi-hemisphere auditory responses to further our understanding of how inter-hemisphere differences and interplays contribute to normal brain processes.

1.2. Organization of the Thesis

The structure of the thesis is as follows: some background information relevant to the subject of the thesis is first provided, and then the instrumentation and relevant techniques to detect and make use of the minute magnetic fields in MEG are discussed. Then emphasis is turned to the inverse problem, demonstrating why the inverse problem is non-unique and outlining methods employed extensively and successfully in recent years to tackle the problem. The next chapter deals with lead fields, which provide insight into the sensitivity of magnetic measurements and specify to what sources a given detection system is principally sensitive. Building on the above knowledge, the vector signal transformation V_3 is introduced and examples are given to demonstrate its practical usefulness. Subsequently, auditory evoked MEG measurements obtained from the KRENIKON 37-channel system in Erlangen and the BTi twin MAGNES probe (2×37 channels) in San Diego are analysed. Both the average signal and single trials are used, in an effort to understand how the two are linked. Three specific aspects of brain function are explored with the tools we have used and developed: activity in the gamma band (40 Hz), the relationship between average and single trials, and interhemispheric interplays and differences. Finally, conclusions are drawn and further possible work are proposed.

CHAPTER 2.

BACKGROUND INFORMATION

This chapter aims at reviewing some literature and providing the background information relevant to the subject of the thesis. The neural origin of MEG is first provided, followed by the discussion of the widely used current dipole modeling for sources. Other techniques for studying brain structure and function are reviewed next, and finally different models for the medium within the brain are discussed.

2.1. Neural Basis of MEG

Electrical activity in the brain is caused by movements of ions inside and outside cellular membranes. Movements of electrical currents are responsible for magnetic fields measurable outside the head (as well as the potential differences across the scalp). Magnetoencephalography (MEG) refers to the detection and study of fields produced by ionic movements associated with neuronal activity.

This section provides the general background for the generation of the MEG signal; it discusses how MEG studies can provide information on the location and structural organization of cortical generators in primary sensory areas, from which we can gain insights into higher functions of the brain, such as perception and cognition.

2.1.1. Constituents of the Brain

The principal building blocks of the brain are neurons and glial cells (glia). The glia are important for structural support and responsible for maintaining the environment around the neurons. The composition of the extracellular fluid around a neuron is critical in maintaining the membrane potential and therefore for generating the action potentials. Some glial cells are in close contact with blood vessels;

these control what substances can enter the environment of neurons. Specialized glial cells, the oligodendrocytes, form an insulating myelin sheath around certain nerve fibers, acting as electrical insulation and hence speeding up the transmission rate of the action potential [4].

The neuron is the functional unit of the brain and the human brain is thought to consist of perhaps 100 billion (10^{11}) individual neurons [5]. Neurons are the information-processing unit. Despite their differences in shape, all the neurons have a common plan (see Figure 2.1). From the cell body (which contains the nucleus) there extends one extra long, thin tube called the *axon* (1 μm) and a collection of shorter, often highly branched extensions called the *dendrites* (4 μm). The region of the cell between the axon and the cell body is called the *axon hillock*. The dendrites and cell body receive the inputs to the cell; the output from the cell is sent down the axon. The cell bodies and dendrites are concentrated in the grey matter, the largest part of which is the cerebral cortex forming the surface of the brain and responsible for the strongest MEG signals. Axons are often very long and thin, and they are referred to as nerve fibers. Because of the bright appearance, the myelinated axons are also called white matter. Axons connect neurons together and they have branches: the axon of one neuron usually contacts many other cells. Contacts between axons and other neurons are found on the dendrites and the cell body. At these contact points, the axon forms a swelling called the *axon terminal*. When viewed using an electron microscope, the structure of this special contact point is called the *synapse*. For convenience, the membrane of the axon terminal is often referred to as the *presynaptic membrane*, and that of the neuron it connects with as the *postsynaptic membrane.*

The neuron's membrane plays a very important role in transmitting and receiving information, which it does with small electrical signals called action potentials. In the neuron, the potential difference across the membrane is usually called the *membrane potential*. If the permeability of the membrane to specific molecules changes, then the distribution of the charged molecules on either side will change. As a result, the membrane potential will also be changed. A specific pattern of such changes in membrane potential constitutes the action potential recorded during the transmission of signals along axons. Hence, changes in membrane potential underlie the ability of neurons to communicate with each other.
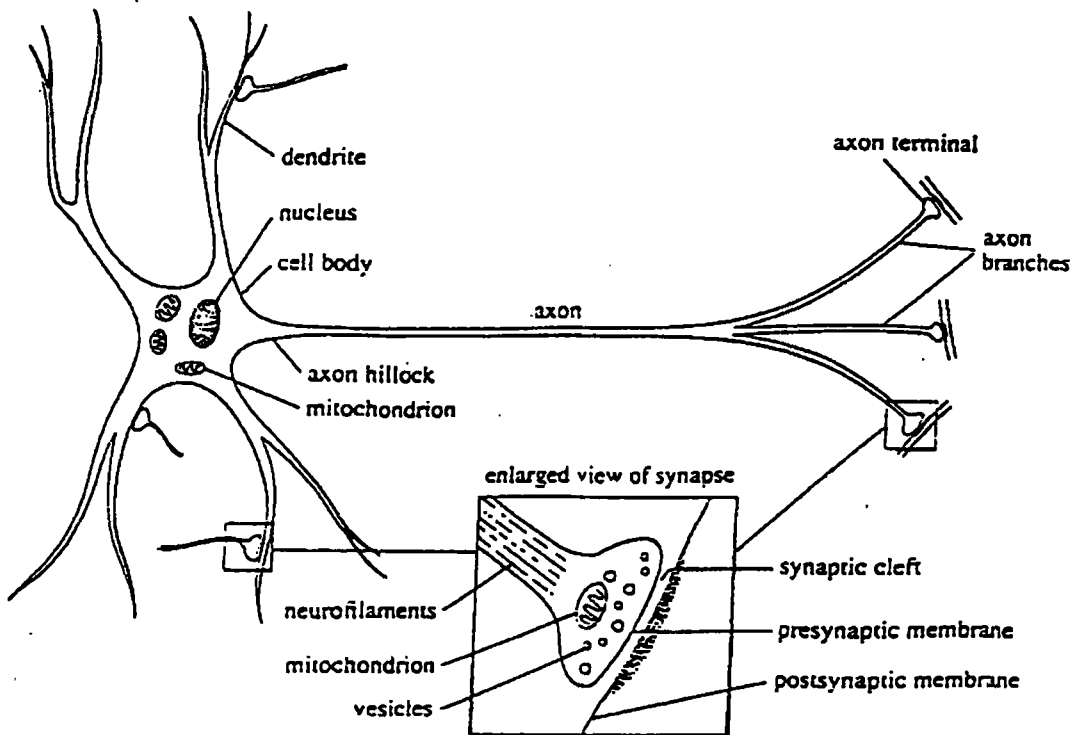
Figure 2.1 The main features of a typical neuron with an enlargement of an axon terminal showing the structure of the synapse. Modified from [4].

2.1.2. Electric Neural Activity

Ionic currents at a cellular level produce scalp potentials and neuromagnetic fields outside the scalp. In particular, action potential currents and postsynaptic currents are two distinct ionic currents generated by neural activities. Both are related to exchange of Na^+ and K^+ ions between active cells and the surrounding tissue. Although other ions are involved, their effect will not be discussed here.

Action Potential Currents:

The *action potential* is a propagating excitation initiated at the axon hillock. It involves a fast variation of the transmembrane potential initiated by the summated effect of many synapses. Once an action potential is triggered at the axon hillock, it travels along the entire length of the axon and into its branches without any significant change in size; it is conducted in an 'all or none' fashion [4, 6].

In the resting state, the inside potential of a neural cell is -70 mV with respect to the outside potential. During the first part of the action potential (depolarization), the cellular membrane selectively admits Na^+ ions from the outside environment, increasing the inside potential up to about +20 mV. At this point, the permeability of the membrane changes again and an outward flow of K^+ ions is established (repolarization), eventually restoring the original potential. The normal concentration of K^+ and Na^+ is finally recovered by means of the *Na-K* pump. During the depolarization process, the local excess of positive charges includes an axial current flow within the axon (*intracellular current*), thus causing an accumulation of positive charges near the end of the arrow (see Figure 2.2(a)). This portion of the membrane is still in its normal condition, so that the excess of positive charges may induce an outward current (*extracellular current*) flow through the membrane which continues in the extracellular space backward to the place where the depolarization first originated. Analogously, during the repolarization process, the ions move back to their original place, producing an intracellular current with opposite sign as well as producing the transmembrane and the extracellular counterpart. All this activity lasts about 1 ms, and thus if any such activity contributes to the MEG signals, it will be in the "high-frequency" region [6].

Postsynaptic Currents:
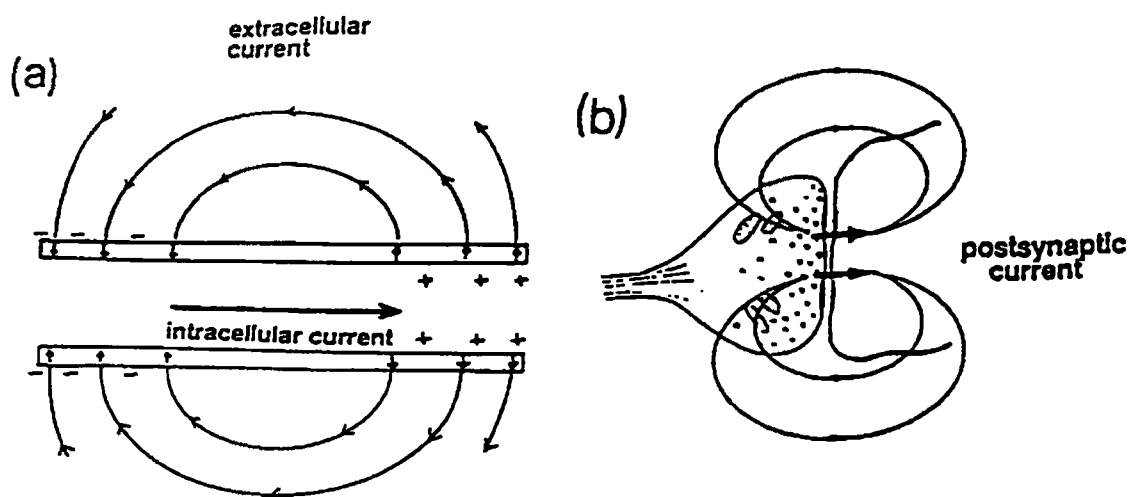
Figure 2.2 (a) Action potential currents, intracellular and extracellular currents, associated with the depolarization front of the action potential. (b) Currents associated with postsynaptic activity.

When an action potential reaches a synapse (see Figure 2.2(b)), the intracellular current produces an accumulation of positive charges on the presynaptic membrane. Because of the crucial effect of specific neurotransmitters, some ions then become free to move toward the postsynaptic membrane, possibly causing a new action potential. The ionic flow across the synapse produces also a relatively "steady" potential distribution extending beyond the narrow spatial limits of the synapse itself, usually referred to as *postsynaptic potential*.

The postsynaptic potential is quite different from the action potential: it is not conducted in an 'all or none' fashion, but rather it is a local change that travels away from the synapse in all directions, getting smaller the farther it goes. This passive spread of the electrical activity is rather like a ripple spreading out on a pool of water: the ripple gets smaller until eventually it disappears. Moreover, in contrast to action potentials which last about 1 ms, postsynaptic potentials can last for several tens or even hundreds of milliseconds. As a consequence of this slower time scale, the related neuromagnetic activity is usually classified as being in the "low-frequency" region [6].

2.1.3. Columnar Organization of the Cerebral Cortex

The cerebral cortex is the uppermost layer of the human brain which is the main concern in MEG. The cortex is a 2–4 mm thick sheet of grey tissue folded in a complicated way so that it fits into the cranial cavity formed by the skull. There are six layers of cells identified by the sizes and shapes of their cell bodies. Each layer is conventionally referred to by number, with the lowest number at the cortical surface. The largest cell bodies are found in layers 5 and 6, which have a definite pyramidal shape. These pyramidal neurons have long dendrites that span most of the six layers and extend laterally along the cortex by as much as 0.5 mm (the longest pyramidal neurons being in layer 5), and they are the principal output neurons of the cortex. In layer 2 and 3, there are smaller pyramidal cells. The neurons, especially in layer 3 and 4, are arranged in strings perpendicular to the cortical surface and separated by columns of fibers (a column width of approximately 50-75 μm). The way in which the connections up and down between the different layers of the cortex are arranged is referred to as a *columnar organization* [4, 7]. Because neurons guide the current flow, the resultant direction of the electrical current flowing in the dendrites is also perpendicular to the cortical sheet of grey matter, and this explains why MEG/EEG technique can reflect neural activity by taking measurements of magnetic fields/electric potentials generated by electrical currents. By simulating and recording from the brain, one can then describe pathways and regions of different functions in the cerebral cortex (mainly in primary sensory areas).

2.2. Equivalent Current Dipole Model

The relationship between neural activity and the generated electrical and magnetic fields may be explained with the help of the current dipole model. A *current dipole* **Q** can be thought of as a short current element I, with length **L** and negligible cross section. It is characterized by its position and orientation, it is a vector. The strength of a current dipole, or current dipole moment, is defined as $Q = IL$, and therefore the units are ampere-meter (A-m). As a consequence of the conservation of the electric charge, in a conducting medium this current source produces a current outflow into the medium at one end (source) and a current inflow at the other end of the source (sink).

The current patterns associated with an action potential may be described with a

pair of opposite dipoles travelling along the axon. Their separation is related to the conduction velocity of the fiber and is typically a few millimeters for a cortical unmyelinated axon. Postsynaptic activity may also be accounted for by a single current dipole. It is useful to evaluate the strength of a current dipole generated by a single postsynaptic potential. The calculation may be simply performed using Ohm's law: $I = V/R$. The total resistance is $R = 4L/(\pi d^2 \sigma)$, where d is the diameter of the dendrite and σ is the intracellular conductivity [8]. Therefore, the strength of the current dipole is given by the equation:

$$Q = IL = \pi d^2 \sigma V/4 \tag{2.1}$$

According to [9], typically, for an apical dendrite of a pyramidal cell, $d \approx 4\,\mu\text{m}$, the intracellular conductivity $\sigma \approx 0.25\,\Omega^{-1}\text{m}^{-1}$, and $V \approx 10$ mV. Then, $Q \approx 3 \times 10^{-14}$ Am. The resulting magnetic field, strictly speaking, the magnetic induction **B**, may be deduced from the Biot-Savart law [8]:

$$\mathbf{B(r)} = \frac{\mu_0}{4\pi} \frac{\mathbf{Q(r')} \times (\mathbf{r} - \mathbf{r'})}{|\mathbf{r} - \mathbf{r'}|^3} \tag{2.2}$$

where μ_0 is the permeability of free space and has a value of $4\pi \times 10^{-7}\text{Hm}^{-1}$ in SI units, and $\mathbf{r'}$ and $\mathbf{r}$ are the position vectors where the current dipole **Q** is located and the point where the magnetic field is evaluated, respectively. The permeability of biological tissues may be considered equal to that of free space, as long as there are no ferromagnetic particles within the tissue. The magnetic field is a vector described by three independent components (B_x, B_y, B_z) if Cartesian coordinates are used, or by one radial component B_n plus two tangential components (B_{t1}, B_{t2}) in the case of spherical coordinates. The field strength decreases as the square of the distance from the dipole (refer to Equation 2.2): for a pyramidal cell, which can be perhaps 4 cm from the sensor, the strength of the generated magnetic field is then $B \approx 0.002$ fT. The field is too weak to be detectable, even by the most sensitive magnetometer; consequently, the magnetic measurement is never sensitive to a single neuron. If n current dipoles are simultaneously operating, the total magnetic field is expressed by the vector sum of all the single fields: $\mathbf{B} = \mathbf{B_1} + \mathbf{B_2} + \cdots + \mathbf{B_n}$. If the dipoles are located very close to one another, say within few cubic millimeters, and oriented in the same direction, **B** may be considered as being generated by only one equivalent current dipole with strength equal to n times the strength of the single dipoles. More than 50,000 neurons must be simultaneously active to produce a magnetic field about 100 fT, which is typically recorded over the scalp in response

to simulation of a sensory system [10]. Therefore, MEG is a macroscopic recording of the neural activity. This also explains why postsynaptic activities give a much larger field than a lot of action potentials do: to build up a detectable field, many action potentials must occur in adjacent axons within 1 ms, since the signal is only 1 ms long. On the other hand, postsynaptic activities last for 10 ms or more, so that there is much more time to add up all single fields [10]. Furthermore, in case of an action potential, the generated field is the sum of the two fields coming from two opposite dipoles (namely a magnetic quadrupole), so that its amplitude decreases more rapidly with the distance between the source and the sensor.

It is commonly agreed that postsynaptic activity is responsible for the measured middle- and long-latency components of evoked response potentials (ERPs) and evoked response fields (ERFs), whereas the earliest components of cortical activity and certain components of brain-stem response may well represent coherent volleys of action potentials [9].

2.3. Quasistatic Approximation of Maxwell's Equations

The previous section described structural details of the brain as well as neuronal electrical activity. When the conductivity σ and the electric current generators in the brain are known, Maxwell's Equations and the continuity equation $\nabla \cdot \mathbf{J} = -\partial \rho / \partial t$ can be used to calculate the electric field $\mathbf{E}$ and the magnetic field $\mathbf{B}$, where $\mathbf{J}$ and ρ are the total current density and the charge density, respectively [8].

Maxwell's Equations are the fundamental laws describing how the electric and magnetic fields arise and interact. They are considerably simplified if the following two approximations are made: first, the permeability of tissue in the head is that of free space, i.e., $\mu = \mu_0 = 4\pi \times 10^{-7} \mathrm{Hm}^{-1}$; secondly, in the calculation of $\mathbf{E}$ and $\mathbf{B}$, $\partial \mathbf{E}/\partial t$ and $\partial \mathbf{B}/\partial t$ are ignored as source terms [11]. With these two approximations, to compute the electric field $\mathbf{E}$ and the magnetic induction $\mathbf{B}$ caused by the bioelectric source $\mathbf{J}$, which is often referred to as the *forward problem*, the use of the quasistatic approximation of the Maxwell's Equations is justified [11, 12] and the approximation is stated by the equations

$$\mathbf{E} = -\nabla V \tag{2.3}$$

$$\nabla \times \mathbf{B} = -\mu_0 \mathbf{J} \tag{2.4}$$

$$\nabla \cdot \mathbf{B} = 0 \tag{2.5}$$

$$\mathbf{J} = \mathbf{J}^i + \sigma \mathbf{E} \tag{2.6}$$

where V is the electric potential and $\mathbf{J}$ is the total current density, which is the the sum of the *impressed current* $\mathbf{J}^i$ due to the electromotive force impressed by biological activity in conducting tissue and the *Ohmic current* $\sigma \mathbf{E}$.

Based on the above equations, we can derive expressions for the electrical potential V and magnetic induction $\mathbf{B}$ measured at point $\mathbf{r}$ due to the current density $\mathbf{J}$ at point $\mathbf{r}'$, with the electrical conductivity σ assumed to be constant:

$$V(\mathbf{r}) = \frac{1}{4\pi\sigma} \int \frac{\mathbf{J}(\mathbf{r}') \cdot (\mathbf{r} - \mathbf{r}')}{|\mathbf{r} - \mathbf{r}'|^3} d^3 \mathbf{r}' \tag{2.7}$$

$$\mathbf{B}(\mathbf{r}) = \frac{\mu_0}{4\pi} \int \frac{\mathbf{J}(\mathbf{r}') \times (\mathbf{r} - \mathbf{r}')}{|\mathbf{r} - \mathbf{r}'|^3} d^3 \mathbf{r}' \tag{2.8}$$

The second of these equations is known as the Biot-Savart law.

For a dipolar source, V is given by

$$V(\mathbf{r}) = \frac{1}{4\pi\sigma} \frac{\mathbf{Q}(\mathbf{r}') \cdot (\mathbf{r} - \mathbf{r}')}{|\mathbf{r} - \mathbf{r}'|^3} \tag{2.9}$$

and $\mathbf{B}$ is obtained from Equation 2.2.

2.4. Primary Sources

With the help of the simple current dipole model, many aspects of the brain electrical activity may be explained in terms of equivalent dipoles and their related extracellular currents, because the transmembrane contribution is so weak that it can be negligible [9, 13]. Usually the intracellular currents are modelled as current dipoles and referred to as *primary sources*, since they represent the active origin of the neuromagnetic field, whereas extracellular currents are referred to as *volume currents* (or *return currents*) and affected by the conductivity and shape of the surrounding medium. The expression of the total current density flowing inside the

medium is therefore $\mathbf{J} = \mathbf{J}^p + \mathbf{J}^v$.

The electric potential V^p and magnetic field $\mathbf{B}^p$ generated by $\mathbf{J}^p$ can be considered as coming from a focal point-like generator, i.e., a current dipole, whose contributions to V^p and $\mathbf{B}^p$ are given in Equations 2.9 and 2.2, respectively.

The generator model for the volume currents is more flexible and can be viewed as a continuous distributed source. The contributions to the two physical measurements outside the brain (V and $\mathbf{B}$) may be expressed in terms of the electric potential V and the conductivity of the tissue σ. According to Ohm's law, the volume current density is proportional to the electric potential: $\mathbf{J}^v = \sigma \mathbf{E} = -\sigma \nabla V$. The expression for the magnetic field $\mathbf{B}^v$ generated by $\mathbf{J}^v$ is therefore

$$\mathbf{B}^v(\mathbf{r}) = -\frac{\mu_0}{4\pi} \int \frac{\sigma \nabla V(\mathbf{r}') \times (\mathbf{r} - \mathbf{r}')}{|\mathbf{r} - \mathbf{r}'|^3} d^3 \mathbf{r}' \tag{2.10}$$

If there is more than one change in σ, such as in a three-sphere head model, but each is a uniform and finite medium (i.e., piecewise homogeneous conductor), by using some vector calculus, $\mathbf{B}^v$ may be expressed as the sum of all the discontinuities in σ:

$$\mathbf{B}^v(\mathbf{r}) = \frac{\mu_0}{4\pi} \sum_{j=1}^{n} (\sigma_j^{out} - \sigma_j^{in}) \int \frac{V(\mathbf{r}')\mathbf{n}(\mathbf{r}') \times (\mathbf{r} - \mathbf{r}')}{|\mathbf{r} - \mathbf{r}'|^3} dS_j \tag{2.11}$$

where σ_j^{in} and σ_j^{out} are the conductivities on the inner and outer sides of S_j, $\mathbf{n}$ is an outward unit vector normal to the surface S_j, and dS_j is a surface element. The fact that the integral is carried out over the surface of the conducting object means that only the shape of the boundary is important.

Similarly, V^v can be written as:

$$V^v(\mathbf{r}) = \frac{1}{4\pi\sigma} \sum_{j=1}^{n} (\sigma_j^{out} - \sigma_j^{in}) \int \frac{V(\mathbf{r}')\mathbf{n}(\mathbf{r}') \cdot (\mathbf{r} - \mathbf{r}')}{|\mathbf{r} - \mathbf{r}'|^3} dS_j \tag{2.12}$$

where σ is the electrical conductivity of the medium surrounding the point $\mathbf{r}$.

2.5. Secondary Sources

The terms $(\sigma_j^{out} - \sigma_j^{in})V(\mathbf{r}')\mathbf{n}(\mathbf{r}')dS_j$ in Equation 2.11 are not real currents and are often termed as secondary currents. They are equivalent *secondary sources* at the boundaries and oriented perpendicular to them. This leads to two important implications. First, the effect of secondary sources is stronger for large changes in conductivity between the inside and outside the conducting medium and for large electric potential on its surface. This is true for any shape of the conducting object. Secondly, if the sphere model is used for modeling the head, all the secondary sources are <u>radially</u> oriented and thus produce no <u>radial</u> magnetic field outside the head.

These fictitious currents are the first evidence of the non-uniqueness of the inverse problem in MEG. The interesting point about the secondary currents is that the only information we need to calculate them (and thus to calculate the effect of volume currents) is the information on the conductivity discontinuity at the boundaries and on the electrical potential only at those surfaces, and not anywhere else.

The fact that different sources may induce the same magnetic field maps implies that one has to restrict the class of sources acceptable to explain the maps from anatomical considerations or often simplifying argument. The neuroscientist is not interested in multipole moments, equivalent current loops, not even in the magnetic field or the field gradient. These are mere tools in the determination of the location and other characteristics of brain activity [1]. Therefore, our goal is to express the neuromagnetic data in the form of estimates of primary currents in the brain. The task of the analysis of MEG (and/or EEG) signals is to determine the focal generators (primary sources) and to model the properties of the medium and its boundaries (medium contributions to the signal) [3]. To date, most of the MEG data has been processed using the model for the "equivalent current dipole" immersed in a conductor. This model corresponds to a well-localized generator and therefore a well-localized primary source, confined to a small region of the brain. In this model, the structure of the head has still to be further specified in order to predict the MEG maps from the sources.

2.6. Tangential Components of the Magnetic Field

As discussed previously, the magnetic field is completely described by three independent components: one component normal to the surface $\mathbf{B}_n$, plus two tangential components $\mathbf{B}_{t1}$ and $\mathbf{B}_{t2}$. By measuring only $\mathbf{B}_n$, it seems that we are somehow losing information from the source we are investigating. However, as Hari and Ilmoniemi pointed out [14], the other components can be calculated from the derivatives of $\mathbf{B}_n$ by means of Maxwell's Equations. Since the measurements are made outside the body, $\nabla \times \mathbf{B} = 0$. Take a Cartesian coordinate system for example, where $\mathbf{B}_n = \mathbf{B}_z$, the above vectorial equation gives three scalar equations. In particular, we have the following equation for the y component:

$$\frac{\partial B_z}{\partial y} = \frac{\partial B_y}{\partial z} \tag{2.13}$$

The field $\mathbf{B}_y(z)$ can then be recovered by demanding that $B(\infty) = 0$:

$$B_y(z) = \int \frac{\partial B_z}{\partial y} dz \tag{2.14}$$

This argument can also be applied to B_x, and it is correct regardless of the conductor geometry. This means that, from the computational point of view, all field components can be utilized easily and that there is no preferred component.

In practical measurements, when the simple sphere model is used, the radial component B_n of the magnetic field should be preferred, because B_n is produced by the primary current alone (though the way B_n changes in space is determined by both primary and secondary fictitious currents). The derivative of B_n may be detected more easily by using axial gradiometers (measuring B_z) than using planar gradiometers (measuring B_x and B_y). On the other hand, a planar gradiometer peaks right above a current-dipole source (refer to later Chapters 3 and 4), hence a less extensive set of sensors is needed to pick up the essential field data from a local source. In this case, the planar gradiometer senses the tangential components (or their derivatives) of the magnetic field.

2.7. General Techniques for Brain Studies

For the last few decades, many advances have been made in illuminating the structure and function of the brain. Several successful biomedical imaging methods have

been developed, such as X-ray tomography, magnetic resonance imaging (MRI) and positron emission tomography (PET), electroencephalography (EEG) and magnetoencephalography (MEG). In the following discussion, emphasis will be placed on the potential uses of the these techniques; their advantages and disadvantages will also be outlined.

2.7.1. Brain Imaging Techniques

The study of the regional anatomy of the living brain has been revolutionized by the development of two imaging techniques: PET and MRI. These methods, particularly MRI, depict both brain structure and aspects of brain function. As a result, clinicians can now localize lesions of the the brain with remarkably accuracy without invasive procedures that interfere with normal function and even endanger life. Moreover, a neuroscientist can examine the brain while people think, perceive, and initiate voluntary actions.

Imaging the brain with X-rays depicts structures with large differences in absorbency of radiation:

Until recently only three radiological techniques were available to obtain images of the living brain: conventional radiography, still used for examining the skull; pneumoencephalography, replaced by newer imaging techniques; and angiography, still the best method for studying brain vasculature. Each of these methods relies on transmission of X-rays through the tissue and consequently cannot image neural structures.

A *conventional radiograph* of the head is a picture of the skull and its contents. To produce a radiograph, a broad beam of X-rays is passed through the skull towards an X-ray film. Different tissues appear on X-ray films in inverse proportion to their absorption of X-rays. A radiograph is thus a two-dimensional representation of a three-dimensional object, a major limitation in studying the brain. Another major limitation is that only those structures with large differences in X-ray absorbency are distinguished. Therefore it cannot detect the grey matter or white matter, nor distinguish between them.

The advantage of a conventional radiograph is that it has high spatial resolution, on the order of millimeter. Radiographs are therefore suitable for studying the skull

and for detecting the distribution of radio-opaque compounds that enhance the contrast between intracranial structures, such as those used in angiography to image the arteries and veins of the brain.

Unlike bone and other calcified tissue, air absorbs very little radiation and appears dark in radiography. This fact has been exploited by neuroradiologists for imaging the ventricular system of the brain by a method called *pneumoencephalography*. To obtain a pneumoencephalogram, a small amount of cerebrospinal fluid is removed from the subarachnoid space by spinal tap and replaced with air. Studying the path by which air enters the ventricles enables one to review the organization of ventricular system. Although pneumoencephalography is informative, it is also painful and sometimes dangerous. It is therefore rarely used now having been superseded by computerized tomography (CT) and magnetic resonance imaging (MRI).

Angiography provides a wealth of information on the anatomy of the cerebral vasculature and the speed of circulation of blood in the brain in normal and diseased regions. In angiography the patient receives an intravascular injection of a radio-opaque material. This results in the precise definition of blood vessels that contain the circulating radio-opaque material. Angiography is the optimal procedure for diagnosing lesions of the intracranial vascular system. Its drawback is that it is invasive; it involves intravascular injection of radio-opaque material, which may cause neurological complications. Recent advances in MRI allow intracranial vessels to be imaged through a non-invasive technique called magnetic resonance angiography (MRA). With MRA it is possible to show the entire vascular system from many angles, to evaluate accurately the morphology of vessels and the detection of small atherosclerotic plaques, and to measure brain perfusion as well. However, compared with conventional angiography, it has poorer spatial resolution.

Computerized Tomography has improved the depiction of brain structures within the skull:

X-ray computerized tomography (CT) allows us to explore the regional anatomy of the brain in normal subjects and in patients suffering from neurological disease. In contrast to conventional radiography, the CT scan distinguishes grey and white matter. Computerized tomography is similar to conventional radiography in that the image is produced by the differential absorbtion of X-rays, but is more sensi-

tive. The CT scan is an image of a single plane or section of tissue, which is a true two-dimensional representation of a two-dimensional object, in contrast to a conventional radiography, which represents a three-dimensional object in two dimensions.

X-ray computerized tomography provides images of bone, brain tissue, and cerebrospinal fluid. Even structures within the brain can be distinguished, such as the thalamus and basal ganglia. Because it reveals anatomical detail, CT scanning was immediately recognized by the clinical community as being a method which provided enormous help with the diagnosis and treatment of clinical disease. The cost of a fourth generation CT scanner is US\$ 3 to 4 million. Nevertheless, the views of the brain produced by computerized tomography are static, that is, CT scans allow one to explore the structure but not the function of the brain.

Electrical Impedance Tomography offers a safe, portable and non-invasive way to monitor what is happening inside the body:

Electrical Impedance Tomography (EIT) is a recently developed imaging technique which enables images of the impedance distribution within a subject to be obtained from measurement with a ring of external electrodes [15].

EIT produces pictures of "slices" through the body, similar to those from CT scanners. At present, images are two-dimensional, i.e. they are made as if all current flowed in the plane of the electrodes, so that the image represents impedance changes in the electrode plane only. As current flows in 3-D, this is an over-simplification. However, CT scanners cost over £1 million and are large, so cannot be used at the bedside for long-term monitoring. By comparison, EIT equipment is small, simple and cheap. The machine which produces instant pictures costs about £30,000 and is the size of a tea chest. It takes 24 frames a second and is controlled by a small computer [16]. However, EIT cannot take images through the skull, so surgery is still necessary, though the electrodes can be placed around the brain instead of penetrating it. Furthermore, at present EIT cannot compete with most other brain imaging methods in terms of spatial resolution [17].

There is currently considerably interest in the technical development of EIT. 'The Sheffield EIT system' has been constructed and is available for clinical use. One potentially fruitful application of this technique lies in imaging the impedance in-

creases of tens of percent which occur in the brain in conditions such as cerebral ischaemia, epilepsy or spreading depression [18, 19, 20]. The common feature of these conditions is that neurons outrun their energy supplies and as a result ions and water move from the extracellular to the intracellular compartment. With measurements using alternating current at above 10 kHz for less risk of exciting nerves and reducing electrode problems [20], most current travels in the extracellular space, so this causes an impedance increase.

Positron Emission Tomography yields images of biochemical processes of the living brain:

Positron emission tomography (PET) provides images of brain function and has revolutionized the study of human cognitive processes and of psychiatric and neurological disease. PET combines the principles of CT and radioisotope imaging. In CT, the X-ray source and detector are rotated around the head and the image is generated by differences in radiodensity. In PET, a positron-emitting isotope, usually oxygen-15 or carbon-11, is substituted for the normal stable isotope in a compound used in the body. The radiochemical is either inhaled or injected as a very low concentration tracer. After a little while, it is transported to the brain (the subject lies with the head inside a ring of many closely spaced γ-ray detectors). The chosen isotope decays by emitting positrons and its distribution in the brain marks spatial variations in cerebral blood flow (CBF). Each emitted positron travels for a short distance before meeting an electron and then annihilates by giving off two γ-rays in opposite direction. The detection of the two gamma rays in coincidence provides an estimate of where the original positron/electron annihilation took place. This in turn provides estimates of the regional CBF (rCBF) distribution. Because rCBF is regulated by the demand made by neural activity, a map of rCBS changes in response to a particular brain task gives a good indication of the areas of increased neural activity [21, 22, 23, 24]. Another very similar technique to PET is the single-positron emission computed tomography (SPECT) [25]. SPECT is less sophisticated relative of PET, but still radioactive tracers are either injected or inhaled, and the level of brain radioactivity is imaged. A gamma camera is also used, so spatial resolution is not as high as that achieved by PET, which has a resolving power of 5-10 mm in the best PET systems.

A powerful application of PET scanning is the mapping of the glucose metabolism

of neurons. The method reveals active nerve cells, where activity is related to the utilization of glucose. At present, the resolution of PET systems has increased to a level that individual gyri are visible so that information relating to the metabolic functioning of detailed brain structures is possible.

PET's disadvantages are its high initial cost (over US$ 6 million), inability to measure short-term changes in brain function due to the low levels of radioactivity, and the necessity of inflicting a significant radiation dose on the subject. With a single subject, it is not possible to study multiple conditions, involving multiple tracer injections. Up to very recently (1990), almost all the PET studies were based on the data averaged over 10 or more subjects, which caused serious problems in analysis because of the inter-subject differences in terms of brain structure and functional organisation. Follow-up studies on the same subject(s) were also difficult due to the length of time required to elapse between scanning sessions. A recent advance in PET at Hammersmith Hospital (London), namely, removing the γ-absorbing plates between the detectors, has made it possible to perform single-subject studies in which no cross-subject averaging was needed, and consecutive scans (up to 12) on a subject performing a series of tasks [26].

Magnetic resonance imaging reveals the structure and the functional state of the central nervous system:

Like PET, magnetic resonance imaging (MRI) is based on computerized tomography and can be used to explore function as well as structure, but with much better spatial resolution. This powerful imaging technique can distinguish different body tissues because of their individual chemical compositions. For example, grey matter can be strikingly differentiated from white matter. As a result, the spatial resolution of MRI is comparable to that of fixed and sectioned anatomical material. Apart from showing the water content of grey and white matter, MRI can show the distribution of naturally occurring elements with paramagnetic properties or artificially introduced substances.

An MRI image of the brain is based on the fact that many nuclei, such as hydrogen nuclei (protons) have a tiny nuclear magnetic moment and by exciting the magnetic nuclei with a circularly polarized radio-frequency magnetic field, quantum transitions can be induced and hence enable a signal to be detected by a conducting

receiver coil placed around the subject [27]. MRI can reveal minute differences in tissue water concentration and is therefore a sensitive technique for the detection of brain lesions. As a matter of fact, until very recently, the majority of MRI scans have been directed towards anatomy and pathology. Only in the last few years, there has been a surge in research into developing MRI sensitive to some aspect of physiology related to brain function, namely, changes in blood oxygenation (related to changes in neuronal activity) [28].

Furthermore, MRI scanners also image other atomic nuclei of biological importance. For example, sodium scans reveal cerebral infarcts, neoplastic changes, and metabolism. MRI can also show the distribution of phosphorus. It is possible to discriminate among various compounds of phosphorus involved in energy production. By providing an in vivo chemical analysis, MRI can detect metabolic processes, but PET is currently more sensitive than MRI for detecting small concentrations of a labelled compound. MRI spectral imaging, a promising non-invasive technique, provides physiological information about the structures being examined, and thus has enormous potential in the investigation of brain functioning.

A newer development in MRI is the advent of functional MRI (fMRI), which is the study of structure-function relationship [29], e.g., links between particular regions of the brain and specific perceptual or cognitive competencies. Using pulsed magnetic fields, e.g., echo-planar imaging, a time series of brain images is collected, typically a hundred or more multi-slice volume scans in about 10 minutes. Sampling rates well within 100 ms are easily attainable, at the expense of spatial resolution; the crucial point however remains that change in blood oxygenation follows a much slow rate (a few seconds). While the brain images are taken, the subject alternates between the task of neurological interest and a control task [30, 31]. For instance, the subject may tap the fingers of their left hands and then rest. More complex control tasks may be chosen, such as tapping the fingers of the other hand − the choice depends on the neurological question being addressed. If there is strong activity, the active regions of brain cortex can often be seen in a simple difference image. More subtle changes can be picked out by statistical techniques, though substantial data is needed beforehand. An advantage of this technique over PET is that it is completely non-invasive and thus can be repeated many times in the same subject. This allows studies to be performed that involve monitoring a subject over a number of weeks, such as memory tasks. Additionally, the information obtained is of sufficient quality

that no inter-subject averaging is needed to achieve an acceptable signal-to-noise ratio. Many MRIs now in hospitals are easily converted to fMRIs, hence it is no surprise that fMRI has become one of the fastest growing new techniques of attempting functional brain studies.

Overview:

The high spatial resolution techniques now available allow both the structural and the functional organization of the human brain to be imaged. A key to these techniques is the ability to reconstruct two- and three-dimensional spatial information from simple radiographic or biochemical measurements. Therefore, computerized X-ray tomography has allowed us to evaluate the gross characteristics of brain structure. With the greater sensitivity of magnetic resonance imaging, the precise structure of the brain has been revealed with resolution that approaches that of low-magnification microscopic sections. With positron emission tomography, the biochemical composition of neural tissue can be monitored. Thus, the biochemical function of local neural circuits can be studied during perception, movement, and thought. By combining PET and MRI we have obtained new insights into behaviour by seeing how it is represented in the functional architecture of the human brain. These techniques have enabled us to localize more precisely disease processes and traumatic lesions in the brain, and develop therapies to deal with them. We now consider techniques with high temporal resolution.

2.7.2. EEG and MEG

An obvious similarity between EEG and MEG is that both techniques can record physiological signals in the millisecond range (recordings of functional brain activity). This feature separates these two techniques from CT and MRI, which evaluate anatomical features the brain, as well as from PET (or SPECT) and fMRI, which measure physiological brain activity (but on a time scale of seconds rather than milliseconds).

Origin of EEG and MEG signals:

As discussed in previous sections, EEG and MEG signals arise mostly from fluctuations in the resting membrane potential of the dendritic tree of cortical neurons caused by synaptic input, for example, excitatory and inhibitory postsynaptic potentials [32, 33, 34]. The fluctuations in the membrane potential cause passive

compensatory current flows both intracellularly and extracellularly. The extracellular currents spread through the brain and pass through the skull to the scalp. The amplitudes of the currents are severely attenuated as they pass through the poorly conductive skull. The surface distributions of the currents are also distorted because the conductivity and thickness of the skull vary considerably from one region to another. The currents produce voltage potentials that vary in amplitude over the scalp and that are measured with the electrodes of the EEG. Apart from the intracranial sources of currents, extracellular currents arise locally in the scalp from muscle membrane depolarizations. The muscle activity also appears in the EEG signal because of its proximity to the electrodes.

If the simple sphere model is used, and the axis of a gradiometer is oriented perpendicular to the head such that it measures just the radial component of the magnetic field, the measured magnetic field will only depend on the primary sources. If the axis is tilted relative to the head and measures the tangential component of the magnetic field, the measured magnetic field will be associated with both the primary and secondary sources [35, 36]. In practice, the axis of the gradiometer is usually oriented perpendicular to the head to measure just the primary currents. However, with the newer multichannel systems, one or more of gradiometers is often tilted relative to the head.

Signal measured with EEG:

The EEG measures the difference in potential between two electrodes. Since two electrodes are always compared, the choice of which pairs of electrodes are compared becomes very important. The main strategy is to place electrodes in straight rows over the head and compare each electrode to the electrodes on either side of it in the same row (bipolar recording). This technique reduces unwanted noise from distant sources (e.g. cardiac signal) because of common mode rejection, and draws attention to electrodes at regions of peak positive or negative electrical potential because of an apparent "phase reversal" in the pen deflection of the EEG machine. The strategy has had great clinical usefulness in the qualitative analysis of the EEG. However, some problems arise in the quantitative analysis of the resulting signal. Because the signal represents the difference in potential at two electrodes, the time course of the recorded signal may reflect simultaneous changes in electrical potential at both electrodes and may therefore not represent the actual time course of ampli-

tude changes at either electrode. In order to have a clearer picture of the change in amplitude with time at each electrode, a second strategy for linking electrode pairs is used. The second electrode of each pair is placed at an electrically quiet location on the scalp (referential recording). However, no electrode site is completely electrically quiet. A topographic map of electrical potential distribution over the head can be constructed from a referential recording; however, the map may be misleading. The choice of the reference electrode determines the location of zero potential [37]. One cannot look at an EEG topographic map with regions of positive and negative potential and assume that the source lies below the zero line between the oppositely signed regions. A change in the reference electrode can change the location of the zero line [37]. More likely, an inappropriate choice of reference electrode may make one of the two oppositely signed regions of electrical potential disappear, or it may give the impression of two oppositely signed regions when only one exists.

Some of the problems with reference electrodes can be overcome if the electrical potentials are converted to scalp currents. If one knows the conductivity of the scalp (poorly conductive), and the electrical potential at several points, one can estimate the amount of current between the adjacent electrodes by using the surface Laplacian, which acts as a spatial filter emphasizing local sources (both tangentially and in depth) over distant sources [38, 37]. One must use an array of electrodes to obtain a scalp current map, and the current estimates become less certain for electrodes at the outer edges of the array [37]. Although one can estimate scalp currents, it is not yet clear how useful this information will be for non-invasive intracranial source localization, since one must additionally include the uncertainty of the conductivity and the thickness of the skull.

Signal measured with MEG:

MEG measures magnetic fields that are mainly associated with intracranial currents that pass into the skull and scalp. If the ratio of conductivity of brain to skull is taken as 80:1 [9, 39], computer simulation strongly suggests that the contribution of scalp currents to MEG is not higher than 5% [39]. The small value means that it may be possible to ignore the skull and scalp. Furthermore, a magnetometer measures the absolute magnitude of the magnetic field (flux) and does not require a reference.

EEG and MEG differ in the neuronal populations they record. The EEG is in principle sensitive to dipoles oriented in any direction. However, the EEG may receive a larger contribution from a radially oriented dipole when both radial and tangential dipoles are present, if the head's conductivity is assumed to be spherically symmetric [40]. The MEG is only sensitive to tangentially oriented dipoles or the tangential component of a current distribution, due to the fact that a radially oriented dipole in a conducting sphere does not produce a magnetic field outside the sphere. As mentioned above, the inner surface of the skull is the relevant surface. In regions where this surface is not spherical, such as the floor of the temporal lobe and frontal fossa, or if the head is not spherical(!) [41], a radially oriented dipole may be detected to some degree. This different emphasis on neural population in sulci and gyri may be particularly helpful in charting neuronal activity that spreads from one region to another.

Topographic mapping with EEG and MEG:

The topographic maps of EEG and MEG also differ relative to the source of the measured neuronal activity. The actual differences depend on the particular EEG montage and on the configuration of the MEG detection coil. For the following discussion, the electrical potential map, obtained with a referential montage and distant reference electrode, will be compared with the magnetic field map obtained with a magnetometer, oriented to measure the radial magnetic field [40]. The EEG topography depends on whether only either radial or tangential dipoles are present, or both radial and tangential dipoles are present; while the pattern does not change for MEG. Figure 2.3 shows the difference between MEG and EEG maps due to a current dipole, with and without a radial component.

In the MEG map, the radial component B_z (in Cartesian coordinates) of the magnetic field is plotted. In the EEG maps, the potential V is plotted. Referring to Figure 2.3 (a) and (b), for a tangential dipole, the positive and negative regions of electrical potential will be at either end of the dipole and along the axis of the dipole. The two magnetic field extrema will be on either side of the dipole, and the magnetic field map will appear to be rotated $90°$ relative to the electrical potential map. For both maps, the source will lie halfway between the two regions of opposite sign. The slope of the electrical map is steepest along a line joining the regions of positive and negative electrical potential (i.e., in y direction). During source localization, errors
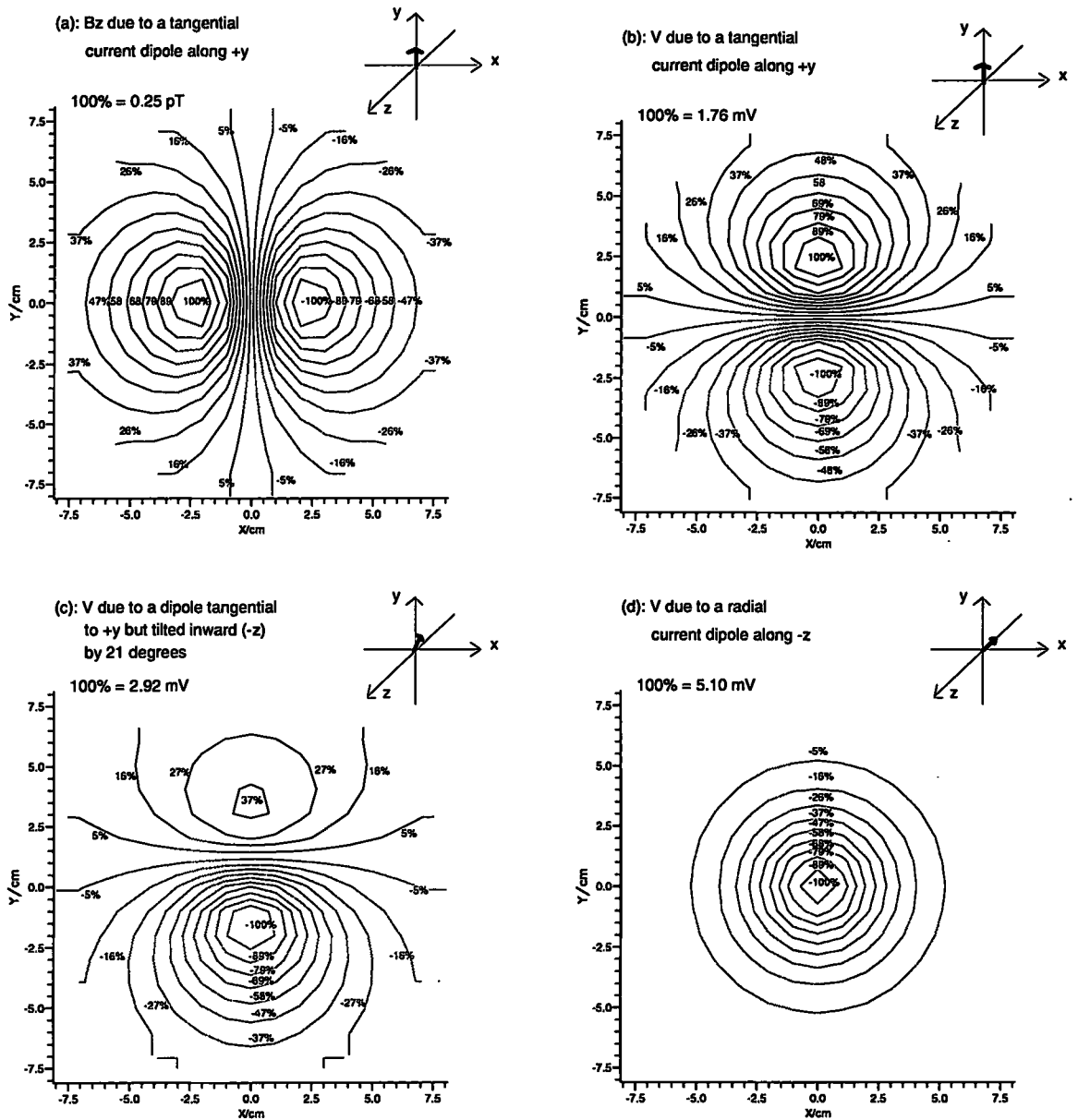
Figure 2.3 Comparison of topographic differences between EEG and MEG maps: a current dipole with its dipole moment of 1 A-m at 3 cm below the measurement point. The calculations of B_z and V are based on Equations 2.2 and 2.9, with $\sigma = 1\,\Omega^{-1}\mathrm{m}^{-1}$ for a simple simulation.

of localization in this direction will be most easily detected and corrected because of the steep slope of the potential map. This direction parallel to the dipole axis has been termed the "preferred" direction of localization for EEG [40]. The regions of positive and negative electrical potential change only gradually in the direction at right angles to the dipole axis (i.e., in x direction), and EEG should have more difficulty localizing sources along this direction. The situation is just opposite for MEG, because two magnetic field extrema are on either side of the dipole and steepest slope of the magnetic field map is at right angles to the dipole axis (i.e., in x direction). MEG should be better able to localize sources in the direction at the right angles to the dipole axis (i.e., in x direction) and should have difficulty to localize the sources parallel to the direction of dipole axis (i.e., in y direction). This difference in "preferred" direction of localization may have implications for certain clinical applications of the two techniques.

The electrical potential map becomes more complicated for a combination of tangential and radial dipoles, as well as for a dipole that has both tangential and radial components. If the dipole is tilted just 21° from the tangential orientation towards radial (see Figure 2.3 (c)), the ratio between the two peaks of electrical potential has been estimated to change from 1:1 to nearly 2:1. If the dipole is further tilted so that it is oriented radially (see Figure 2.3 (d)), only one of the two electrical potentials is detected on the surface above the dipole. The magnitude of the detected electrical potential has been estimated to be nearly three times of the electrical potential peak when the dipole is oriented tangentially. The above observations are in agreement with those in [40].

In the brain, the radially oriented pyramidal cells are located in the crowns of gyri, whereas tangentially oriented pyramidal cells are located in the sulci and are farther from the scalp. If just a tangentially oriented dipole is present, the EEG should show both electrical potential peaks. However, if a radially oriented dipole is present in the vicinity of the tangentially oriented dipole, the EEG pattern will be dominated by the contribution from the radial dipole and may show primarily one peak [40]. The magnetic field pattern does not change if both tangential and radial oriented dipoles are present because the MEG still detects just the tangentially oriented dipole. Examples of predominantly tangentially oriented dipoles that can be seen in the EEG are the N20 of the somatosensory evoked response and the epileptiform spikes of benign Rolandic seizures. On the other hand, most epileptiform spikes from

the temporal lobe show just one potential peak on the scalp surface, and many other EEG features such as slow waves and vertex sharp waves show just one potential peak. Some evoked potentials, such as the N100 of the auditory evoked response, have been difficult to interpret with EEG because of complex combinations of tangentially and radially oriented dipoles. MEG has been helpful in localizing temporal lobe epileptiform discharges [42] and in interpreting the auditory N100m [43].

Source localization accuracy:

The strongest contributions to both EEG and MEG come from postsynaptic currents flowing in the dendritic tree of neurons, located mainly in the cerebral cortex for MEG and in the whole brain for EEG [44]. MEG is most sensitive to activity in fissure cortex, where the source currents flow tangentially to the surface of the head. EEG receives contributions from both radial and tangential currents and is also relatively more sensitive than MEG to deep sources.

In practice, one of the most important differences between EEG and MEG recordings is encountered in the case of concurrently active multiple sources. MEG 's selectivity to tangential currents and the more localized field patterns significantly facilitate data interpretation. Examples include successful differentiation between activities of the first and second somatosensory areas SI and SII [45], detection of new aspects of spontaneous brain rhythms, detection of selective activation in subareas of SI, and detection of somatosensory activity [46].

EEG's ability to detect both tangential and radial sources has yielded interesting results as well. Examples include successful differentiation between tangential and radial sources for cortical auditory and somatosensory evoked potentials and identification of radial sources in the frontal areas for some cognitive evoked potentials.

The differences between EEG and MEG explain, for example, the discovery of different aspects of the topographic organization of the human brain auditory cortex with the two methods. A study for the comparison between EEG and MEG by Cohen and co-workers has since provoked heated discussions about aspects of the comparisons. Cohen et al. claimed that MEG is only marginally more accurate than EEG in locating cerebral electrical activity [47]. The statement was however challenged by Williamson [48] and Hari [49] on methodological grounds. It now ap-

pears that the controversy is settling to what one would expect anyway from basic electromagnetic theory [50, 3].

In general, if the conductivities of all tissues were exactly known, the locating accuracy for a single dipole within a spherical model in the absence of noise would be about one-third better for EEG than for MEG [44]. In reality, the exact conductivities are not known, and thus the relative accuracy of EEG is decreased; while on the other hand, concentric inhomogeneities do not affect the magnetic field. Moreover, the source location accuracy of both methods depends on the signal-to-noise ratio and on the adequacy of source and medium models and is best for superficial sources.

Cost and capability of EEG and MEG:

One of the main differences between EEG and MEG is cost. A 128-channel EEG machine costs about US$ 100,000, whereas a seven-channel magnetometer with a magnetically shielded room costs about US$ 1 million. However, MEG represents a new and changing technology. A dual 37-channel system, or a helmet, each costs about US$ 2.5 million. With the emergence of new multichannel systems, MEG recordings have become clinically feasible to the point that the price of MEG instrumentation per channel is decreasing, albeit rather slowly.

Another obvious difference between the methods is in the recording technique. EEG uses electrodes applied to the scalp with conductive paste, and it measures scalp potential differences. MEG uses a magnetometer that is positioned close to the head surface, and it measures extracranial magnetic fields. For the routine EEG, electrodes are evenly spaced around the head, and recording of the EEG signal is done over the entire head at one time. Therefore, one advantage of the EEG is the ability to record the complete scalp potential of spontaneous events such as epileptiform discharges. In addition, since the scalp electrodes are small and secured to the head, continuous monitoring can be accomplished without too much discomfort to the patient, and the likelihood of recording rare events such as seizures is increased.

With the advent of larger magnetometer arrays, such as the Siemens and BTi (twin) 37-channel systems, and the latest CTF and Helsinki whole-head coverage systems, the differences in length of recording time and coverage of the head between EEG and MEG are expected to diminish. For example, an EEG with 128 closely spaced

electrodes for careful mapping of evoked response or epileptiform discharges may require a hour or so for the placement of the electrodes and recording signals; while for MEG, as no electrodes are needed for MEG recordings, the preparation and recording time for a MEG mapping is very short, it may just take minutes.

Furthermore, no problems similar to the variations in electrode conductivity, electrode-skin interface or electrode polarization are encountered in MEG. In addition, DC-coupled MEG recordings are possible, although technically it is difficult to implement because even shielded rooms are not very effective at low frequency (e.g., below 1 Hz), the availability of software for noise elimination undoubtedly facilitates the problem.

However, during MEG recordings the subject has to stay immobile. Therefore, MEG can not be used to measure activity during motor seizures with major motor symptoms or in uncooperative subjects. Moreover, MEG can not be used in electrically noisy environments such as intensive care units, operating rooms and so on. The implementation of the MEG technique will be discussed fully in the next chapter.

Overview:

EEG and MEG are the only non-invasive methods with millisecond temporal resolution for studying the functions of the human brain. For quite a long time, many controversies have existed regarding the comparisons and relationship between EEG and MEG [47, 48, 49, 44]. It is probable that the best results in localization and three-dimensional description of an intracranial source will be obtained through the use of MEG and EEG together. MEG will be useful in recording the tangential components of the source and in obtaining their intracranial location, whereas EEG will provide necessary information about the radial components.

2.8. Models for the Medium within the Brain

The pattern of extracellular currents is established by the conductivity and shape of the conducting medium surrounding the primary source. This medium consists of several components: cerebral tissue, cerebral fluid, membranes, skull, and scalp. The conductivity of these different tissues varies from one tissue to the other. The task of modeling such a complicated medium is not easy. Therefore, it is essential

to propose some simple, practical but yet fairly realistic models of the medium for getting round the inhomogeneous problem of the head. One possible way to avoid this problem is to model the head by such special geometric shapes as a sphere or semi-infinite slab and use the radial or perpendicular component of the magnetic field only.

2.8.1. Infinite Half Space

This model consists of a flat surface of infinite extent, with an insulating material on one side (e.g. air) and a uniform conductor on the other. According to [51], for a dipolar source, the magnetic field **B** is given by,

$$\mathbf{B} = \frac{\mu_0}{4\pi K^2}(\mathbf{Q} \times \mathbf{a} \cdot \hat{\mathbf{e}}_z \nabla K - K \hat{\mathbf{e}}_z \times \mathbf{Q}) \tag{2.15}$$

where **r** is the point where **B** is measured and **r**′ is the location of the current dipole; $\mathbf{a} = \mathbf{r} - \mathbf{r}'$, $a = |\mathbf{a}|$, $K = a(a + \mathbf{a} \cdot \hat{\mathbf{e}}_z)$, and $\nabla K = (2 + a^{-1}\mathbf{a} \cdot \hat{\mathbf{e}}_z)\mathbf{a} + a\hat{\mathbf{e}}_z$.

From the above equation, it can be seen that only the horizontal component of the dipole (i.e., parallel to the surface) contributes to **B** outside the conductor. In other words, neither the boundary nor any component of $\mathbf{J}^p$ perpendicular to the boundary contributes to the component of **B** which is normal to the boundary. Therefore, the component of **B** field normal to the surface in the infinite half space modeling is solely due to tangential components of $\mathbf{J}^p$ [9, 52].

2.8.2. Homogeneous Head Model

A typical choice, developed for electroencephalographic (EEG) modeling, is the so-called *three-sphere model*, which is concentric and homogeneous [53, 54]. Despite its crudeness, this model works well especially when used with magnetic data recorded over the occipital area, whereas more realistic models are likely to be used in the temporal area. The reason for this is that when the homogeneous spherical model is selected, the magnetic field does not depend on medium conductivity, as will be shown later.

The concentric and homogeneous sphere model is very convenient for other reasons. The component of the magnetic field normal to the sphere $\mathbf{B}_n$ is not affected by volume currents [55, 1]. This means that $\mathbf{B}_n$ reflects only the distribution of intra-

cellular currents, hence simplifying the localization task. Furthermore, because the cortical pyramidal neurons are oriented perpendicularly to the cortex surface, generators located inside the fissures are optimally detected by magnetic measurement. This is not a crucial limitation, at least as long as primary areas (most of them are located in the fissures) are to be investigated. Additionally, the single homogeneous sphere model and the multiple homogeneous sphere model are completely identical, in other words, any spherical model can be generalized to spheres with a purely radially changing conductivity. As a matter of fact, this model is so commonly used that it is usually referred to as a "spherical model" without mentioning homogeneous, and the magnetic field normal to the surface $\mathbf{B}_n$ is referred to simply as "magnetic field".

In the usual situation where magnetic measurements are performed outside the head (i.e., the conducting medium), there is a different method which can be used to evaluate $\mathbf{B}$. Outside the conductor, there are no biological currents and the magnetic field must obey the equation $\nabla \times \mathbf{B} = 0$. In this case, a magnetic potential U can be given, similar to the usual electric potential V. From the magnetic potential the magnetic field can be obtained as $\mathbf{B} = \mu_0 \nabla U$. If a conductor with spherically symmetric conductivity is used, $\mathbf{J}^p$ is assumed as a current dipole $\mathbf{Q}$ at $\mathbf{r}'$ inside the conductor, and the origin is chosen to coincide with the center of the conducting sphere, according to [51], we have

$$U(\mathbf{r}) = -\frac{\mathbf{Q} \times \mathbf{r}' \cdot \mathbf{r}}{4\pi F} \tag{2.16}$$

where $F = a(ra + r^2 - \mathbf{r}' \cdot \mathbf{r})$, $\mathbf{a} = \mathbf{r} - \mathbf{r}'$, $a = |\mathbf{a}|$ and $r = |\mathbf{r}|$. Applying $\mathbf{B} = \mu_0 \nabla U$, we obtain the expression for $\mathbf{B}$ outside the conductor:

$$\mathbf{B}(\mathbf{r}) = \frac{\mu_0}{4\pi F^2}(F\mathbf{Q} \times \mathbf{r}' - \mathbf{Q} \times \mathbf{r}' \cdot \mathbf{r} \nabla F) \tag{2.17}$$

where $\nabla F = (r^{-1}a^2 + a^{-1}\mathbf{a} \cdot \mathbf{r} + 2a + 2r)\mathbf{r} - (a + 2r + a^{-1}\mathbf{a} \cdot \mathbf{r})\mathbf{r}'$

The above expression looks rather complicated, but it implies an important feature, that is, the magnetic field does not depend on the medium conductivity. Additionally, it points out immediately that a radial dipole does not generate magnetic field outside the sphere: If the current dipole is radially oriented, $\mathbf{Q}$ is parallel to $\mathbf{r}'$; therefore, $\mathbf{Q} \times \mathbf{r}' = 0$ and $\mathbf{B} = 0$. Furthermore, with this approach, the volume currents and primary currents are combined together in a single expression. This is very convenient especially when analyzing multichannel data, where perhaps not

all the pickup coils are simultaneously positioned perpendicularly to the subject's head. This is justified by the fact that in this model the radial component of the magnetic field is due to the tangential component of the primary source only, while the tangential component of the magnetic field may be a mixture of the fields due to both the primary and secondary sources as secondary sources only contribute to the magnetic field in the tangential direction. However, when such data are analysed, it must be remembered that some contributions from secondary sources are likely to be present due to the approximate nature of the spherical assumption for the head surface.

Furthermore, the magnetic field pattern generated by a current dipole inside a homogeneous conducting sphere is very distinct and thus easy to interpret the map from the source: there are two field extrema; a maximum and a minimum. The position of the dipole inside the sphere is simply related to the characteristics of the pattern: the dipole lies half-way between the maximum and the minimum of the field, at a depth d which can be evaluated by $d = D/\sqrt{2}$, where D is the distance between the two maxima with opposite polarity [11]. For superficial sources, the spherical model gives similar results to the infinite half space model.

Finally, it is worth noting that computing V on the surface of an infinite half space or a spherical conductor is more complicated than the calculation of $\mathbf{B}$ discussed above due to the fact that radial sources usually produce a non-constant V on the surface of such a conductor [51].

2.8.3. Realistic Head Model

In the temporal and frontal regions, spherical models are not good representations of the inner surface of the skull. The studies in [39, 56, 57, 58] indicate that the spherical model provides accuracies of 2 mm or so in occipital areas for determining equivalent dipole source positions from magnetic data. In temporal, especially frontal areas, the errors for magnetic location are expected to be much greater [59]. One of the problems in applying a uniform spherical model is to determine the position for the center of the sphere, or the radius of curvature. Hari suggested that it should be determined by the curvature of the inner surface of the skull just above the source [14]. Yamamoto experimentally demonstrated that an accuracy of better than 3 mm with a sphere model can be obtained consistently for sources in superior

temporal lobe, provided that the center of the sphere is determined by the curvature of the skull over this area [60]. In this way, the source of the N100 component of the auditory evoked response was located in the cortical layer forming the floor of the Sylvian fissure.

On the other hand, in trying to go beyond the spherical approximation, an important point to take into account is that the small contribution of scalp currents to MEG (less than 5%) makes a good approximation for studying the currents confined to the intracranial cavity, since the skull is a good insulator. Recent numerical studies indicate that a realistically shaped head of uniform conductivity may provide quite good accuracy for analyzing magnetic data. This is computationally a relatively simple task and could be carried out within a few minutes by a laboratory computer. Hence, one has grounds to simulate the head as a homogeneous conductor with conductivity σ bounded by the inner surface of the skull [39, 57, 61]. For this model, the magnetic field produced by the primary current $\mathbf{J}^p$ in a homogeneous conductor can be calculated from [39]

$$\mathbf{B}(\mathbf{r}) = \mathbf{B}_0(\mathbf{r}) - \sigma \frac{\mu_0}{4\pi} \int \frac{V(\mathbf{r}')\mathbf{n}(\mathbf{r}') \times (\mathbf{r} - \mathbf{r}')}{|\mathbf{r} - \mathbf{r}'|^3} dS' \tag{2.18}$$

where $\mathbf{B}_0(\mathbf{r})$ is the magnetic field that would be generated by the same primary source in a homogeneous conductor and dS' is the surface element at $\mathbf{r}'$. The above equation shows that the magnetic field is easily obtained once the the electric potential on S has been calculated. To compute V on S, a surface integral equation for V is introduced, which holds for all $\mathbf{r}$ on S [62]:

$$V(\mathbf{r}) = 2V_0(\mathbf{r}) + \frac{1}{2\pi} \int_S V(\mathbf{r}') d\Omega_r(\mathbf{r}') \tag{2.19}$$

where $d\Omega_r(\mathbf{r}')$ is the solid angle subtended at $\mathbf{r}$ by a surface element dS' at $\mathbf{r}'$ and V_0 is the potential caused by $\mathbf{J}^p$ in an infinite homogeneous medium with conductivity σ.

The equation for the potential can be solved through replacement of the inner surface of the skull by a set of several hundred triangles obtained through digitization of points of the intracranial surface [39, 57, 61], which, in processing data from patients or normal subjects, can be done from MRI scans. With this approximation for dipoles implanted in a skull in the temporal area, and with about 1200 triangles, one has to solve a system of 1200 linear equations; furthermore, one obtains errors on localization from the MEG maps of only around 3-4 mm [61] in cases where

spherical models, with inclusion of volume currents, give only accuracy on the order of 1 cm. Before deciding to use the homogeneous head model, one should bear in mind that this is a much more complex calculation than with spherical models and that to get this degree of accuracy it is necessary to be extremely careful at all the steps of recording the necessary data, in particular, in digitizing the MRI scans, where, for example, the thickness of the slices is often 5 mm or more and where nonlinear effects on the image can be well above 2-3% in some instruments.

2.8.4. Overview

The magnetic field generated by intracellular and extracellular currents may give direct information about the electrical activity of the brain. The contribution to the magnetic field due to extracellular currents is specified by the boundaries between media with different conductivities. If a spherical model is selected and the magnetic field normal to the surface B_n is measured, the field pattern provides direct information on the location of the underlying current dipole. In practice, the spherical models are good in the occipital and parietal areas, and they are easy to handle even with volume current effects due to the high symmetry of the model, only radial dipoles produce magnetic field. For the lower temporal and frontal areas, one still can use the homogeneous head model if accuracy of a few millimeters is important.

If a realistic shape model is selected, the magnetic field is affected also by radial dipoles as well as by the conductivity of the medium; however, the relatively good performances of the spherical model suggest relatively poor detection of radial sources. A complete analysis of brain activity must therefore rely on different kinds of measurements, such as EEG (electric) and MRI (anatomic) measurements, to provide a good estimate of the conductivity of the medium. Modeling EEG and MEG together will be an important step toward a better understanding of brain electrical activity. Furthermore, the signals detected in MEG involve excited areas of the cortex which are not points but rather areas of a few square centimeters, therefore it is necessary to go beyond the equivalent current dipole model when looking for clinical applications or neurophysiological data from MEG and to try to get information concerning extension or multiplicity of the sources.

CHAPTER 3.

INSTRUMENTATION FOR MEG

Biomagnetic fields arising from neural activity in the brain are weak; they are roughly one million to one billion times weaker than the earth's geomagnetic field; furthermore, they are weaker than typical environmental field generators. Biomagnetic measurements allow the detection of extremely weak signals immersed in a very noisy background. A sensitive device called SQUID (Super-conducting QUantum Interference Device) is essential for measuring these minute fields. In this chapter, instrumentation and related techniques to detect and make use of MEG measurements are discussed.

3.1. Noise Sources

Magnetic noise is produced by several sources: steady geomagnetic field generated by the Earth, the magnetic fields produced by everyday activities, such as power lines, elevators, electric motors, buses, trains and trolleys and so on. In addition, laboratory and hospital instruments generate strong noise. In particular, superconducting magnets used in MRI systems produce fields that are 15 times larger than the brain signals! It is often the case that an MEG system is operated in a shielded room, but often, only a few tens of meters away from an MRI installation.

Many stimulus generators also produce artifacts. To minimize this problem, sounds are typically presented to the subject via plastic tubes and earpiece, and electric stimuli in somatosensory experiments are delivered through tightly twisted pairs of wires. For visual stimuli, the video monitor must be outside the shielded room and behind a hole in the wall, while visual stimuli can be led into the room via a mirror system or along optical fibers.

The subject itself can also be a noise source. Eye movements and blinks are important biological sources of artifacts; both may be time-locked to the stimuli, especially if they are strong and infrequent. The magnetic field due to cardiac activity can contaminate cerebral measurements because the peak field from the heart's contraction measured over the chest is two to three orders of magnitude larger than that of typical evoked brain responses. However, the heart is farther away, and cardiac artifacts can usually be dealt with signal averaging or filtering. Evoked magnetic fields generated by electric currents in muscles generally do not pose severe problems during MEG recordings. Additionally, artifacts may be caused by mechanical movements of the body in the rhythm of the heartbeat or breathing. Therefore, all magnetic material on the subject, such as spectacles, watches, and hooks must be removed before the experiments.

Furthermore, the brain itself produces magnetic fields that are often irrelevant to the experiment being conducted: for the normal awake brain, the largest magnetic field intensity is due to spontaneous activity, such as the α rhythm observed over the posterior parts of the head. Abnormal subjects, such as epileptic patients, may elicit spontaneous spikes of even larger amplitude. In comparison, typical evoked fields following sensory simulation are weaker by an order of magnitude or more, i.e., their strength is only several tens or hundreds of femtoteslas. This background brain activity limits the signal-to-noise ratio in measurements made with the SQUID magnetometers. Of course, during studies of brain spontaneous activity, this background "noise" is the study subject and the actual signal! In contrast to other noise sources, the background activity is at least in principle correlated between the different brain areas, i.e., different magnetometer channels, and thus can be separated in multichannel recordings. The spectral density of the brain background activity is typically 20-40 fT/$\sqrt{Hz}$ below 20 Hz, decreasing towards higher frequencies and showing peaks at the spontaneously occurring rhythms of the brain, such as 10 Hz [2].

Finally, noise can also be caused by the thermal noise in the SQUID sensor, which is as a result of the aluminum foils used as radiation shields in dewars. With modern thin-film dc SQUIDs, the magnetometer noise can be well below the level of the brain signals. Figure 3.1 shows the amplitudes and spectra of various noise sources in MEG measurements [10].
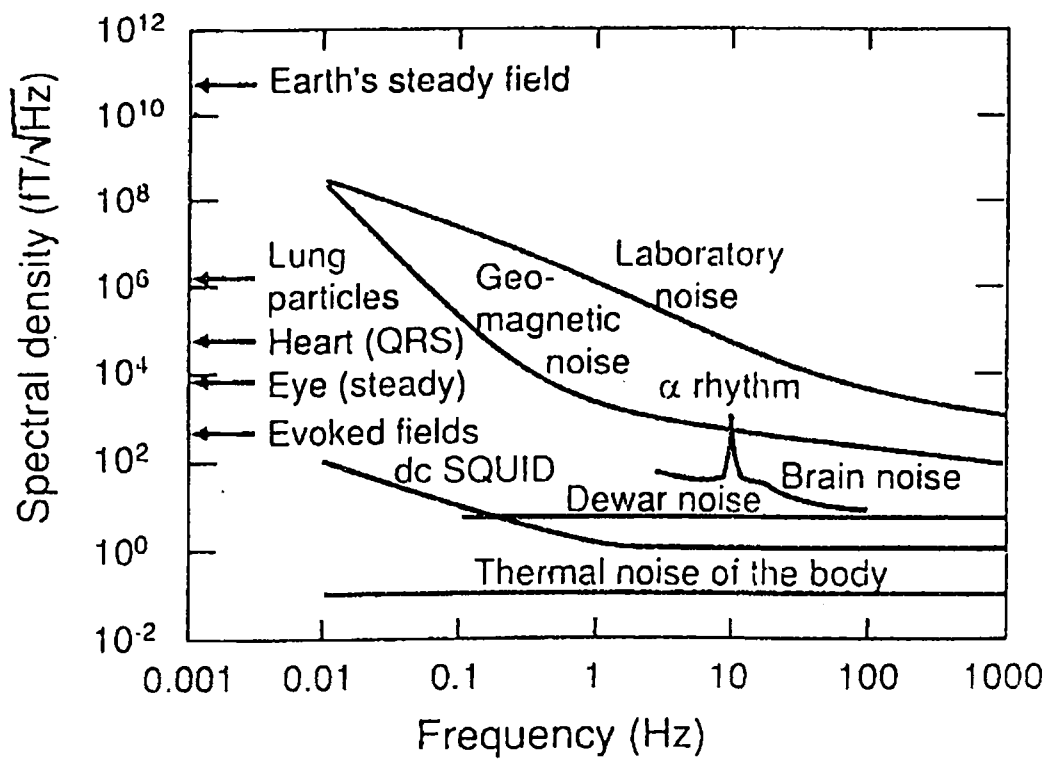
Figure 3.1 Amplitudes and spectra of various noise sources in MEG measurements with arrows indicating peak amplitudes. Modified from [10].

3.2. Noise Reduction

With the presence of the above noise sources, the magnetic field signal produced by the brain is much weaker and some strategies of eliminating noise sources are thus essentially for the quality of the recordings and the follow up analysis.

3.2.1. Shielded Rooms

For rejecting the remotely generated noise, it is natural to think of building a magnetically shielded room. There are four different methods to achieve this, namely, ferromagnetic shielding, eddy-current shielding, active compensation and the high-T_c superconducting shielding. Many rooms have been built for biomagnetic measurements employing combinations of the above four techniques.

The walls for the shielded rooms are made from μ-metal and aluminum, or μ-metal and copper, or aluminum only for less expensive shielded rooms. Magnetic and eddy-current shielding can greatly reduce the influence of external electromagnetic fields. By using very thin metal plates, fields with high frequencies can be easily attenuated, whereas low frequencies (e.g. 50- or 60-Hz power-line frequencies) require walls with thickness at least several centimeters.

Undoubtedly, constructing shielded rooms offers an effective method which yields better performance in terms of reducing noise sources, but on the other hand, the price paid for it is rather high, though there is always a compromise between performance and price. In addition, owing to the limited space of the shielded rooms, it may cause unease, discomfort or even minor psychological problems for the subjects. Furthermore, the ultimate performance of magnetically shielded rooms is determined by Nyquist current noise in the conducting walls [63]. In other words, each shielding room has its own effective frequency ranges for noise reduction, and shielding cannot eliminate all the noise sources. Therefore, for obtaining a sufficiently quiet space for practically all types of biomagnetic measurements, suitable gradiometers are also needed.

3.2.2. Gradiometers
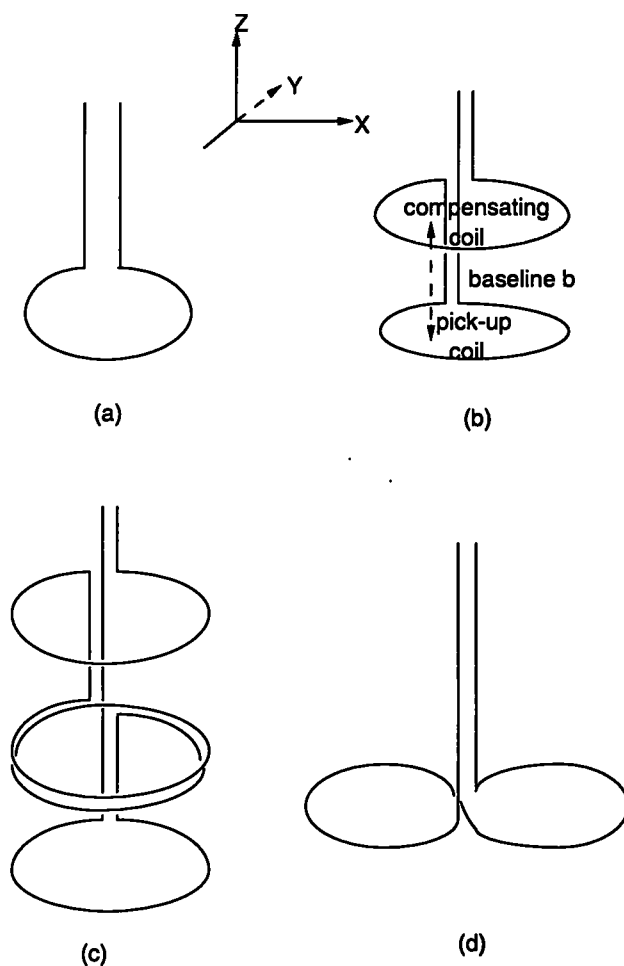
Figure 3.2 Examples of detection coils: (a) a magnetometer, (b) a first-order axial gradiometer, which detects the the first spatial derivative of the field $\frac{\partial B_z}{\partial z}$, (c) a second-order axial gradiometer, which detects the second spatial derivative of the field $\frac{\partial^2 B_z}{\partial z^2}$, (d) a first-order planar gradiometer, which detects the first spatial derivative of the field $\frac{\partial B_z}{\partial x}$.

A gradiometer is a set of detection coils that are wound in such a way that it is sensitive to a gradient of the field rather than the field itself. In other words, it is sensitive to the nearby sources of interest but less sensitive to distant noise sources. This can be achieved by taking advantage of appropriate geometries for detection coils. Compared with the magnetometer (as shown in Figure (3.2(a)), which has only one detection coil, the gradiometer comprises a couple of detection coils. As illustrated in Figure 3.2(b), the gradiometer includes a pick-up (sensing) coil and a compensating coil. The pick-up coil is placed closest to the source of interest, and the compensating coil has the same area and number of turns as the pick-up coil, but is wound in the opposite sense. The planes of the two coils are separated by a distance of "b" termed as "baseline". With this geometry arrangement, the gradiometer provides what is known as "spatial discrimination", that is, it is insensitive to spatial uniform fields, because the coils produce the same signal but with opposite sign. On the other hand, any field having a spatial gradient along the axis of the coils will produce a net signal to be transferred to the SQUID. In the case of Figure 3.2(b), the gradiometer is sensitive to the gradient of fields in the z direction, and it is called "first-order axial gradiometer" as it is only the first spatial derivative of the field. The first-order gradiometer can be used successfully in relatively quiet environment, where the ambient field noise is small. However, in noisy environments, such as hospitals and laboratories, for rejecting both spatially uniform fields and spatially uniform field gradients, a "second-order axial gradiometer" with more sophisticated geometry is needed. An example is shown in Figure 3.2(c), a second-order axial gradiometer can be regarded as two first-order axial gradiometers connected in series and oppositely wound.

Traditionally, most neuromagnetic measurements have been performed with axial gradiometers. However, the coils may be shaped in order to measure differences in the vertical component of the field B_z along a transverse direction (x, y, or both). These devices are referred to as first-order or second-order planar gradiometers, as shown in Figure 3.2(d). The advantage of the diagonal planar configuration design coils over axial coils lies in that the double-D construction is compact in size and can be fabricated easily with thin-film techniques.

Though the locating accuracies of planar and axial gradiometers are essentially the same for typical cortical sources [64, 65, 66], there are arguments in favour of the choice of either axial or planar detection coils. These arguments have been discussed

in detail in a few papers [66, 67, 64] and deserve to be briefly summarized here. The main advantage in using an array of axial gradiometers is that the measured quantity is the neuromagnetic field generated by primary currents, provided that the baseline is chosen sufficiently large and that the source is located in the cortex. On the other hand, planar gradiometers have been employed to identify multiple sources successfully [64], due to their intrinsically better sensitivity to higher spatial frequencies. A planar double-D gradiometer gives its maximum response just over the source, with the direction of the source being perpendicular to that of the field gradient.

It is worthy of note that a higher degree of spatial discrimination to the noise provided by the gradiometers is at the expense of reducing the sensitivity to sources, because of the flux cancellation as the contributions from the pick-up coil and the compensating coils are opposite; this reduces the flux coupled to the SQUID. As the order of the gradiometer is increased, the loss in sensitivity increases as well. In practice, it is advisable to decrease the distance between the source and the pick-up coil as much as possible so that the flux through the compensating coils could be negligible compared with that through the pick-up coil, especially when the distance is relatively much shorter than the baseline. The signal measured by the SQUID is then roughly proportional to the field of interest rather to the gradient of the field. Hence, the choice of the appropriate baseline for the gradiometer must be a compromise between reducing the contribution from ambient noise and maximizing the sensitivity to sources deep within the brain.

Furthermore, it is understandable that an increase of the diameter of the pick-up coil will increase the sensitivity to the field, but as a consequence, the spatial resolution in the lateral direction will be decreased.

3.2.3. Filtering and Averaging

Filtering and averaging of neuromagnetic data offer simple special solutions to the general problem of extracting a signal from noisy data. The necessity of filtering to reject the outband noise and to reject some inband single frequencies is obvious. The external noise is particularly important in unshielded urban areas, where the peak-to-peak line frequency noise to be rejected may exceed 1 nT. In the case of observation of transient signals (evoked for instance), the inband phase distortion can give rise to an important modification in the shape of the signal [68]. More

sophisticated filtering and estimation procedures have been developed, such as the time-varying filter [69], which is based on continuous estimation of the signal-to-noise ratio in several frequency bands.

Besides bandpass filtering, averaging is a simple and powerful way of improving the signal-to-noise ratio. Averaging, to enhance a stimulus-time-locked response relative to non-time-locked background "noise", is the basic technological development upon which recording of evoked potentials or fields is based. Averaging was considered especially necessary for recording very low amplitude evoked potentials or fields from auditory brain stem; the average response is at least 10 times smaller than the typical single trial responses in amplitude.

Background noise is random, hence with repetition, its amplitude at any given instant will tend to average to zero. However, the time-locked response waveform will not be "averaged out" in this way.

A complete description of an averaged response includes the number of individual responses included in the average (N), the total time period of the averaged waveform (the epoch), and the time relationship between the start of the average and delivery of the stimulus. Reduction in noise amplitude is proportional to the square root of N [70]. Assuming that in the unaveraged epoch the signal/noise ratio is 1:1, if $N = 1$, then the ratio is 1:1; if $N = 100$, then the signal to noise ratio will become 10:1. However, as N is increased, there will be diminishing benefits in terms of increased signal/noise ratio. For example, signal/noise ratio increases only 12% when the same increment of 100 is added to an N of 400. It was found that no significant effects as a function of epochs averaged for a minimum 256 responses to a maximum of 57344 responses in case of auditory brain-stem evoked response (BSER) [70].

If the stimulus rate is an even multiple of the frequency of the non-random noise, the background noise will be "averaged out" at a much slower rate compared with the random background noise. If non-random noise is known to be present, one can therefore most effectively eliminate it by selecting a stimulus rate that is not an even multiple of the noise's frequency, e.g. 8 sec^{-1} or 9.2 sec^{-1}, rather than 10 sec^{-1}, to eliminate 50 Hz hum.

Although sophisticated filtering and averaging methods (e.g., weighted averaging [71, 72]) exist for extracting the signal from noisy data, the main effort should be directed towards noise reduction in the flux sensed by the SQUID. Clean raw data, obtained with proper magnetic shielding, low-noise sensors, and well-designed gradiometers are the most important preconditions for good MEG results.

3.3. SQUID Basic Principles

A typical SQUID magnetic field sensor consists of a magnetometer (or gradiometer), a SQUID detector and its associated control and output electronics, and a dewar to encase the sensor in liquid helium in order to maintain the superconducting state, as depicted in Figure 3.3. By definition, SQUIDs are superconducting electrical circuits whose behavior is governed by the macroscopic quantum behavior of the electrons [73].

In practice, SQUIDs are superconducting rings in which there are one or more weak links which are often described as Josephson junctions. A superconducting input coil connected the detection coil(s) with the SQUID forming a closed superconducting circuit is called a "flux transformer". When magnetic flux change is applied to the detection coil(s) by a biomagnetic source, a current I that is proportional to this rate of change of flux flows around the flux transformer. As the current flows through the input coil, it produces a magnetic field that can be sensed by the SQUID. The SQUID electronics then provides an output voltage V that is proportional to the magnetic flux applied to the SQUID. In summary, the SQUID sensor changes its output voltage linearly with changes in the flux through the detection coils, i.e., the system acts like a current to voltage amplifier. Hence, there are two distinctive features of the SQUID sensor. First, because the SQUID sensor is sensitive to changes in the field rather than the absolute field, it can detect minute field changes while sitting in a field that is many orders of magnitudes larger. Secondly, its sensitivity is frequency independent from d.c. to a maximum frequency defined by the electronics circuit. It is worthy of note that if the input field changes too quickly, the output jumps discontinuously to a new value and information about the field change is lost. This may limit their use in magnetically noisy environments and hence noise elimination before detection of the field is very desirable.

Output   V

SQUID

detection

electronics

Dewar

helium   liquid

SQUID

input coil

I

B through
detection coil

tail area
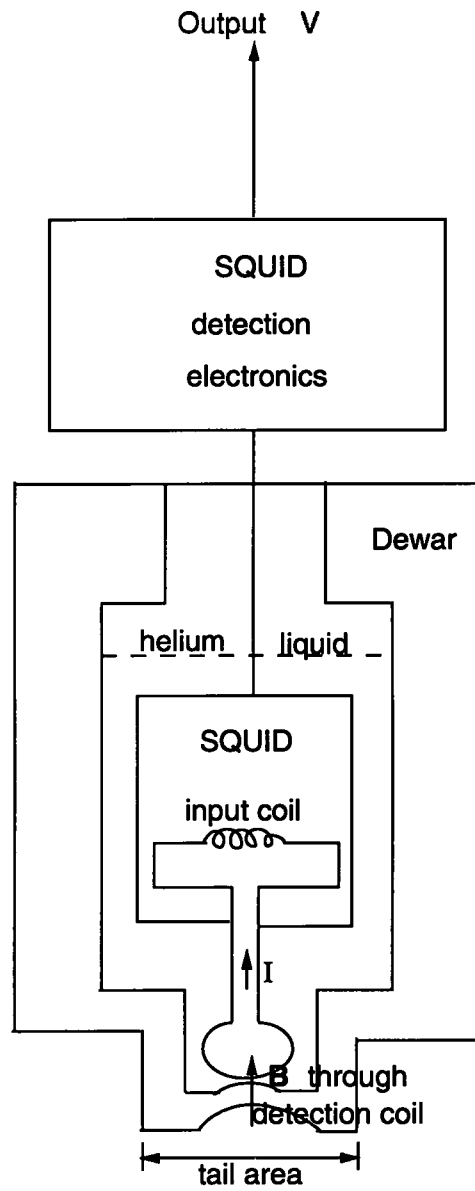
Figure 3.3 Block diagram of a typical biomagnetic dewar

For the past few years, improvements in the instrumentation used for neuromagnetic measurements are continually being introduced, for instance, the use of integrated SQUID pick-up coil arrangements constructed by thin-film deposition for reducing the resolution against noise and the introduction of refrigerators capable of keeping SQUIDs at liquid helium temperatures by appropriate use of helium gas, e.g. the CryoSQUID [74].

Conventional SQUID-based magnetic sensors rely on a reservoir of several liters of liquid helium to maintain a low-temperature environment for the superconducting components. A typical evaporation rate is 3 liters per day. Such a system requires refilling approximately every three days, which entails waste of helium, and may be tipped up to only 45 degrees from the vertical, thus imposing a constraint on neuromagnetic measurements. Special dewars with canted tail surfaces and detection coils have been designed to overcome this problem, but still do not allow a full range of measuring positions. The recent development of a system called "CryoSQUID" based on refrigeration with helium gas virtually eliminates these limitations. CryoSQUID has a completely closed system so it conserves helium and can be oriented in any direction, including upside down. However, it is not an efficient system, requiring several kilowatts of electrical power for a set of compressors, as well as cooling water. Refrigeration depends on the fact that helium remains a gas at temperatures as low as 4.2 kelvin (K) at atmosphere pressure. Therefore, cooling cycles were considered that make use of the fact that gaseous helium cools when it is allowed to rapidly expand at a sufficiently low temperature. This can be achieved by using a cascaded sequence of two refrigerators, one that reaches a stable temperature of 15 K, and a second that cools from there to 4 K.

Significant progress has also been made on the SQUID sensor system, such as the introduction of multichannel instruments to measure simultaneously the field at a number of positions, which may include the measurement of the field at many different positions allowing one to generate a contour map representing isofield contours and "event-related" fields by measuring the field at several places outside the head at the same time, making it possible for us to capture a snapshot of a brain state.

3.4. Multi-SQUID Systems

The ability to identify active sources in the brain depends on the choice of the coil geometry. This geometry, together with the configuration of the detection array, determines an optimum range for source location and depth, resulting in a greater ability to distinguish multiple sources.

In this section, the factors relevant to the performance of localization will be considered, which include different kinds of arrays of gradiometers, system positioning with respect to the subject's head, reproducibility of measurements, and identification of the head shape. Finally, some examples of multichannel systems are briefly reviewed, with the aim of demonstrating the present state-of-the-art and the future perspectives of further improvements of instrumentation.

3.4.1. Array Definition

One of the constraints set by the need for liquid helium as a refrigerator for the superconducting circuitry is that the sensing "head" must fit the circular tail of the dewar. The present technology in superconducting dewar manufacturing permits commercial availability for neuromagnetic dewars with tails as large as 16 cm. A relatively large number of sensors may fit this space, depending on the configuration chosen to position the detection coils.

The two simplest geometries are a "cartesian" alignment and a "hexagonal" packing. The former provides a simple orthogonal grid, but it does not take full advantage of the inner space of the dewar tail; the latter permits us to insert in the available space the maximum number of detection coils, but it may produce some problems if planar gradiometers are adopted. In both cases, however, the relevant quantities are the grid spacing D and grid total width W. On the basis of simple considerations on the spatial sampling theorem, it has been shown that D establishes the minimum depth of a source to be detected by a specific array, whereas W sets the maximum depth [75]. In other words, D and W set constraints on the high and low spatial frequencies, respectively. In [75], it has been shown that a spacing of 2.5 cm was ideal for detecting sources as shallow as 3 cm from the detection coil, i.e., about 1.5 cm from the scalp, if a typical value of 1.5 cm is assumed for the spacing between the inner and outer surface of the dewar bottom.

For multichannel systems which allow whole-head coverage and generally have hel-metlike Dewar base (see Section 3.4.3), determining a proper sensor spacing is to a large extent an economic question: in order to have sufficient coverage of the whole head, over 100 SQUIDs are needed. The bottom must also be large enough to ac-commodate most heads, as a result, some of the channels are inevitably bound to be quite far away from the sources in the brain. This implies that a high sensitivity and low environmental noise level must be achieved for the helmetlike multichannel systems.

3.4.2. Experimental Accuracy and Reproducibility

Large effects are introduced by errors in positioning the dewar with respect to the subject's head. Many researchers in neuromagnetism have long discarded the tape measure as a means of determining sensor positions with respect to reference points on the scalp. Even mechanical devices that accurately position the sensor with re-spect to the bed or chair supporting are giving away to new technology.

Many different procedures have been proposed and adopted by different research groups around the world. Only two of them are mentioned here. The first uses the same superconducting array to record an alternating current (AC), low-frequency signal fed to tiny copper coils (i.e. magnetic dipoles) fixed in specific locations of the subject's head. In this case a localization procedure is carried out immediately before and after the experimental run to check possible variations in system posi-tioning [65, 76].

The second makes use of additional detectors and consists in taping around the subject's head three small radiofrequency (rf) transmitters, and in monitoring their position by means of an appropriate rf receiver [77, 60]. Accuracy better than 2 mm for the position of a sensor with respect to the subject's head can be achieved in a head-based coordinate system, which make possible real-time monitoring of evoked activity at several widely separated locations over the scalp, thus allowing some subject movements.

Determining sensor positions as well as orientations with millimeter precision almost

requires that distances across the scalp be abandoned as the reference system for expressing positions. Many coordinate systems have been extensively employed for experiments and analyses. For the work to be described in later chapters, two are discussed fully in Appendix A.

Before concluding this section it is worth discussing a last point, regarding signal reproducibility. The assumption that a biological signal is generally reproducible is the basis of many methods for improving the signal-to-noise ratio, and specially in evoked response measurements. This assumption, that the brain response is stationary, is rarely true. Indeed, an analysis performed on evoked potential response by means of an AutoRegressive Moving-Average procedure (ARMA) [78], together with first results obtained with the same approach in the case of evoked field measurements, has shown that the cerebral response varies significantly across repetitive simulation, ranging from what is currently referred as to "actual evoked signal" to weaker responses and even completely missing one. This effect may be of fundamental importance, in that the final morphology of the averaged signal is profoundly affected by the "invalid" response, and consequently a "topographic" analysis is misleading or even wrong. Even when great care is taken to ensure a reproducible cerebral response, by controlling all the psychological parameters that may influence subject's concentration and motivation, the assumption that the subject is stationary is not guaranteed to be true. Additionally, advanced response selection criteria, such as the one mentioned above or any other which may provide statistical significance to the chosen response, should be used any time more than a single cerebral response is needed for source localization. Much of this work aims at clarifying the relationship between average and single trial responses, and in providing tools of the analysis of individual trials.

3.4.3. Examples of Multichannel Systems

Multichannel systems have enough channels spread out on a sufficiently large area for locating cortical sources from measurements without moving the instrument, provided that the magnetometer (or gradiometer) is correctly positioned initially. Since 1989, a new generation of instruments has emerged, having typically more than 20 SQUID channels distributed over an area exceeding 10 cm in diameter. In the following discussion, several multichannel systems including the two used for the experiments and analyses in the following chapters are briefly reviewed.

The Siemens 37-channel "KRENIKON" system [79]

The system was manufactured by Siemens AG (Germany) and installed in Erlangen and Stockholm (Siemens has withdrawn the installations recently). It consists of 37 axial first-order gradiometers. The hexagonal arrays of hexagonal pick-up and compensation coils were fabricated on flexible printed-circuit boards and glued onto a support structure so that axial gradiometers were formed. The pick-up area of the coil is 6 cm^2 and the pick-up and compensation coils are within a 19-cm-diameter cylinder in two planes separated by 70 mm. The gap between the liquid-helium space and the outer surface of the dewar is 20 mm. The system includes three additional magnetometers to measure the x, y, and z components of the external magnetic field for noise cancellation, though they have rarely been used during experiments. The system was designed for use inside a moderately shielded room and the noise of the system is typically less than 10 fT/$\sqrt{Hz}$ at frequencies over 10 Hz.

Because of the flat-bottomed dewar, the system is suitable for both brain and cardiomagnetic measurement; some of the outer channels are quite far away from the brain. In a test using a current dipole in saline solution, accuracy was better than 2.5 mm up to a distance of 9 cm from the centre of the sensor array. In a test for localization accuracy within the human body using a magnetic pacing catheter, the biomagnetic image of the current dipole as introduced by the simulated catheter correlated well with the anatomical position of the catheter electrodes within an error of a few mm [79]. Successful operation in many investigations in MEG and MCG has been demonstrated since the 37-channel system was built in 1989.

The BTi 37-channel "MAGNES" system [77]

The system has been installed and used in several places worldwide, such as in Scripps Clinic (San Diego), in the National Institute for Physiological Sciences (Japan), in New York University Medical Center, and in the University of Münster (Germany). The system has a hexagonal sensor arrangement similar to the Siemens system. They are spaced 22 mm apart and are located on a spherical cap with a 120-mm radius of curvature. The diameter of the coil array is 144 mm [77]. With the curved dewar bottom, the Magnes system fits the curvature of human brain better in MEG measurements than the Krenikon system, but covers less area. In addition to the 37 first-order gradiometers, there are eight additional SQUIDs for

cancelling external disturbances. The noise of the system is 10-20 fT/$\sqrt{Hz}$.

Whole-head Coverage Systems

During various complex investigations in clinical studies, it is important to measure over a larger area and monitor the brain activity in the left and right hemisphere in the same experiment, the whole-head coverage systems are operational for meeting this goal.

Based on the 37-channel MAGNES system, the BTi twin MAGNES probe (2 × 37 channels) was developed and installed in Scripps Clinic and recently in the Institute of Medicine (Jülich, Germany) as well. The system is capable of taking measurements of both hemispheres simultaneously.

The "Neuromag-122" system was developed in the Low Temperature Laboratory (Helsinki, Finland) in 1992 [80]. The system employs 61 planar first-order two-gradiometer units, measuring $\partial B_r/\partial x$ and $\partial B_r/\partial y$. The dewar bottom is helmet-shaped with radii of curvature between 83 and 91 mm, covering the entire scalp. The distance from the outer surface of the dewar to the gradiometer coils is only 16 mm. The sensors have an equivalent gradient noise of 3-5 fT/$\sqrt{Hz}$.

The CTF system was built in Canada with 128 axial symmetric first-order gradiometers on a quasiregular grid covering the whole head [81]. The system also contains 16 reference channels to measure three field components and first- and second-order gradient components to characterize the background noise. With the help of these reference channels, a noise level of 10 fT$\sqrt{Hz}$ in the frequency range from a few Hz to 60 Hz was reached in an unshielded environment, so it is possible to operate in an open environment without a magnetically shielded room.

CHAPTER 4.

INVERSE PROBLEM

The inverse problem in EEG and MEG is of both theoretical and practical importance. A simple statement of the inverse problem can be expressed as making a convergent iteration towards the true current sources and their locations based on MEG (or EEG) measurements from the surface. Theory shows that there is no unique solution to this problem; noisy data only makes this worse. In this chapter, some of the relevant information necessary to gain insight into the inverse problem will first be outlined, followed by a discussion of why the inverse problem is "ill-posed". Finally some of the approaches being used in practice to handle the inverse problem, as well as approaches with potential for future development will be outlined and compared, and their clinical relevance discussed.

4.1. General Comments

The task of the neuromagnetic *inverse problem* is the estimation of the cerebral current sources generating a measured distribution of the magnetic field. The magnetic field obeys the principle of superposition. "Superposition" means that if a source gives rise to a particular field, and another source gives rise to another field, then the field due to both sources is simply the vector sum of the fields. If two dipoles are close together relative to the distance at which the field is measured, the resulting field can be indistinguishable from the field of a single different dipole. In part because of superposition, the inverse problem as it arises in bioelectromagnetism is often part of a class of inverse problem called "ill-posed problems". In MEG, there are sources which produce no external field; for example, radial dipoles in a conducting sphere; such sources are termed silent sources.

There are three conditions which must be satisfied for the inverse problem to be well-posed.

1. There must exist an inverse. In EEG and MEG, the inverse is the source.

2. The inverse must be unique. In EEG and MEG, because of superposition and the presence of silent sources, the inverse is not unique.

3. The inverse must be stable. In EEG and MEG, stability is a consideration in the sensitivity of an inferred source to noise.

If any one of these three criteria (existence, uniqueness, and stability) fails in physical experiments, the interpretation of the cause of the physical observation is often an ill-posed problem.

Ultimately, to solve an ill-pose problem, one must appeal to information outside the domain of the problem. In this context, the realistic modeling of the head completed with the use of the anatomical information of magnetic resonance imaging (MRI) scans and other neurophysiological constraints have been employed effectively.

4.2. Functional Localization Models

As discussed, in general there is no unique result; nevertheless, there are approaches that are taken to simplify the problem. One may introduce constraints that result in a tractable problem. One may make assumptions concerning the source such as the single current dipole assumption, and one may similarly make assumptions concerning the geometry and conductivity of the head. The simplest model is a dipole in a homogeneous infinite head, which is not realistic. In one approach, assumptions are made regarding the source and the head model, and the forward problem may be solved analytically or numerically. In many situations the source depends on a finite parameter set, in which case the inverse problem reduces to estimating the values of the parameters that give a solution that best fits the measured field data. If the constraints are suitably defined, the inverse problem thus reduces to a problem of parameter estimation. In practice, validation of models requires comparison of such estimates with actual source parameters from fixed or *a priori* known sources.

4.2.1. Single-Dipole Models

Much of the work that has been done in MEG to date has employed a model of the source as a current dipole. Such a model is certainly reasonable for a small area of cortex which is relatively distant from the measurement point, but this model may be inappropriate when large areas of cortex are activated. In addition to defining a dipolar source, the head model needs to be specified.

Dipolar source, homogeneous space and infinite half space:

This quite simple model allows the estimation of location and depth of the dipole quite readily from measurements made on the field map. To begin with, in homogeneous space the forward problem is easily solved; the expressions for the electric potential and the magnetic field generated by a dipole are given by Equations 2.9 and 2.2, respectively. The inverse solution amounts to locating the dipole in the designated space and is easily performed as the dipole location must be at the midpoint joining the extrema of the field while the dipole depth is estimated by dividing the inter-extrema distance by $\sqrt{2}$ (refer to Section 2.8).

The same procedure can be used for an infinite half space provided that only the field component perpendicular to the boundary is measured. Alternatively, the location of the dipole is found via Equation 2.15.

Dipolar source, spherically symmetric head:

The forward problem for a dipole in a spherically symmetric conductor has been expressed by Equation 2.17. The equation shows that there is no external magnetic field for a radial current dipole, and the radial component of the magnetic field of a tangential dipole depends on the source current and is independent of the volume current. Other components do depend on volume currents, although in principle they are derivable from the radial component. This obviously has important implications for the inverse problem, since it implies that there is no unique inverse in this model. To any derived tangential dipole estimated from magnetic measurements, an arbitrary radial dipole may be added without worsening the fit. Note however, that this radial dipole will contribute a strong signal to the EEG, hence this is one aspect of the complementarity between electric and magnetic measurements.

Approaches to this inverse problem have included making the simplistic assumption that only the radial component of the magnetic field is measured, in which case parameters of dipole location can once again be estimated from the dipole map. As demonstrated by Rose in [82], in certain brain regions the geometry of the skull and the placement of the magnetometer (or gradiometer) make it unlikely that only the radial component is measured, in which case one has to take into account tangential components of the magnetic field as well. This, in turn, means incorporating volume current effects. The simple derivation of the tangential components of the magnetic field given by Ilmoniemi [1] allows easy solution of the forward problem, in which case the inverse problem reduces to a search for the parameters of the dipole that gives the best agreement with measured data. The solution of the forward problem highlights the independence of the magnetic field from radial variation in conductivity. Search methods and reliability of estimation are discussed by Sarvas [51].

Dipolar source, nonhomogeneous spherical head:

In MEG, as long as spherical symmetry holds, the radial component of the magnetic field is independent of radial variation in conductivity. By contrast, in EEG, the use of a spherical head model requires further treatment when dealing with the forward and inverse problems, because the conductivities vary by as much as a factor of 70 for multiple layers of tissue surrounding the brain [37], which influences strongly the electrical potential at the scalp. As a result, solution of the forward and inverse problems requires reasonable estimates of the conductivities. Theoretical background for this is given by Sarvas [51], Nunez [37], Stok [35] and de Munck [83], and will not be discussed here further except to note that if estimates of conductivity are made, the forward problem may be solved and again a least-squares search for best parameter estimates may be made for the inverse problem.

Dipolar source, realistic head models:

These methods are still being developed in a number of places. In general, they rely on the use of imaging studies to define the surfaces of the various interfaces between regions of differing conductivity. In practice, the surfaces are divided into triangles, and the potential on the surfaces may be estimated by a finite element evaluation of the required surface integrals. The surface potentials may then be used to calculate the components of the volume current that contribute to the magnetic field, and finally a term is added for the dipole in an infinite homogeneous

conductor. This computer-intensive calculation solves the forward problem for an arbitrary dipole; once again a minimizing search can be performed to tackle the inverse problem, although this requires tremendous computing power. Descriptions of this technique are given by Hämäläinen and Sarvas [39], Stok [36], de Munck [83] and Meijs [58, 84]. Some simulations were made and significant differences between the spherical model and the realistic model were also shown in [58].

An example of single-dipole models: single current dipole inversion

The standard method of estimating the location of a simple source is to determine the equivalent current dipole by a least-squares search [85]. In the so-called moving-dipole model, the source is assumed to be dynamic so that its location, orientation, and strength are allowed to change with time. The data are fitted at each time instant, and temporal correlations are ignored.

The single dipole model is useful even for identifying multiple, simultaneously active sources lying far away from each other or nearby sources acting at different time, as demonstrated by measurements of activity in the first and second somatosensory cortices S1 and S2 [45]. When both S1 and S2 are simultaneously active, the magnetic field pattern for each dipole is distinct and the existence of three separate sources is evident. By contrast, the electric potential distributions are smeared and largely overlapped, which makes it difficult to see there are three spatially separated sources.

In the following formulation, it is assumed that there is a total number of M magnetic field measurements. The generator of the magnetic field is assumed to occur in a small area, i.e. the source space. Because the location, orientation and magnitude of the single current dipole can be all varied in the source space and are determined by the measurement, we need first to pinpoint the dipole. With this view, the source space is divided into N small sub-areas, in which a current dipole is hypothesized. For these N hypothesized current dipoles, using the least-squares method enables us to obtain the magnitude and direction for each dipole which best fits the external measurements, and then to find the one producing a signal which is most similar to the target signal, in a least square sense.

Suppose the medium of the head is modelled as an infinite half space, from Equation 2.2, we can easily deduce that the z component of external magnetic field at a

position vector $\mathbf{r_m}$ due to a current dipole Q_n located at $\mathbf{r_n}$ is as follows,

$$B_{z:m} = \frac{\mu_0}{4\pi \left| \mathbf{r}_m - \mathbf{r}_n \right|^3} (Q_{xn} R_{y:m,n} - Q_{yn} R_{x:m,n}) \tag{4.1}$$

where m and n are the indices of the sampled points in space, $R_{x:m,n}$, $R_{y:m,n}$ and $R_{z:m,n}$ denote the x, y and z component of $(\mathbf{r}_m - \mathbf{r}_n)$ respectively, and Q_{xn}, Q_{yn} and Q_{zn} are the three components of $\mathbf{Q}(\mathbf{r}_n)$.

We then define a function F as follows,

$$F(Q_{xn}, Q_{yn}) = \sum_{m=1}^{M} \left[B_{z:m} - C_{m,n} \left(Q_{xn} R_{y:m,n} - Q_{yn} R_{x:m,n} \right) \right]^2 \tag{4.2}$$

where

$$C_{m,n} = \frac{\mu_0}{4\pi \left| \mathbf{r}_m - \mathbf{r}_n \right|^3} \tag{4.3}$$

Apply the least-squares method, a necessary condition for $F(Q_{xn}, Q_{yn})$ to be minimum is

$$\frac{\partial F}{\partial Q_{xn}} = 2 \sum_{m=1}^{M} \left[B_{z:m} - C_{m,n} \left(Q_{xn} R_{y:m,n} - Q_{yn} R_{x:m,n} \right) \right] \left[- \sum_{m=1}^{M} C_{m,n} R_{y:m,n} \right] = 0 \tag{4.4}$$

$$\frac{\partial F}{\partial Q_{yn}} = 2 \sum_{m=1}^{M} \left[B_{z:m} - C_{m,n} \left(Q_{xn} R_{y:m,n} - Q_{ny} R_{x:m,n} \right) \right] \left[- \sum_{m=1}^{M} C_{m,n} R_{x:m,n} \right] = 0 \tag{4.5}$$

from which we can obtain the equations for Q_{xn} and Q_{yn} for each hypothesized current dipole which best fits the measurements,

$$Q_{xn} \sum_{m=1}^{M} C_{m,n} R_{y:m,n}^2 - Q_{yn} \sum_{m=1}^{M} C_{m,n} R_{x:m,n} R_{y:m,n} = \sum_{m=1}^{M} B_{z:m} R_{y:m,n} \tag{4.6}$$

$$Q_{xn} \sum_{m=1}^{M} C_{m,n} R_{x:m,n} R_{y:m,n} - Q_{yn} \sum_{m=1}^{M} C_{m,n} R_{x:m,n}^2 = \sum_{m=1}^{M} B_{z:m} R_{x:m,n} \tag{4.7}$$

Once Q_{xn} and Q_{yn} have been obtained from the above two equations, we can calculate the magnetic fields $M_{z:m}$ based on these calculated Q_{xn} and Q_{yn}, and then obtain the error between the actual measurements $B_{z:m}$ and the calculated magnetic fields $M_{z:m}$ using

$$Error = \frac{\sum_{m=1}^{M} \left(B_{z:m} - M_{z:m} \right)^2}{\sum_{m=1}^{M} \left(B_{z:m} \right)^2} \leq 1 \tag{4.8}$$

Comparing the *Error* for all the hypothesized current dipoles, we can find the current dipole with the least error with the measurements, in other words, has the highest goodness-of-fit value G, where $G = 1 - Error$.

The choice of G is analogous to the measure widely used in linear regression analysis [86]. If $G = 1$, the model agrees completely with the measurement. If $G = 0$, the model is irrelevant and does not describe the measurements any better than a zero field would. Deviations of G from 1 are caused by measurement noise and by the inadequacy of the source model. If the noise levels are over- or under-estimated, one easily obtains misleading results [87]: overestimation leads to missing some of the details in the actual source configuration, while underestimation may fool the experimenter to a more complex model than is actually allowed by the noisy data.

The problem of finding suitable and adequate confidence limits for the dipole model has been discussed by several authors [88, 86, 89, 90, 91], especially care must be exercised when the accuracy of estimates for current dipole depth is determined. If one compares the confidence limits in the longitudinal direction (the direction of the current dipole), in the transverse direction (perpendicular to the dipole and its location vector), and in depth (along the location vector), one finds that the deviation in the transverse direction is smallest, being about half of the deviations in the longitudinal direction and in depth. This difference can be explained by the effect of dipole displacements on the field pattern [40]. Furthermore, using the single current dipole model, one has to be aware of the resemblance between the field distributions produced by a single dipole, a side-by-side dipole pair, and a dipole distribution along a line. Simulations indicate that the application of a single-dipole model to the interpretation of the field produced by a side-by-side distributed source results in an equivalent dipole that is deeper and stronger than the actual one [92, 93]. This is a serious problem, because the modeling error is only weakly reflected in the goodness-of-fit value G.

4.2.2. Multiple Dipoles

The principle of superposition allows for the straightforward solution of the forward problem for multiple dipoles; however, the inverse problem is limited by non-uniqueness. In model studies, several investigators have attempted to gain insight into the circumstances under which the MEG would be able to discriminate multiple

dipoles from single dipoles. For instance, Okada [92] used a statistical technique based on a calculated F ratio to establish lack of fit to a single-dipole model. Assuming a single-dipole solution (when in fact two dipoles are simulated), Okada [92] was able to estimate the distance and angular separation of two simulated dipoles necessary before a single-dipole model would demonstrate lack of fit. With noise levels similar to actual experimental levels, lack of fit was apparent when the dipoles were 1-2 cm apart. As the angular separation of the dipoles increased, lack of fit was more apparent. Importantly, depth estimates based on the single-dipole model worsened as the dipole separation increased, and depth was generally overestimated. A similar experiment has been conducted by Hari [91], who also considered variables relevant to the measuring apparatus. Nunez [94] has also demonstrated simulations in which the assumption of a single dipole (when in fact two are present) may also underestimate dipole depth.

In general, if the distance between the individual dipoles is sufficiently large (> 4 cm) and their orientations are favourable, i.e. the two dipoles are oriented in the same direction, the field patterns may show only minor overlap and they can be fitted individually using the single-dipole model. An example of this approach is the separation of activities from the first and second somatosensory cortices. Similarly, if the temporal behaviours of the dipoles differ, it is often possible to recognize each source separately.

However, when the sources overlap both temporally and spatially, we must then resort to a multidipole calculation to obtain correct results. Barth et al. have recently demonstrated a method of spatiotemporal analysis using multiple current dipoles which they have applied in several epileptic patients [95]; this method holds promise for further development.

An effective approach to this modeling problem is to take into account the spatiotemporal course of the signals as a whole instead of considering each time sample separately. In general, there are three spatial-temporal dipole models: 1) unconstrained (moving and rotating) dipoles; 2) dipoles with a fixed location (rotating) and 3) dipoles with a fixed location and a fixed orientation (fixed). This method was first applied to EEG analysis [96], but the same approach can be used in MEG studies as well [97].

The basic assumption of the model is that there are several dipolar sources that maintain their position, and optionally also their orientation, throughout the time interval of interest. However, the dipoles are allowed to change their strengths in order to produce a field distribution that matches the experimental values [98]. In [99, 100], Mosher et al. assume that the location, orientation and magnitude of the dipoles are unknown, and show how the parameter estimation problem may be decomposed into the estimation of the time invariant parameters using non-linear least-squares minimization, followed by linear estimation of the associated time varying parameters. A subspace formulation is presented and used to derive a suboptimal least-squares subspace scanning method. The resulting algorithm is a special case of the well-known MUltiple SIgnal Classification (MUSIC) method [101, 102], in which the solution (multiple dipole locations) is found by scanning potential locations using a simple one dipole model. The beauty of the method is that one can sort out the feasible source positions relatively quickly. It has been shown with both simulations and applications to actual measurements that the method produces reasonable results. However, if there are strongly correlated sources whose field patterns overlap, the predictions could be misleading [99].

An example of multiple dipole: NeuroMagnetic Imaging (NMI) method

The NeuroMagnetic Imaging (NMI) method presented in [103, 104] extends the dipole model by assuming a large set of current dipoles, each with a fixed location at the center of a voxel (volume element) of a three-dimensional volume within the brain. In other words, the current source is modelled as a discrete number of current dipoles and simply built up from a linear combination of these current dipoles, therefore, the MEG data and image are linearly related. In the following formulation of the method, the total number of measurements and current dipoles is hypothesized as M and N respectively. The relationship between Q_{xn}, Q_{yn} and Q_{zn} and $Q(r_n)$ is expressed in the following equation,

$$
\begin{bmatrix}
Q_{x1} \\
Q_{y1} \\
Q_{z1} \\
Q_{x2} \\
Q_{y2} \\
Q_{z2} \\
\vdots \\
Q_{xN} \\
Q_{yN} \\
Q_{zN}
\end{bmatrix}
=
\begin{bmatrix}
\alpha_1 & 0 & 0 & \cdots & 0 \\
\beta_1 & 0 & 0 & \cdots & 0 \\
\gamma_1 & 0 & 0 & \cdots & 0 \\
0 & \alpha_2 & 0 & \cdots & 0 \\
0 & \beta_2 & 0 & \cdots & 0 \\
0 & \gamma_2 & 0 & \cdots & 0 \\
\vdots & \vdots & \vdots & \ddots & \vdots \\
0 & 0 & 0 & \cdots & \alpha_N \\
0 & 0 & 0 & \cdots & \beta_N \\
0 & 0 & 0 & \cdots & \gamma_N
\end{bmatrix}
\begin{bmatrix}
Q_1 \\
Q_2 \\
\vdots \\
Q_N
\end{bmatrix}
\tag{4.9}
$$

where $\alpha_1, \beta_1, \gamma_1, \cdots, \alpha_N, \beta_N, \gamma_N$ are coefficients, which are the <u>known</u> direction cosines of constrained dipole orientations. Based on the above equation, Equation 2.2 can then be rewritten in matrix form as,

$$
\mathbf{B}_m =
\begin{bmatrix}
B_x(\mathbf{r}_m) \\
B_y(\mathbf{r}_m) \\
B_z(\mathbf{r}_m)
\end{bmatrix}
= \frac{\mu_0}{4\pi} \sum_{n=1}^{N} \frac{1}{|\mathbf{r_m} - \mathbf{r_n}|^3}
\begin{bmatrix}
\beta_n R_{z:m,n} - \gamma_n R_{y:m,n} \\
\gamma_n R_{x:m,n} - \alpha_n R_{z:m,n} \\
\alpha_n R_{y:m,n} - \beta_n R_{x:m,n}
\end{bmatrix}
\begin{bmatrix} Q_n \end{bmatrix}
\tag{4.10}
$$

For M measurements, the above equation can be rewritten by introducing a matrix H as follows,

$$
\begin{bmatrix}
B_1 \\
B_2 \\
\vdots \\
B_M
\end{bmatrix}
=
\begin{bmatrix}
H_{1,1} & H_{1,2} & \cdots & H_{1,N} \\
H_{2,1} & H_{2,2} & \cdots & H_{2,N} \\
\vdots & \vdots & \ddots & \vdots \\
H_{M,1} & H_{M,2} & \cdots & H_{M,N}
\end{bmatrix}
\begin{bmatrix}
Q_1 \\
Q_2 \\
\vdots \\
Q_N
\end{bmatrix}
\tag{4.11}
$$

where

$$
H_{m,n} = \frac{\mu_0}{4\pi |\mathbf{r_m} - \mathbf{r_n}|^3}
\begin{bmatrix}
\beta_n R_{z:m,n} - \gamma_n R_{y:m,n} \\
\gamma_n R_{x:m,n} - \alpha_n R_{z:m,n} \\
\alpha_n R_{y:m,n} - \beta_n R_{x:m,n}
\end{bmatrix}
\tag{4.12}
$$

Once matrix H is known, the above equation gives solutions to the inverse problem by finding Q_n from B_m. Because the dimension of matrix H is $3M \times N$ and in general $3M \neq N$, therefore H is not a square and full rank matrix, i.e. the determinant of

matrix H is zero, Q_n can not be obtained by means of inverting H and hence special technique has to be employed. H can be expanded as below by using the Singular Value Decomposition (SVD) and the matrix outer product expansion techniques to turn singular problems into nonsingular ones [105]:

$$H_{m,n} = \sum_{i=1}^{R} \lambda_i^{1/2} U_{m,i} V_{n,i}^T \tag{4.13}$$

where R is the rank of H, U and V are matrices with columns equal to the eigenvectors of HH^T (the product of H and its transpose) and $H^T H$ respectively, and λ is the eigenvalues of U and V in descending order of magnitude.

Because U and V are derived from the products of HH^T and $H^T H$ respectively, their dimensions are $3M \times 3M$ and $N \times N$. Hence, in order to obtain λ, the eigenvalues λ_U of U and λ_V of V have to be calculated first, then by comparing them and discarding the different eigenvalues between them, a total number of R eigenvalues λ can be obtained; U and V will then change to $\tilde{U}$ and $\tilde{V}$ of dimensions $3M \times R$ and $N \times R$.

By applying the expanded H, Equation 4.11 can be expressed as

$$B_m = \sum_{i=1}^{R} \lambda_i^{1/2} \tilde{U}_{m,i} \tilde{V}_{n,i}^T Q_n \tag{4.14}$$

From the above equation, it can be seen that

$$Q_n = \sum_{i=1}^{R} \frac{1}{\lambda_i^{1/2}} \tilde{V}_{n,i} \tilde{U}_{m,i}^T B_m \tag{4.15}$$

After Q_n is calculated, its three components x, y and z can be obtained from Equation 4.9 based on the known coefficients.

In summary, using the NMI method to reconstruct the current source, the following steps are needed: firstly define the matrix H, secondly decompose H through matrixes U and V, thirdly study the spectrum of eigenvalues and select a threshold for them, and finally carry out the reconstruction.

From Equation 4.15, it can be seen that if the eigenvalues λ are very small, then $1/\lambda$ will be large and hence the component in B due to measurement noise will be amplified enormously and disproportionately. To tackle this problem, it is common

to truncate the summation in Equation 4.15, in other words, Q_n is only summed up to P where $P \leq R$. However, this will unavoidably introduce a truncation error and thus reduce the quality of the reconstruction due to the loss of the details for the reconstruction which may be provided by the small eigenvalues. Therefore, the choice of P must be considered very carefully, taking into account of the sensitivity to noise and the truncation error in different specific reconstructions, because as P is increased towards R, the quality of the reconstruction will be increased, but at the expense of the increased sensitivity to noise.

In a typical set of MEG signals, much of the "power" is concentrated in the first few eigenvalues, e.g., according to [104], in a typical case 90% of the power is contained in the first 10 eigenvalues, and 99% in the first 40 eigenvalues. Furthermore, increasing the number of measurements past some limits yields little improvement in reconstruction because additional measurements contain virtually no useful information.

From the above formulation of the NMI method, we can see that for solving the inverse problem the NMI makes use of eigenvalues and eigenvectors of a matrix, which in this case is matrix H. H plays a key role in the reconstruction process. Referring to the definition of the lead field in the following Chapter 5, H can be treated as a matrix in terms of the lead field, because it contains the exact information about the locations of the sensors, and the locations and orientations of the presumed sources (the more prior knowledge about the source, the higher quality of the reconstruction will be). In principle, the method can be employed to reconstruct sources like single or multiple current dipoles and even more complex current distribution fields, which describe the brain's response to an applied stimulus or spontaneous activity.

4.2.3. Multipole Model

Improvements in the MEG signal-to-noise ratio have opened opportunities to analyze the magnetic field with greater sophistication [106, 107]. Since the electrocardiogram and magnetocardiogram have much higher signal-to-noise ratios than signals obtained from the head surface, some of these techniques have already been applied there. In 1958, Yeh [108] described a theory for sources in a homogeneous sphere, with a demonstration that traditional electrocardiographic techniques are approximations of this general approach. In 1970, Arthur and Geselowitz introduced a

mathematical model to investigate the effects of electrical inhomogeneities on the apparent location and magnitude of a cardiac current dipole source [53]. This was recently reviewed by Katila and Karp [109], and by Titomir and Kneppo [110]. There has also been some work on the multipolar nature of magnetic dust loads in lungs [111].

Generally, a distribution of currents will give rise to a field which can be expressed as a mathematical series. Wikswo and Swinney provide a very general theory deriving and comparing various expansion series for approximately static fields [112]. Among the most useful and elegant is the so-called scalar spherical harmonic series. The first term of the series, the monopole, is a linear term which has not been found to apply to magnetic fields. However, there are practical situations which arise that can approximate a magnetic monopole, and Ferguson and Durand have suggested that there are mathematical simplifications inherent in monopoles which make them a good model for certain distributed current sources [113]. The next three terms represent the dipole, which has been described above. The next set of terms represents the quadrupole, which falls off much faster with distance from the source than does the dipole. The series continues infinitively, with successive terms typically contributing less to the magnitude of the field. Katila and Karp [109] point out that if too many terms are included, the number of coefficients will exceed the number of measured data and there will be no reduction. Usually the series is cut off after the quadrupole or octapole terms.

A mathematical advantage of including terms higher than the dipole terms is that the second criterion of well-posed inverses (uniqueness) is more neatly met. However, the third criterion, stability, might become problematic. Small changes in the measured field due to noise have the potential to dramatically change the postulated multipole source.

A potential clinical advantage of the multipole technique is that a distinction can be made between sources that otherwise appear to reside in the same location. However, it is perhaps too soon for clinically relevant encephalographic distinctions to be found in the literature. A clinical disadvantage is the difficulty in thinking of a physiological basis for the multipoles.

4.2.4. Distributed Sources Models

Distributed sources are the most flexible yet computer-intensive, often requiring many hours of mainframe time, or access to parallel computer systems, such as transputers [114, 115]. They are often called model-independent, because no particular geometry is assumed for the source.

The basic idea of the model is that the source is unknown but can be guessed. In particular, the source is considered to be an array of current elements. Then the measurements which such a guessed source would yield are compared with the actual measurements, and the guessed source is chosen to minimize the difference between the actual measurements and the measurements implied by the guessed source.

This method is very flexible, and various requirements can be imposed along with the minimization just described in [51, 116]. For example, the postulated source should be biologically realistic: 20 Ampere sources are not likely in the human brain. And the sources should be constrained to lie within the volume of interest [117]. Such modifications fit naturally into the distributed source methods.

Simulations have shown that the distributed source techniques are capable of revealing complex sources. Kullmann [118] and Kado [116] demonstrated the reconstruction of a vortex source. Simulations by Clarke [119] provide empirical evidence that the inferred distributed sources are robust.

How do the distributed source techniques hold up in the experimental conditions? Greenblatt found agreement between the distributed source solution and the dipole solution for the auditory evoked response to 500-Hz tone bursts [120]. Kullmann used a saline phantom to demonstrate that the distributed source technique can distinguish dipole 3 cm apart, whereas the dipole fit guesses just one at the midpoint [118].

An example of distributed sources models: magnetic field topography (MFT)

An exciting application of the distributed source techniques is dynamic imaging. Magnetic Field Topography (MFT) developed and implemented at the Open Uni-

versity (O.U.) estimates 3-D brain activity millisecond by millisecond from magnetic field measurements. The method also provides empirical evidence that the inferred distributed sources are stable. A source is inferred from a "snapshot" of a magnetic field configuration. Another source is inferred from a snapshot made a short time later. This process is repeated, with no input to the algorithm of the previous solutions. When the sequence of sources is viewed, the source appears to change smoothly. By definition, a stable solution is one that changes smoothly as the input is varied smoothly.

The original algorithm of MFT was described in detail by Ioannides in [121], and reviews of the method have been given fully in recent papers [3, 122]. The method has been successfully applied to the analyses of both averaged and unaveraged MEG data, obtained from a wide range of experiments and studies, such as auditory evoked experiments in normal subjects [123, 124] and in Alzheimer patients [125], Contingent Magnetic Variation (CMV) studies [126, 127, 128], and interictal epileptic activity studies [129]. Results from these analyses provide insights into how the brain works and prove that MFT offers a powerful platform of functional localization, especially when marrying with other brain imaging techniques, such as PET and fMRI in recent studies.

MFT makes use of the vector-valued expansion functions $\phi(\mathbf{r}, \mathbf{r}')$ (or simply ϕ) known as the lead field, which will be the main theme of the next chapter. The magnitude m_i of the magnetic field of the ith coil at position $\mathbf{r}$ generated by a continuous current density $\mathbf{j}(\mathbf{r}')$ at position $\mathbf{r}'$ within the source space Q can be defined as

$$m_i = \int_Q \phi_i \cdot \mathbf{j}(\mathbf{r}')\, d^3\mathbf{r}' \qquad (4.16)$$

where ϕ_i is a vector field determined completely by the orientation and geometric details of the sensors, while the current density $\mathbf{j}(\mathbf{r}')$ can be expressed as a linear combination of the expansion functions, which is given by,

$$\mathbf{j}(\mathbf{r}') = \sum_{k=1}^{s} A_k\, \phi_k\, \omega(\mathbf{r}') \qquad (4.17)$$

where s is the total number of sensors, $\omega(\mathbf{r}')$ is an *a priori* probability weight function defined throughout the source space incorporating any prior information about the source, and A_k are coefficients of the expansion functions that can be determined as

follows by combining Equation 4.16 with 4.17,

$$m_i = \sum_{k=1}^{s} P_{ik} A_k \tag{4.18}$$

where matrix P is defined by

$$P_{ik} = \int_Q \phi_i \cdot \phi_k \, \omega(\mathbf{r}') \, d^3\mathbf{r}' \tag{4.19}$$

Ideally, if P is sufficiently non-singular, A_k can be obtained from Equation 4.18, and then substitute A_k into Equation 4.17 for obtaining the reconstructed current density $\mathbf{j}(\mathbf{r}')$.

But when a large number of expansion functions are used for the reconstruction, P will become almost singular due to the similarity of the expansion functions ϕ_i. The ill-posed nature of the inverse problem manifests itself in the probabilistic method through the ill-conditioned nature of matrix P; this is similar to matrix H discussed in the NMI method. To tackle this problem, we can employ the SVD technique to turn a nearly singular matrix into a nonsingular one. As an alternative, $\mathbf{j}(\mathbf{r}')$ can be expanded in terms of a smaller subset of these expansion functions and thus replace Equation 4.17 by

$$\mathbf{j}(\mathbf{r}') = \sum_{k=1}^{t} A_k \, \phi_k \, \omega(\mathbf{r}') \tag{4.20}$$

where t is the number of the selected sensors which holds $t \leq s$.

The selection of the number t (i.e., which lead fields to include) is crucial for avoiding the singular behaviour of matrix P. In general, it is better to select t sensors which are farther away from one another because they correspond to more differences in the form of ϕ_i functions. Moreover, the selection has effect on the reconstruction of $\mathbf{j}(\mathbf{r}')$, because if t is too small, the reconstructed $\mathbf{j}(\mathbf{r}')$ is stable, but its accuracy is low due to the insufficient information about $\mathbf{j}(\mathbf{r}')$. On the other hand, if t is too big, P tends to become singular and thus unstable and more sensitive to noise.

A controlled way of increasing the stability of the reconstruction is through regularization as described in [121]. Probabilistic treatment of continuous current density

lead to a modified system [130]:

$$\tilde{m}_i = \sum_{k=1}^{t} \tilde{P}_{ik} A_k \qquad i = 1, \ldots, t \tag{4.21}$$

where $\tilde{m}_i$ and $\tilde{P}_{ik}$ are given by

$$\tilde{m}_i = \sum_{k=1}^{s} P_{ik} \, m_k \tag{4.22}$$

$$\tilde{P}_{ik} = \sum_{j=1}^{s} P_{ij} P_{jk} + \zeta P_{ik} \tag{4.23}$$

and

$$\zeta = \frac{\bar{\zeta} T_r P}{s} \tag{4.24}$$

where $\bar{\zeta}$ is a dimensionless quantity and can be adjusted according to the total number of sensors, and $T_r P$ denotes the sum of the diagonal elements of matrix P.

From the above formulation, it seems that the second set of formulas (Equations 4.21 to 4.24) are much more complicated than the first set (Equations 4.18 to 4.19) when implemented in computer, but it is valuable in reducing the singular behaviour of matrix P, in other words, reducing the sensitivity to the noisy data gathered by magnetic field measurements, though regularization itself does not eliminate singularity completely. In addition, with the introduction of ζ, it is possible to limit the likelihood of very large current density. To demonstrate this, we write explicitly the expression for $s = 1, t = 1$ (we ignore for this demonstration Equation 4.24 because we want to let P_{11} tend to zero but retain a nonzero value for $\tilde{m}_1$). From Equations 4.22 and 4.23, we have,

$$\tilde{m}_1 = P_{11} \, m_1 \tag{4.25}$$

$$\tilde{P}_{11} = P_{11} P_{11} + \zeta P_{11} \tag{4.26}$$

Substituting the above two equations into Equation 4.21, we have,

$$A_1 = \frac{m_1}{P_{11} + \zeta} \tag{4.27}$$

Hence, from Equation 4.20, it gives,

$$\mathbf{j}(\mathbf{r}') = \frac{m_1}{P_{11} + \zeta} \, \phi_1 \, \omega(\mathbf{r}') \tag{4.28}$$

Note that P_{11} can not be negative; it is zero if the single measurement is not sensitive to the activity in the source space. From the above equation, it can be seen that even if $P_{11} = 0$ or very small, $\mathbf{j}(\mathbf{r}')$ will only have a maximum instead of an infinity, and thus restrict the likelihood of a very large reconstructed current density. Therefore, a nonzero value of ζ ensures that the current density modulus is limited in magnitude.

From the above formulation, it can be concluded that MFT offers the following distinctive advantages and flexibilities:

1. For a given source type in a given source space, the expansion function of each sensor is completely determined by the orientation and geometric details of the sensor. Therefore, the expansion functions ϕ_i need .to be calculated only once for each experimental arrangement, which is a great advantage and convenience for implementation on computers.

2. It is possible to define different expansion functions ϕ_i for different source types, e.g., a current density in an infinite half space and within a conducting sphere.

3. The definition of the source space Q can be very flexible and is based on the sensitivity profile of the sensors and the brain areas of interest in different experiments and analyses, which can be a cylinder, hemisphere or cone (part of a hemisphere) [131]. As a consequence, the source space fits more naturally with the curvature and structure of the brain.

4. Having specified the source type and source space, any prior knowledge or assumptions about the source can be included via an *a priori* probability weight function $\omega(\mathbf{r}')$ which can be defined as different functions, such as the following delta function:

$$\omega(\mathbf{r}') = \varpi(\mathbf{r}') \sum_{n=1}^{N} \delta(\mathbf{r}' - \mathbf{R}_n) \tag{4.29}$$

where $\mathbf{R}_n$ is the likely position vector of the nth source, and $\varpi(\mathbf{r}')$ is the guess probability which reflects the information about the source, such as its

location and depth in space etc. If the current sources are assumed having a uniform probability, then $\varpi(\mathbf{r'})$ can be taken as a constant throughout the source space.

5. It is possible to vary the probability weight in three dimensions according to the emphasis of the different profile of the postulated source(s), i.e., a probability weight is chosen for reconstructing deep sources (e.g., in y direction), while another different probability weight is selected for sources at a superficial level (e.g., in the xz plane). Hence, a more complicated probability weight can be introduced either to focus on one region of the brain, or to include some prior information (e.g., constraints from anatomy).

6. For the analyses employing the MFT method by the Biomagnetism group at the O.U., a very simple form of the probability weight has been used so far: a Gaussian centered at or close to the center of the conducting sphere. As a result, the only adjustable parameter of the method is the regularization parameter ζ, or $\bar{\zeta}$, a choice involving between resolution and insensitivity to noise. When implementing the algorithm on the transputer at the O.U., $\bar{\zeta}$ is substituted by a smoothing parameter called τ, where $\tau = \log(1/\bar{\zeta})$. In general, when applying the MFT method to the analyses of average data, the difference made by τ is not so prominent; however, it plays an important role in single epoch analysis, as averaging increases the signal-to-noise ratio, although what is considered as noise in averaging could be in some cases physiologically important. In any event, care must be taken in the selection of τ to make sure that the noise is not amplified, because as τ increases, the reconstruction becomes more sensitive, but also it tends to be less tolerant to noise. It has become a routine now at the O.U. that before the application of the MFT analysis to real data, a test using computer generated data is conducted to define the optimal parameter combination, i.e., the probability weight and the smoothing parameter.

7. It has been shown that it is plausible to conduct the tests (or 'training' as referred to in [122]) for the parameter choice by using point generators, namely, a few current dipoles and their combinations are sufficient to determine the optimal parameters. Once the parameters are set, they can be applied to the real signal timeslice by timeslice without further adjustment.

In practice, the MFT method offers a very efficient approach for solving the inverse

problem. It can reveal the number and locations of activated areas, with the only prior assumption being that there is a small number of localized sources. Moreover, it possesses the ability to define deep sources. In other words, it is possible to place the focus of the analysis on either superficial or deep sources or both. It is worthy of mention that deep sources can be "imaged" even when the source space was intended to emphasize superficial sources. In this work, we have used MFT to analyse how the left and right hemisphere of the brain interact and we have included reconstructions in the depth, as hints of what the generators might be in these regions. As the method gets more refined, it will hopefully become a powerful clinical tool for diagnosis and treatment of patients as well.

CHAPTER 5.

LEAD FIELDS

Lead fields are vector fields which are used to reflect the sensitivity of magnetic measurements. The lead field **L** specifies both the spatial and vectorial sensitivity of a given detection system. It is no surprise then, that, as we will see, lead fields can play a very important role in solving the inverse problem.

In this chapter, the basic theory of lead field is used to compare the sensitivity pattern associated with the two basic coil shapes used in most modern multichannel MEG systems. For ease of visualization, we use a plane of measurements to display properties of the lead fields.

As discussed in Section 4.2.4, a measurement can be expressed as a linear function of the current density $\mathbf{J}(\mathbf{r}')$. We will use specifically for demonstration purpose the *ith* component of the magnetic field, corresponding to a measurement with a point magnetometer. For this case,

$$m = \mathbf{B}(\mathbf{r}) \cdot \hat{\mathbf{e}}_i = \int_Q \mathbf{L}^i(\mathbf{r}, \mathbf{r}') \cdot \mathbf{J}(\mathbf{r}') \, d^3\mathbf{r}' \tag{5.1}$$

where $\mathbf{L}^i(\mathbf{r}, \mathbf{r}')$ is often termed the lead field corresponding to the given detector; the lead field is of course identical to ϕ defined earlier in Section 4.2.4. When no confusion arises, we will denote the lead field as **L**.

The integral in the above equation extends over all space, or eventually over a source space Q, which contains all regions where the current density $\mathbf{J}(\mathbf{r}')$ is non-zero. An MEG measurement involves the flux, i.e., the integral over a finite area, or set of areas, S. The lead field for such a measurement is simply the corresponding integral of the lead field for **B** over the(se) area(s).

73

The above equation reveals a very important principle about lead fields, that is, if
the lead field **L** of a given sensor happens to be perpendicular to some hypothesized
current source at a given point **r'**, then the measurement with this sensor clearly
gives us no further information about the source; while they have maximum sensi-
tivity when **L** and **J** are parallel (of course if the same sensor is displaced or related
the corresponding lead field could become non-zero). This implies that contribu-
tions from a certain region of the body may be enhanced by choosing the location
and coil geometry, which makes **L** and assumed **J** parallel and strong in the region
of interest and weak elsewhere. Consequently, a weighted parameter could be intro-
duced to the lead field **L** so that the contribution at each point **r'** is weighted and
it is possible to design the lead field pattern in the region of interest, such as a zero
field or a uniform field and so on.

Figure 5.1 illustrates simple "generated" lead fields. For the MEG, the detection coil
is reciprocally energized by a time-varying current I that produces a time-varying
magnetic field **B**. By Faraday induction, this field produces the current **L** known
as the lead field. The direction of the lead field can be obtained by Lenz's law,
which states that the direction of the induced electromotive force (e.m.f.) is such
that the induced current produces a magnetic flux tending to oppose the original
change of flux. If the shape of the coil is circular, the lines of the lead field form
closed loops for satisfying Laplace's equation [8]. Hence, in the case of Figure 5.1,
the induced lead fields form clockwise concentric circles when looked downwards. In
MEG measurements, V is the induced voltage output of the magnetic field **B**.

5.1. Formulation

This section is devoted to formulating the expressions for lead fields, which depend
on details of the medium within the brain and the detector configuration.

By comparing Equation 5.1 with the expressions for magnetic fields generated by
different models of medium in Chapter 2, we can easily derive the corresponding
formulas for lead fields in the different medium within the brain.

As an example, for a current density in an infinite half space, based on Equations
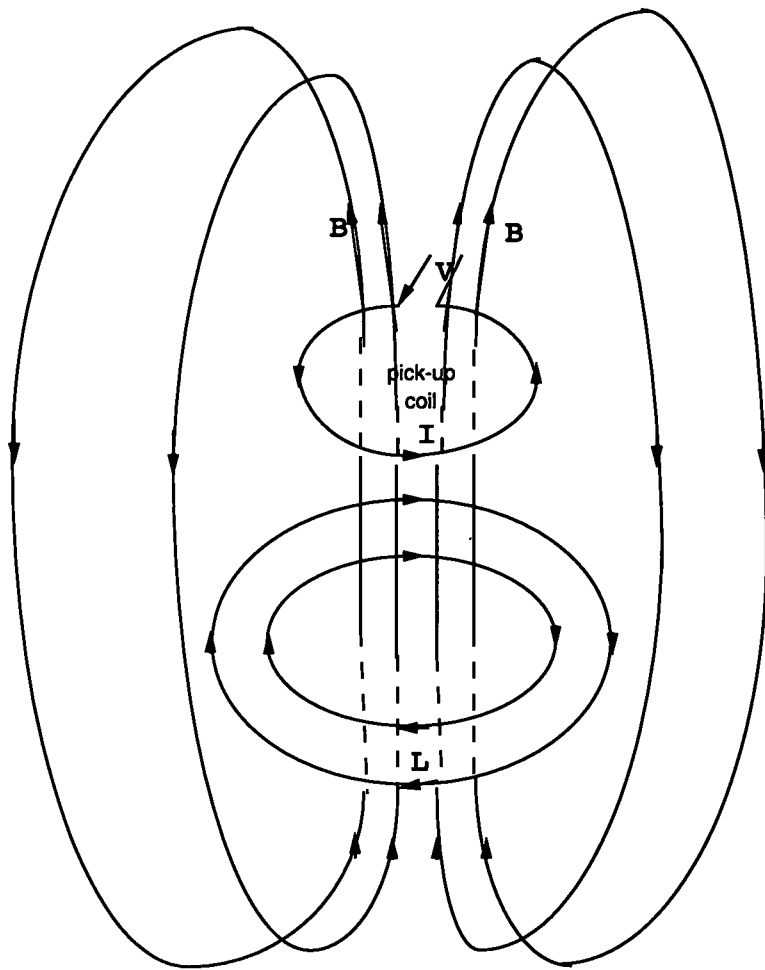
Figure 5.1 Schematic of the MEG lead field when a single-turn circular detection coil is placed above the current source.

5.1 and 2.8, and $\hat{e} \cdot J(r') \times (r - r') = (r - r') \times \hat{e} \cdot J(r')$ with $\hat{e} = r/|r|$, it yields

$$L = \frac{\mu_0}{4\pi} \frac{(r - r') \times \hat{e}}{|r - r'|^3} \tag{5.2}$$

Because of the finite area of a coil, the above equation is rewritten as,

$$L = \frac{\mu_0}{4\pi} \int_{coil} dS_{coil} \frac{(w + s - r') \times \hat{e}_{coil}}{|w + s - r'|^3} \tag{5.3}$$

where w is the position vector of the coil's center, r' denotes the position vector of the current source, $\hat{e}_{coil}$ is the unit normal vector of the coil and s is a displacement vector from the center of the coil to an arbitrary point in the coil.

For a current density within a conducting sphere, whose center is at a position vector k, the lead fields L are defined as follows:

$$L = \frac{\mu_0}{4\pi} \left\{ [(r' - k) \times \hat{e}_{coil}] \int_{coil} \frac{dS_{coil}}{F} + \int_{coil} dS_{coil} \frac{\hat{e}_{coil} \cdot \nabla_{(w)} F}{F^2} [(w + s - k) \times (r' - k)] \right\} \tag{5.4}$$

where

$$F = |w - r'| [|w - r'| |w - k| + (w - r') \cdot (w - k)] \tag{5.5}$$

and

$$\nabla_{(w)} F = \left[\frac{|w - r'|^2}{|w - k|} + \frac{(w - r') \cdot (w - k)}{|w - r'|} + 2(|w - r'| + |w - k|) \right] (w - k)$$
$$- \left[|w - r'| + 2 |w - k| + \frac{(w - r') \cdot (w - k)}{|w - r'|} \right] (w - r') \tag{5.6}$$

From the above formulas for lead fields, several conclusions can be made: first, lead fields are vector fields and affected by the relative location of source space and the detection coils; secondly, lead fields are obtained by the integration over the sensors, hence, the coil shape has impact on the lead field pattern; thirdly, different medium models have effect on the lead field pattern.

5.2. Patterns and Analysis

For the remainder of this section, we will explore the lead field patterns arising from various coil shape designs and specific models of the medium. We will use a concrete example of a measurement set and source space configuration, which mimic typical real experimental situations.

The geometry of the source space and measurement plane is as shown in Figure 5.2: the source space is a disc of 5 cm radius and the measurement plane is a square of 16 cm side. The planes are parallel to each other and have a separation of 5 cm. For representing the lead fields conveniently, the source space is discretized on a square of 10 cm side, as shown by the dashed square in Figure 5.2(b), divided into 17×17 small squares. The lead fields are evaluated at the centers of these small squares. It is important to note that the lead fields are continuous functions and that this discretization is performed for representation purpose only. With these geometry arrangements, lead fields are evaluated as the coil moves along the 25 positions, which are 4 cm away from each other, in the measurement plane parallel to the source boundary in the xy plane. Hence, the evaluated lead field pattern at each of these 25 positions shows how well and what the detection coil can reveal of generators within the postulated source space. Note that the setting of lead fields to zero outside the disc mimics the case of imposing a zero probability for the current distribution outside the source space, e.g. the head.

Though a plane of measurements is chosen for the following simulations, which does not seem realistic simulations because the dewar base of most modern multichannel MEG systems is either a helmet shape (e.g. the Neuromag-122 and the CTF system) or a curved shape (e.g. the BTi twin MAGNES probe), it is the sensitivity profile of different coil shapes that we will emphasize here. We wish to generalize the advantages and limitations of the different coil shapes used in most MEG systems, rather than make it specific to any MEG system. To this end, two kinds of coil shapes, which covers the majority coil designs in the MEG systems available worldwide, will be discussed, i.e., one is full circular and the other is half circular (2-D shaped), as shown in Figure 5.3. The effect of such different coil geometries as magnetometers and gradiometers on the characteristics of the lead field patterns will also be assessed. Furthermore, the effect of relative position of the postulated source space and the measurement plane on the lead field patterns will also be addressed.
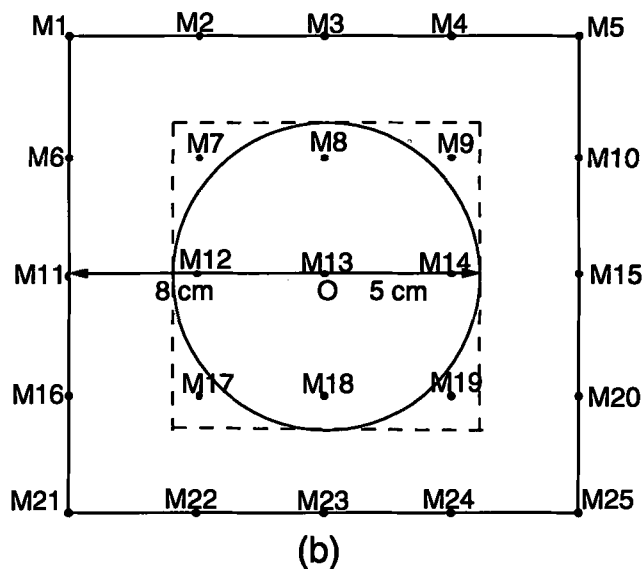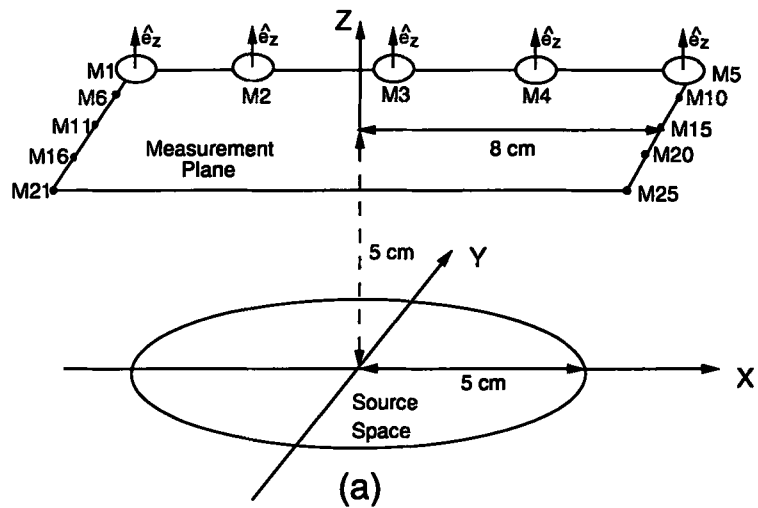
Figure 5.2 Geometry of the source space and measurement plane: (a) The source space disc and measurement plane in space, (b) A projection of the 25 measurement points ($M1$, $M2$, $\cdots$, $M25$) on the source space plane. The dashed square shows the square mesh used to discretize the lead fields.
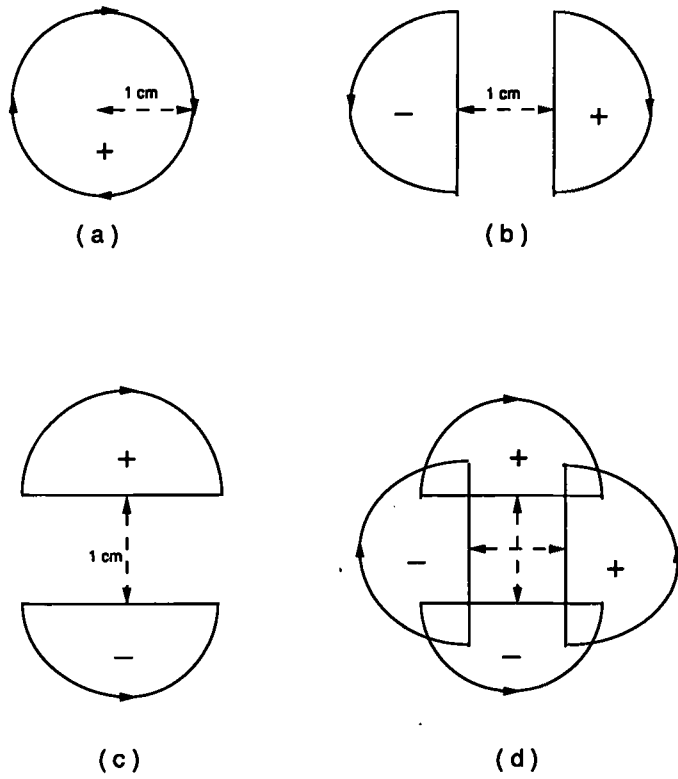
Figure 5.3 Different coil shapes as viewed from above: the arrow on the circle indicates the integration direction, the positive sign shows the flux change through the coil is in the $+z$ direction.

5.2.1. Circular Coils

In this section, lead fields are evaluated for the two medium models respectively by using a full circular coil (e.g., the Siemens 37-channel KRENIKON system, the BTi twin 37-channel MAGNES system, and the Canadian CTF 128-channel system, see Section 3.4.3), as shown in Figure 5.3(a). For discussing the lead field conveniently, the coil was placed on the z axis with $\hat{e}_{coil} = \hat{e}_z$. The lead fields are displayed within an xy plane parallel to the measurement plane. Figure 5.4 shows the lead field pattern for an infinite half space, where the directions of the lead fields are shown as the arrows and the intensities are indicated by the thickness of the arrows and the darkness of the background.

In Figure 5.4, a circular disc boundary is introduced in anticipation of physiological constraints which later on will be used to restrict the extent of the source space. Referring to Figure 5.2(b), which depicts the relative positions of the measurement plane and the source space, we can see that the directions of the lead fields form anticlockwise loops (refer to the earlier discussion in this chapter on the MEG lead fields), while the magnitudes of the lead fields decrease as the distances between the source space and the measurement plane increase. This can be easily verified by the following example: refer to point $M1$ in Figure 5.2(b) and the lead field pattern in the most top left of Figure 5.4, as the distance between $M1$ and the point (one of the 17x17 points) in the source space increases, the magnitude of the lead field decreases. In other words, points in the top left of the source space have greater lead field magnitudes than those in the bottom right ones in the source space when the measurement is taken at point $M1$. It is worthy of note that when the measurement plane is directly above the source space with both centers overlapping (refer to the middle of Figure 5.4), the lead field pattern shows symmetric characteristic with the central area being close to zero, where the distance between the measurement plane and the source space is at its minimum. This can be explained by the fact that the cross product in Equation 5.3 is zero. The lead fields at points near the center of the source space are likely to be close to zero. Therefore, the magnitude of the lead field at a specific point depends on its relative position with the source space and the distance between them. Basing on this, we can predict that if the coil, which is just placed above the source space, moves further away from the source plane along the $+z$ direction, the same evaluated point will have smaller magnitude than before. Moreover, the changing rate of the lead fields for the proximate points is
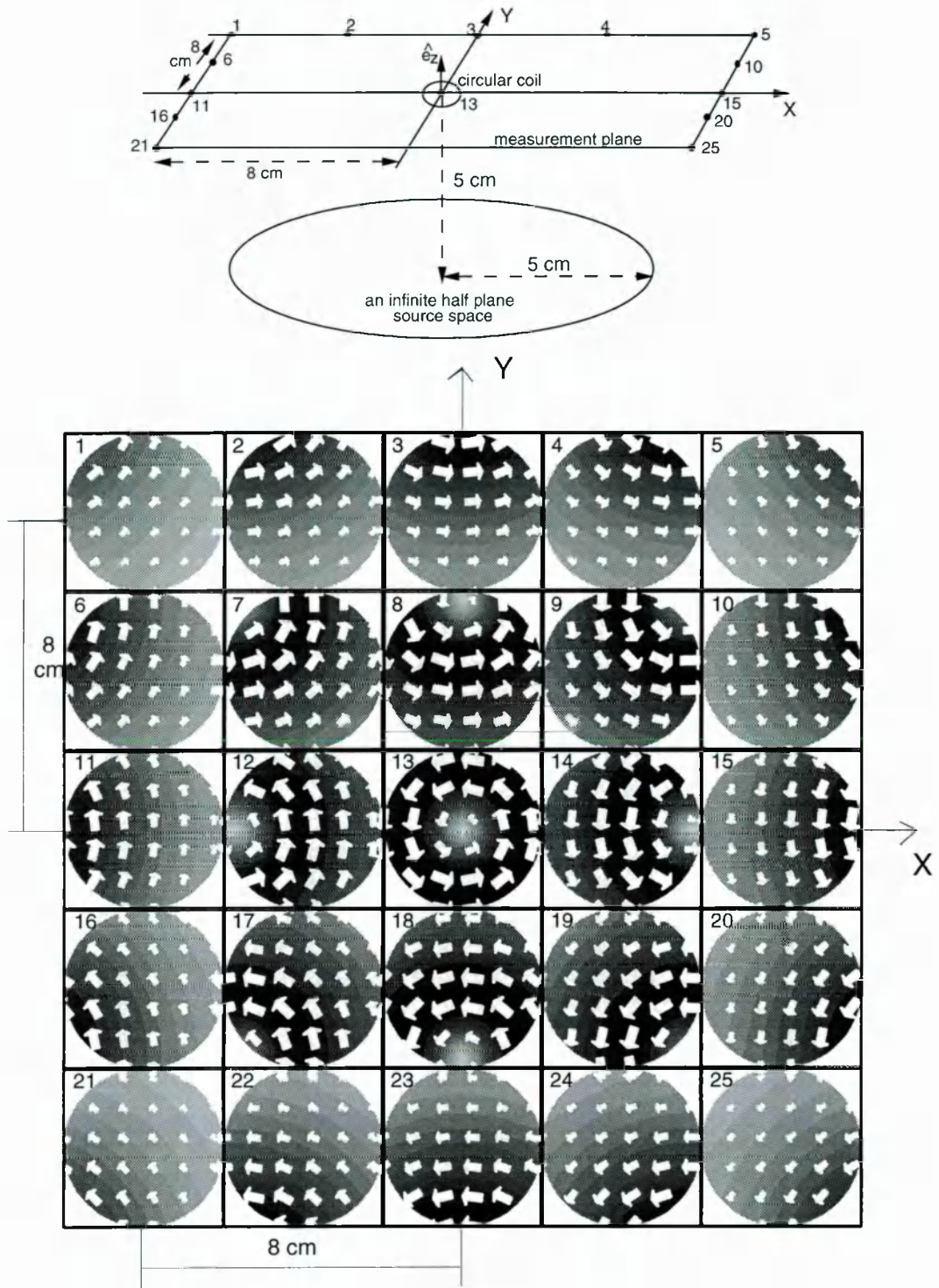
Figure 5.4 Lead field pattern for an infinite half space along a measurement plane parallel to the source boundary in the xy plane with the unit vector normal to the coil's plane $\hat{\mathbf{e}}_{coil} = \hat{\mathbf{e}}_z$, using a circular shaped magnetometer. Notice the symmetry and effect of the coil position on the magnitude of the lead field.

much more steady and moderate for the source space farther away from the measurement plane than that closer to it. Consequently, the "zero-zone" (the area of the lead field being close to zero) is much bigger for the source space farther away the measurement plane than that closer to it. This implies that as the measurement plane becomes closer to the postulated source, as one would expect, the sensitivity to sources is increased but the stability is deteriorated, i.e. it becomes more sensitive to the position of the postulated source related to the measurement plane.

The above test is carried out by using a magnetometer, which consists of a simple detection coil. In practice, gradiometers, which are composed of a series of detection coils, will be used for discriminating against the magnetic noise. As discussed in Section 3.2.2, using a gradiometer will reduce the sensitivity to sources because the compensating coils are wound in the opposite sense to the pick-up coil. In other words, the net magnetic fields that the sensor can detect has been decreased by the differential relationship between the pick-up coil and the compensating coils. Hence, it can be predicted that in the case of using gradiometers, the magnitudes of lead fields will be smaller than those of magnetometers, an effect which increases with the order of the gradiometer.

The current density for generators within a conducting sphere, whose center is at the origin of the coordinate system, produces lead field pattern as shown in Figure 5.5. The figure reveals that the lead field pattern of a current density in a conducting sphere is very similar to that in an infinite half space. In comparison, the magnitudes of the lead fields within a conducting sphere are stronger than those in an infinite half space under the same simulation condition; in numeric values, for the same point in the source space, the lead field in the conducting sphere is roughly twice as strong as that in an infinite half space. Additionally, the lead field pattern for the conducting sphere is more stable than that for an infinite half space, i.e. the lead field changes more dramatically for the proximate points in an infinite half space than in the conducting sphere medium.

The above simulations are sampled with the unit vector normal to the coil's plane in the $+z$ direction, which means that the coil measures the z (radial) component of the magnetic field only. If the coil is turned by 90^0 to examine the lead field pattern when the x (tangential) component of the magnetic field is sampled, i.e., $\hat{\mathbf{e}}_{coil} = \hat{\mathbf{e}}_x$,
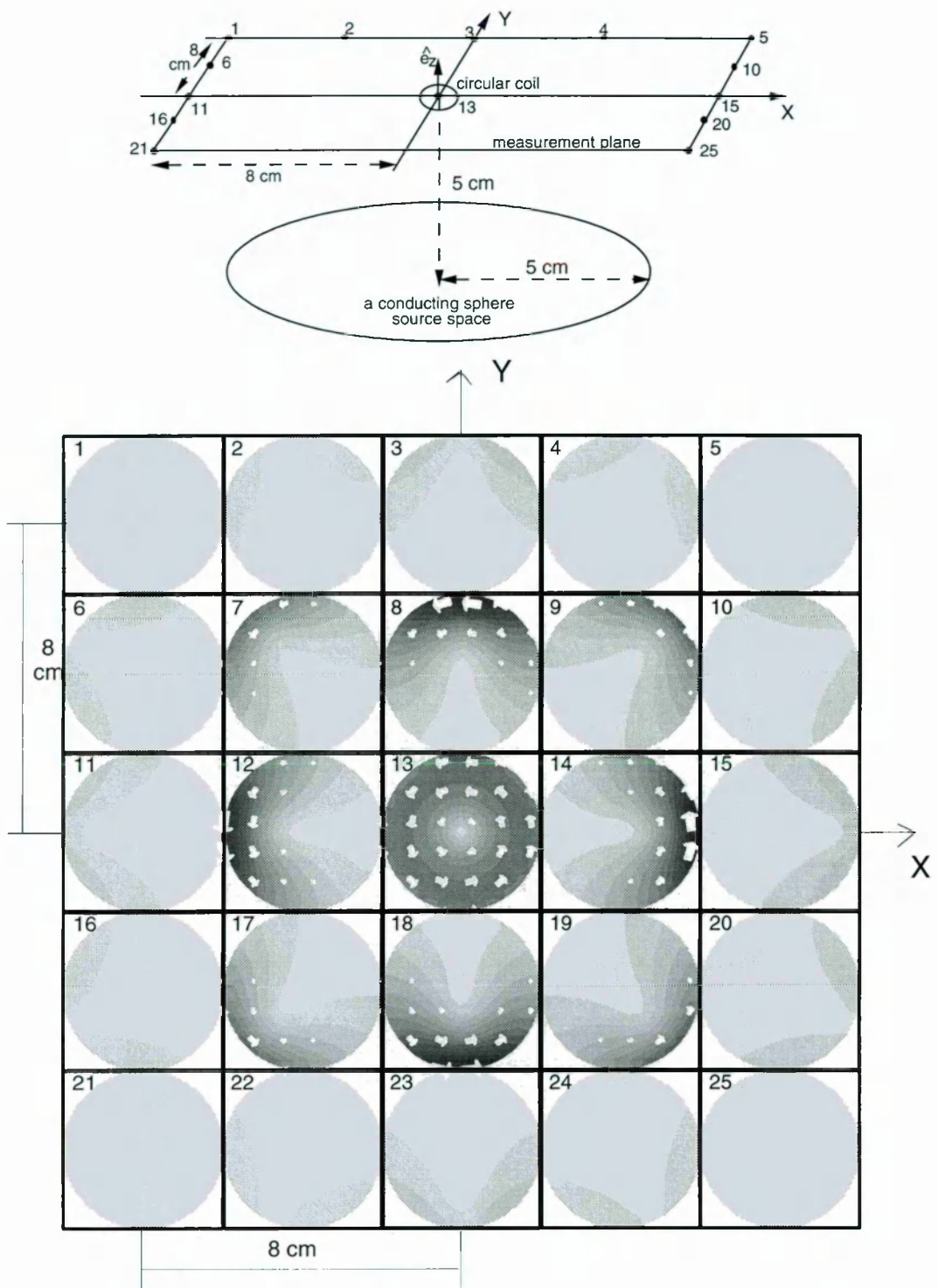
Figure 5.5 Lead field pattern for a current density within a conducting sphere whose center at (0,0,0) in (x,y,z) along a measurement plane parallel to the source boundary in the xy plane with the unit vector normal to the coil's plane $\hat{\mathbf{e}}_{coil} = \hat{\mathbf{e}}_z$, using a circular shaped magnetometer. Note that the figure is similar to Figure 5.4 for the infinite half space, but shows more focused for nearby sources.

the lead field pattern is as illustrated in Figure 5.6.

Compared with Figure 5.5, Figure 5.6 demonstrates better spatial resolution, especially at the edges of the source space (i.e., the lead field changes more rapidly between adjacent points). This improvement in spatial resolution is, however, accompanied by a poorer stability. Moreover, the figure shows that the directions of the lead fields are generally in y direction and symmetric to the y axis, which indicates that the coil is most sensitive to sources in y direction while relatively insensitive to those in x direction. By symmetry, it can be predicted that when $\hat{e}_{coil} = \hat{e}_y$, the lead field patterns will be symmetric to the x axis. This suggests that a special geometry arrangement for the coil might be made so that it would be most sensitive to sources in one special direction. The above observation is also valid for sources in an infinite half space.

The above figures illustrate the lead field patterns in the xy plane, we now turn to investigate the relationship between the lead fields and the depth of the source. The geometric arrangement of the measurement plane is the same as above, while the source space (a disc of 5 cm radius perpendicular to the measurement plane) is now in the xz plane with the minimum distance between the measurement plane and source space being 3 cm, i.e. the source space is perpendicular to the measurement plane, with the top and closest point to the measurement plane in the source space is 3 cm. Figure 5.7 shows the lead field pattern for a current density in the conducting sphere medium.

Referring to the middle of Figure 5.7, which shows the lead field pattern when the coil is above the center of the source space, we can conclude the following characteristics of the lead fields as the depth function of the source:

1. The lead field pattern is symmetric with respect to the y axis: the lead fields in the left and right of the source space have the same magnitudes but opposite directions. The maxima occur at the top left and top right of the source space, while the minimums are in the middle. This can be explained by the fact that the relative positions and distances between the coil and the source space.

2. As the depth of the source increases, the magnitudes of the lead fields decrease.
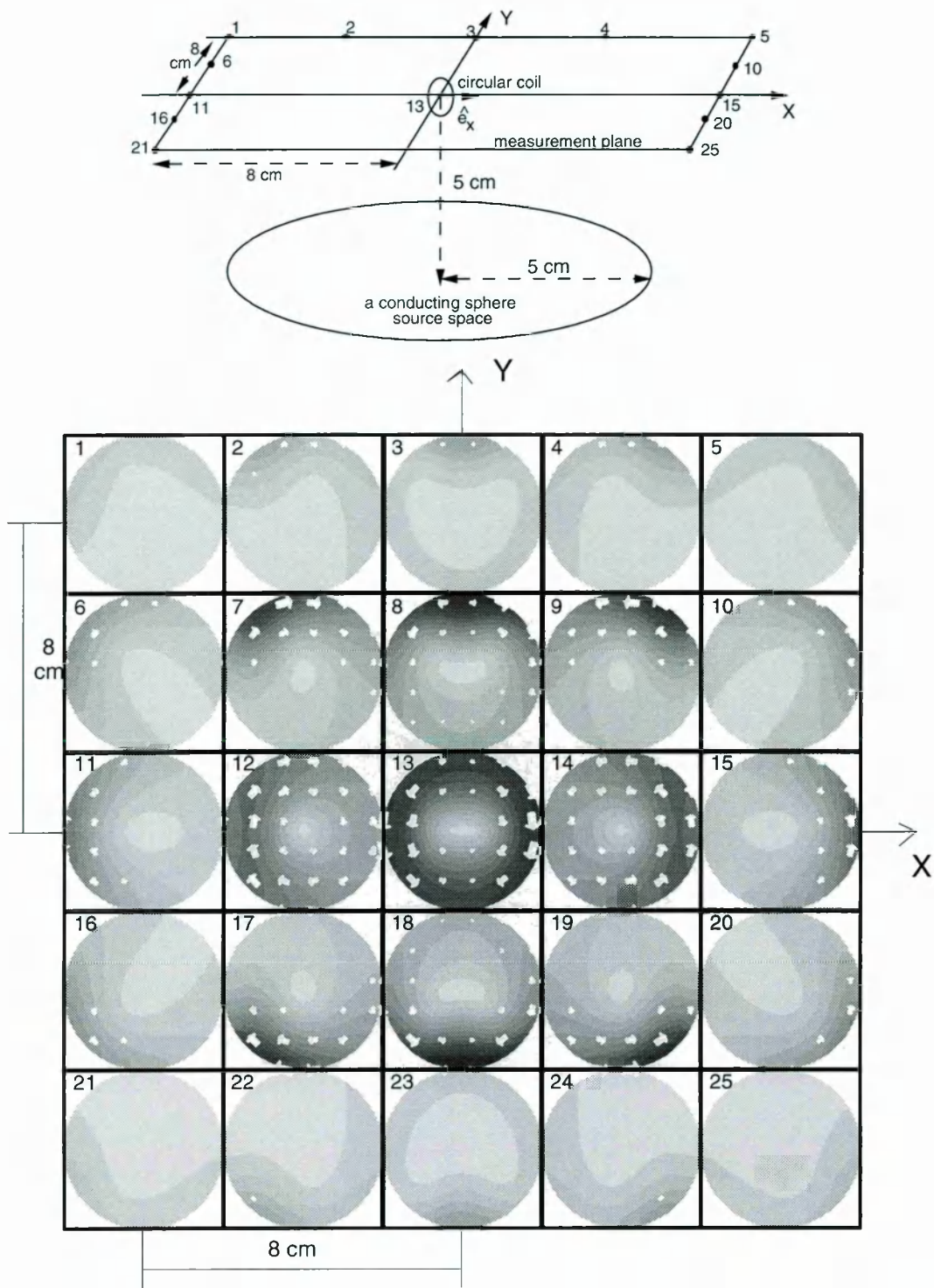
Figure 5.6 Lead field pattern for a current density within a conducting sphere whose center at (0,0,0) in (x,y,z) along a measurement plane parallel to the source boundary in the xy plane with the unit vector normal to the coil's plane $\hat{\mathbf{e}}_{coil} = \hat{\mathbf{e}}_x$, using a circular shaped magnetometer.
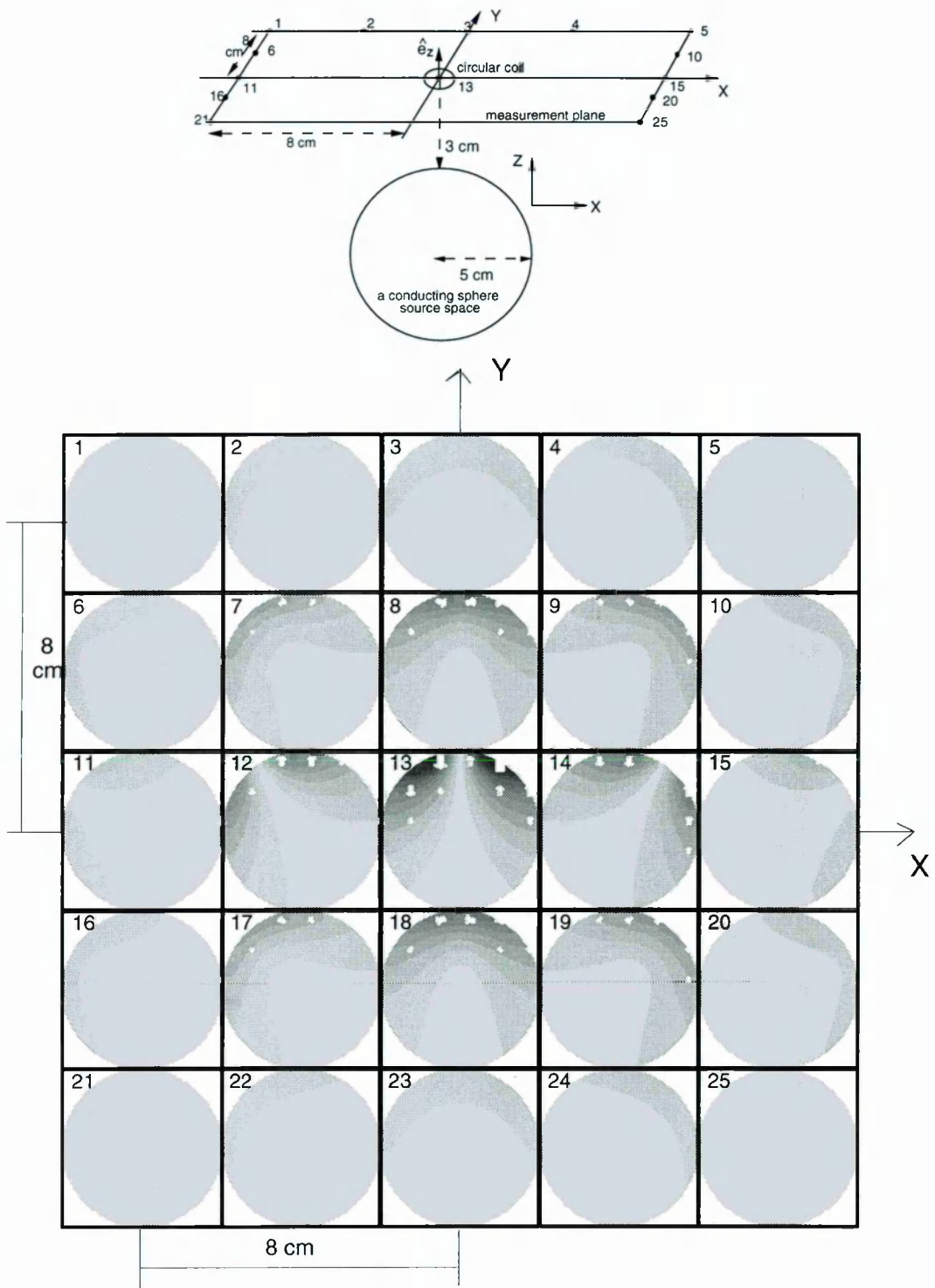
Figure 5.7 Lead field pattern as a depth function of the source for current density within a conducting sphere whose center at (0,0,0) in (x,y,z) along a measurement plane parallel to the source boundary in the xy plane with the unit vector normal to the coil's plane $\hat{\mathbf{e}}_{coil} = \hat{\mathbf{e}}_z$, using a circular shaped magnetometer. Notice the symmetry, dropping off with distance, and effect of coil position.

This provides insight into how deep a source can be revealed by the coil.

3. Based on the figure, it can be predicted that as the distance between the coil and the source space increases, the lead fields change much more slowly, e.g., if the distance between the coil and the source space increases to 5 cm instead of 3 cm as in the above test, the maximum regions of the lead fields will be enlarged, and the lead field differences in value between the neighbouring points within the source space will be decreased. Hence, with the distance increased, the lead field patterns reveal the source in a less sensitive and subtle way. In other words, as the coil comes closer to the source, the lead fields are more sensitive to the source.

4. The source detected by the coil is not only limited by its depth, but also its position relative to the coil. If the source is far away from the detection coil, the lead fields are substantially smaller. Hence, based on the above figure, we can predict that the lead fields for the source space which has translated its center from (0,0,0) to (0,2,0) will be decreased in value, e.g., the lead fields in the middle of the figure will be decreased in comparison with that of the center at (0,0,0) because of the increased distance between the coil and the source space.

5. Gradiometers can significantly affect the characteristics of the lead field patterns in such way that they are less sensitive to the source due to the effect of the compensating coil(s). This effect increases with the order of the gradiometer and the smaller baseline 'b', because in both cases, the magnetic flux transferred to the SQUID is decreased. Furthermore, the size of the coils has an impact on the lead field patterns that the bigger size of the coil, the more flux through it, and therefore more sensitive to the remote sources. This however is at the expense of the nearby sources. In the lead field pattern, this will be shown as the maximum regions enlarged and the lead fields changing more slowly for two neighbouring regions. Hence, some compromise has to be made for achieving the appropriate sensitivity and resolution for a specific experiment. The above conclusion is also applicable to the source(s) in an infinite half space.

5.2.2. 2–D Shaped Coils

In the following simulations, the shape of the coil is changed from the above full circular into 2–D shaped, in which case the coil consists of two half circular coils of the same size, whose radius is 1 cm and the separation between two centers is 1 cm as well, as shown in Figure 5.3(b). Refer to Figure 3.2(d), with this first-order gradiometer, the sensor samples the spatial gradient rather than the field itself. Specifically for the arrangement shown in Figure3.2(d), with coils with symmetry axes along $\hat{e}_{coil} = \hat{e}_z$ and centers separated along the x-direction, the measurements are sensitive to $\frac{\partial B_z}{\partial x}$. The geometric arrangement for the source space and measurement plane is the same as before (see Figure 5.2). The lead field pattern for an infinite half space is shown in Figure 5.8.

From Figure 5.4, it can be seen that when the coil is above the center of the source space, the lead fields are at maxima, which are greatly different from those using the full circular coil (refer to Figure 5.8). This suggests that the 2–D shaped coil is much more sensitive to sources in the nearby region of the coil compared with the full circular one; while much less sensitive to the source in the remote region. Furthermore, the figure demonstrates very high symmetry and sensitivity to sources in one special direction, e.g., in Figure 5.8, the coil is more sensitive to sources in y than x direction (notice for a 2-D coil wound in the opposite sense, the lead field directions are similar for the coil at symmetric positions, e.g., M7 and M19, M7 and M19 and so on). By symmetry, we can predict that if the gradiometer is placed along the y axis with $\hat{e}_{coil} = \hat{e}_y$, the lead field pattern will display very similar characteristics except of being symmetric to the x axis. Hence, the local current density can then be reconstructed by placing two such 2–D shaped first-order gradiometers perpendicular to each other, as shown in Figure 5.3(d). The gradiometer is called a second-order 2–D shaped gradiometer, and sensitive to sources in both x and y directions because it detects the derivations of magnetic fields $\frac{\partial B_z}{\partial x}$ and $\frac{\partial B_z}{\partial y}$. An example of such a gradiometer design is the Neuromag-122 system in Helsinki University of Technology (see Section 3.4.3). The above characteristics of the lead field pattern for the 2–D gradiometers can also embody in the lead field pattern for the measurement of the tangential component of the magnetic fields, when the gradiometer is placed along the x axis with the unit normal vector to the coil's plane $\hat{e}_{coil} = \hat{e}_x$. The lead field pattern is as illustrated in Figure 5.9.

Figure 5.8 Lead field pattern for an infinite half space along a measurement plane parallel to the source boundary in the xy plane with the unit vector normal to the coil's plane $\hat{\mathbf{e}}_{coil} = \hat{\mathbf{e}}_z$, using a 2–D shaped first-order gradiometer. Notice better spatial resolution for nearby sources but worse for remote sources compared with using the circular coil in Figure 5.4, and the directions of the lead fields.

Figure 5.9 Lead field pattern for an infinite half space along a measurement plane parallel to the source boundary in the xy plane with the unit vector normal to the coil's plane $\hat{\mathbf{e}}_{coil} = \hat{\mathbf{e}}_x$, using a 2–D shaped first-order gradiometer. Notice better spatial resolution but poorer stability compared with Figure 5.8.

We now turn to investigating the sensitivity to sources as a function of depth by using a 2–D shaped first-order gradiometer. For comparing the result of the circular shaped gradiometers, all the geometry arrangements are the same as in the previous section, i.e. the source space and the measurement plane is perpendicular to each other with a minimum distance of 3 cm between them. The lead field pattern is shown in Figure 5.10.

Compared with Figure 5.7, Figure 5.10 demonstrates better resolution and more detail about the source, especially the region close to the detection coil. This suggests that the 2–D shaped gradiometers have a higher sensitivity to sources not far away from the pick-up coil than the circular ones. But on the other hand, owing to the special geometric structure, in which two half circular coils are wound in the opposite sense, the flux through the coil is decreased by the comparison of the full circular one. The sensitivity is therefore decreased as well. In other words, the 2–D shaped gradiometer is less sensitive, particularly to distant sources, compared with the full circular coils.

5.2.3. Off Diagonal Non-planar 2nd-order Gradiometers

In the following simulations, an example is given to evaluate the sensitivity pattern (i.e., the lead fields) of a gradiometer system designed by Kathia Fiaschi in the Biomagnetism group at the O.U. [132]. A sketch of the sensor array is as shown in Figure 5.11: the array has 10 channels and each channel consists of a pair of off diagonal non-planar second-order gradiometers. There are two channels in each hypothesised cylinder, and thus there are five such cylinders altogether, whose geometric arrangement is as shown in Figure 5.11(b). The shape of the gradiometer is like a segment of the surface of a cylinder, and the curved sides are arcs of $\frac{4}{9}\pi$ radians and 1.25 cm radius. The pick-up coil of the gradiometer has two turns with a length of '$L1$' cm, and the two compensating coils have one turn: one has a length of '$L2$' cm and a distance of '$b1$' cm away from the pick-up coil; while the other has a length of '$L3$' cm and a distance of '$b2$' cm away from the first compensating coil. Hence, the gradiometer detects the derivative of magnetic fields, $\frac{\partial B_z}{\partial r}$, in a cylindrical polar coordinate system.

In the following simulations, a pair of gradiometers (1 channel) are employed. The gradiometer has a dimension of $b1$ =1.8 cm, $b2$ =1.2 cm, $L1$ =1.2 cm, $L2$ =4.8
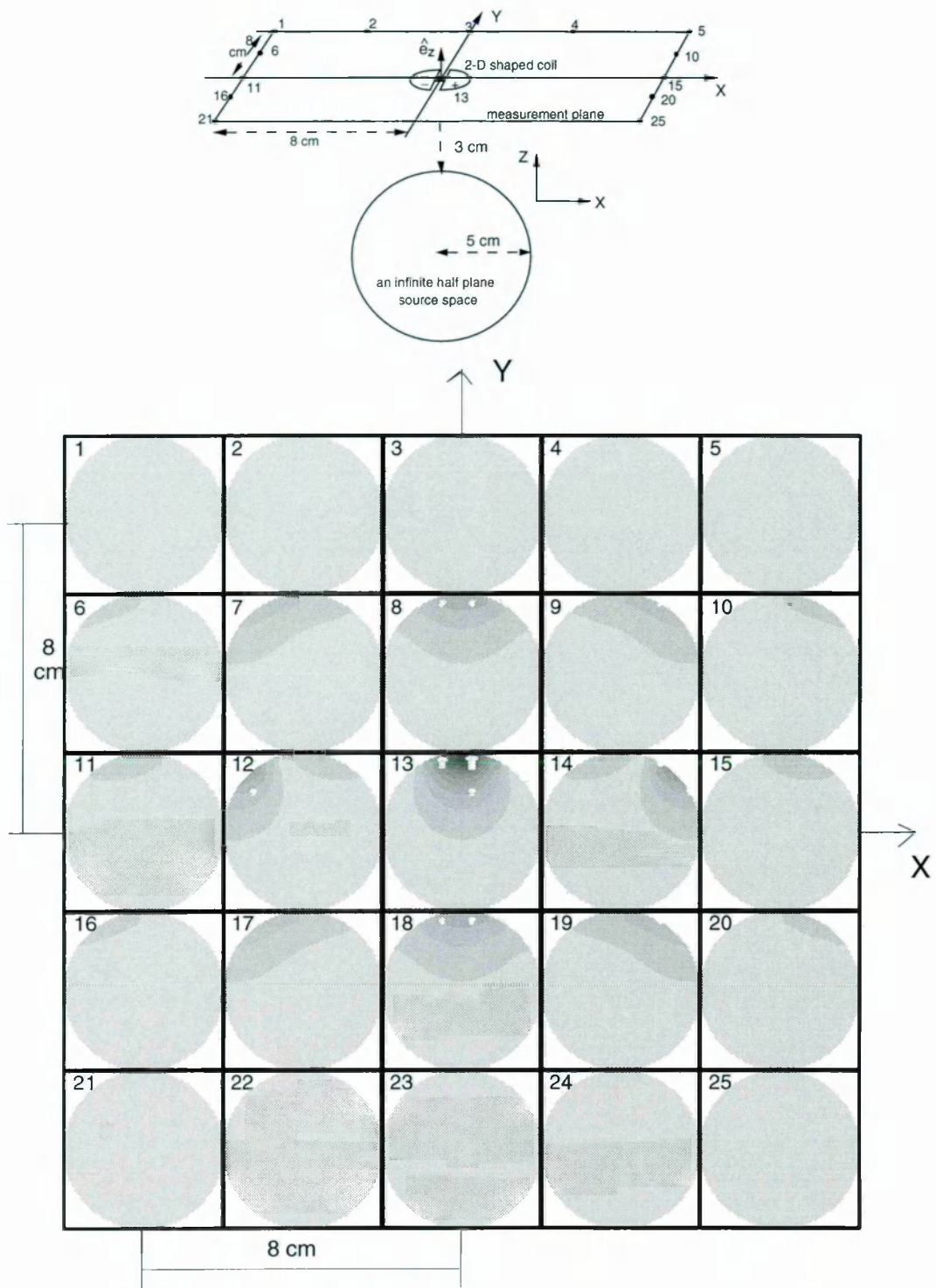
Figure 5.10 Lead field pattern as a depth function of source for an infinite half space along a measurement plane parallel to the source boundary in the xy plane with the unit normal vector to the coil's plane $\hat{\mathbf{e}}_{coil} = \hat{\mathbf{e}}_z$, using a 2–D shaped first-order gradiometer. Notice better resolution for nearby sources, but worse for remote sources compared with Figure 5.7.
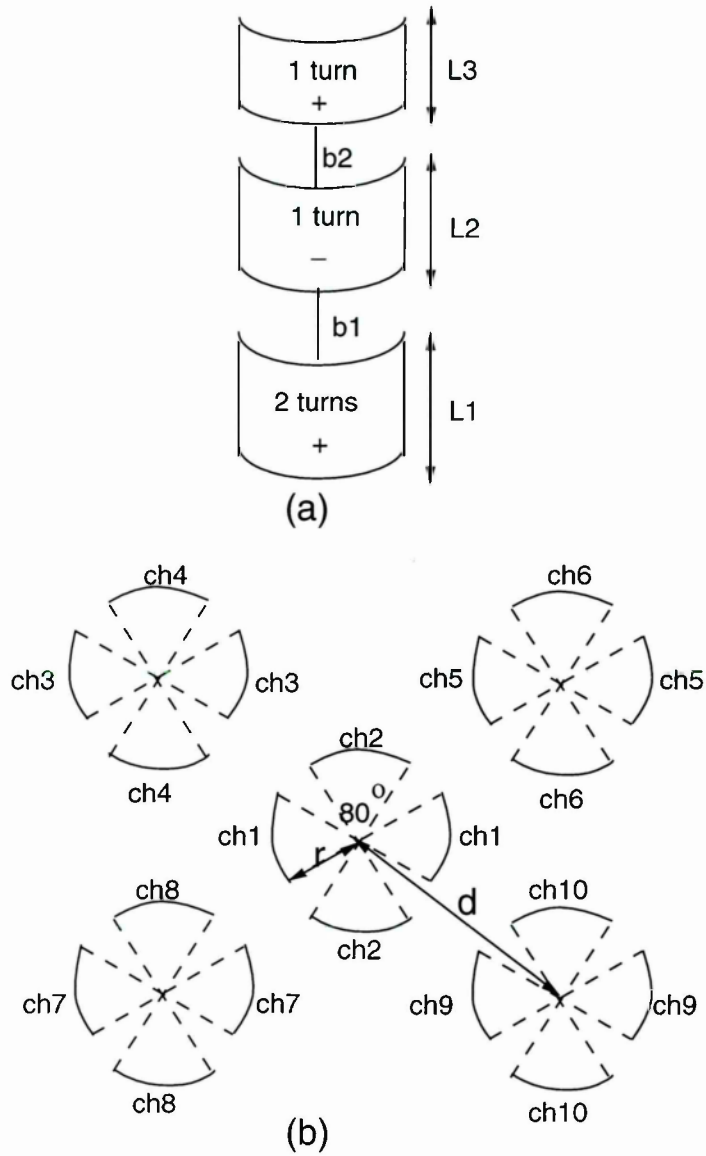
Figure 5.11 Diagram of the off diagonal non-planar second-order gradiometers: (a) the shape of the gradiometers, (b) the geometric arrangement of the 10 channels.

cm, and $L3$ =2.4 cm, and is placed along the x axis and symmetric to the y axis with $\hat{\mathbf{e}}_{coil} = \hat{\mathbf{e}}_z$. For each channel, the coils are assumed to be wound in the same direction. The geometric arrangement for the source space and the measurement plane is the same as for the full circular and the 2–D shaped coil. The lead field patterns for an infinite half space when the source spaces in the xy plane and in the xz plane (as a function of depth) are as shown in Figure 5.12 and Figure 5.13, respectively.

The patterns in Figures 5.12 and 5.13 show strong similarity with Figure 5.9 for the measurement of the tangential component of the magnetic fields using the 2–D shaped coil: both have a maximum region in the center, indicating much more sensitive to sources in the near region of the detection coils while less sensitive to remote sources. This characteristic also reflects in the figure showing the lead field pattern as a function of depth, i.e. Figure 5.13. Compared with the 2–D shaped coil, the magnitudes of the lead fields are bigger due to the fact that the coils are wound in the same direction. Basing on the above observations, one can predict that using a pair of off diagonal non-planar second-order gradiometers wound in the same direction can detect sources in a relatively deeper and wider region compared with the 2–D shaped coil, which is wound in the opposite sense.

If for each channel, the coils of the pair of the gradiometers are wound in the opposite direction, the lead field patterns will then become as shown in Figures 5.14 and 5.15, which show great difference from those of the coils wound in the same direction: the minimum region occurs in the center, which means that the channel consisting of a pair of off diagonal non-planar second-order gradiometers wound in the opposite direction is insensitive to nearby sources close to the center while sensitive to those in a relative remote region. This characteristic of the lead field patterns is similar to that of the circular coil. Hence, using a pair of off diagonal non-planar second-order gradiometers for detecting the current source in the center region, it is better to have the coils wound in the same direction; while for the relatively remote sources, it is better to have coils wound in the opposite direction.

Furthermore, for a pair of off diagonal non-planar second-order gradiometers, the dimension of the gradiometer design has an effect on its sensitivity to the source. This reflects in the choice of the parameters of the gradiometer, i.e. $L1, L2, L3, b1$
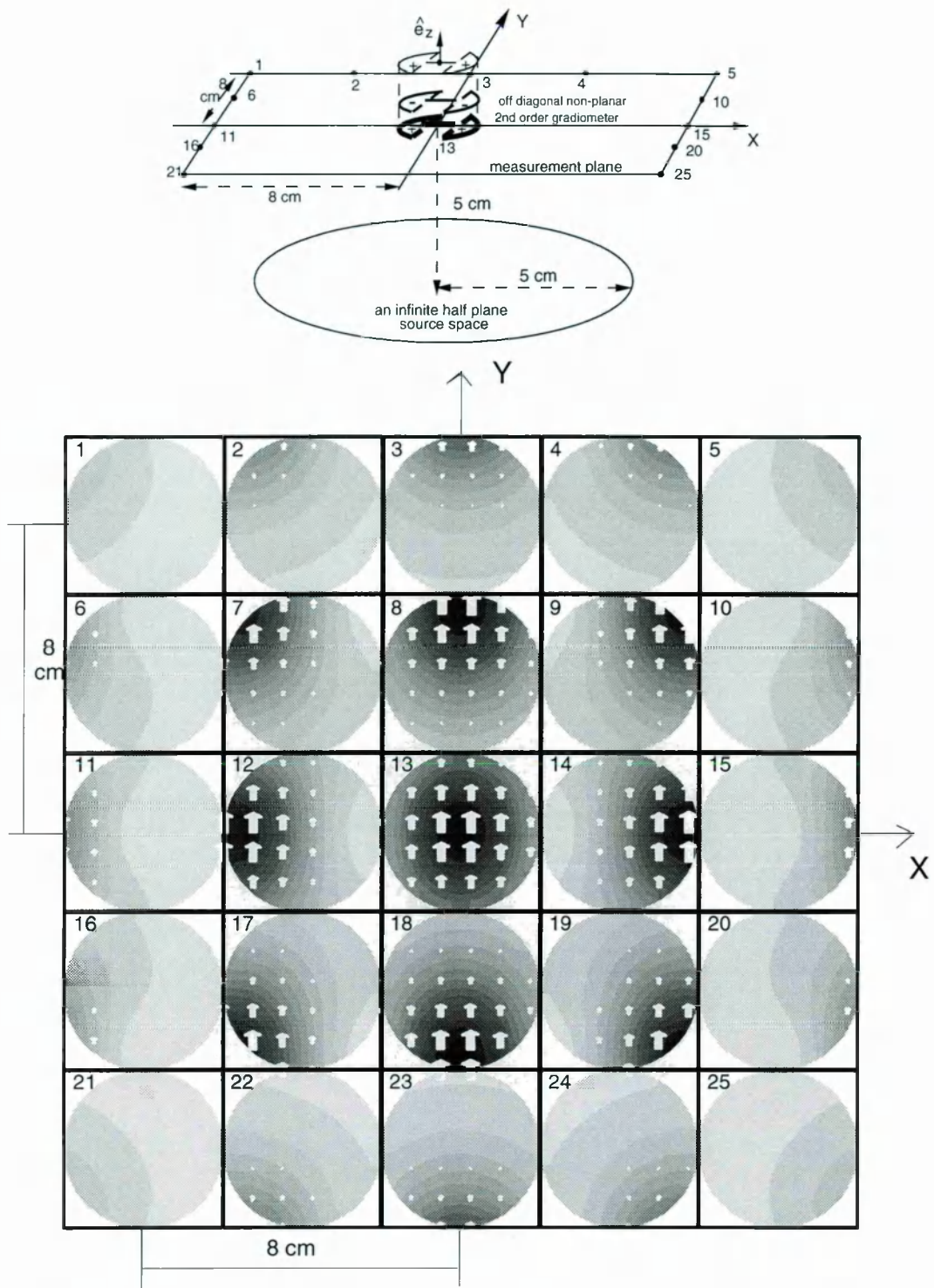
Figure 5.12 Lead field pattern for an infinite half space along a measurement plane parallel to the source boundary in the xy plane with the unit vector normal to the coil's plane $\hat{\mathbf{e}}_{coil} = \hat{\mathbf{e}}_z$, using a pair of off diagonal non-planar second-order gradiometers wound in the same direction. Notice the figure shows similar characteristics as the 2–D shaped coil, but higher sensitivity to sources in wider regions.
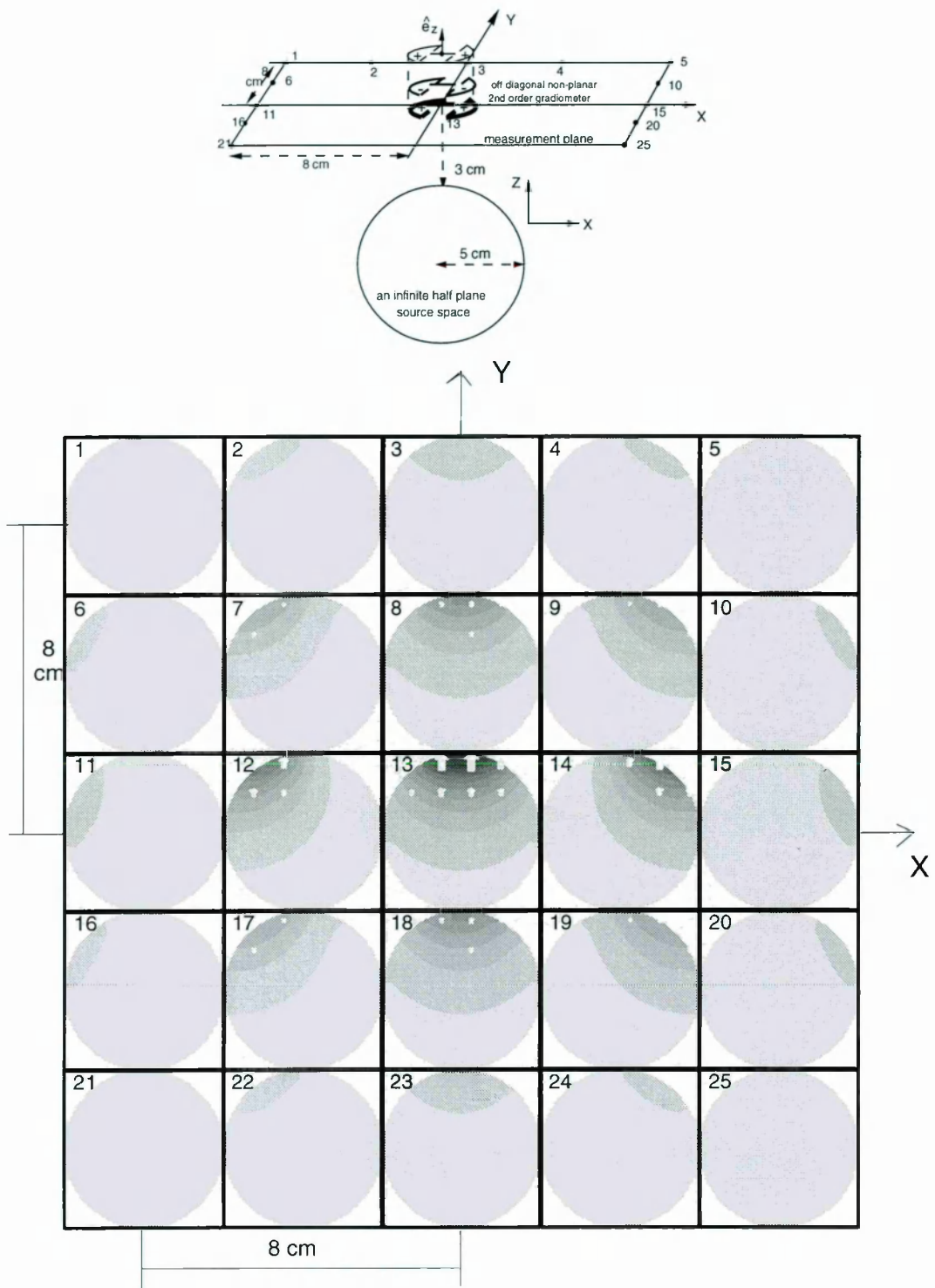
Figure 5.13 Lead field pattern for an infinite half space along a measurement plane parallel to the source boundary in the xy plane with the unit vector normal to the coil's plane $\hat{\mathbf{e}}_{coil} = \hat{\mathbf{e}}_z$, using a pair of off diagonal non-planar second-order gradiometers wound in the same direction. Notice the figure shows similar characteristics as the 2–D shaped coil, but higher sensitivity to sources in deeper regions.

and $b2$. It is understandable that if $L1$, $L3$ and $b2$ are increased, the magnitudes of the lead fields will be increased, in other words, the gradiometers will become more sensitive to the source. On the other hand, when $L2$ is increased or $b1$ is decreased, the sensitivity will decrease due to the effect of the compensating coils.
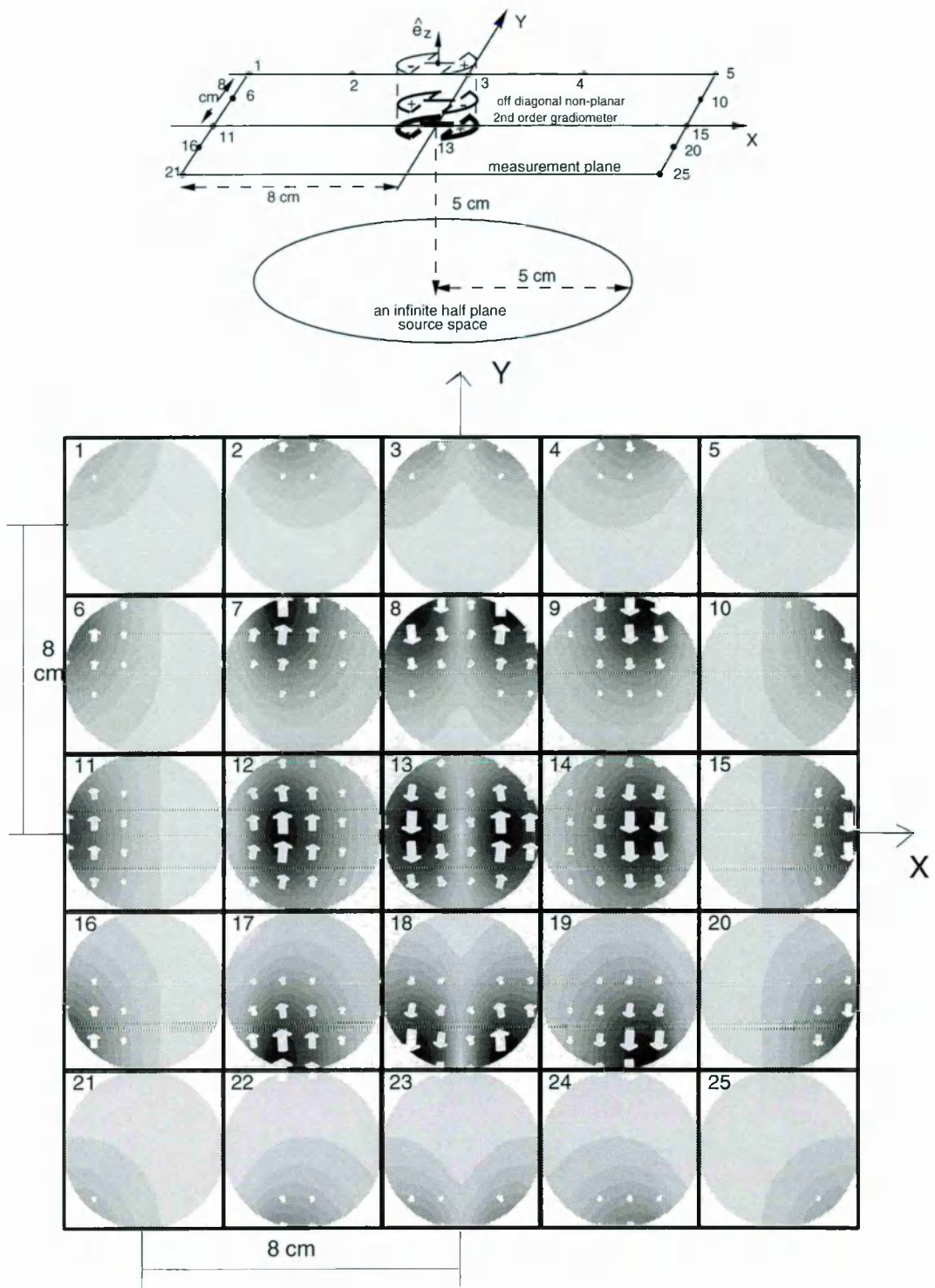
Figure 5.14 Lead field pattern for an infinite half space along a measurement plane parallel to the source boundary in the xy plane with the unit vector normal to the coil's plane $\hat{\mathbf{e}}_{coil} = \hat{\mathbf{e}}_z$, using a pair of off diagonal non-planar second-order gradiometers wound in the opposite direction. Notice the better sensitivity to remote sources but poorer for nearby ones.
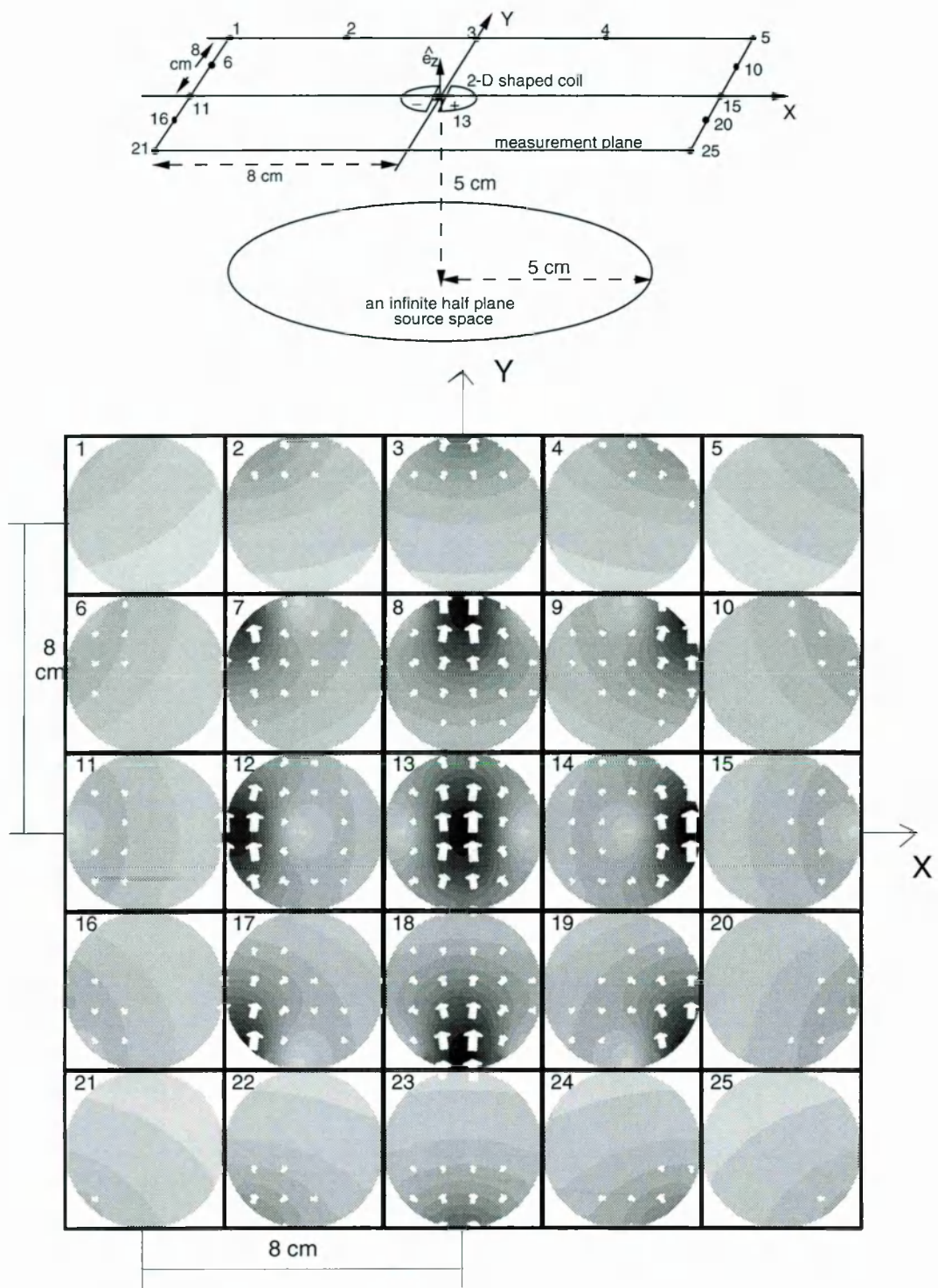
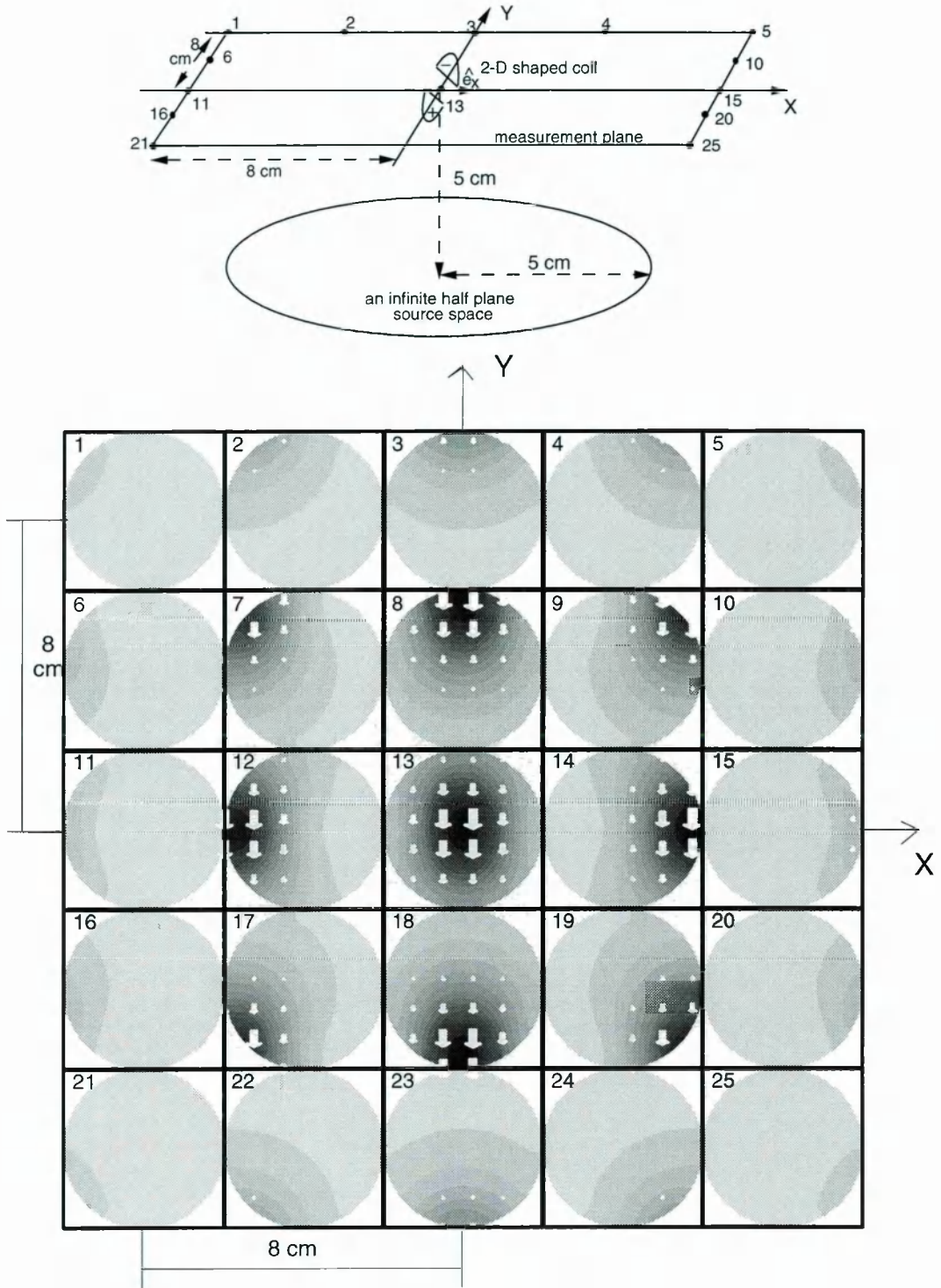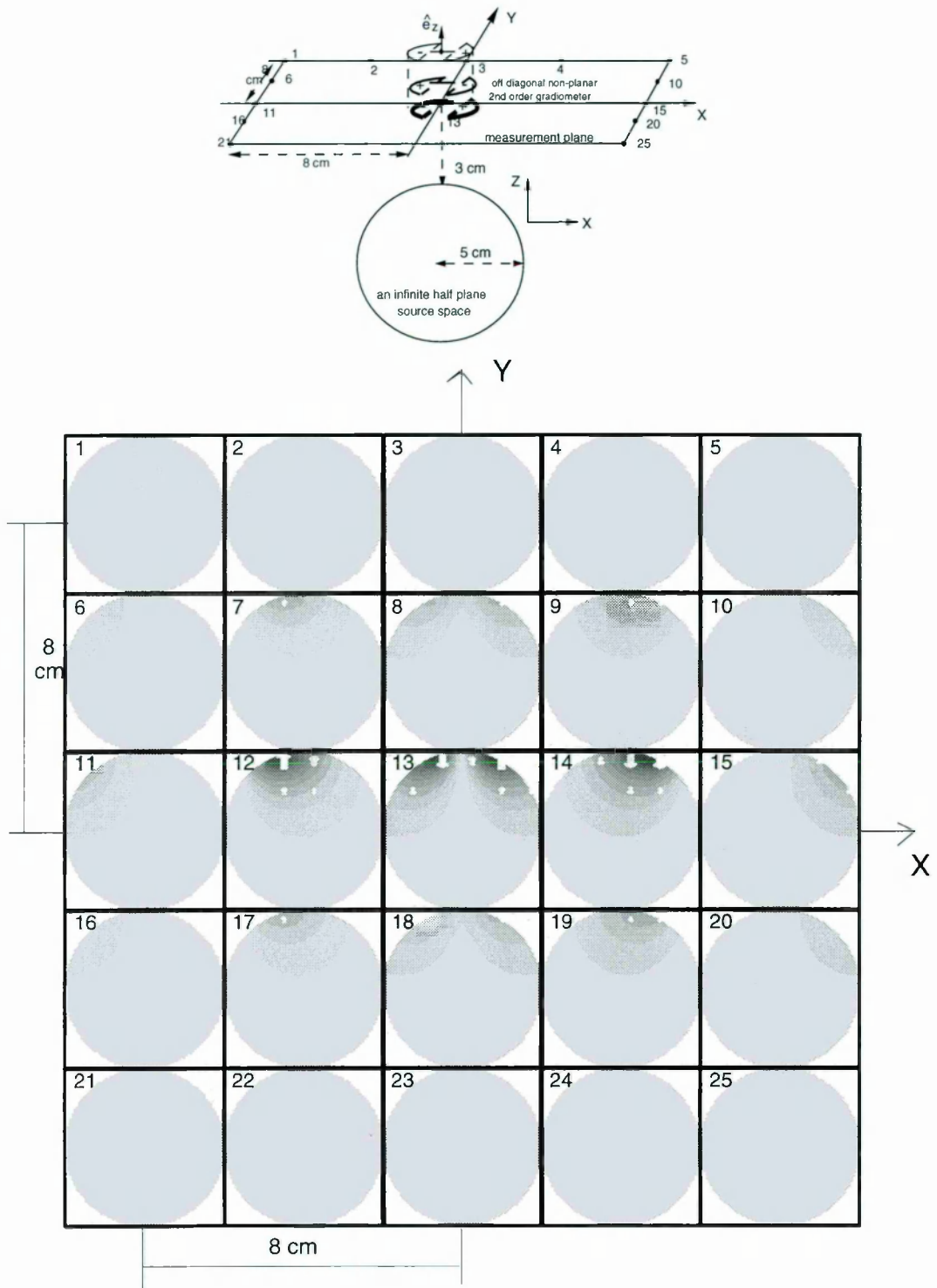**Figure 5.15** Lead field pattern for an infinite half space along a measurement plane parallel to the source boundary in the xy plane with the unit vector normal to the coil's plane $\hat{\mathbf{e}}_{coil} = \hat{\mathbf{e}}_z$, using a pair of off diagonal non-planar second-order gradiometers wound in the opposite direction. Notice the better sensitivity to remote sources but poorer for nearby ones.

CHAPTER 6.

SIGNAL TRANSFORMATION VECTOR V3

In Chapter 4, several functional localization methods have been discussed in detail for solving the inverse problem. All these methods depend on a model for the sources. Some, but especially the distributed source analysis (e.g. MFT), have been successfully applied to both average MEG signals and single trial records. However, the process of obtaining the solutions is computationally demanding and the follow up inspection of a huge number of three-dimensional images makes it too cumbersome to apply to each and every single trial. To overcome these limitations, a simple model independent signal transformation which highlights nearby sources is applied to both average and single trial signals, in an effort to provide a link between abstract, signal space descriptions of single epochs and the anatomically coregister spatiotemporal sequence of events extracted from point and distributed source analysis of average signal.

6.1. Formulation

Equation 2.2 reveals that the z-component of $\mathbf{B}$, B_z, in an xy plane above a current dipole exhibits a characteristic dipolar pattern with a zero crossing directly above the current dipole. The features of B_z in an xy plane are sufficient to identify the location and direction of the dipole in the xy plane, including its depth along z. The dipole lies half-way between the two extrema, at a depth of $d = D/\sqrt{2}$, where D is the distance between the two maxima. This of course assumes that the field is indeed generated by a single point source.

Even if the point source assumption is valid, extracting information from real biomagnetic signals is more difficult because of noise and discreteness in measurements.

Furthermore, the presence of another dipole nearby can move the characteristic zero crossing value substantially or even remove it completely. The uncertainty can be reduced by examining higher order derivatives of the signal. For a general signal $S(x, y)$ on the xy plane, the signal transformation vector $\mathbf{V}_3$ is defined as $\mathbf{V}_3 = \nabla(S) \times \hat{\mathbf{e}}_z$ [133], that is,

$$\mathbf{V}_3(x, y) = \frac{\partial S}{\partial y} \hat{\mathbf{e}}_x - \frac{\partial S}{\partial x} \hat{\mathbf{e}}_y \qquad (6.1)$$

Substituting the expression B_z due to a single current dipole (Equation 2.2) into $S(x, y)$ on the xy plane, we have,

$$\mathbf{V}_3(x, y) = \frac{\mu_0}{4\pi r_0{}^3} \left[\mathbf{Q} + \frac{3}{r_0{}^2} (r_{0x} Q_y - r_{0y} Q_x)(r_{0y} \hat{\mathbf{e}}_x - r_{0x} \hat{\mathbf{e}}_y) \right] \qquad (6.2)$$

where $\mathbf{r}_0 = \mathbf{r} - \mathbf{r}'$, and the subscripts x and y denote the x and y components of the vectors on the xy plane.

The above expression shows that on the xy plane above the current dipole, $\mathbf{V}_3$ is to the lowest order in r_{0z}, proportional in both magnitude and direction to $\mathbf{Q}$. In contrast to B_z, which is identically zero at the point of closest proximity to a source, $\mathbf{V}_3$ exhibits a pronounced maximum near the source location and this is only weakly influenced by other sources, provided that these two sources are not too close to each other. Moreover, plots of $\mathbf{V}_3$ as arrow maps exhibit a characteristic pattern around the source location which reflect the vector properties (position, shape and direction) of the current dipole source.

Figure 6.1 illustrates the characteristic differences between the V_3 and B_z maps. The z component of the magnetic field B_z generated by one or two dipole(s) in an infinite half space is computed for a magnetometer at 4 cm above the xy plane. The zero crossing directly above the current dipole is clearly seen when a single dipole is present, but the pattern is severely disturbed, even if another dipole is many centimeters away. In contrasting the V_3 maps the signature of the central dipole remains reasonably unchanged. Note that if the distance between these two dipoles are very small and their orientations are the same, e.g. in y direction, both the B_z and V_3 maps are very similar to those produced by a single dipole. In other words, these two dipoles can be treated as one single dipole located between these two dipoles. If these two dipoles are oriented opposite to each other, the V_3 map reflects the characteristics of the sources very well, even when the separation is 2

cm, as shown in (d,4). In comparison, the B_z map exhibits a maximum between the sources, whose strength is rather weak. Furthermore, it is worthy of note that the V_3 map not only reveals the locations of the nearby sources very well, it also gives good indication of the orientations of the sources. In summary, there are several advantages provided by $\mathbf{V}_3$, namely,

1. it is independent of the details of the source and only dependent on the experimental geometry.

2. the contribution to the transformed signal from a single localized source exhibits a profound feature in the neighbourhood of this source.

3. it decays rapidly as it moves away from the source.

4. the vector properties of the source are reflected in the transformed signal.

For biomagnetic measurements, because the signal $S(x, y)$ is only taken at discrete points (x_j, y_j), it is necessary to approximate the signal at any arbitrary point on the xy plane by a linear sum of functions centered around each sensor. For the KRENIKON 37-channel axial 1st-order magnetometer at Erlangen University, Germany [79] employed in the following applications, the signal on the xy plane $S(x, y)$ can be approximately expressed as a linear combination of the known measurements S_j $(j = 1 \cdots 37)$, that is,

$$S(x, y) \approx \frac{1}{37} \sum_{j=1}^{37} \frac{\omega}{(x - x_j)^2 + (y - y_j)^2 + R^2} S_j \tag{6.3}$$

where ω and R are parameters to be determined. For sources at different depths related to the sensors, different combinations of ω and R provide an optimal fit for the approximated signals using the above equation. Table 6.1 shows the error expressed as a percentage of the raw signals [1] generated by a dipole of $Q_x = 0$, $Q_y = 1$ A-m, $Q_z = 0$ in an infinite half space at different positions on the xz plane ($y = 0$), with $\omega = 0.0033$ m^2 and $R = 0.011$ m (assume the plane of the sensors locates at $z = 0$).

---

[1] The estimate of the error is obtained according to the following steps: 1) find the peak reading of the raw signals $max1$; 2) find the peak reading of the corresponding approximated signals $max2$; 3) calculate the error in the approximation $E(\%) = \frac{|max2 - max1|}{|max1|} \times 100$.
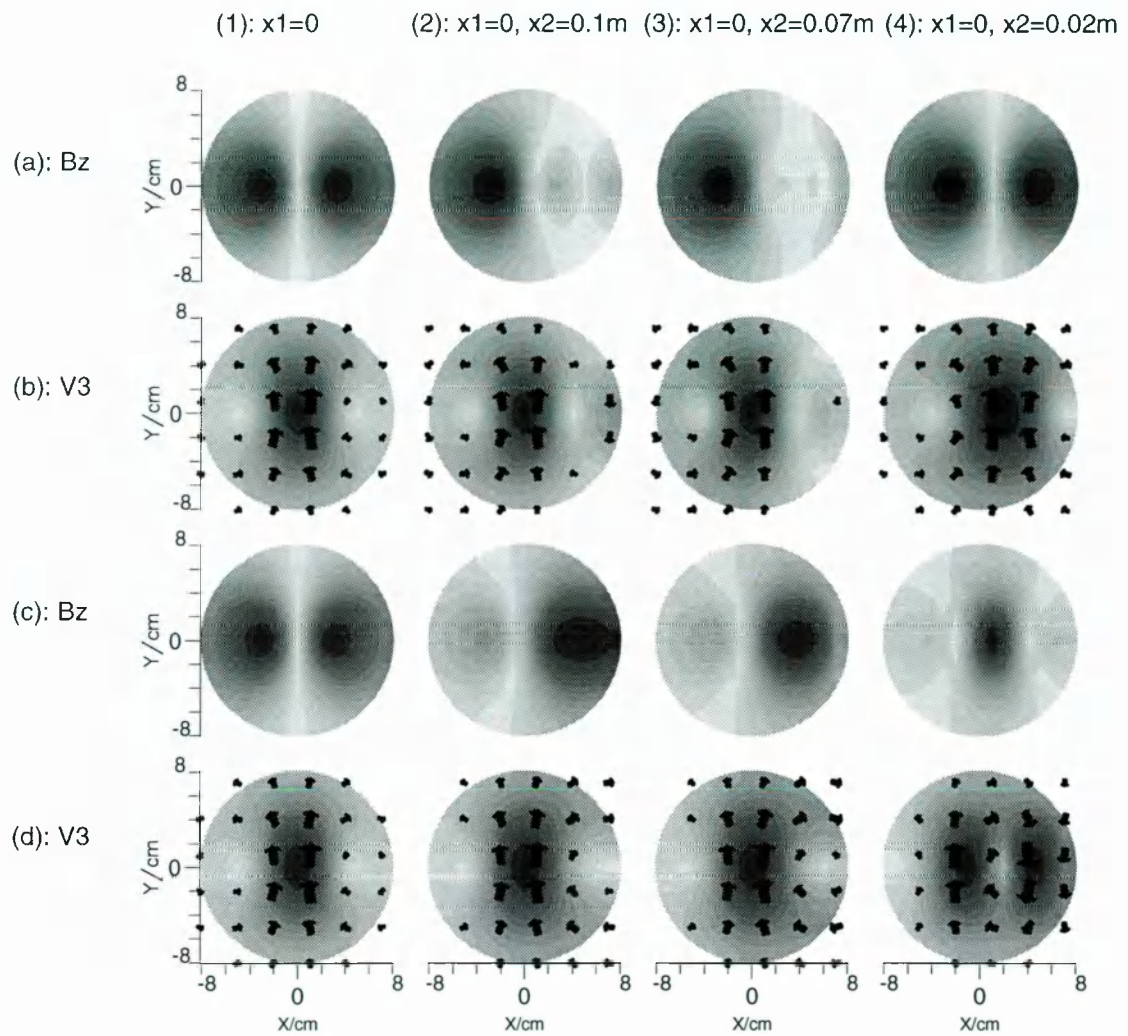
Figure 6.1 Comparison between B_z and $\mathbf{V}_3$: The first row (a) and third row (c) show B_z while the second and fourth row (b) and (d) show $\mathbf{V}_3$. In the first column the signal is generated by a single current dipole 4 cm below the middle of the display. In columns 2, 3 and 4, a second dipole is introduced on the right along the x-axis 10, 7 and 2 cm away from the first one, respectively. In the first two rows the two dipoles point in the same direction, while in the third and fourth rows the second dipole points in the opposite direction. The strength of all the dipoles is the same (1 A-m). Notice $\mathbf{V}_3$ shows maximum near the source location and remote sources have little influence on nearby sources, which is in contrast with B_z.

depth(z/cm):		-1	-3	-5	-6	-7	-9
along the	0	72.6	5.24	10.5	21.5	26.1	27.0
positive	3	51.2	1.62	23.9	38.8	47.2	53.5
x-axis	8	68.5	1.51	37.7	50.6	58.6	72.4
(x/cm):	11	3.3	2.25	24.5	38.7	47.9	68.9

Table 6.1 Error estimation in the approximated signal at different depths obtained from a linear combination of the known measurements from the KRENIKON 37 channels with $\omega = 0.0033$ m^2 and $R = 0.011$ m.

From Table 6.1, it can be seen that the combination of parameter values $\omega = 0.0033$ m^2 and $R = 0.011$ m is reasonable for a source at a depth of about 3 cm below the plane of the sensors. For other depths, Table 6.2 shows the corresponding optimal combination of ω and R with the error estimation. In the following application, we wish to apply V_3 to the estimation of superficial sources (a source having a depth of about 3 cm will count as a superficial source) and therefore we will choose to use $\omega = 0.0033$ m^2 and $R = 0.011$ m. For purposes of identifying the generators, the shape properties are the crucial features, rather than the actual value of the peak signal. The approximation of the signal by a linear sum is only a device to allow us to precompute the contribution from any sensor to V_3 anywhere in the plane and hence compute quickly any given V_3 distribution from the measurements. Other more refined linear sums can be defined, but we have found the one described here adequate, as the following figures demonstrate. Figure 6.2 shows the difference between the raw signal and the linear approximated signal.

From Figure 6.2, it can be seen that the patterns between the raw signals and the approximations are very similar, provided that the source(s) is (are) superficial with respect to the sensor array, i.e., within 3 cm below and 8.1 cm (the radius of the sensor array) central around the center of sensor array. For deeper and remote source(s), the error in the approximation increases. In this case, one can just modify the parameter combinations to obtain the optimal approximation (see Table 6.2). For example, for a depth of 6 cm, the parameter values $\omega = 0.0087$ m^2 and $R = 0.03$ m, produce an error in the linear approximation of the signal in (b,2) of only 0.86%.

A further generalization of V_3 can be obtained with the introduction of a scale
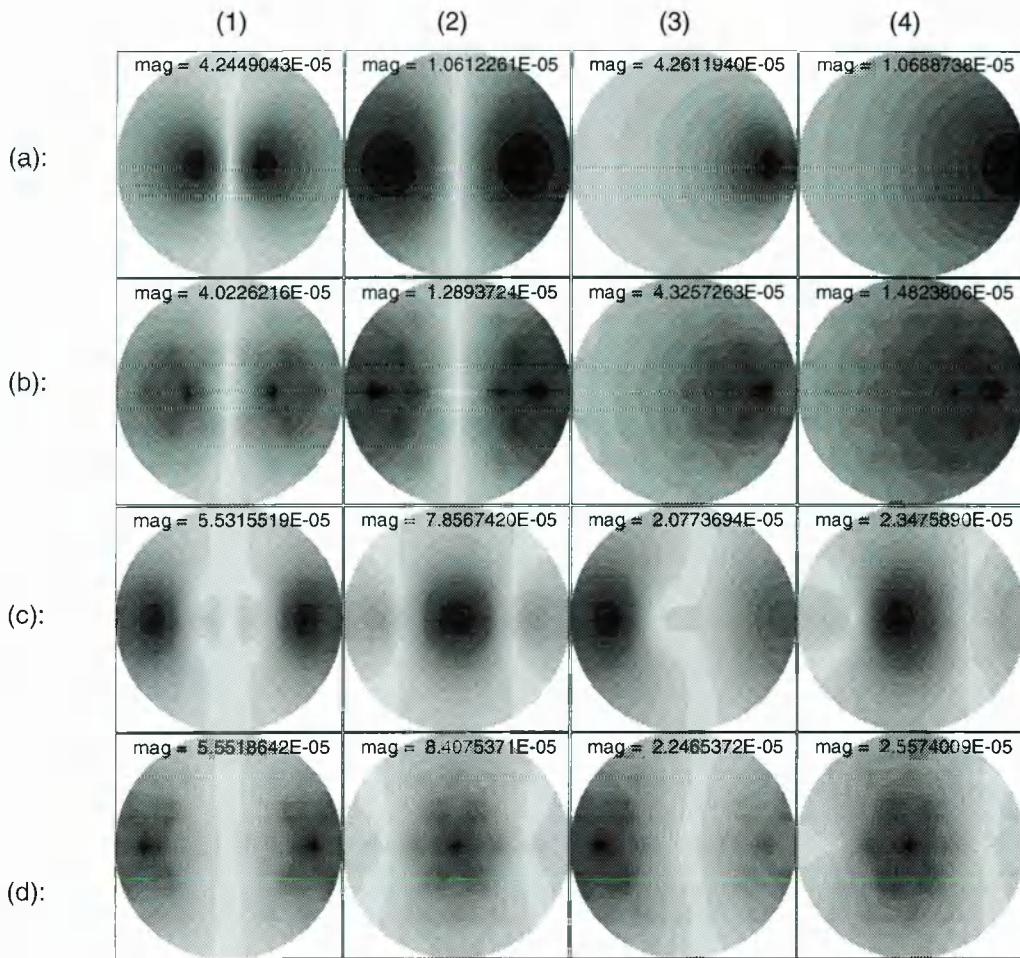
Figure 6.2 Signal approximations from a linear combination of the known measurements from the KRENIKON 37 channels: (a) and (c) are raw signals, while (b) and (d) are the corresponding linear approximated signals. (a,1), a single dipole locates 3 cm below the center of the sensor array with $Q_y = 1$ A-m; (a,2), similar to (a,1) but the dipole is 6 cm below; (a,3), a single dipole is at $x = 8$ cm, $y = 0$, $z = -3$ cm and $Q_y = 1$ A-m; (a,4), similar to (a,3) but further away from the center of the sensor array with $x = 11$ cm, $z = -6$ cm; (c,1), two dipoles locate at $x = \pm 3$ cm, $y = 0$, $z = -3$ cm and both $Q_y = 1$ A-m; (c,2), similar to (c,1), but one $Q_y = 1$ A-m and the other $Q_y = -1$ A-m; (c,3), two dipoles locate at $x = 0$, $y = 0$, $z = -3$ cm and $z = -6$ cm, with the shallower dipole $Q_y = 0.3$ A-m and the deeper one $Q_y = 1$ A-m; (c,4), similar to (c,3), but the deeper dipole $Q_y = -1$ A-m. Notice the similarity between the approximated signals and the real signals in terms of shape and magnitude.

depth	parameters		$E(\%)$			
(z/cm)	$\omega(\text{m}^2)$	$R(\text{m})$	x=0(cm)	x=3(cm)	x=8(cm)	x=11(cm)
-3	0.0033	0.011	5.24	1.62	1.51	2.25
-5	0.0052	0.019	3.60	1.28	2.99	1.72
-6	0.0087	0.030	0.86	3.31	5.99	4.86
-7	0.0095	0.032	4.95	4.57	8.00	7.20
-9	0.0096	0.032	8.00	6.10	10.5	10.3

Table 6.2 Optimal combination of ω and R for sources at different depths and the corresponding error estimation in the approximated signals obtained from a linear combination of the known measurements from the KRENIKON 37 channels.

parameter τ [134],

$$\mathbf{V}_3(x, y, \tau) = \frac{1}{4\pi\tau} \int dy' \int dx' \, e^{-\frac{x'^2 + y'^2}{4\tau}} \mathbf{V}_3(x - x', y - y') \tag{6.4}$$

where the integration over x' and y' is over the measurement plane. The introduction of the scale parameter τ provides stability in the presence of noise; its use interferes with the choice of ω and particularly R, and all must be chosen together to optimize sensitivity for a specific depth. As the parameter τ is varied, details of the source profiles are revealed at different scales. Referring to the linear signal approximations in Figure 6.2, the corresponding $\mathbf{V}_3$ maps are as shown in Figure 6.3, where τ was chosen as 0.004 m^2 (the lower and upper limits of x' and y' for the integration were 0 to $5\sqrt{\tau}$ and 0 to 2π respectively in the polar coordinate system, under which is easier to implement the double integration in Equation 6.4). When τ is chosen in this way, $\mathbf{V}_3$ is smoothed within a region having a radius of approximately 8 cm ($\sqrt{5\tau/\pi}$).

Figure 6.3 shows how insight can be gained about the source(s) by looking at the characteristics of the $\mathbf{V}_3$ maps: for a superficial source, which is about 3 cm below the sensor array, the $\mathbf{V}_3$ maps reveal the characteristic of the source very well (see (b,1), (b,3), (b,4)). When two sources are present, as a general rule, the characteristics of the shallower source are expected to be more prominent than the deeper one, as seen in (d,3) and (d,4), though in both cases the strength of the shallow source (3 cm) is only one third of the deeper source (6 cm). Moreover, it is worthy of note that the orientations and the relative distance between these two sources play a role in the estimation of the sources, that is, if these two sources have the same (or very
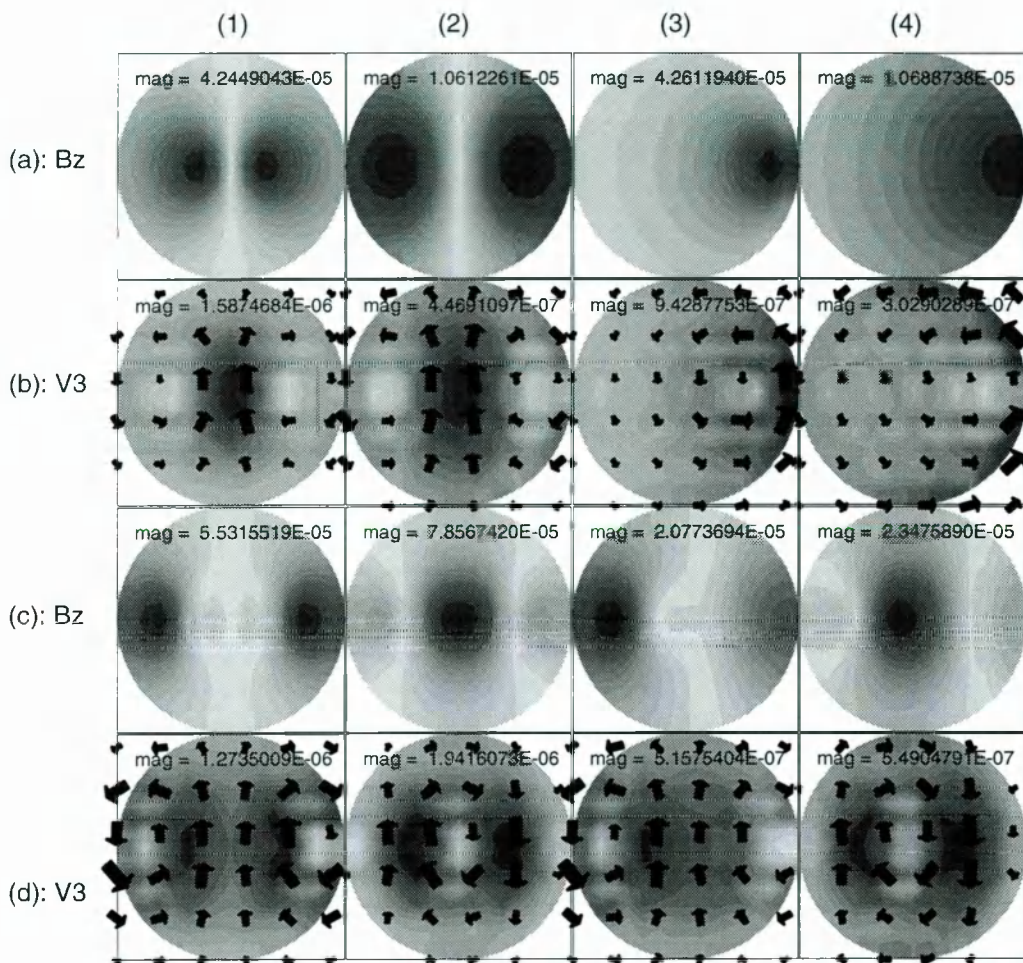
Figure 6.3 V_3 montage plot corresponding to the linear signal approximations in Figure 6.2. Notice V_3 reveals the characteristics of superficial sources very well, using Equations 6.4 and 6.2.

similar) orientation, as they are getting closer, the $\mathbf{V}_3$ map tends to be more similar to that produced by a single dipole. Refer to (b,2) and compare it with (b,1), we can conclude that the $\mathbf{V}_3$ map for the deeper source is more wide-spread than that of the superficial one. How focused the map can be is determined by varying and optimizing the parameter τ, as shown in Figure 6.4. Hence, the presence of a superficial source will interfere with the identification of a deep one. By contrast, the presence of a deep generator does not affect strongly the signature of a superficial one. A possible way forward is therefore to isolate the superficial generators first and then look for the deep ones in the remainder signal. However, since the task in hand is to use $\mathbf{V}_3$ to identify superficial generators, we will not pursue this further.

Figure 6.4 demonstrates the effect of τ on $\mathbf{V}_3$. As τ increases, the $\mathbf{V}_3$ map tends to be more wide-spread and reveals more details about the deeper sources, but edge effect (the error in the estimation of the source at the edge of the sensor array) tends to increase as well. As τ gets smaller, the estimated source from $\mathbf{V}_3$ map is more focused, though the magnitude of the $\mathbf{V}_3$ is smaller. The irreducible limit for the width of the point spread function is determined by Nyquist frequencies and increases with increasing depth. In the following analyses, with emphasis on superficial sources, τ was chosen as 0.004 m^2 with $\omega = 0.0033$ m^2 and $R = 0.011$ m.

With the above linear signal approximation at any arbitrary points, we can express $\mathbf{V}_3$ in linear combinations and precompute a constant distribution on the xy plane $\mathbf{f}_j(x, y)$ as the contribution from the jth sensor to $\mathbf{V}_3$ for any specific timeslice t. Hence the transformed fields at any arbitrary point on the measurement plane can be expressed as,

$$\mathbf{V}_3(x, y; t) = \sum_{j=1}^{37} S_j(t) \mathbf{f}_j(x, y) \tag{6.5}$$

Based on Equations 6.1, 6.3, and 6.4, $\mathbf{f}_j(x, y)$ is given by,

$$\mathbf{f}_j(x, y) = \int\int dx' dy' \frac{e^{-\frac{x'^2 + y'^2}{4\tau}}}{4\pi\tau} \frac{2\omega}{37} \left[\frac{-X}{(X^2 + Y^2 + R^2)^2} \hat{\mathbf{e}}_x + \frac{Y}{(X^2 + Y^2 + R^2)^2} \hat{\mathbf{e}}_y \right] \tag{6.6}$$

where $X = x - x' - x_j$ and $Y = y - y' - y_j$. To perform the double integration in the above equation, we make use of Gaussian Quadratures formulae to approximate
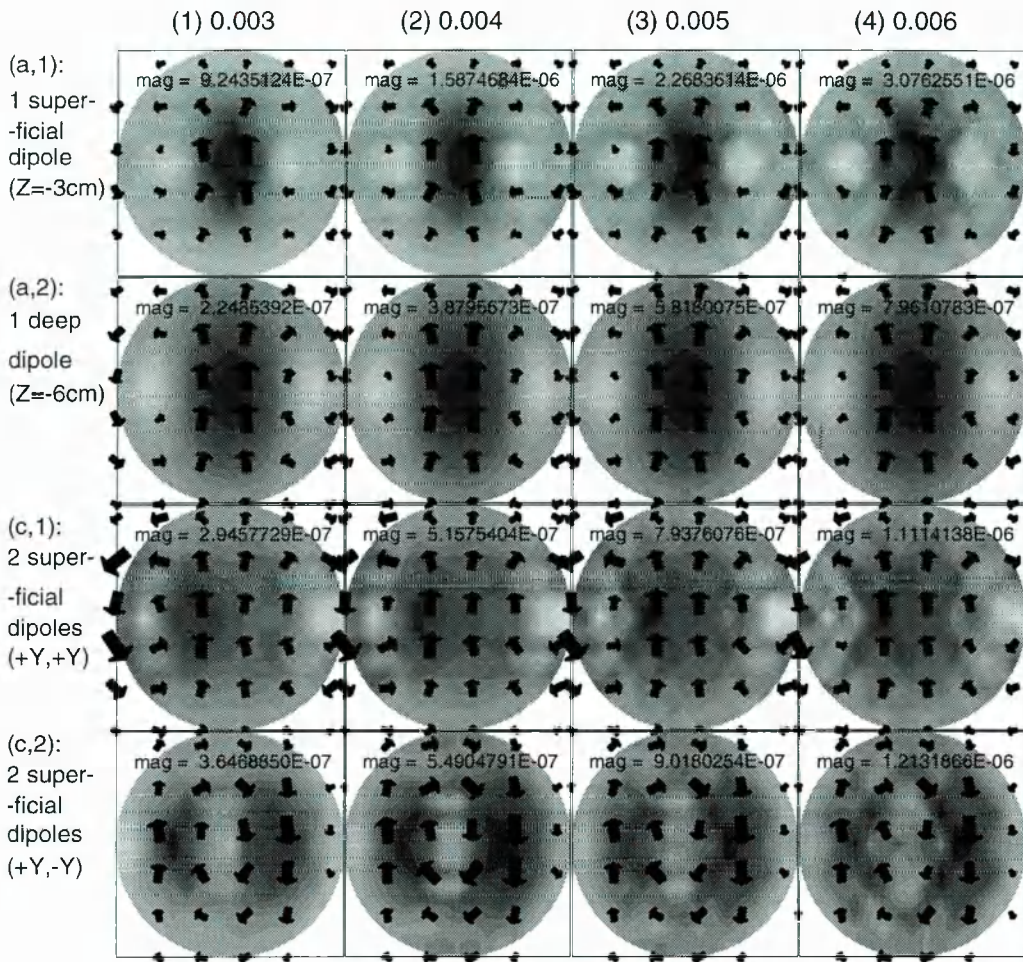
Figure 6.4 The effect of the choice of τ on $\mathbf{V}_3$: τ changes from 0.003 m^2 to 0.006 m^2, as shown from the first to the fourth column. The raw signals are generated from dipole(s) of (a,1), (a,2), (c,1) and (c,4) as described in Figure 6.2, respectively. Notice as τ decreases, V_3 tends to be more focused but reveals less details about deep sources.

the integral as the sum of a set of weights w_i and abscissa x_i, namely,

$$\int_a^b f(x)dx \approx \sum_{i=1}^N w_i f(x_i) \tag{6.7}$$

where N is the number of points for x_i, for the following applications, N is taken as 6. Because the configuration and relative positions of the 37 sensors (x_j, y_j) are known, $\mathbf{f}_j(x, y)$ for any arbitrary points on the sensors' plane can be precomputed and stored as coefficients in a data file. When $\mathbf{V}_3$ is applied to the analysis of the signals obtained from the system, the saved coefficients can then be used in Equation 6.5 to calculate the $\mathbf{V}_3$ directly. Take the KRENIKON 37-channel MEG system for instance, the 37 sensors are in a hexagonal array, with the distance between the central sensor and the most outside sensor(s) 8.1 cm, as shown in Figure 6.5. Using Equation 6.6 we can calculate the coefficients $\mathbf{f}_j(x, y)$, e.g., (x, y) is an arbitrary point close to one of the sensors and on the same plane as the sensors. To discretize the calculation procedure for the coefficients, we assume that the points are in a square of 16.2 cm side, divided into 17×17 sub-squares, and the coefficients are then calculated for the centers of these sub-squares. This allows us to use the software developed for the display of continuous 3-D solutions [124]. If the centers locate outside the circle of 8.1 cm radius drawn from the center of the sensor array, V_3 is regarded as zero. It is worthy of note that V_3 is a continuous function and the discretization is performed for display purpose only. If coefficients for other points are needed, e.g., points between the two (or more) of the 17×17 evaluation points, one can use Equation 6.6 to calculate the coefficient for this specific point. In our computer implementation of the V_3, the coefficients are saved in a data file with the format of $f_s(i)$, $f_s(j)$ and 0.0 corresponding to the three components of $\mathbf{f}$ for the s sensor, and the changing order is i fastest, then j and finally s ($i, j = 1 \cdots 17$ and $s = 1 \cdots 37$). Hence, the data file including the coefficients has $17 \times 17 \times 37$ lines and three components in each line. When the signals taken from the KRENIKON system, using Equation 6.5 we can obtain the $\mathbf{V}_3$ for each experiment easily.

6.2. Auditory Cortex Activity Revealed by V3 Analysis

We use as examples a set of auditory evoked measurements obtained with the KRENIKON 37 channel system [124]. The experiments were carried out to measure the ipsilateral and contralateral response of the left and cortices when auditory stimuli (600 ms long, 1 kHz auditory tone) were applied monaurally to the left or
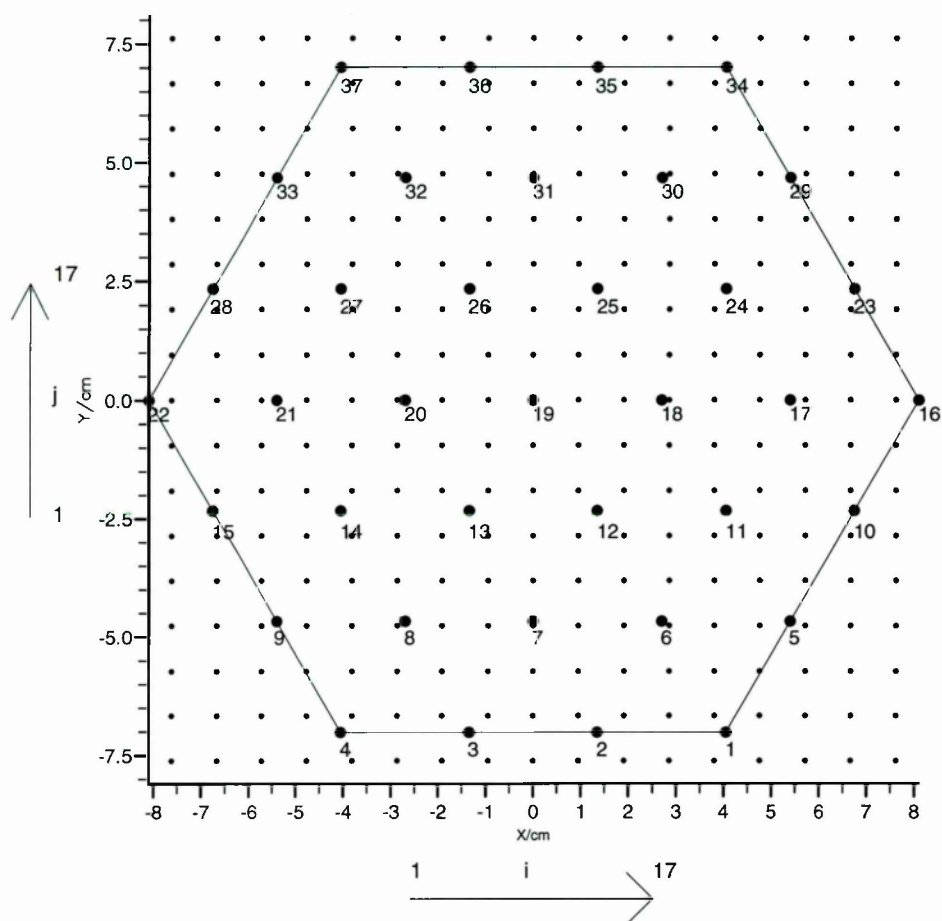
Figure 6.5 Plan view of the 17×17 evaluation points (smaller dots) for V_3 and the 37 sensors (bigger dots with numbers denoting the channel numbers) for the KRENIKON system.

right ear, and separate experiments for eyes open or closed (8 experiments in total). The subject (KS) is a normal right-handed male. The responses from 8 sensor placements were recorded, which were coded with three labels: the first index labels the temporal area which the dewar was over, Left or Right; the second index labels the side which the simulation was used, ipsilateral (IPSI) or contralateral (CONTRA); and finally the third index labels the condition of the eyes, open (EO) or closed (EC). For example, experiment L-CONTRA-EC, means that the dewar was over the Left temporal area, the simulation was at the CONTRAlateral side and the Eyes were Closed. The sensor arrangement for the two dewar positions is shown in Figure 6.6. Details of the experiment are listed in Table 6.3, and the first full MFT analysis of the average signal has been published recently [124].

dewar pos.	stim. pos.	eyes condi.	exp. name	no. of epochs	exp. time/day
right	left	open	R-CONTRA-EO	129	10:32, 1st day
right	left	closed	R-CONTRA-EC	107	10:45, 1st day
right	right	open	R-IPSI-EO	123	11:00, 1st day
right	right	closed	R-IPSI-EC	123	11:11, 1st day
left	left	open	L-IPSI-EO	145	11:54, 3rd day
left	left	closed	L-IPSI-EC	144	12:04, 3rd day
left	right	open	L-CONTRA-EO	123	18:41, 3rd day
left	right	closed	L-CONTRA-EC	125	18:57, 3rd day

Table 6.3 Experiment details for the 8 sensor placements: the conditions of the experiment set-ups, artefact free epochs used in each average and the time and relative day of the experiment.

Figure 6.7 shows the average signal traces without digital filtering from the onset of the stimulus to 200 msec onwards for experiment L-CONTRA-EC, which also provides a plan view of the sensor arrangement with the relative orientation with respect to the head being portrayed, and a signal difference is constructed as an illustration of the effect of the V_3 transformation.

In Figure 6.7, it can be seen that there exists a transition in channel 19; its two neighbouring channels, channel 18 and 20, both have large magnitudes but opposite phase. Hence, it is not an appropriate way of localizing the source based on channel 19 (which detected very weak signal). If we form the difference of between channel 18 and 20 (thus approximating the derivative), a strong signal will emerge (see the
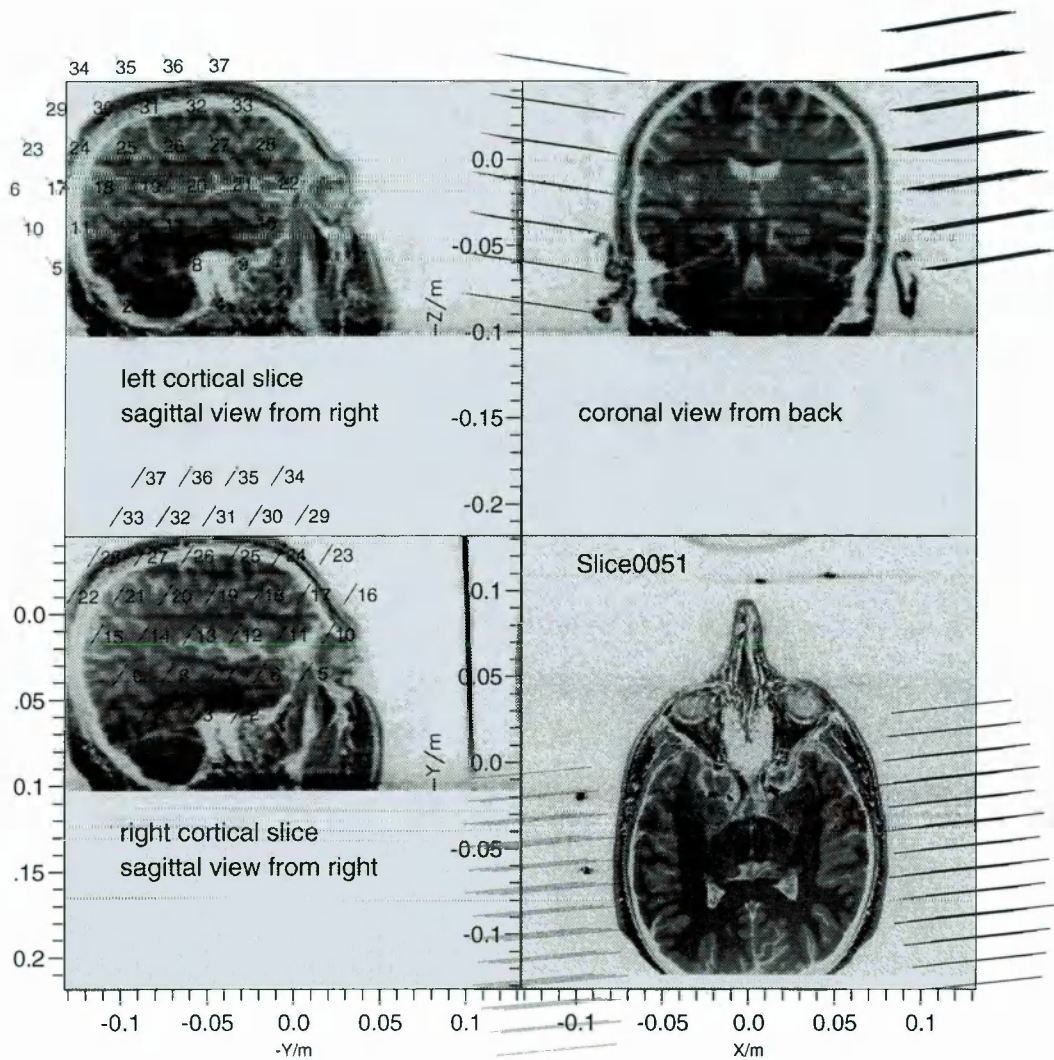
Figure 6.6 The experiment set-ups for auditory evoked response for subject KS in Erlangen: the lighter lines is for the sensors over the left hemisphere, while the darker lines is for the sensors over the right hemisphere.
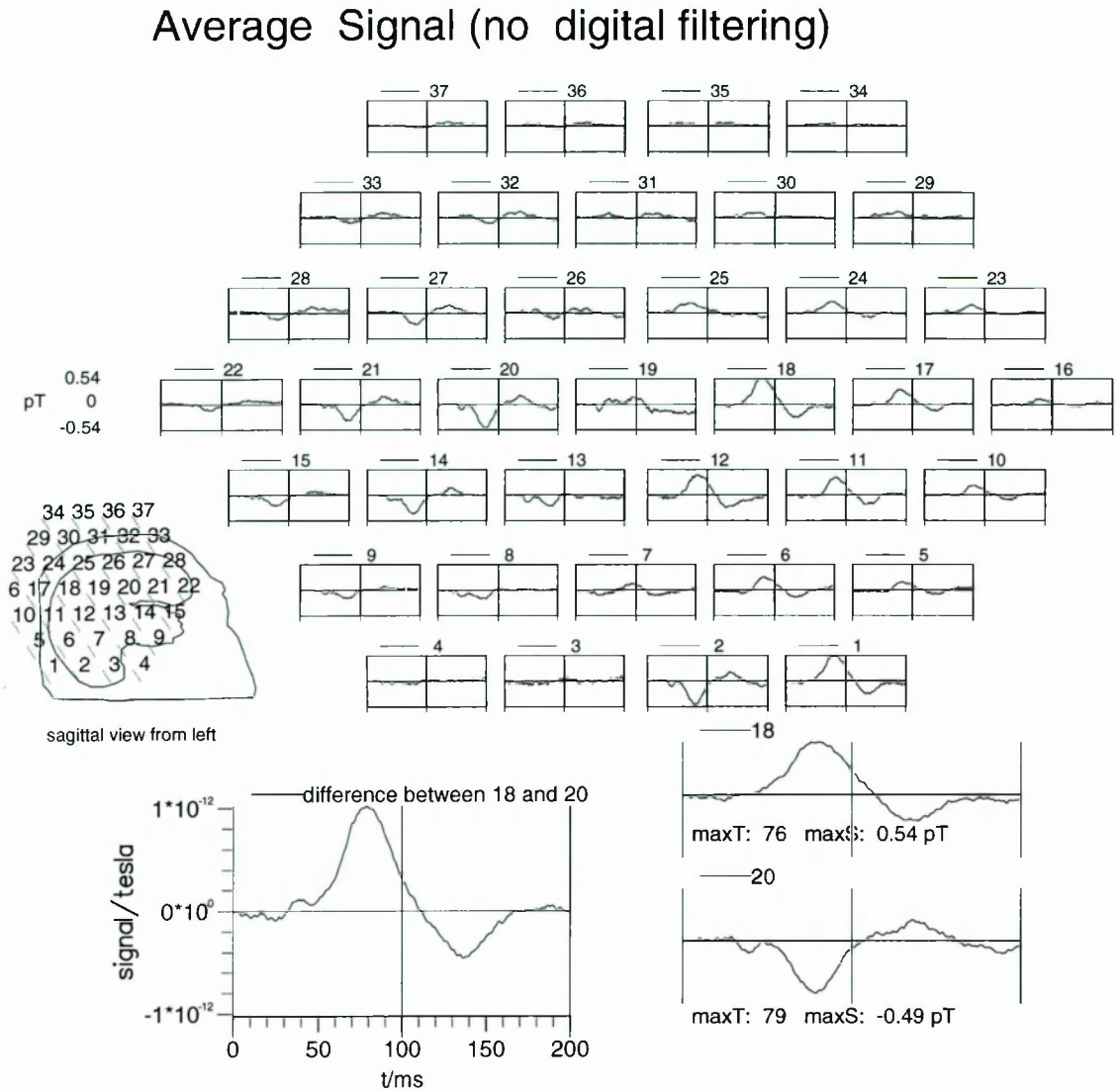
Figure 6.7 Experiment L-CONTRA-EC: average signal for the 37 MEG channels without digital filtering. The sketch of the head shows the relative position of the channels in relation to the head. The lower right part of the diagram shows the signals for channels 18 and 20, which have very similar high magnitude but opposite phase to each other; the difference mimicking the effect of $\mathbf{V}_3$ at channel 19 (between channels 18 and 20) is displayed on the left.

very bottom left of the figure). This difference is similar to V_3 (refer to Equation 6.1), illustrating simply but effectively the effect of the transformation on the signal.

As discussed before, V_3 is evaluated at the 17×17 points at the same plane where the 37 sensors locate. For each timeslice, a maximum of V_3 from these 17×17 evaluation points is calculated and can be represented as a single arrow, mimicking the current dipole format; this maximum on every point then is projected onto the brain surface by drawing a line between the V_3 evaluation point on the sensor's plane and the center of a hemispherical source space (i.e. the best hemisphere to describe the curvature of the brain surface on the sensor side), and the cross-section of this line with the brain surface obtained from the closest MRI slice is estimated as the projection position. Figure 6.8 illustrates the V_3 evaluation and projection procedure.

We have computed a full 3-D inversion for average signals (of all the epochs in each experiment) [124] and single epochs (see the following Chapters 7 and 8) and obtained estimates of the superficial generators using V_3. For the analysis of the MEG data in all the experiments shown in Table 6.3, we chose to use a hemispherical source space [131] to cover the half of the brain on the sensors' side for each experiment. The source spaces for the left and right hemisphere are symmetrically placed and together they cover all the brain (see Figure 6.9). Each hemispherical source space is sliced along 9 levels. At each slice the estimates obtained from the MFT distributed source analysis is computed for storage and display. Each slice is a circle cut through the hemispherical source space. A uniform square 17×17 display grid is used, which is chosen so that it just fits the biggest circular slice of the source space. The MFT estimate at each grid point is computed if the point is within the source space or assign a zero value if outside. After the co-registration (see Appendix A), the MFT estimates are finally superimposed onto the MRI slices, by searching for the closed MRI slice(s) based on the estimated position (x, y, z) from the MFT estimates.

Figure 6.10 shows the V_3 distribution for the average signal in experiment L-CONTRA-EC, plotting from the onset of the stimulus to 99 ms onwards. During this period, the maximum of V_3 distribution is roughly at 80 ms. The V_3 distribution on the measurement plane is then projected onto the brain surface, as shown in Figure 6.11. The agreement between the V_3 estimates for the generators and that obtained
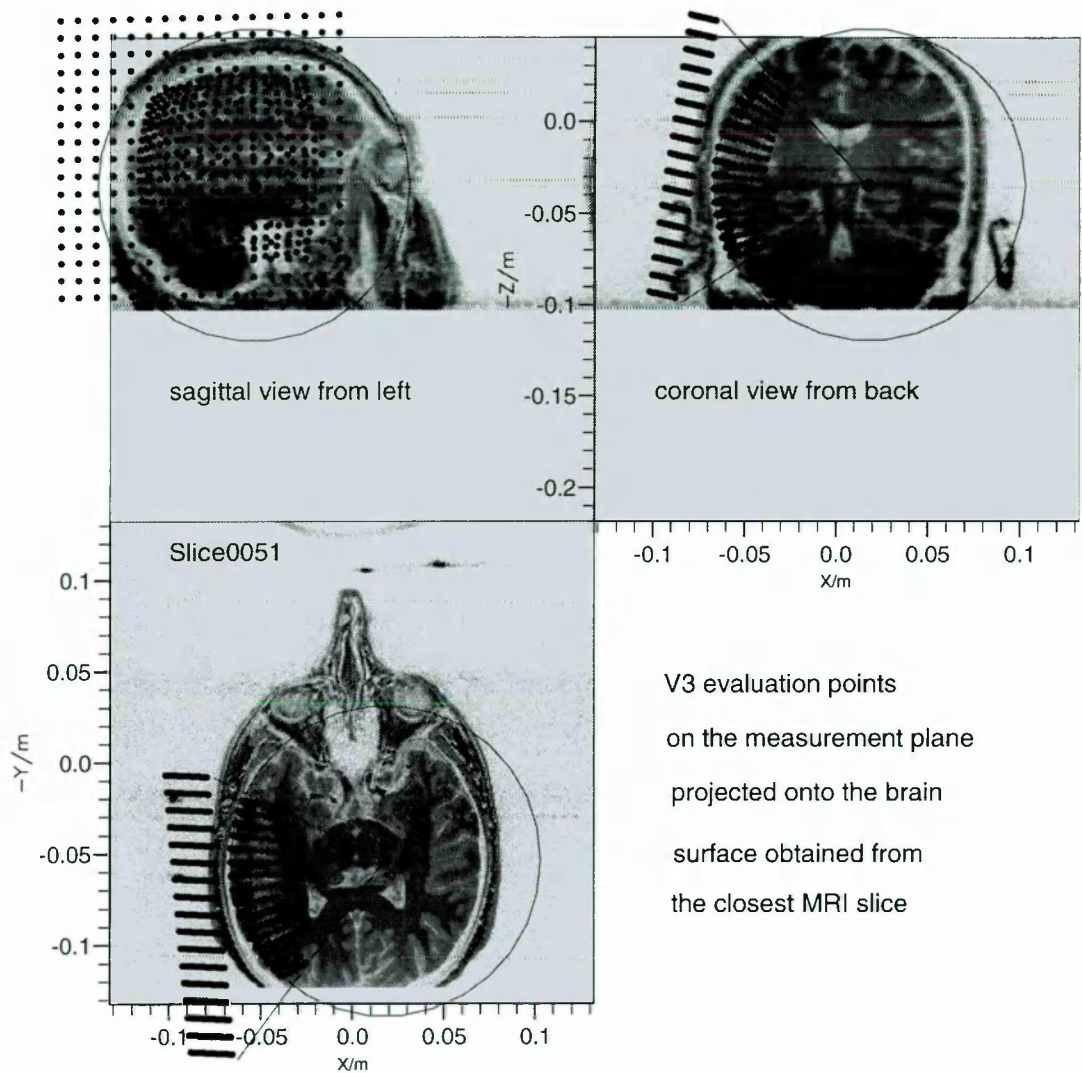
Figure 6.8 V_3 distribution projected onto the closest MRI slice: the darker dots are the 17×17 evaluation points on the measurement plane, and the lighter dots are the corresponding projected points on the brain surface. The circle stands for the hemispheric source space projected onto the closest MRI slice, and the lines show how the projection points are obtained.
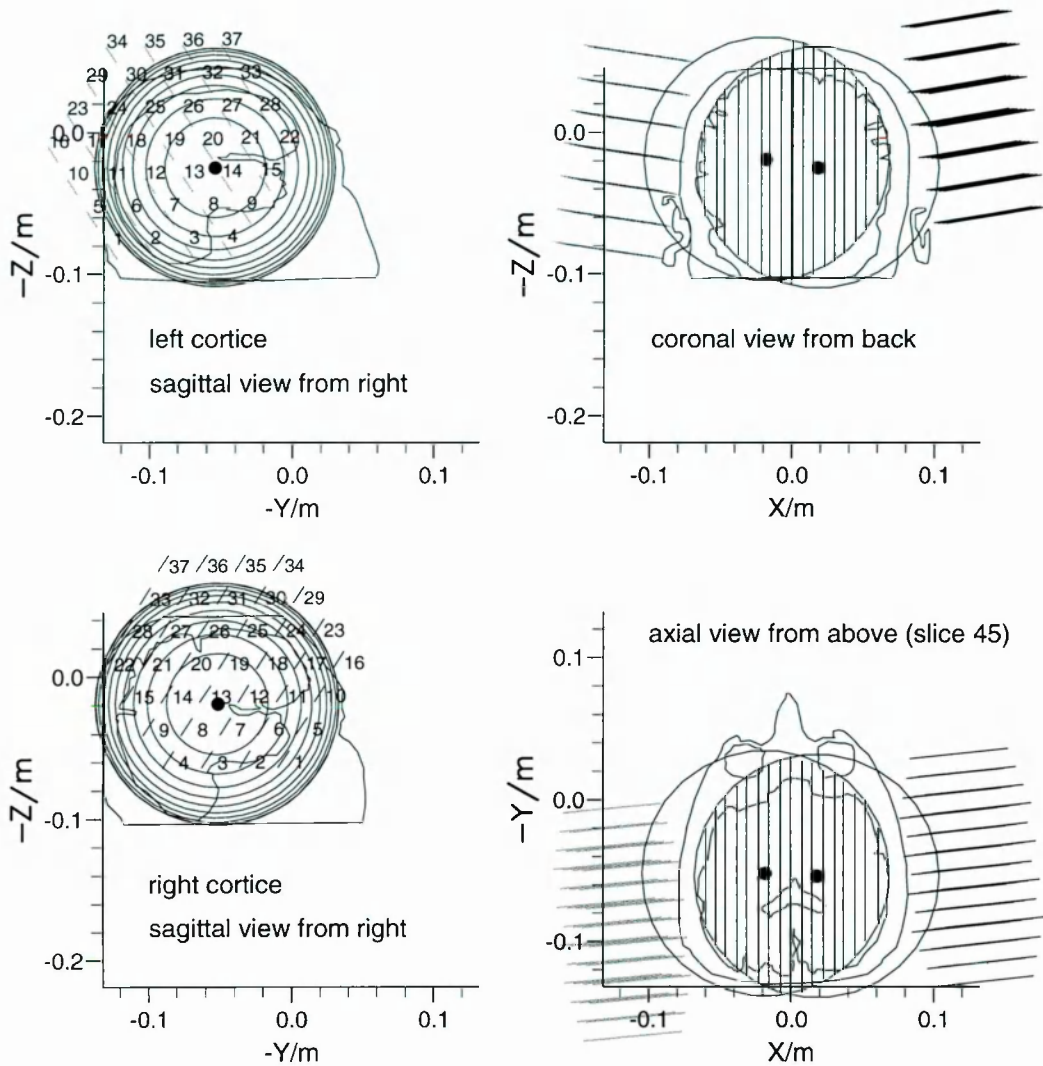
Figure 6.9 Hemispherical source space for the auditory evoked experiments for subject KS in Erlangen: the dots represent the centers of the source spaces for the left and right hemispheres. The source spaces are depicted as the circles in the sagittal views and as lines in the coronal and axial view, and are divided by 9 levels for the inspection purpose of the MFT 3-D full inversion.

from full 3-D inversions is excellent, both in terms of position and direction. Hence, if V_3 projected onto the surface of the brain, with parameters optimal for superficial sources, it is likely to be a good approximation for the superficial generators. In other words, the vector signal transformation V_3, offers a quick and efficient way to estimate the superficial sources, without running the computationally demanding inversion directly. For instance, to compute the V_3 distribution for 1 sec long signal, it takes 88 seconds; by contrast, it takes 1 hour to compute the corresponding full MFT inversion. There is however a limit for employing V_3 to obtain crude estimates for generators, mainly for estimating the deeper generators. Figure 6.12 is a contour cylinder plot for the MFT estimates at the 9 levels from 69 to 105 ms (the rough whole process of the N100m component). The top part of the figure corresponds to the most superficial level in the source space (level 9). The grey level of the plot represents the strength of the MFT estimates. The positions of the V_3 maxima at each time slice for the superficial generators obtained from the V_3 estimates (represented as if they were dipoles on the brain surface), are also shown in the figure as cross-hairs, with the normalization factors calculated from -100 to 200 ms, representing the relative strengths of the dipoles for easy comparison of how the superficial activity revealed by the V_3 changes over this period, are printed at the bottom part of the figure. The figure confirms the excellent agreement for the generators from the V_3 and the MFT inversion at the superficial level, even when deep activities are at present (revealed by the MFT estimates). However, accuracy decreases as the estimated sources go deeper. In order to retrieve the deeper generators, we then need to turn to MFT distributed source analysis. In this work, we did not vary the V_3 definition parameters ω and R to optimize for deep generators, as the original aim of the thesis was to probe the relationship between the activity in single trials and average signal for superficial generators, where we expect reliable signatures.
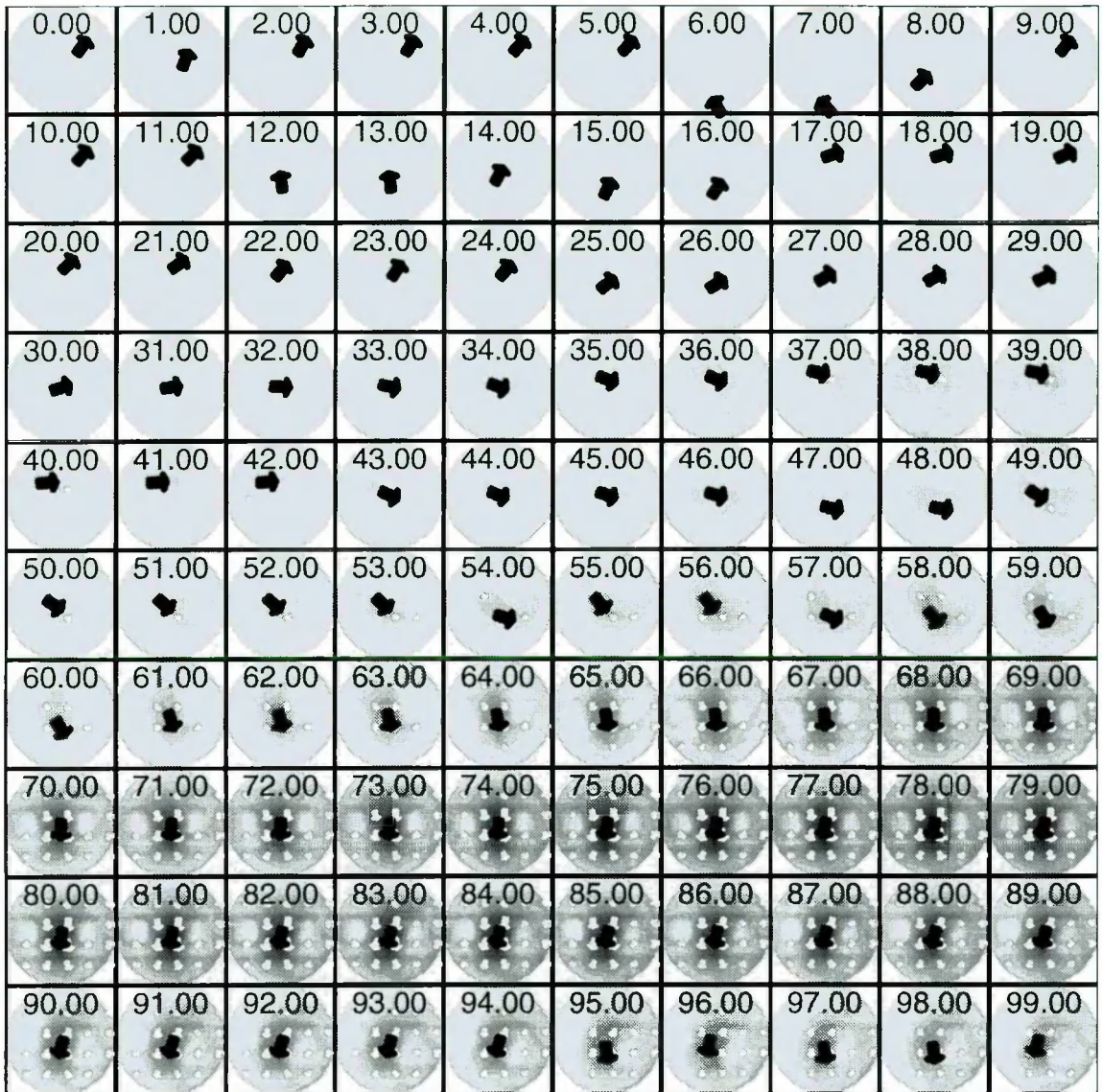
Figure 6.10 Contour map for the V_3 distribution for the average signal in experiment L-CONTRA-EC: the directions of the V_3 are indicated by the white arrows, normalized over the display period 0-99 ms. At each timeslice, the maximum of each V_3 map is calculated separately and marked by a darker arrow.
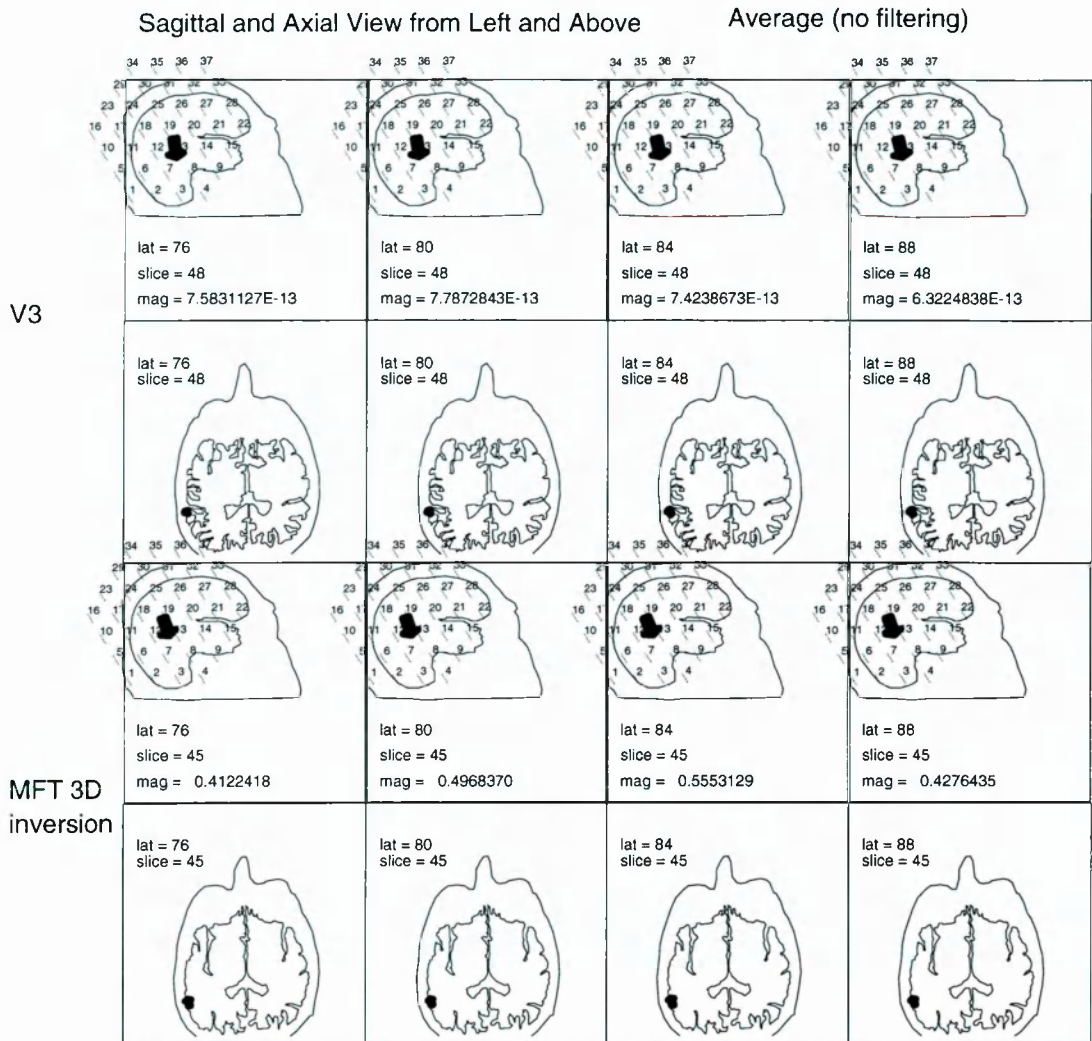
Figure 6.11 Estimation for generators obtained from V_3 and full MFT inversion superimposed on the outline of the sagittal and axial MRI slices, for experiment L-CONTRA-EC. The first two rows are for V_3 distribution, while the third and fourth rows show the full inversion obtained from the MFT distributed current analysis. Both results are represented by an arrow, which shows the maximum magnitude among all the evaluation points for the V_3 and the maximum whole source space for the full inversion. Notice excellent agreement between V_3 and MFT estimates for superficial generators in terms of position and direction.
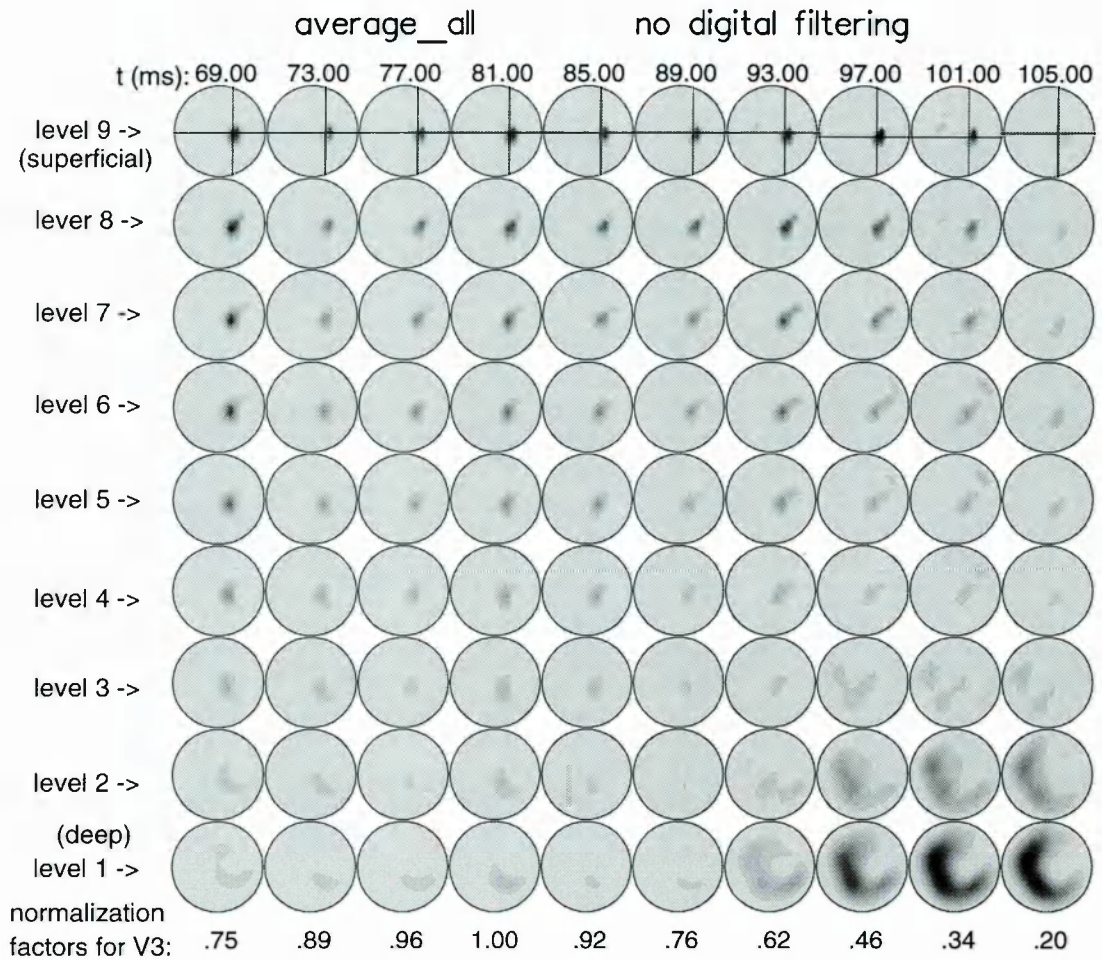
Figure 6.12 A contour cylinder plot for MFT estimates using the hemispherical 9-level source space, with the cross-hairs marking the positions of the dipoles representing the estimates obtained from V_3 projected onto the brain surface. Notice the good agreement and a limit for V_3 to reveal deep sources.

CHAPTER 7.

SINGLE EPOCH ANALYSIS

Despite its obvious limitations, averaging is widely used to improve the signal-to-noise ratio. The traditional view is that the eliminated signal by averaging is background "brain noise", what remains after averaging is a small fraction of the original signal. The development of modern multi-channel systems make it possible to map single epochs in real time. In this chapter, we use as examples a set of auditory evoked measurements to explore the relationship between the average and single trial signals, by comparing the 40-Hz (or gamma band) auditory responses in these signals, which are obtained from the signal transformation vector V_3 and the MFT distributed source analyses.

7.1. Introduction

The cortex receives inputs from receptors after it is preprocessed along the afferent pathways. The information content in the MEG/EEG can be accessed respectively by time ensemble and space ensemble averaging of fields/potentials recorded from arrays of sensors on or near the head. The use of averaging is necessary for EEG and for single or a few channel probe MEG. However, improvements in instrument design and assembly provide multiple sensors in compact arrays; improved shielding greatly increases the signal-to-noise ratio; and new software packages improve the decomposition and analysis of multichannel recordings with rapid display of results. All these give brain theorists substantial new data from which to devise and test new models of cortical dynamics. Therefore, averaging is not necessary when MEG probes with a large number of channels are available, and it is only history and inertia which makes its use still predominant with multichannel MEG probes [3].

In a typical experiment, identical stimuli are presented repeatedly, each "evoked"

response trial is aligned with respect to its stimulus onset and the ensemble is averaged, hence averaging can only contain contributions from activity which repeats with a constant phase in relation to the onset of a stimulus or other marker from trial to trial. In general such activity contributes a small fraction of the signal (10% or less). The eliminated signal by averaging is background "brain noise". Arguments against treating background brain activity as noise have been voiced many times, e.g. showing that the pre-stimulus EEG tends to attain a phase-order pattern prior to expected stimulation [2].

The averaging produces "clean" signals which at their peaks can often be described well by point sources, localized close to regions of the brain which are known to be associated with the processing of the stimulus used in the experiment. The use of one or few point sources as models for the generators does not produce good fits to single epoch data, and hence inferences about single epoch behaviour has relied on signal space descriptions. It is however difficult to relate the results of such analysis to what is happening in the brain.

MFT distributed source analysis has been successfully applied to both average MEG signals and single trial records [3, 122]. The method is however computationally demanding and it is prohibitively long to apply the method to all the single trials. With this view, we first applied the simple vector signal transformation $\mathbf{V}_3$ to both average and single trial signals to highlight nearby sources. In particular, we chose the comparison of the 40-Hz (or gamma band) auditory response in the average and single trial signals as the study subject. We find that in single epochs similar patterns of high frequency activity are observed in the area around the auditory cortex well before, close to and well after the stimulus onset [135].

Consequently, throughout the remaining sections, emphasis will be placed on the commonly known as "40 Hz" rhythms or, preferably, as "gamma" activity [136]. Papers concerning these low amplitude, high frequency oscillations in the MEG/EEG are reviewed first, followed by the analysis of 40-Hz auditory evoked response to the monaural stimulus obtained with the 37-channel KRENIKON system in Erlangen.

7.2. Spontaneous 40-Hz Activity

A substantial, perhaps major, portion of the new MEG technology is now used to identify high-amplitude components, such as segments of "spontaneous" alpha, theta and delta activity [137, 138, 139, 140], epileptiform spikes during seizures and interictal periods, and the peaks of event related potentials (ERPs). Striking successes have been reported in locating these sources within the cortex and deeper structures, in millimeters at depths within the brain of several centimeters [139, 140].

40-Hz oscillations were first postulated by Berger [141] over half a century ago to be "... the physical aspect of psychic processes ...". They have been studied extensively in the olfactory system [140, 136, 141, 142, 2, 143, 144]. In recent years, they have been found in the EEGs of all areas of cerebral cortex [144], and still more recently in the MEGs of sensorimotor [139, 140] and auditory cortexes [143, 145, 146, 147]. Experimental studies have shown that these waves contain or express both sensory and perceptual information, and theoretical studies have shown that the neural mechanisms that are responsible for these waves may be crucial for the integrative processes that support consciousness [141, 142, 144, 148].

According to Freeman, the reason that a "40 Hz" rhythm appears to be pre-eminent is because it manifests the interactions between excitatory and inhibitory neurons in what is basically a two-neuron feedback loop [149, 142, 150, 151]. This has been demonstrated in several areas of paleocortex, in which both types of neurons have time constants of 6 ms. Each cycle of oscillation includes four stages: excitation of excitatory neurons, excitation of inhibitory neurons, inhibition of excitatory neurons, and inhibition of inhibitory neurons, which releases the excitatory neurons to start a new cycle. Hence, each cycle takes 24 (4×6) ms, approximately 40 Hz; narrow-band spectral analysis and averaging enhance this part of the signal [142].

Generators of Gamma Activity

The hypothesis is commonly held that gamma activity arises in small networks, by either of two mechanisms. One is that a "pacemaker" neuron drives other neurons at the designated frequency selectively. The other is that single neurons may fire at regular intervals spontaneously and may "resonate" or "entrain" together under some conditions of stimulation. Neither of these hypotheses is consistent with the

structure and function of the vast majority of cortical neurons. Contrary to well publicized examples of units phase-locked to gamma, individual neurons mostly fire at nearly random time intervals and at mean rates well below the gamma range. Moreover, each neuron receives input from thousands of others, sums the synaptic currents at its single trigger zone, and transmits its aperiodic pulse train to thousands of others. There are no privileged networks of small numbers of neurons in the incredibly rich mesh of the millions of interactive neurons in each area of cortex.

These basic facts imply that gamma activity is an emergent macroscopic property of areas of cortex owing to large-scale synaptic interactions. Experimental evidence for this conclusion comes from simultaneous recording of the activities of the excitatory and inhibitory neurons, which shows that the area of commonality of oscillation involves all of the millions of neurons occupying extensive spatial areas [142, 152]. Therefore, selected neurons in an area of cortex participate in sensory events, as revealed by unit studies, but all of them co-operate in the perceptual outcome, as revealed by the gamma waves [153].

This conclusion is important to MEG studies for several reasons. Firstly, gamma sources cannot be localized as point dipoles but are distributed over wide areas of cortex. Secondly, gamma activity manifests the status of populations of neurons rather than of small numbers. It has been shown that perceptual as distinct from sensory information is revealed by macroscopic variables [142, 144] such as the MEG. Hence, the MEG is well suited for study of perceptual functions in the brain [139]. Thirdly, it is the spatial patterns of phase and amplitude of gamma activity that are important in studies of perception. Recent advances in the MEG technique, e.g., the availability of more than 100 sensors with the whole-head coverage, make it possible to record MEG simultaneously from extensive areas of cortex, so that by bandpass filtering and spatial filtering [150, 154], it may be possible to extract perceptual information from the gamma activity for measurement and display.

Characteristics of 40-Hz Activity

From a variety of studies, several main characteristics of the 40-Hz activity, of theoretical and practical interest, can be summarized as follows:

1. A solution to the binding problem of the human brain. The way in which the brain links together neural events at multiple locations to produce unified perceptual experience and behaviour is called the *binding problem.* Binding has been proposed to involve correlated activity at different cortical sites during perceptuomotor behaviour [155], particularly by synchronization of narrow-band oscillations in the gamma-frequency range (30-80 Hz) [136, 148]. The results from the 40-Hz studies showed a coherent recognizable object evoked a specific response in the gamma frequency range, which supports the hypothesis of the role of 40-Hz oscillations in the binding feature of human brain [151, 156, 157, 158, 159].

2. 40-Hz activity is continually generated by the central nervous system. It is random in nature, and occurs at a low level spontaneously, even in the absence of stimuli [160, 159]. However, it is more readily observed after sensory stimulation, which has the effect of synchronizing different sources of 40 Hz signals in the brain [161, 125, 162].

3. 40-Hz oscillatory activity observed in various brain areas reflected a common global mechanism and it has been hypothesized that thalamo-cortical pathways are involved in the organization of this event [125]. The 40-Hz oscillation seemed to be more rigorously in phase in controls than those observed in psychiatric patients, because in control subjects, there is an increased synchronization of cortical 40-Hz activity, driven by subcortical areas, with a focus on the activated sensory area during an auditory 40-Hz stimulation. Studies on Alzheimer patients indicate that while a similar activity pattern is present, the cortical component is reduced in these subjects [125]. Changes in the shape of the waveform may reflect a deterioration of the feedback resonance between the cortex and thalamus [163]. A similar phenomenon was observed using the EEG technique with surgical anesthesia [161]. However, further investigation is necessary to demonstrate the detailed spatial and temporal alterations of the 40-Hz response and how they are correlated to the pathology of the disease.

4. 40-Hz activity is highly organized in three-dimensional space and in time and independent of stimulus parameters, such as patterns and frequencies of the sound stimuli. However, cognitive variables, such as stimulus certainty and task relevance, influence the evoked gamma-band responses, especially more on a cognitive gamma activity than a sensory one, because it is thought to be related to focused arousal as a first order component of the attention process

[164]. A study conducted by Tiitinen and co-workers also shows that selective attention enhances the auditory gamma-band transient response and hence 40-Hz response could be used for diagnostic purposes [165].

5. MEG recordings revealed that the 40-Hz oscillatory activity during auditory processing had the following properties [125]:

- it was recorded over the entire hemisphere;

- it was independent of the stimulus presentation rate;

- it was clearly phase-locked over cortical areas;

- a phase shift of oscillatory activity with apparent motion from the frontal to the occipital pole of the head.

Therefore, the auditory 40-Hz response has a component in the auditory cortex as a result of thalamo-cortical interaction; many people speculate that it may serve perceptual integration and conscious perception.

7.3. 40-Hz Auditory Evoked Response

In this section, we will use as examples a set of auditory evoked measurements, of which details of the experiment have been given in Section 6.2, to study the temporal organization of 40-Hz activity emanating from the auditory cortex in single trials. The simple vector signal transformation $\mathbf{V}_3$ was used to identify auditory cortex activity in both average and single epoch signals.

7.3.1. Methods

We first define an overlap function, to provide an objective estimate of how similar the superficial activity is, within an area of interest A directly below the measurement plane. If we specifically compare an epoch i (from $t = t_1$ to $t = t_1 + \Delta t$) [1] with an epoch j (from $t = t_2$ to $t = t_2 + \Delta t$), we use the following overlap:

$$\langle\, i : t_1 \,|A, \Delta t|\, j : t_2 \,\rangle = \int_A dx\, dy \int_0^{\Delta t} dt\; \mathbf{V}_3^i(x, y\,; t_1 + t) \cdot \mathbf{V}_3^j(x, y\,; t_2 + t) \qquad (7.1)$$

---

[1] An epoch is a period of time $T_{epoch} = T_{epoch-} + T_{epoch+}$, defined in terms of the onset of the ith stimulus, e.g., t_i. Hence, the ith epoch begins at $t_i - T_{epoch-}$ and ends at $t_i + T_{epoch+}$.

Even with this simplified analysis a comparison of all pairs of single epochs with each other is prohibitively long. The average response provides an obvious comparison target. Two comparison criteria have thus been defined,

$$C_1^i(A, \bar{t}, t, \Delta t) = \frac{\langle\, aver : \bar{t}\,|A, \Delta t|\, i : t\,\rangle}{\sqrt{|\,\langle\, aver : \bar{t}\,|A, \Delta t|\, aver : \bar{t}\,\rangle\,|\,|\,\langle\, i : t\,|A, \Delta t|\, i : t\,\rangle\,|}} \tag{7.2}$$

$$C_2^i(A, \bar{t}, t, \Delta t) = \frac{\langle\, aver : \bar{t}\,|A, \Delta t|\, i : t\,\rangle}{|\,\langle\, aver : \bar{t}\,|A, \Delta t|\, aver : \bar{t}\,\rangle\,|} \tag{7.3}$$

In the above two equations, every single trial is compared with the average over all single trial signals from $\bar{t}$ to $\bar{t} + \Delta t$ over the identified superficial cortex A. C_1 provides a measure of how well the pattern of activity matches, without reference to how strong the single epoch activity is compared with the average, while C_2 is also scaled by the relative strength of the single epoch activity compared with that in the average.

The single trials from seven of the eight experiments (the raw signals for one experiment was missing) were analysed by using the $\mathbf{V}_3$ transformation and the comparison criteria C_1 and C_2. We have used the first 50 ms after the stimulus onset for the average signal as template ($\bar{t} = 0$, $\Delta t = 50$ ms). During this period, the bandpass filtered signal [2] in the 35-45 Hz of $\mathbf{V}_3$ transformation showed pronounced gamma-band activity over the posterior end of the Sylvian fissure (see Figure 7.10). The template, computed from this 50 ms interval of the average signal, was compared with a sliding 50 ms window in each trial. Single trials for 1 second, 500 ms on either side of the stimulus onset, filtered in the same way as the average were used for the comparison, i.e., for each epoch, C_1 and C_2 were computed with the above defined $\bar{t}$, Δt and A for 1 second, 500 ms on either side of the stimulus onset ($t =$-500 to 450 ms, see Figure 7.1 (a)). For every timeslice, epochs for which the C_1 and C_2 overlaps exceed predefined thresholds (0.7 for C_1 and 3.47 for C_2) are classified as "high matching epochs". If the matching occurs with a small phase lag (2 ms on either side of the stimulus onset), these high matching epochs are classified further as "correlated epochs", while the high matching epochs with no matching within 50 ms on either side of the stimulus onset, are classified further as "uncorrelated epochs" (see Figure 7.1 (b)).

---

[2] A bandpass filter is one which passes signals in a band between two cut-off frequencies and attenuates signals outside the band.
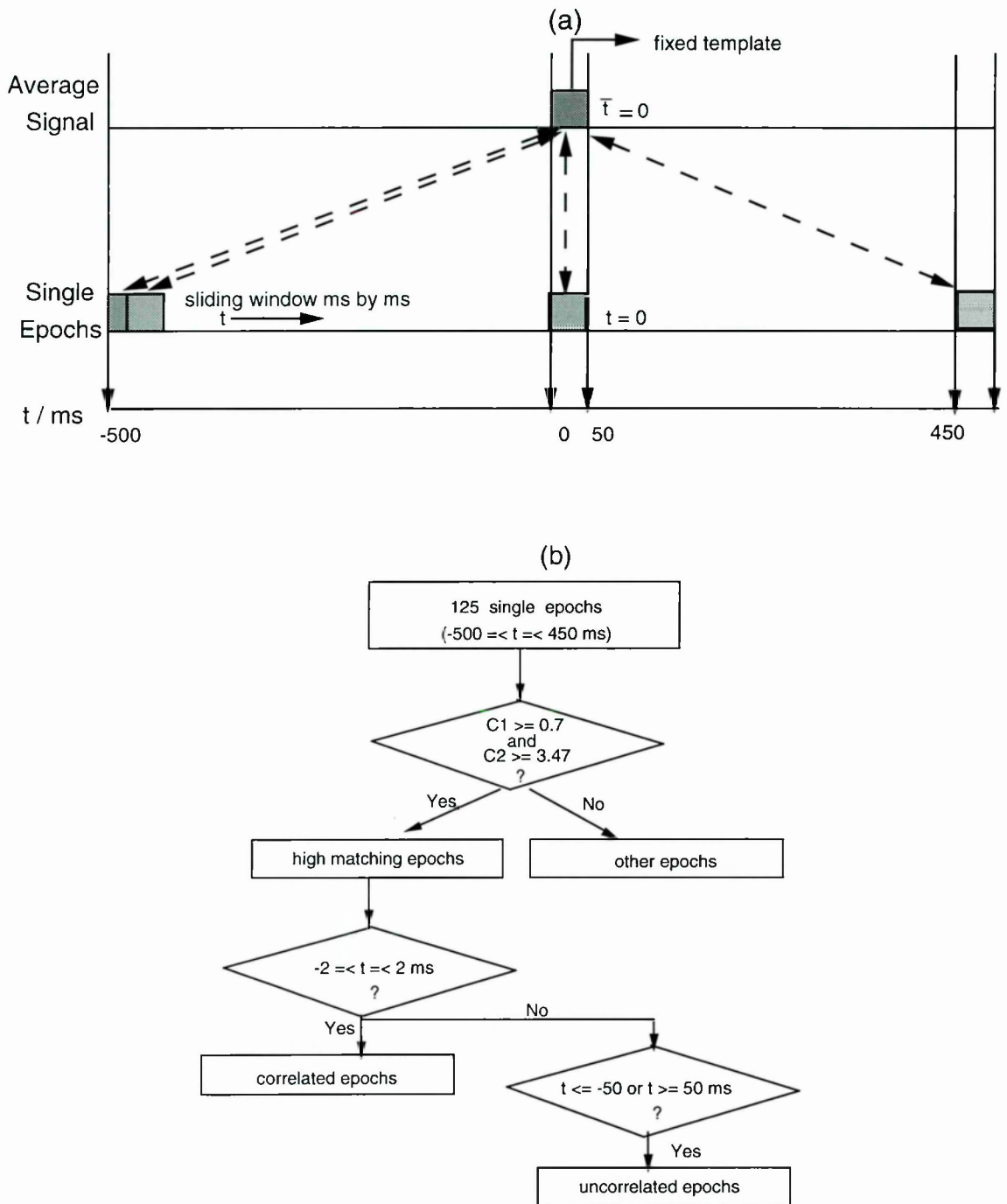
Figure 7.1 A diagram showing the method used in the single epoch analysis: (a) The correlation measures C_1 and C_2 are computed for the (fixed) template for the average signal of the first 50 ms following the stimulus and the (sliding) 50 ms wide window in each single trial from -500 to 450 ms; (b) the epoch classification process.

7.3.2. Results and Discussions

Figure 7.2 summarizes the comparison between the average and single epoch activity in the 40 Hz range within the latency window -25 to 25 ms (C_1 and C_2 are computed for each epoch for all latencies): only the higher matching epochs are printed in the figure. The right hemisphere tends to produce higher relative strength in the high matching epochs than the left, which is explained by the fact that the left hemisphere has more high matching epochs than the right one. The figure also reveals that only a small number of epochs, typically 5–10% of all the trials, produce high matching values with small phase lag ($-2 \leq t \leq 2$ ms) (correlated epochs). For instance, in experiment L–CONTRA–EC, out of 125 epochs, only 8 are correlated – epochs 23, 25, 29, 37, 53, 91, 105 and 118. The correlated epochs are not uniformly distributed in each experiment studied, instead showing distinct clustering, which may reflect shifts in attention. As we will see, these few epochs account for a large part of the gamma-band activity in the average signal during the first 50 ms after the stimulus onset.

Figure 7.3 shows how the C_1 and C_2 overlaps (exceeding the thresholds) for the single trials change over time (-500 to 450 ms). To avoid clustering, we chose to display every 5 epochs starting from epoch 5 (hence 25 epochs for each experiment were shown in the figure). From the figure, it can be seen that a good matching was found in single epochs well before, close to, and well after the onset of the stimulus, a result confirmed by subsequent MFT distributed source analysis of the same epochs. In the following discussion, we use experiment L–CONTRA–EC as an example to explore the relationship between the average and single trials.

In experiment L–CONTRA–EC, there are 125 single trials. Table 7.1 lists the high matching epochs from -5 to 55 ms. Column 2 shows the total number of the high matching epochs at the specific timeslice, with the epoch number is listed in column 3. Column 4 shows the number of epochs which were also highly matched with the average in the previous timeslice, while column 5 is for the number of epochs which are highly matched at the present timeslice. Hence, numerically, column 2=column 4+column 5. Column 6 shows the number of the correlated epochs among the total. The table shows three things – first, the high matching between the single trials and the average lasts for 3-6 ms, i.e., each high matching epoch appears in 3-6 consecutive timeslices. This casually confirms the earlier discussion concerning the
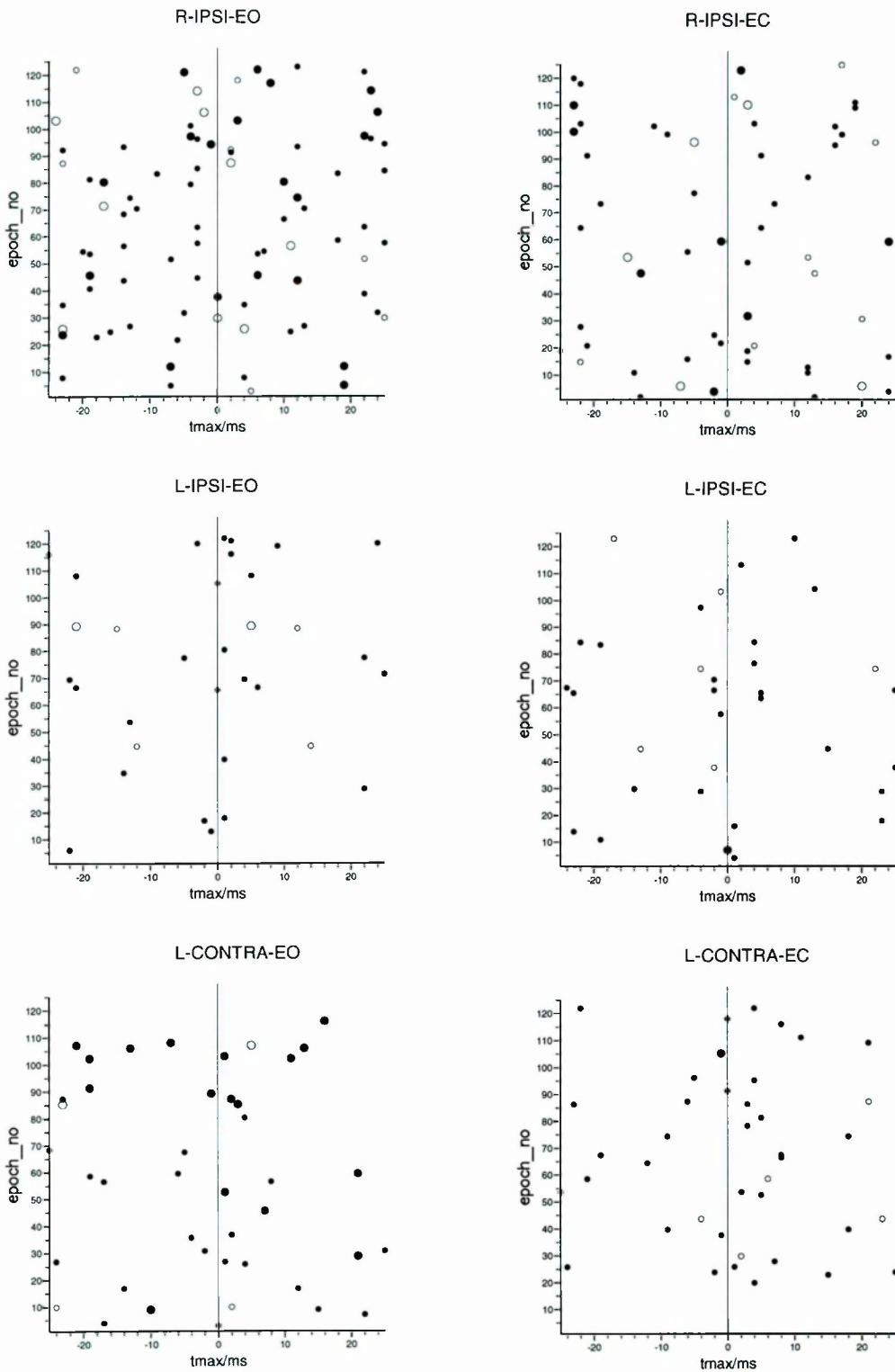
Figure 7.2 Epoch summary for the single trials in the six sensor placements band-pass filtered in 35-45 Hz from -25 ms to 25 ms: an empty dot corresponds to $C_1 \geq 0.85$, and a filled dot corresponds to $0.7 \leq C_1 < 0.85$. The size of the dots indicates C_2, i.e. the big dots stand for $C_2 \geq 7.0$, and the small dots are for those $3.47 \leq C_2 < 7.0$.
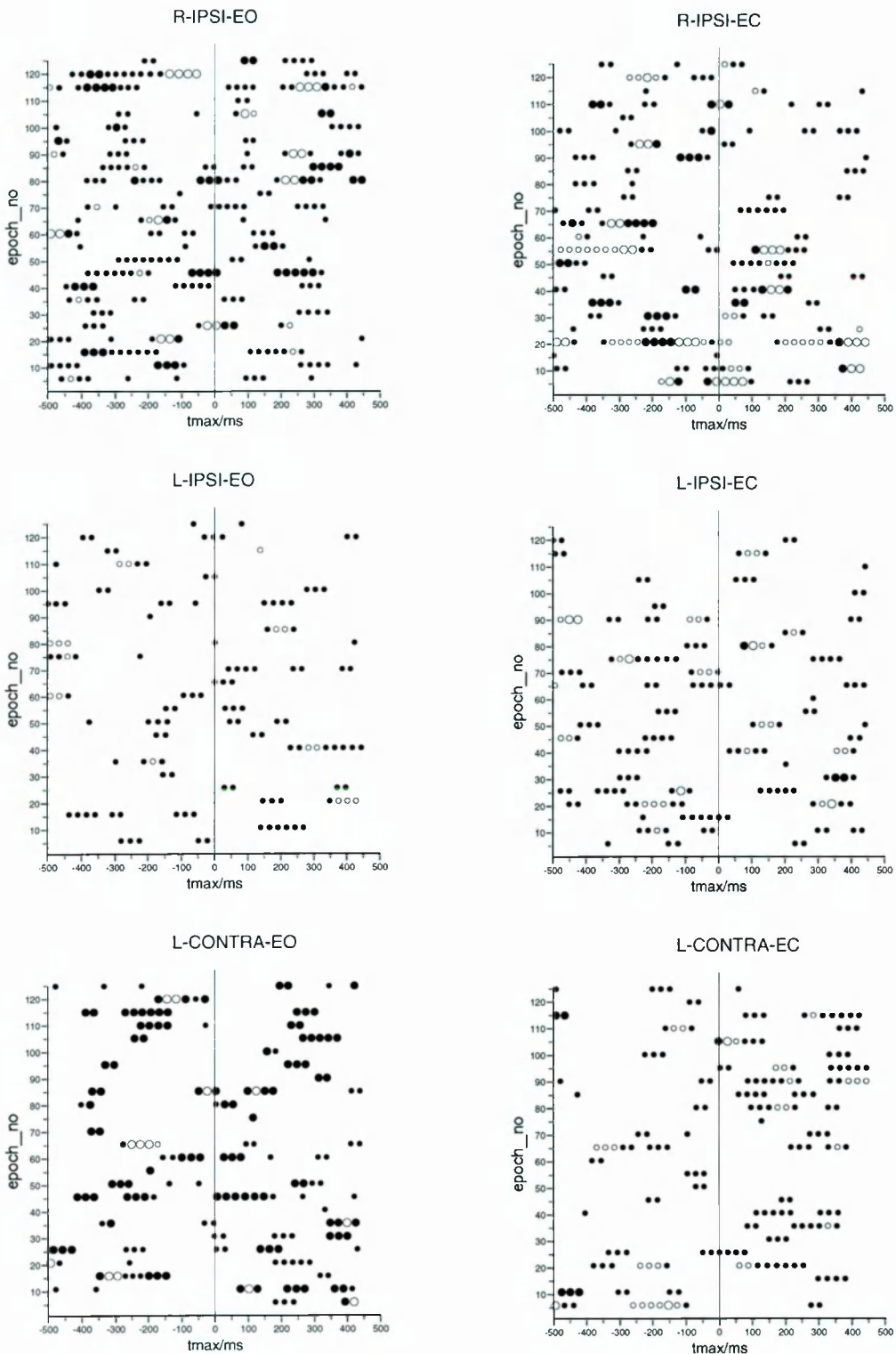
Figure 7.3 Epoch summary for every 5 single trials in the six sensor placements bandpass filtered in 35-45 Hz from -500 to 450 ms: an empty dot corresponds to $C_1 \geq 0.85$, and a filled dot corresponds to $0.7 \leq C_1 < 0.85$. The size of the dots indicates C_2, i.e. the big dots stand for $C_2 \geq 7.0$, and the small dots are for those $3.47 \leq C_2 < 7.0$.

time constant of each 40-Hz oscillation cycle, i.e., 6 ms. Secondly, roughly every 25 ms, the constituents of the high matching epochs are very similar, namely, it is likely that the similar epochs appear again in about 25 ms. Therefore, the 40-Hz oscillation observed in the average signal is basically the contributions from the high matching epochs at each timeslice. Thirdly, for each timeslice, there are up to 10 single trials which match the average activity well, e.g., at the onset of the stimulus, epochs 25, 29, 37, 53, 91, 105 and 118.

The corresponding filtered 40-Hz signals for the central channel 19, which has maximum magnitude among all channels, are as shown in Figure 7.4. The figure shows a similarity between the average and the correlated epochs, while this similarity is not evident for the uncorrelated epochs. It is worth noting that the filtered 40-Hz data the phase matching (forced by our selection) between the full average and the correlated single epochs is excellent. As pointed out earlier, it is the spatial patterns of phase and amplitude of gamma activity that are important in studies of perception. It is likely that the 40-Hz activity seen in the average, like the one classified as correlated epochs by our selection criteria, plays an important role in cognitive studies. We propose that the average signal constructed in such studies is also composed of contributions from distinct epochs at distinct intervals. Moreover, for some epochs, a reorganization of the pattern occurs close to stimulus onset, e.g. epoch 23 in Figure 7.4(a), there is a strong signal enhancement upon the stimulus (i.e. the magnitude of the signal is increasing with the onset of the stimulus), which is in agreement with earlier observations [2].

Figure 7.5 shows the comparison between V_3 and full 3D MFT estimates for well correlated epochs filtered at 40-Hz. Row 1 is for the full average, while the other rows are for the correlated epochs. The display is every 14 ms from 12 ms following the onset of the stimulus for the average, while for the correlated epochs, the corresponding phase shifts with the average have been taken into account for the display. The figure shows three agreements, namely, the agreement between the V_3 and the MFT inversion, the agreement between the average and the correlated single epochs, and the agreement of every cycle of the 40-Hz, in terms of the activation area, maximum direction and position. By contrast, this agreement is not evident in both the average of the uncorrelated epochs and the uncorrelated single epochs during the first 50 ms after the onset of the stimulus (see Figure 7.6); at different periods, sometimes well before, close to, or well after the onset of the stimulus, such

Time (ms)	Total Epoch Numbers	Epoch Number	Encountered Epochs	New Epochs	Correlated Epochs
-5	3	43 87 96	3	0	0
-4	3	43 87 96	3	0	0
-3	4	23 37 43 96	2	2	2
-2	4	23 37 43 105	3	1	3
-1	4	23 29 37 105	3	1	4
0	7	25 29 37 53 91 105 118	3	4	7
1	5	25 29 53 105 118	5	0	5
2	5	25 29 53 78 86	3	2	3
3	8	19 29 53 78 81 86 95 122	4	4	2
4	8	19 29 58 78 81 86 95 122	7	1	1
5	7	27 52 58 78 81 95 122	5	2	0
6	5	27 52 58 66 81	4	1	0
7	5	27 58 66 67 116	3	2	0
8	5	27 58 66 67 116	5	0	0
9	2	66 116	2	0	0
10	1	111	0	1	0
11	1	111	1	0	0
12	1	111	1	0	0
14	1	22	0	1	0
15	1	22	1	0	0
16	3	22 39 74	1	2	0
17	2	39 74	2	0	0
18	2	39 74	2	0	0
19	3	39 74 87	2	1	0
20	2	87 109	1	1	0
21	3	43 87 109	2	1	0
22	3	43 87 109	3	0	0
23	2	43 87	2	0	0
24	4	23 37 43 105	1	3	3
25	6	23 25 37 43 91 105	4	2	5
26	6	23 25 37 43 91 105	6	0	5
27	8	23 25 29 37 53 54 91 105	5	3	7
28	8	29 53 54 78 91 95 105 118	5	3	5
29	10	19 29 53 78 81 91 95 97 118 122	6	4	4
30	9	19 29 53 78 81 95 97 118 122	9	0	3
31	8	13 19 29 58 78 81 118 122	6	2	2
32	7	13 27 29 58 78 81 118	6	1	2
33	5	13 27 58 81 116	4	1	0
34	4	27 58 66 116	3	1	0
35	5	27 58 66 111 116	4	1	0
36	2	66 111	2	0	0
37	2	66 111	2	0	0
38	2	111 121	1	1	0
39	2	111 121	2	0	0
40	1	121	1	0	0
41	1	121	1	0	0
42	3	39 74 121	1	2	0
43	3	39 74 106	2	1	0
44	3	39 74 106	3	0	0
45	2	74 106	2	0	0
46	3	74 87 106	2	1	0
47	3	87 106 109	2	1	0
48	4	43 87 107 109	2	2	0
49	3	43 87 109	3	0	0
50	4	25 43 105 109	2	2	2
51	5	23 25 43 105 109	4	1	3
52	7	23 25 43 54 83 91 105	4	3	4
53	7	23 25 43 54 83 91 105	7	0	4
54	7	23 41 54 83 91 97 105	5	2	3
55	6	29 41 54 91 97 118	4	2	3
SUM	250	N/A	184	66	82
P(%)	N/A	N/A	73.6	26.4	32.8

Table 7.1 List of epochs, bandpass filtered in 35-45 Hz from -5 to 55 ms, producing high matching pattern with the average of the first 50 ms following the stimulus.
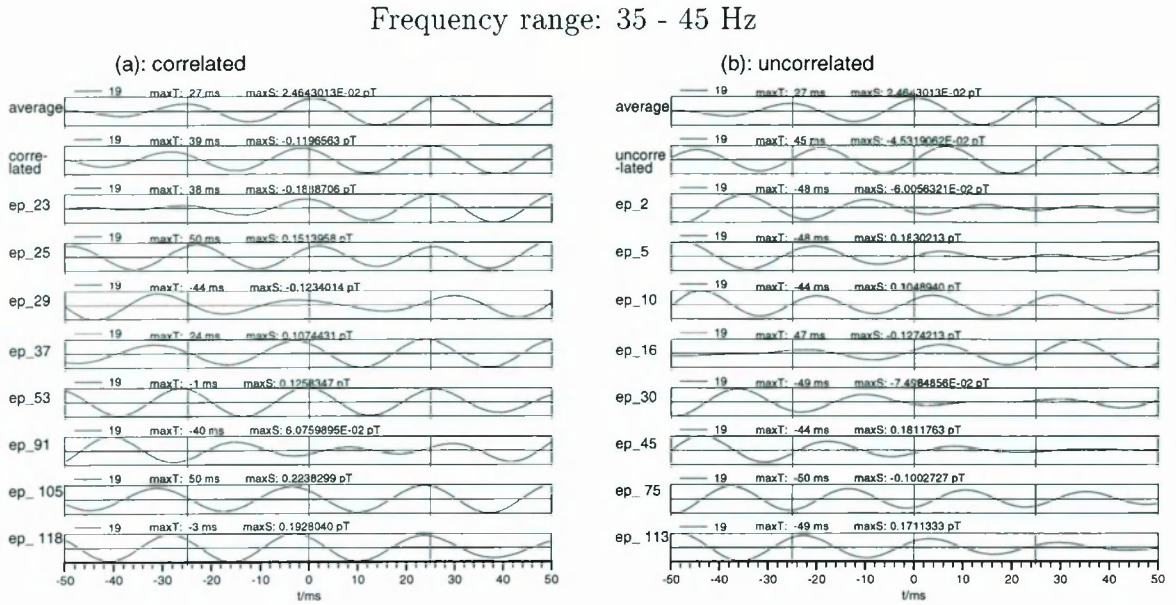
Figure 7.4 Signal traces for the average and single trial signals in experiment L–CONTRA–EC bandpass filtered in 35-45 Hz, from -50 ms to 50 ms for channel 19. Notice the similarity in terms of shape and phase in (a) but absent in (b), following the onset of the stimulus.

a similarity to the average of the first 50 ms sequence is seen in single trials. This similarity period varies from epoch to epoch (refer to Figure 7.7).

The current density $J(\mathbf{r}, t)$ from the MFT estimates has positive and negative components, while the intensity $P(\mathbf{r}, t)$ $(P(\mathbf{r}, t) = J(\mathbf{r}, t) \cdot J(\mathbf{r}, t))$ is a positive scalar. Hence operations like summation and subtraction can be performed on $P(\mathbf{r}, t)$ without the huge cancellations which occur when the same operations are applied to $J(\mathbf{r}, t)$. Furthermore, $P(\mathbf{r}, t)$ can be used in integrals over space and/or time, to provide hints how the brain activity changes over a specific area and/or a longer period [122, 166]. The definitions of the integrals over space $A(t, T)$ and time $I(\mathbf{r}, t, T)$ are given as,

$$I(\mathbf{r}, t, T) = \int_0^T P(\mathbf{r}, t) \, dt \tag{7.4}$$

$$A(t, T) = \int_0^T dt \int_{area} P(\mathbf{r}, t) \, d^3\mathbf{r} \tag{7.5}$$

When the intensity is integrated over time, agreement between the average and these correlated single trials is evident, though the integration period is short, when in
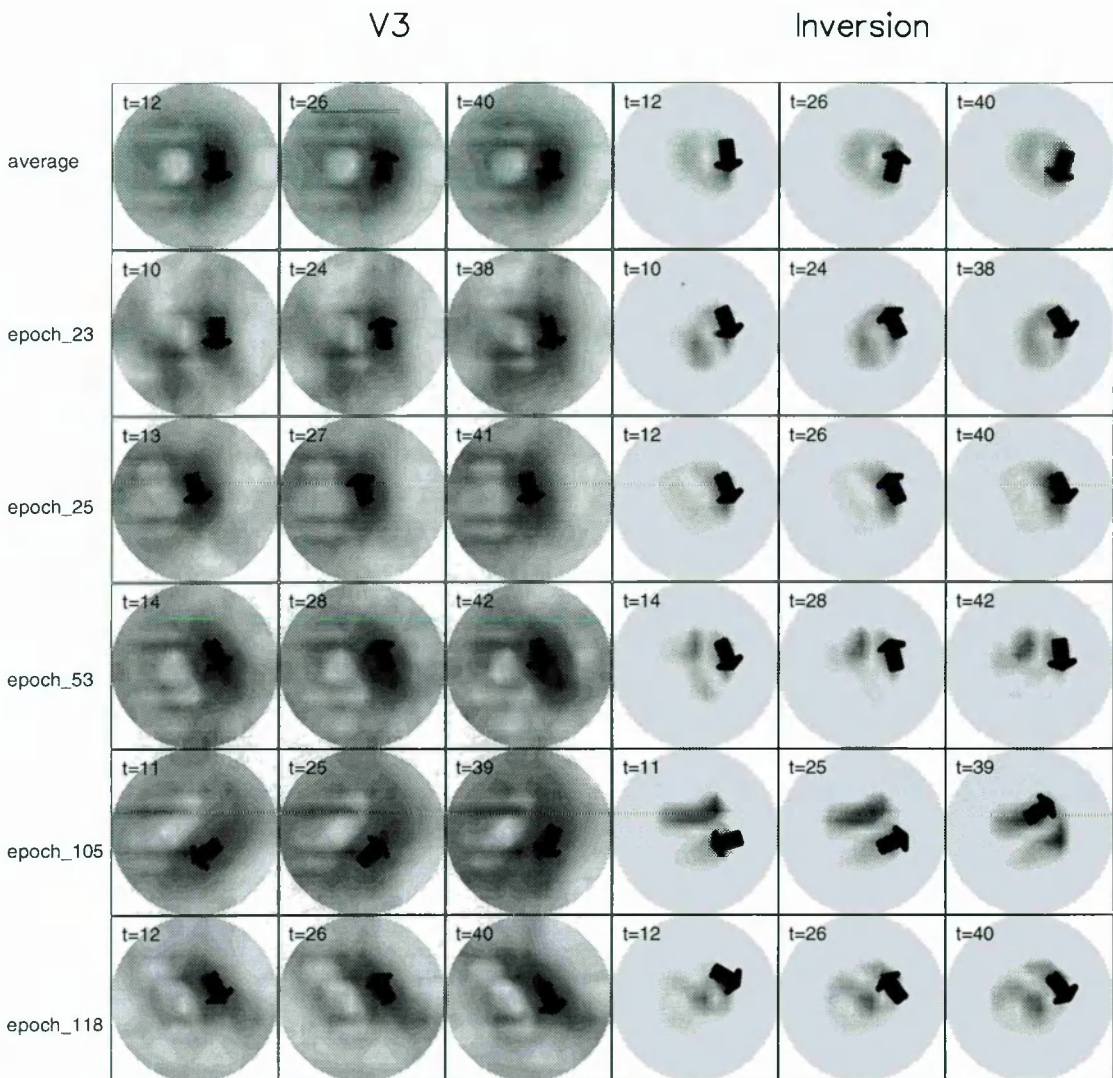
Figure 7.5 Comparison between V_3 and full MFT 3D inversions for well correlated epochs filtered at 40-Hz for experiment L–CONTRA–EC: grey level stands for the strength of the activity, with the darkest shade corresponding to the highest strength. The maximum of each plot is indicated by an arrow. Each plot is normalized independently. Notice the agreement between V_3 and MFT inversion, between the average and the correlated epochs in every cycle (14 ms).
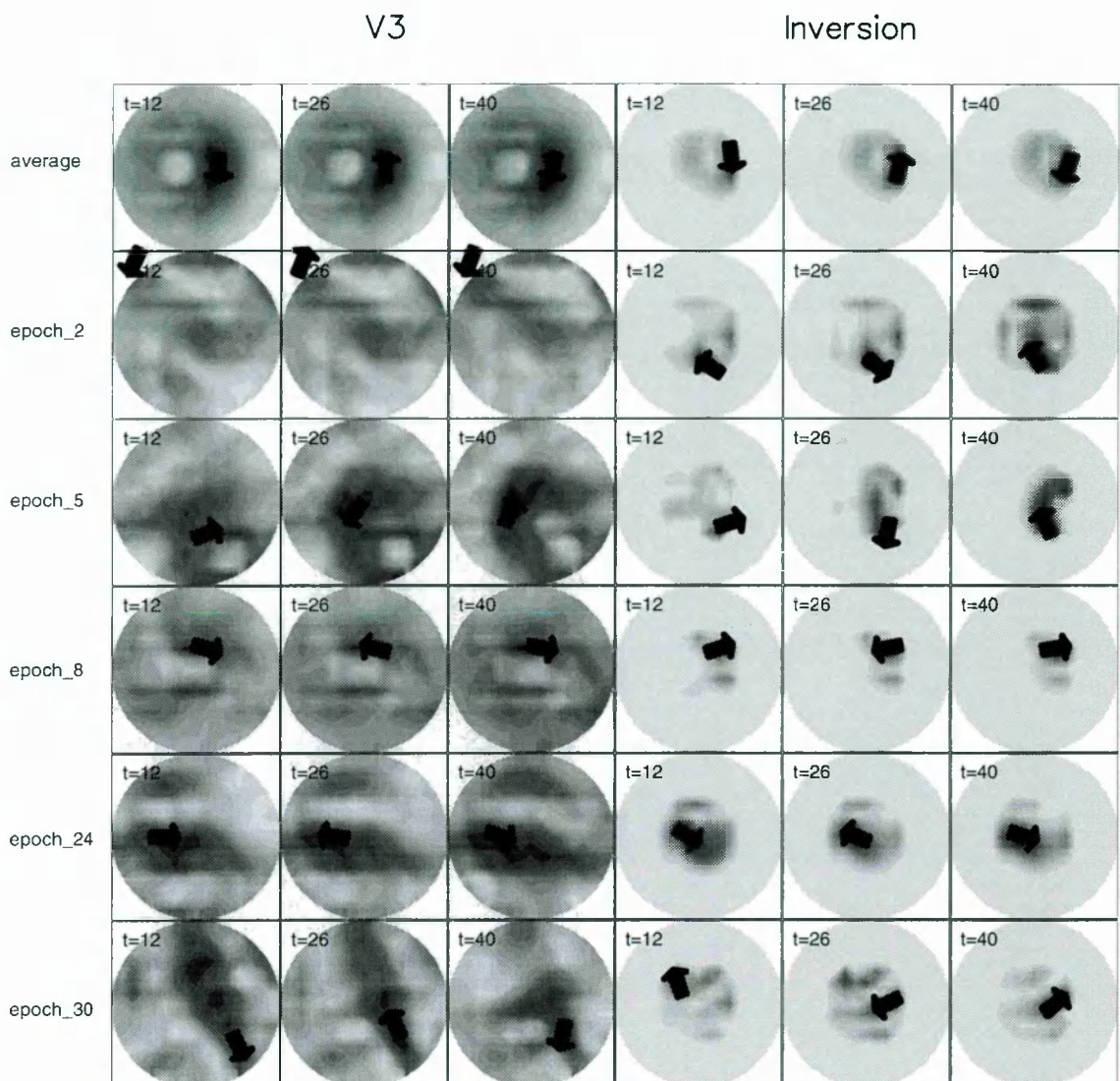
Figure 7.6 Comparison between V_3 and full MFT 3D inversions for uncorrelated epochs filtered at 40-Hz for experiment L–CONTRA–EC: grey level stands for the strength of the activity, with the darkest shade corresponding to the highest strength. The maximum of each plot is indicated by an arrow. Each plot is normalized independently. Notice the difference between V_3 and MFT inversion, between the average and the uncorrelated epochs in every cycle (14 ms).
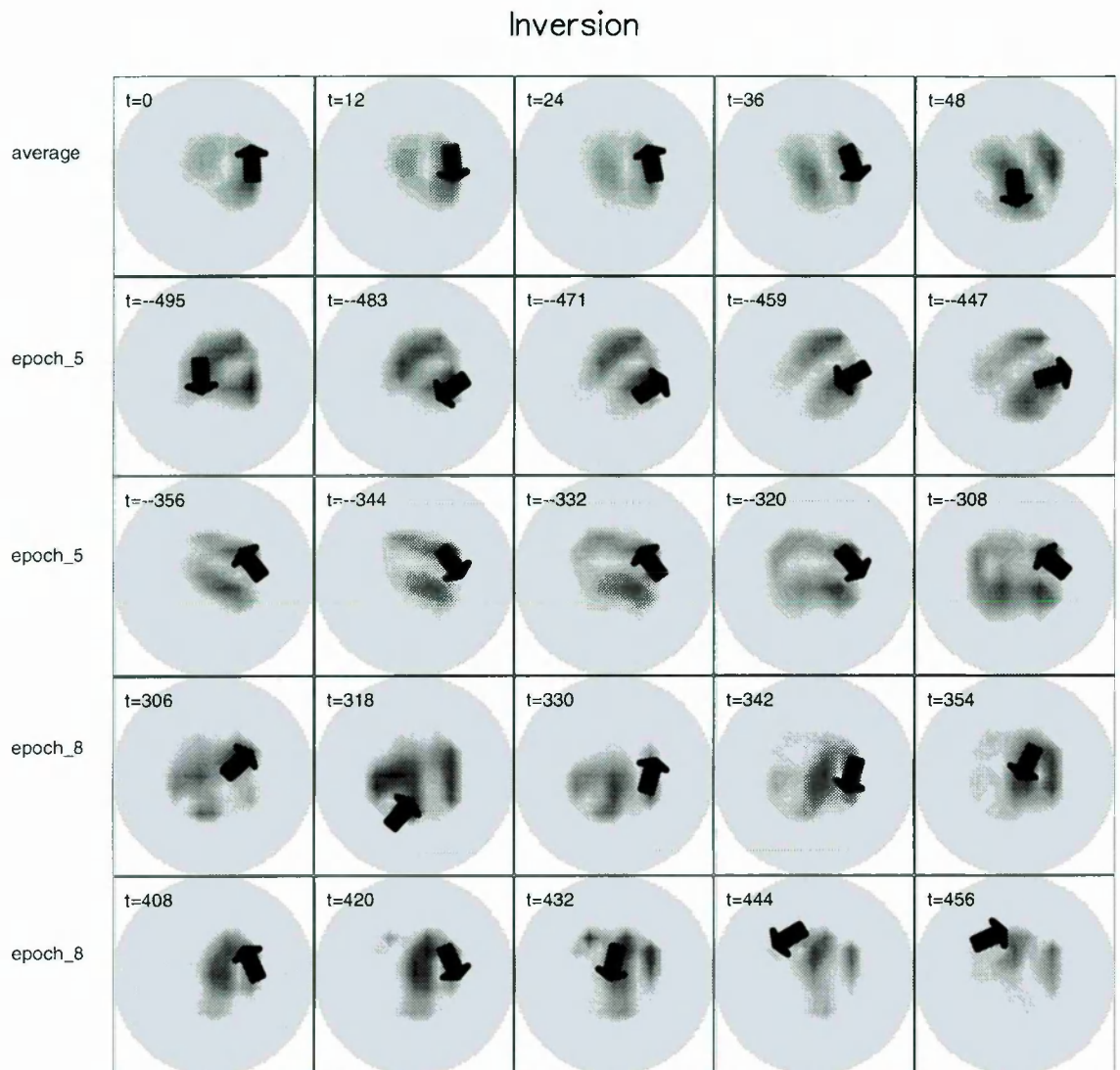
Inversion

Figure 7.7 Full MFT 3D inversions for two uncorrelated epochs at the period of well matching the average signal of the first 50 ms following the stimulus: epoch 5 shows good matching well before the stimulus, while epoch 8 is well after. Grey level stands for the strength of the activity, with the darkest shade corresponding to the highest strength. The maximum of each plot is indicated by an arrow. Each plot is normalized independently.

general, the single trials show high variability.

Figure 7.8 shows MFT estimates: integrals of intensity over 12 ms and transitions (the changes of activation areas) millisecond by millisecond for superficial sagittal slices at the level of the left auditory cortices, with the stimulus delivered to the left ear (experiment L–CONTRA–EC) and the signals bandpass filtered at 40-Hz. The first two rows show MFT estimates extracted from the average signals, the full average and the average of correlated epochs, respectively. The other five rows show the six correlated single epochs. Darker shades represent strong activity, with the relative normalization factors printed in each window. The same cortical areas, normally associated with auditory processing, are identified in the average and single trials. It is the order and precise time of activation area that counts for the similarity between the average and the single trials. In Figure 7.8, there are two main activation areas, A_1 (-5,7,3) and A_2 (-5,7,2) when coordinates are in *cm* and given in the MRI-based coordinate system (see Appendix A). By comparing the first two rows for the averages, it can be seen that both the average for all epochs and the average for the correlated epochs are mainly active in area A_1, while the average for the uncorrelated epochs is mainly active in area A_2. It is interesting to note that the activity of the average for the correlated epochs shows an orderly oscillation – occipital, frontal and occipital. This phenomenon can also be observed slightly in the average for all. For the correlated single trials, the activity areas are seen in both areas, A_1 and A_2. The orderly oscillation between the front and occipital of the brain can also be seen in the correlated single trials. In comparison with the correlated epochs, the uncorrelated epochs show little resemblance with the average during the first 50 ms following the onset of stimulus, as shown in Figure 7.9, in either the main activation areas or the sequence of activations. The above figures show the MFT estimate in superficial sagittal slices, we now superimpose the MFT estimates onto the axial MRI slices, in an effort to provide a hint of the spatial and temporal organisation of the spontaneous 40-Hz activity, with the comparison between the average and the single trials.

The superimpositions of the MFT estimates for the average of all epochs, of the correlated epochs and of the uncorrelated epochs are as shown in Figure 7.10 to 7.12. The display lasts 60 ms, with successive icons separated by 4 ms. The period begins with the onset of the stimulus at the left ear. Referring to Figure 7.10, it can be seen that the filtered 40-Hz average signal shows much more activity at the su-
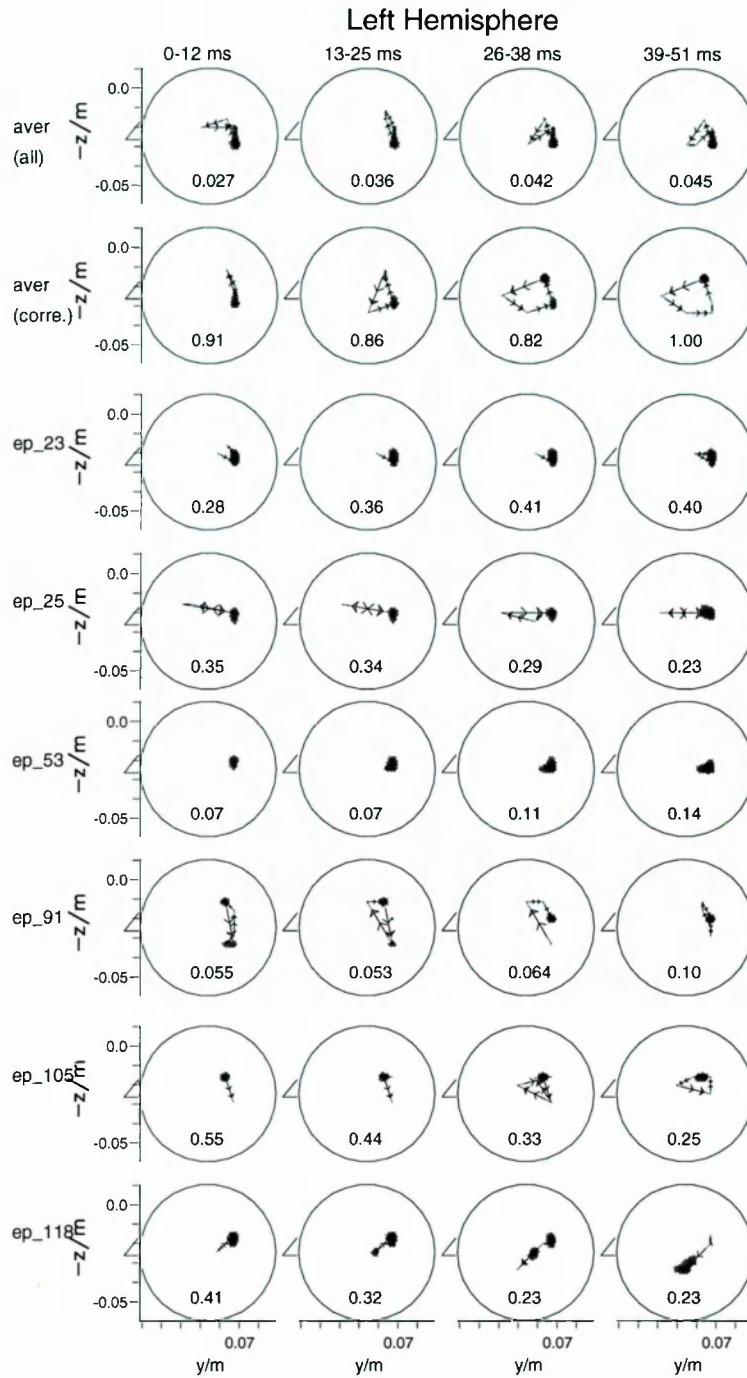
Figure 7.8 Integrals of intensity over 12 ms for MFT estimates of the average and correlated single trial signals bandpass filtered in 35-45 Hz: viewed from outside the brain with the top of the head up and the nose medial, and the circle delineating the intersection of the hemispherical source space. Notice the similar activation pattern between the average and single trial signals.
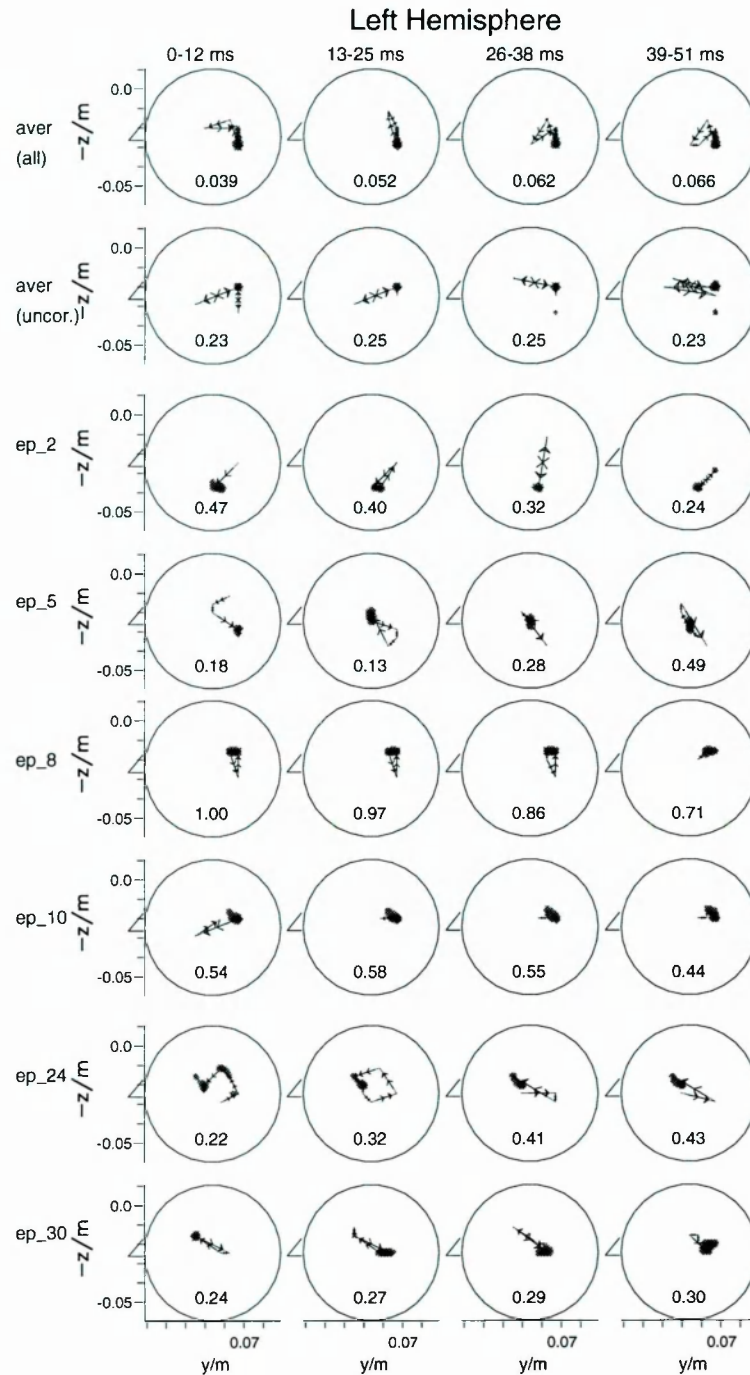
Figure 7.9 Integrals of intensity over 12 ms for MFT estimates from average and uncorrelated single trial signals bandpass filtered in 35-45 Hz range: viewed from outside the brain with the top of the head up and the nose medial, and the circle delineating the intersection of the hemispherical source space. Notice the different activation pattern between the average and single trial signals.

perficial auditory cortex (mainly oscillates along y axis – the maximum points either towards the front or the back of the head), though some traces of activity are seen at deep level. The 40-Hz activity is well organized in three-dimensional space and in time, e.g., when $t = 0$, 12 and 24 ms, the main activity area is at slice 38, 45, and 38 correspondingly. Similarly for the following sequence of $t = 4$ ms, $t = 8$ ms and so on. In addition to the above characteristics, the average for the correlated epochs filtered at 40-Hz shown in Figure 7.11 displays much more activity in depth, which might be a reflection of a thalamo-cortical oscillation. This oscillation is however not prominent for the average of uncorrelated epochs, as shown in Figure 7.12, instead some activity at the back of the head can be traced. For the 40-Hz activity revealed by the single trials, as shown in Figure 7.13 and Figure 7.14, in comparison with the averages, single trials show substantial deep activities, which do not survive the average; only when the superficial activity is also comparable with or stronger than the deep activity in the single trials, is there an agreement between the average and the correlated single trials. Hence, averaging does discriminate against relative weak generators related to the sensors, e.g. deep and central ones, unless these sources activate more strongly than the superficial sources at a specific timeslice.

The superimpositions on the MRI slices described so far rely on anatomic selection of the MRI slice, corresponding to the maxima of the MFT estimates for either the average or the single trials. To make a more direct comparison, we use the MRI slices for the average of correlated epochs (see Figure 7.11) as the target MRI slices, and superimpose the MFT estimates for the averages and the correlated epochs onto them, as shown in Figure 7.15 to 7.18. Referring to Figure 7.11, Figures 7.15, 7.17, 7.18 show similar interplay between superficial and deep activity, suggesting that the correlated epochs contribute substantially to the average for the first 50 ms following the onset of the stimulus; in other words, the average more or less reflects these correlated epochs during this period. By contrast, Figure 7.16 shows very little similarity with Figure 7.11, which consequently demonstrates the "irrelevance" of the uncorrelated epochs with the average during this observation period.

The 40-Hz activity in the auditory cortex identified in this study suggests that the gamma-band oscillations observed when the average of many thousands of epochs is taken [125, 147] corresponds to resetting of an ongoing process which occurs spontaneously, but may also be triggered intermittently by the stimulus.

average_all   filter: 35-45 Hz

lat = 0 slice = 38	lat = 4 slice = 51	lat = 8 slice = 25	lat = 12 slice = 45
Jmag = 1.3040433E-02 Jx = -1.2783628E-04 Jy = -3.3425493E-03	Jmag = 1.2392552E-02 Jx = 2.5672729E-03 Jy = 1.0741476E-02	Jmag = 1.1592004E-02 Jx = -5.0181993E-03 Jy = -8.3049834E-03	Jmag = 1.2172357E-02 Jx = 1.7504393E-03 Jy = 3.5212697E-03
lat = 16 slice = 51	lat = 20 slice = 25	lat = 24 slice = 38	lat = 28 slice = 51
Jmag = 1.4282353E-02 Jx = -2.9485926E-03 Jy = -1.2361825E-02	Jmag = 1.2628113E-02 Jx = 5.5311187E-03 Jy = 7.5520575E-03	Jmag = 1.0618325E-02 Jx = -1.7213908E-03 Jy = -7.9332916E-03	Jmag = 1.4614555E-02 Jx = 2.7627626E-03 Jy = 1.2187630E-02
lat = 32 slice = 32	lat = 36 slice = 25	lat = 40 slice = 38	lat = 44 slice = 51
Jmag = 1.3387228E-02 Jx = -3.6280733E-03 Jy = -1.0355219E-02	Jmag = 9.5595606E-03 Jx = -4.1875970E-03 Jy = -5.7799052E-03	Jmag = 1.3711252E-02 Jx = 1.5519605E-03 Jy = 8.6136125E-03	Jmag = 1.4195452E-02 Jx = -2.8523556E-03 Jy = -1.2148451E-02
lat = 48 slice = 25	lat = 52 slice = 38	lat = 56 slice = 51	lat = 60 slice = 25
Jmag = 1.2625250E-02 Jx = 5.4404535E-03 Jy = 5.9266337E-03	Jmag = 1.2960896E-02 Jx = -1.5130290E-03 Jy = -8.2588401E-03	Jmag = 1.5578425E-02 Jx = 2.7173292E-03 Jy = 1.2549916E-02	Jmag = 1.0713651E-02 Jx = -4.4026417E-03 Jy = -3.4227690E-03

Figure 7.10 MFT estimates superimposed on the outline of the axial MRI slices, for the average signals filtered at 40-Hz in experiment L-CONTRA-EC: the darkness of the plot represents the strength of the activity and each plot is normalized separately. The sensor array is also displayed and represented by the lines. Notice the well organized in space and time 40-Hz activity mainly at superficial level.
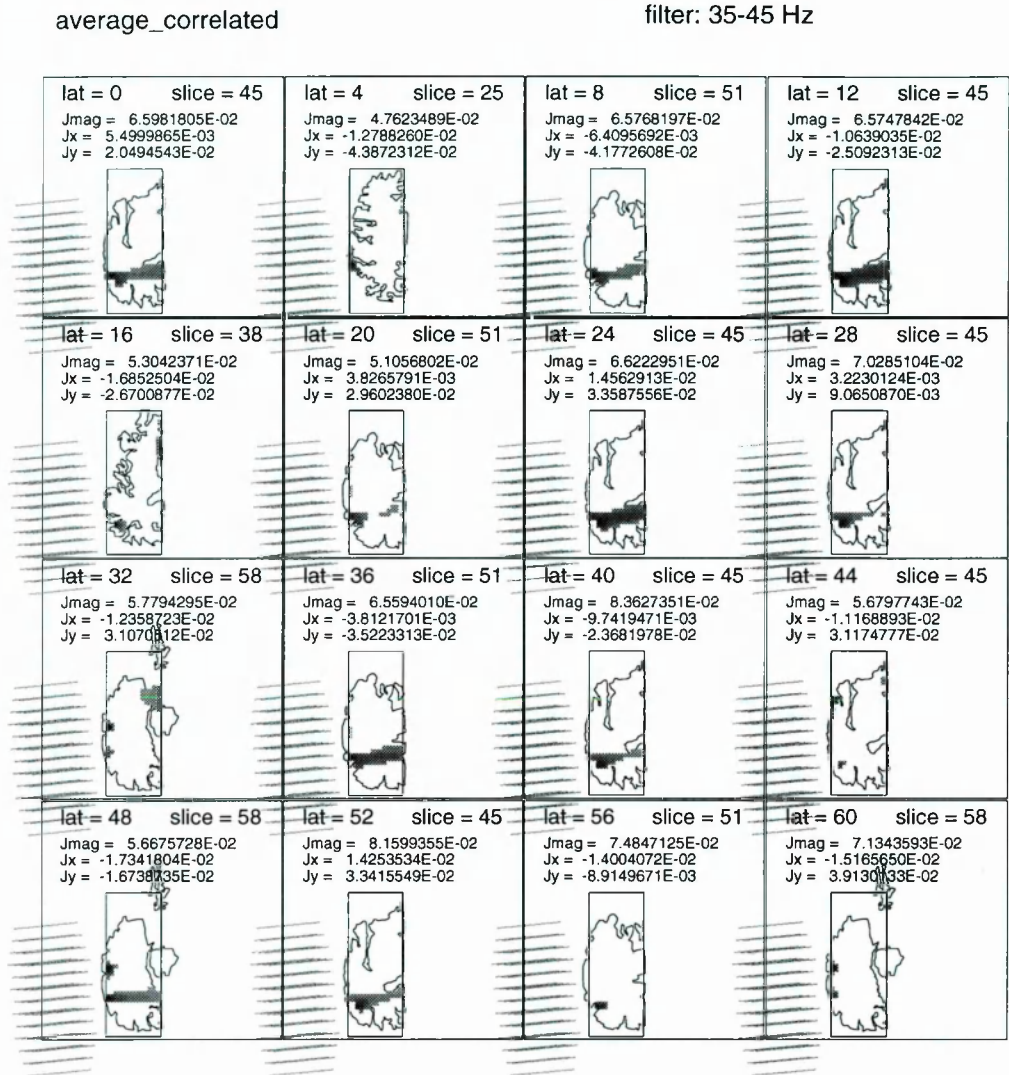
Figure 7.11 MFT estimates superimposed on the outline of the axial MRI slices, for the average of the correlated single trials filtered at 40-Hz in experiment L-CONTRA-EC: the darkness of the plot represents the strength of the activity and each plot is normalized separately. The sensor array is also displayed and represented by the lines. Notice the oscillation pattern.
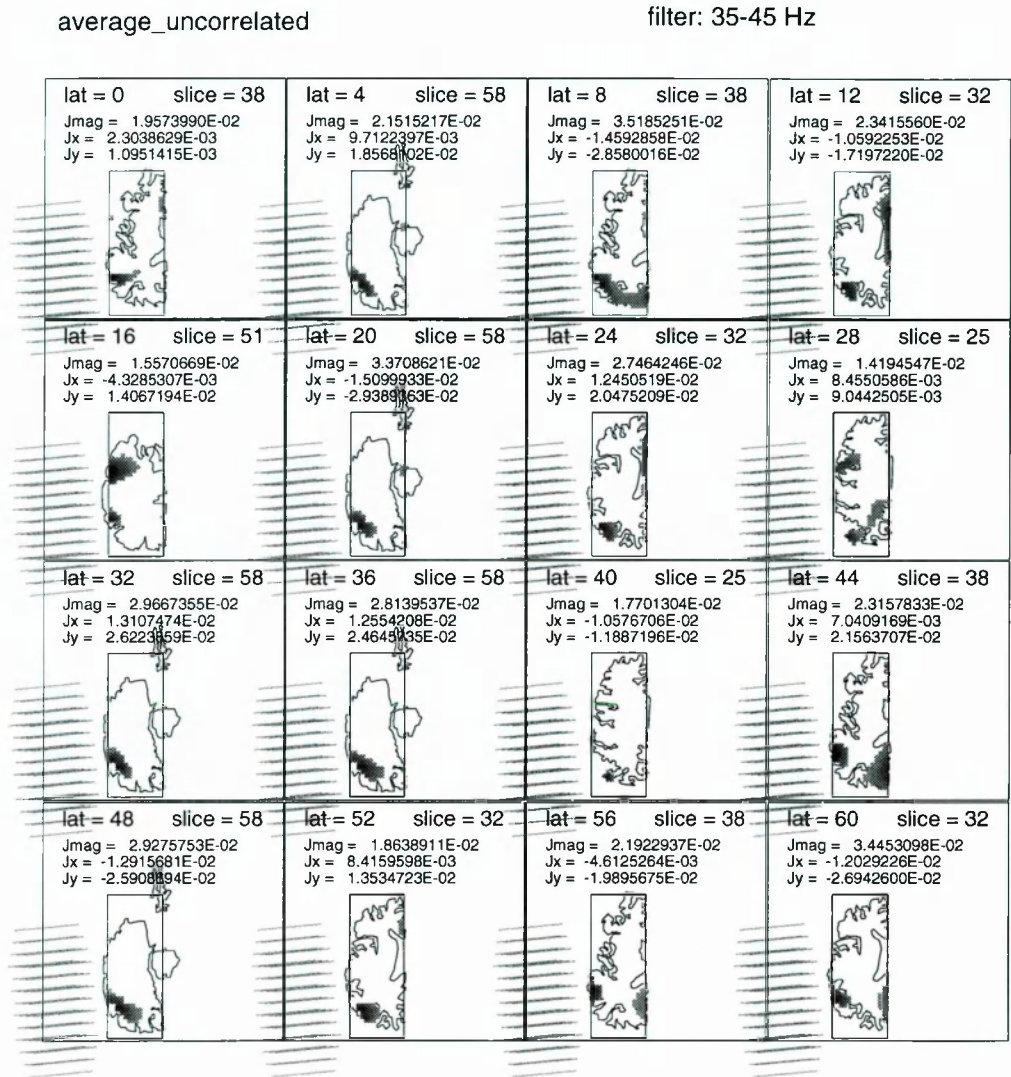
Figure 7.12 MFT estimates superimposed on the outline of the axial MRI slices, for the average of the uncorrelated single trials filtered at 40-Hz in experiment L-CONTRA-EC: the darkness of the plot represents the strength of the activity and each plot is normalized separately. The sensor array is also displayed and represented by the lines. Notice the activity at the back of the head.
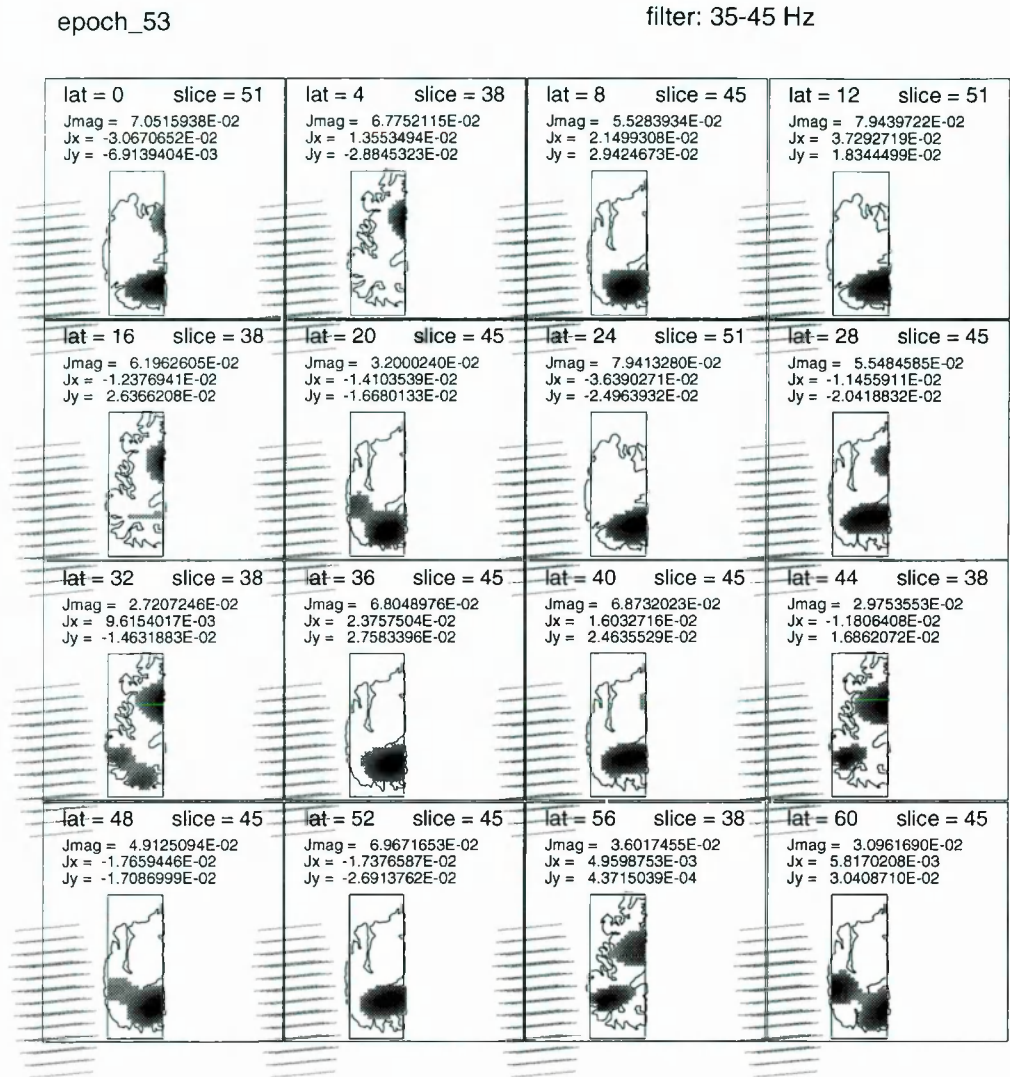
Figure 7.13 MFT estimates superimposed on the outline of the axial MRI slices, for the correlated single epoch 53 filtered at 40-Hz in experiment L-CONTRA-EC: the darkness of the plot represents the strength of the activity and each plot is normalized separately. The sensor array is also displayed and represented by the lines. Notice the deep activity and oscillation pattern.

epoch_105   filter: 35-45 Hz

lat = 0 slice = 45	lat = 4 slice = 51	lat = 8 slice = 51	lat = 12 slice = 51
Jmag = 8.9374334E-02	Jmag = 4.4248525E-02	Jmag = 5.9554812E-02	Jmag = 8.9580551E-02
Jx = 2.4318688E-02	Jx = -1.5667092E-02	Jx = -2.2768410E-02	Jx = -1.2657075E-02
Jy = 3.7593056E-02	Jy = -9.0222200E-03	Jy = -4.5252681E-02	Jy = -5.1158167E-02

lat = 16 slice = 51	lat = 20 slice = 32	lat = 24 slice = 51	lat = 28 slice = 51
Jmag = 6.6527098E-02	Jmag = 5.0096691E-02	Jmag = 7.9566739E-02	Jmag = 7.9309687E-02
Jx = 1.1359630E-02	Jx = -1.3830756E-02	Jx = 1.1356800E-02	Jx = -8.9205755E-03
Jy = -1.1720881E-02	Jy = -3.3859123E-02	Jy = 4.5582801E-02	Jy = 2.4992935E-02

lat = 32 slice = 32	lat = 36 slice = 51	lat = 40 slice = 51	lat = 44 slice = 51
Jmag = 3.4040257E-02	Jmag = 6.3112982E-02	Jmag = 8.1092246E-02	Jmag = 3.5887856E-02
Jx = 9.3326168E-03	Jx = -7.7910353E-03	Jx = 9.2133554E-03	Jx = 8.7020453E-03
Jy = 2.4818996E-02	Jy = -3.2978635E-02	Jy = -2.8512189E-02	Jy = 5.8497238E-04

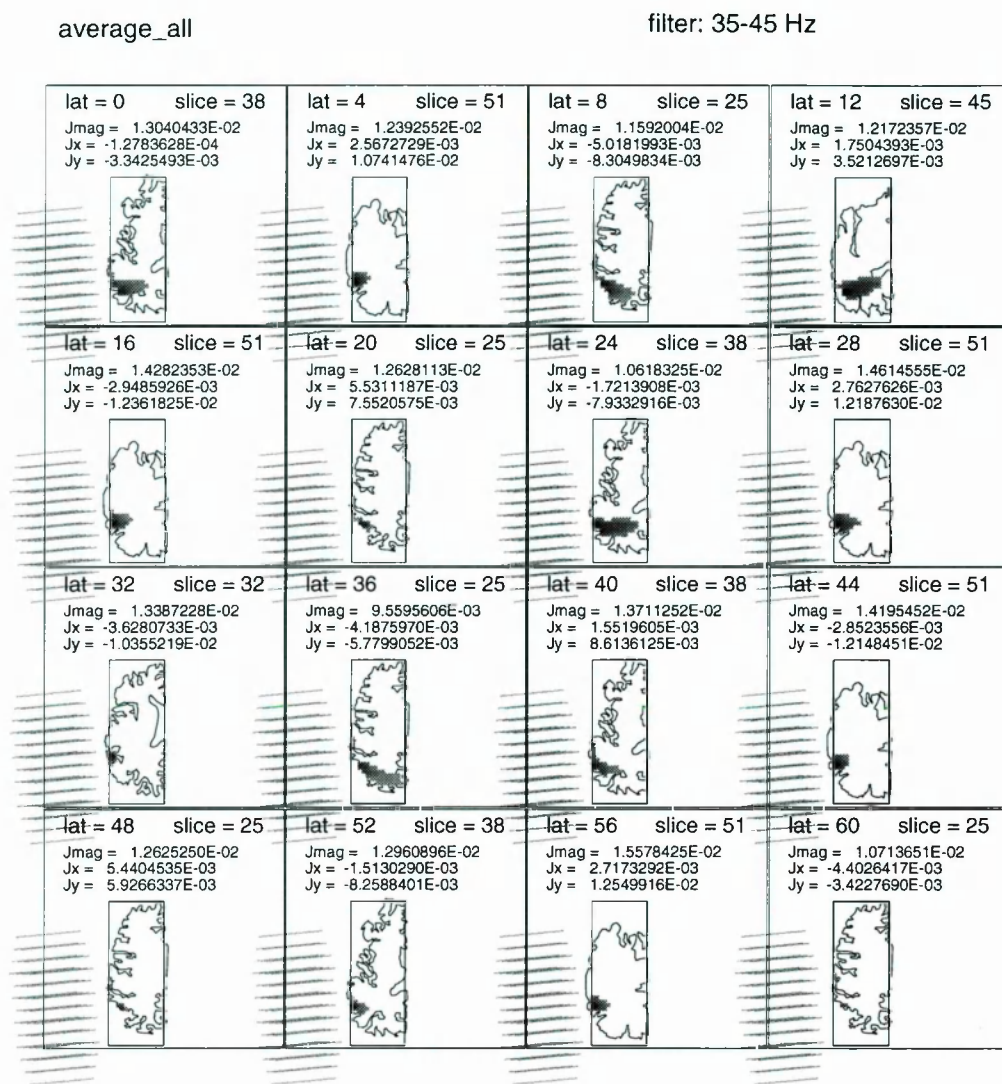| lat = 48 slice = 51	lat = 52 slice = 45	lat = 56 slice = 51	lat = 60 slice = 45
Jmag = 4.6694230E-02	Jmag = 7.7167101E-02	Jmag = 4.7198877E-02	Jmag = 4.3635178E-02
Jx = 3.3509384E-03	Jx = 7.0758220E-03	Jx = -8.2290247E-03	Jx = -1.7593643E-03
Jy = 2.0977506E-02	Jy = 1.3014071E-02	Jy = 7.8889243E-03	Jy = 2.6998611E-04

Figure 7.14 MFT estimates superimposed on the outline of the axial MRI slices, for the correlated single epoch 105 filtered at 40-Hz in experiment L-CONTRA-EC: the darkness of the plot represents the strength of the activity and each plot is normalized separately. The sensor array is also displayed and represented by the lines. Notice the deep activity and oscillation pattern.

average_all   filter: 35-45 Hz

lat = 0 slice = 45	lat = 4 slice = 25	lat = 8 slice = 51	lat = 12 slice = 45
Jmag = 1.3040433E-02 Jx = -1.2783628E-04 Jy = -3.3425493E-03	Jmag = 1.2392552E-02 Jx = 2.5672729E-03 Jy = 1.0741476E-02	Jmag = 1.1592004E-02 Jx = -5.0181993E-03 Jy = -8.3049834E-03	Jmag = 1.2172357E-02 Jx = 1.7504393E-03 Jy = 3.5212697E-03
lat = 16 slice = 38	lat = 20 slice = 51	lat = 24 slice = 45	lat = 28 slice = 45
Jmag = 1.4282353E-02 Jx = -2.9485926E-03 Jy = -1.2361825E-02	Jmag = 1.2628113E-02 Jx = 5.5311187E-03 Jy = 7.5520575E-03	Jmag = 1.0618325E-02 Jx = -1.7213908E-03 Jy = -7.9332916E-03	Jmag = 1.4614555E-02 Jx = 2.7627626E-03 Jy = 1.2187630E-02
lat = 32 slice = 58	lat = 36 slice = 51	lat = 40 slice = 45	lat = 44 slice = 45
Jmag = 1.3387228E-02 Jx = -3.6280233F-03 Jy = -1.0355919E-02	Jmag = 9.5595606E-03 Jx = -4.1875970E-03 Jy = -5.7799052E-03	Jmag = 1.3711252E-02 Jx = 1.5519605E-03 Jy = 8.6136125E-03	Jmag = 1.4195452E-02 Jx = -2.8523556E-03 Jy = -1.2148451E-02
lat = 48 slice = 58	lat = 52 slice = 45	lat = 56 slice = 51	lat = 60 slice = 58
Jmag = 1.2625250E-02 Jx = 5.4404535E-03 Jy = 5.9268837E-03	Jmag = 1.2960896E-02 Jx = -1.5130290E-03 Jy = -8.2588401E-03	Jmag = 1.5578425E-02 Jx = 2.7173292E-03 Jy = 1.2549916E-02	Jmag = 1.0713651E-02 Jx = -4.4026417E-03 Jy = -3.4227490E-03

Figure 7.15 MFT estimates superimposed on the outline of the same axial MRI slices as for the average of the correlated epochs, for the average signal filtered at 40-Hz in experiment L-CONTRA-EC: the darkness of the plot represents the strength of the activity and each plot is normalized separately. The sensor array is also displayed and represented by the lines. Notice some similarity in the interplay between superficial and deep activity as shown in Figure 7.11.

average_uncorrelated   filter: 35-45 Hz
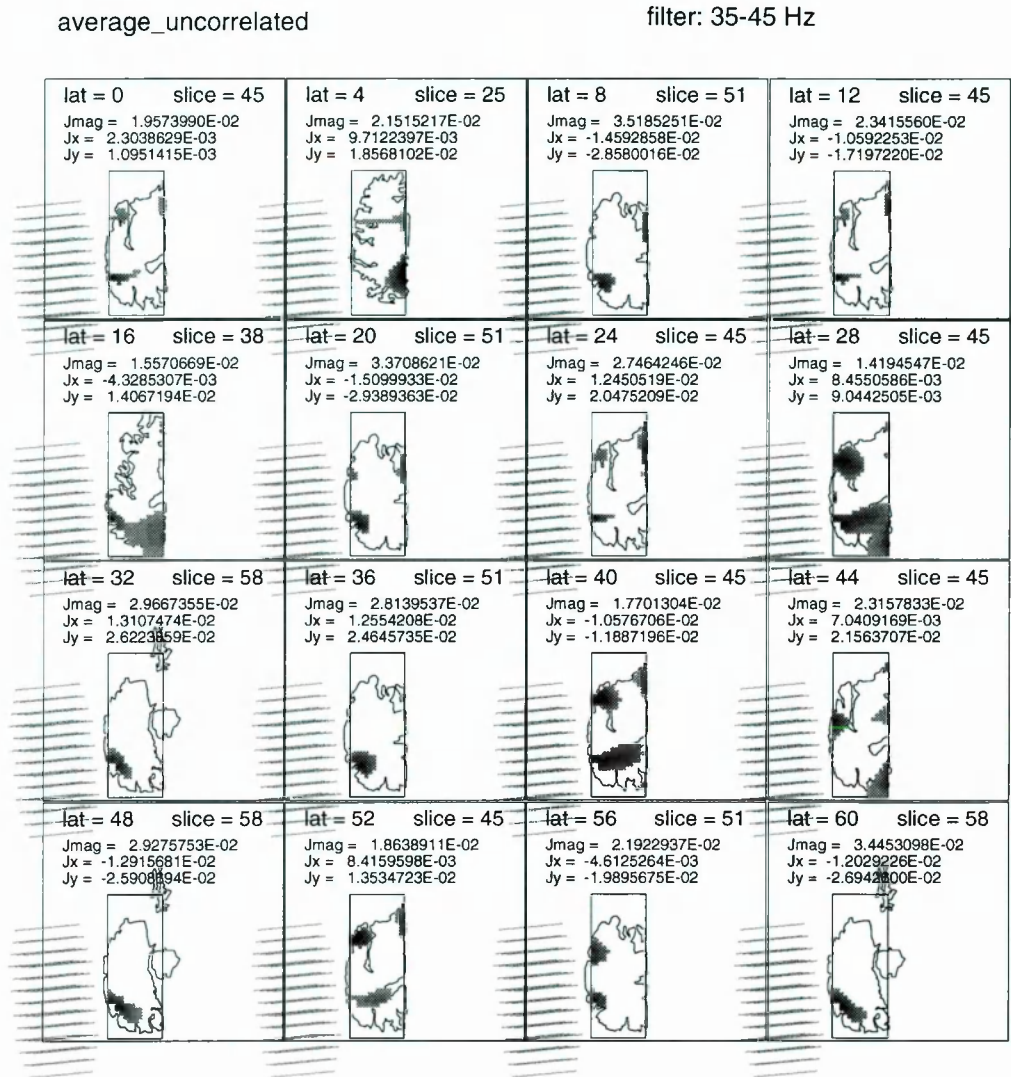
Figure 7.16 MFT estimates superimposed on the outline of the same axial MRI slices as for the average of the correlated epochs, for the average of the uncorrelated epochs filtered at 40-Hz in experiment L-CONTRA-EC: the darkness of the plot represents the strength of the activity and each plot is normalized separately. The sensor array is also displayed and represented by the lines. Notice different activation pattern as shown in Figure 7.11.

epoch_53   filter: 35-45 Hz

lat = 0 slice = 45	lat = 4 slice = 25	lat = 8 slice = 51	lat = 12 slice = 45
Jmag = 7.0515938E-02	Jmag = 6.7752115E-02	Jmag = 5.5283934E-02	Jmag = 7.9439722E-02
Jx = -3.0670652E-02	Jx = 1.3553494E-02	Jx = 2.1499308E-02	Jx = 3.7292719E-02
Jy = -6.9139404E-03	Jy = -2.8845323E-02	Jy = 2.9424673E-02	Jy = 1.8344499E-02

lat = 16 slice = 38	lat = 20 slice = 51	lat = 24 slice = 45	lat = 28 slice = 45
Jmag = 6.1962605E-02	Jmag = 3.2000240E-02	Jmag = 7.9413280E-02	Jmag = 5.5484585E-02
Jx = -1.2376941E-02	Jx = -1.4103539E-02	Jx = -3.6390271E-02	Jx = -1.1455911E-02
Jy = 2.6366208E-02	Jy = -1.6680133E-02	Jy = -2.4963932E-02	Jy = -2.0418832E-02

lat = 32 slice = 58	lat = 36 slice = 51	lat = 40 slice = 45	lat = 44 slice = 45
Jmag = 2.7207246E-02	Jmag = 6.8048976E-02	Jmag = 6.8732023E-02	Jmag = 2.9753553E-02
Jx = 9.6154017E-03	Jx = 2.3757504F-02	Jx = 1.6032716E-02	Jx = -1 1806408E-02
Jy = -1.4631883E-02	Jy = 2.7583396E-02	Jy = 2.4635529E-02	Jy = 1.6862072E-02

| lat = 48   slice = 58 | lat = 52   slice = 45 | lat = 56   slice = 51 | lat = 60   slice = 58 |
Jmag = 4.9125094E-02	Jmag = 6.9671653E-02	Jmag = 3.6017455E-02	Jmag = 3.0961690E-02
Jx = -1.7659446E-02	Jx = -1.7376587E-02	Jx = 4.9598753E-03	Jx = 5.8170208E-03
Jy = -1.7088999E-02	Jy = -2.6913762E-02	Jy = 4.3715039E-04	Jy = 3.0408710E-02

Figure 7.17 MFT estimates superimposed on the outline of the same axial MRI slices as for the average of the correlated epochs, for the correlated single epoch 53 filtered at 40-Hz in experiment L-CONTRA-EC: the darkness of the plot represents the strength of the activity and each plot is normalized separately. The sensor array is also displayed and 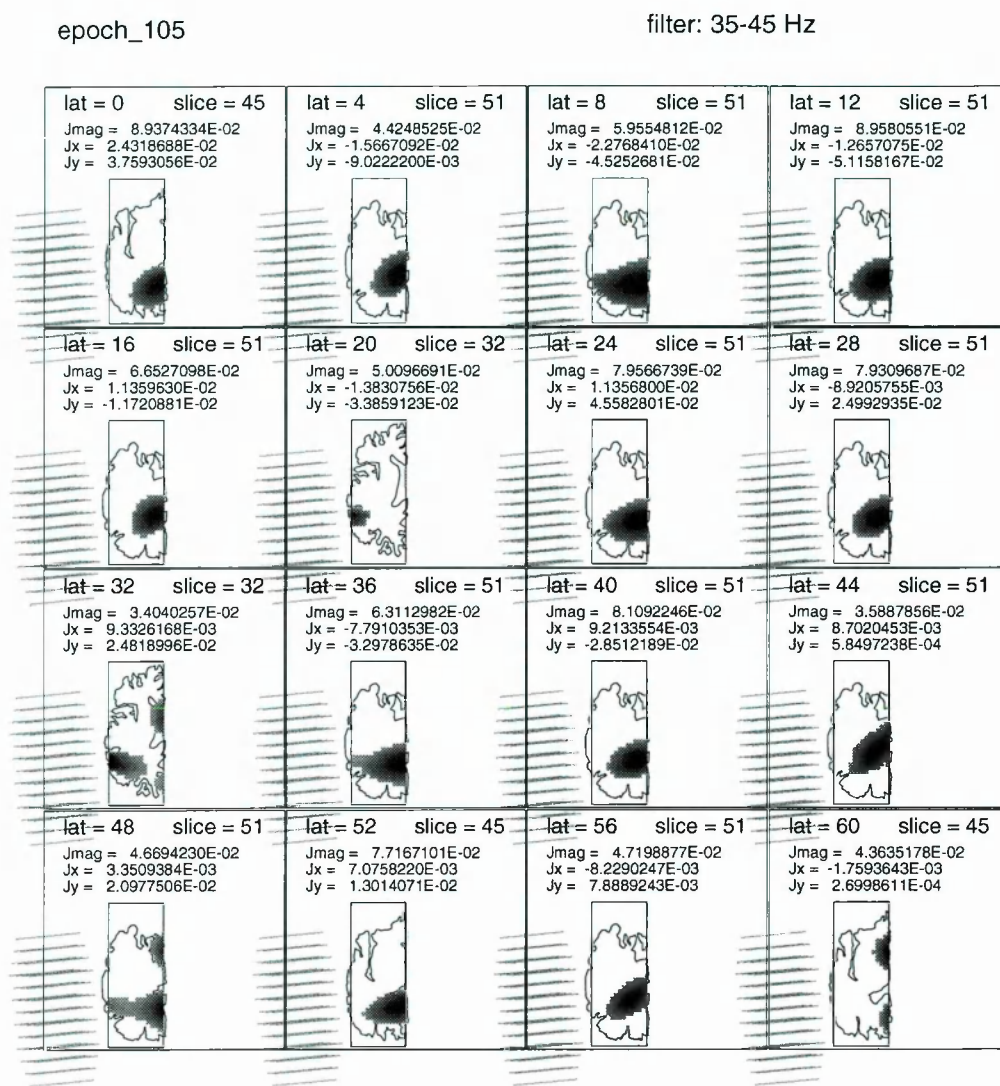represented by the lines. Notice some similarity in the interplay between superficial and deep activity as seen in Figure 7.11.
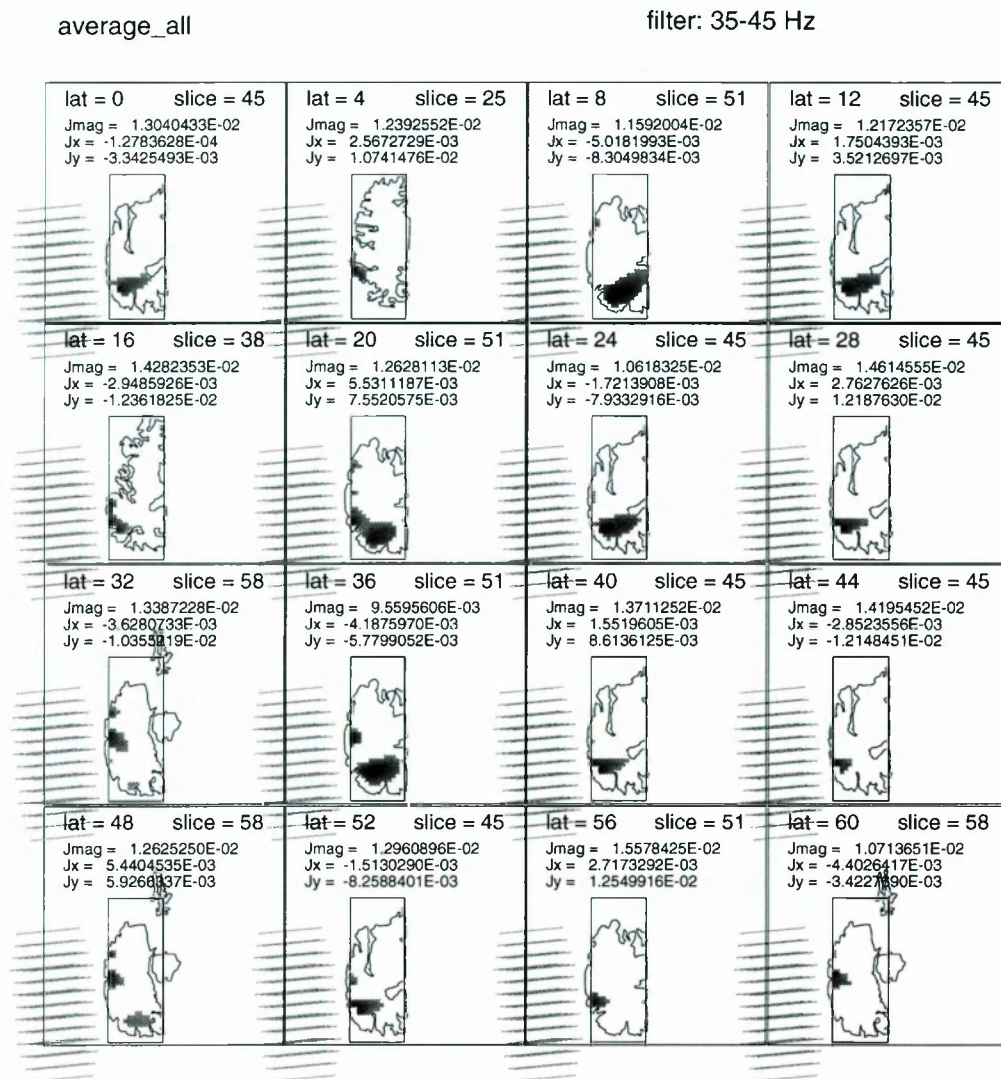
Figure 7.18 MFT estimates superimposed on the outline of the same axial MRI slices as for the average of the correlated epochs, for the correlated single epoch 105 filtered at 40-Hz in experiment L-CONTRA-EC: the darkness of the plot represents the strength of the activity and each plot is normalized separately. The sensor array is also displayed and represented by the lines. Notice some similarity in the interplay between superficial and deep activity as seen in Figure 7.11.
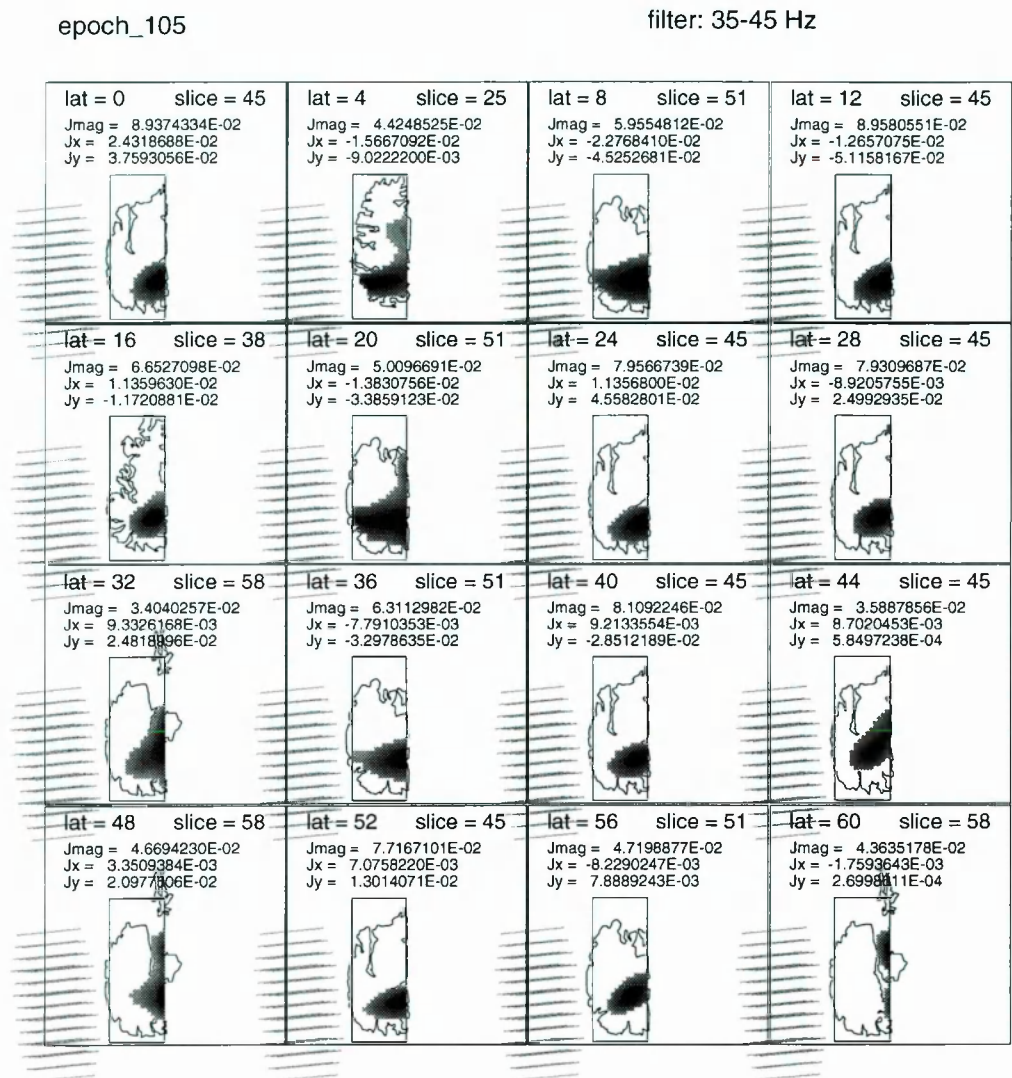
The correlation method developed in this chapter for the single epoch analysis by making use of the V_3 is of practical use, because it allows us to scan through each and every single trial very quickly and address easily the issue of how much of the single trials is represented in the average. To demonstrate this, we chose to use experiment L–CONTRA–EC as an example. Refer to Figure 6.7, there exists a prominent deflection in the average signal at around 80 ms, which is often referred to as the N100m component. Using the full MFT inversion, we identified strong superficial activity at the auditory cortex; then we applied the V_3 to the average signal, which also showed the very similar activation to that revealed by the MFT. Having identified the activation area and period in the average signal for the N100m correlation, we applied the V_3 to all the single trials in the experiment (it took us only 45 minutes to scan through the 125 single trials on a DEC ALPHA machine). Figure 7.19 shows the result for correlating the average signal from 75 to 85 ms with the 125 single trial signals from -495 to 494 ms, i.e. $\bar{t} = 75$ ms, $\Delta t = 10$ ms and $-495 \leq t \leq 494$ ms in Equations 7.2 and 7.3.

From Figure 7.19, it can be seen that (i) during the whole period, the high correlation between the average and single trials occurs well before, close to and well after the onset of the stimulus and (ii) for every single trial, the high correlation occurs at different intervals. The above observation is in agreement with the earlier comparison between the average and single trials for the 40-Hz activity, i.e., the average is not a reflection but a composition of the single trials. This is however more readily observed in the N100m study: in Figure 7.19 (a), a distinct clustering of single trials is seen around 80 ms; in (b), a distinct spike is evident which starts to rise from 61 ms and to drop to the 'normal' number (i.e. 13) of highly correlated single trials at 105 ms. The correlation peaks at 81 ms when there are 64 single trials (51.2% of all the trials) having the very similar activation to the average. From 60 to 100 ms, 82 single trials (65.6% of all) have high correlation with the average at least once. Therefore, the prominent feature of the N100m shown in the average signal can be explained by the fact that during this period, a high percentage of single trials demonstrate a similar activation pattern to that of the average.

The above results show two things – firstly, V_3 offers us a direct way of scanning through each and every single trial and identifying cortical activations which are similar to the ones picked out in the average, and allows us to make the first attempt to build up our understanding of the relationship between the average and single
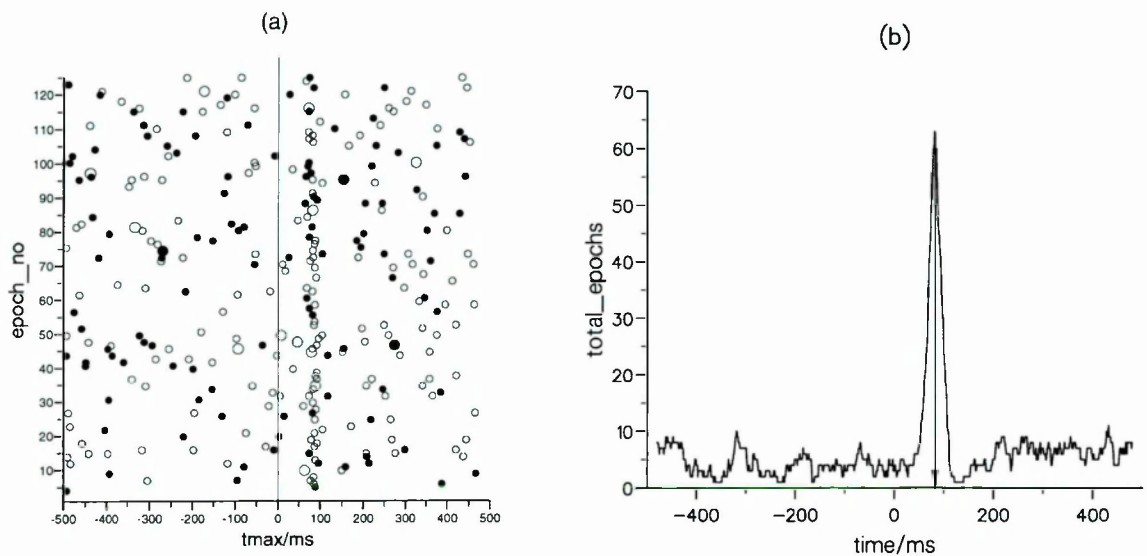
Figure 7.19 Summary for correlating the N100m in the average with those in the 125 single trial signals without any digital filtering for experiment L–CON–EC. (a) epoch summary: an empty dot corresponds to $C_1 \geq 0.85$, and a filled dot corresponds to $0.6 \leq C_1 < 0.85$. The size of the dots indicates C_2, i.e. the big dots stand for $C_2 \geq 2.0$, and the small dots are for those $1.0 \leq C_2 < 2.0$; (b) the total number of single trials having high correlation with the average (i.e., $C_1 \geq 0.6$ and $C_2 \geq 1.0$) millisecond by millisecond: the arrowed line indicates at 81 ms, there are 64 single trials (51.2 % of all the trials) highly correlated with the average.

trials in an efficient and systematic way; secondly, it demonstrates in a convincing way that the average is composed of different components originating in the single trials at different intervals, rather than reflecting the events shown in any of the single trials. Therefore, the correlation method developed in this chapter is ripe to become a routine tool of single epoch analysis.

CHAPTER 8.

BI-HEMISPHERIC AUDITORY EVOKED RESPONSE

The strongest auditory evoked magnetic fields (AEFs) recorded by MEG are generated by neural activity in the cerebral cortex. Pyramidal neurons in the Sylvian fissure are oriented parallel to each other, and thus their currents, flowing tangentially to the scalp, produce a measurable magnetic field. The supratemporal auditory cortex is optimally oriented for MEG studies. It is easy to produce auditory stimuli without causing magnetic artifacts. Consequently, AEFs are a frequent choice for MEG studies. In this chapter, auditory evoked measurements obtained from two MEG systems (the KRENIKON 37-channel system in Erlangen and the BTi twin 37-channel MAGNES probe in San Diego) are used as examples for the study of interhemispheric interplays and differences, by applying the MFT distributed source analysis to both the average and single trial signals. The single epoch analysis goes further in this chapter building up on the foundation developed in the last chapter.

8.1. Introduction

In this section we present the standard sequence of activation following the presentation of an auditory stimulus as defined by the extensive literature on neuroanatomic connections and single unit recordings. How this sequence relates to the mass electrical activity generating the MEG and EEG signal is a question which goes beyond the scope of this thesis, although some comments will be made wherever appropriate.

The auditory pathways in the brain are rather complicated, as shown in Figure 8.1:

auditory information is relayed and processed through several nuclei before it arrives at the auditory nucleus of the thalamus (medial geniculate body), which acts as a gate to the auditory cortex [7, 167]. Each cochlear nucleus (the first centre after the cochlea) sends ascending pathways up to each side of the brainstem: the pathways are bilateral.

Many neurons in the auditory system are exquisitely sensitive to differences in the properties of sounds at the two ears, e.g., neurons in a region called the superior olive (see Figure 8.1) can detect differences in the time of activation from the two ears on the order of microseconds (millionths of a second) [167]. If a sound occurs to one side of the ear, the sound waves reach the two ears at slightly different times, and the sound will also be slightly stronger at the ear closer to it. Though the majority of cells in the auditory cortex react to stimuli from both ears, different cellular groups have preferences to stimuli from either ear. Usually cells are excited by contralateral stimuli, suppressed by the ipsilateral one, and show summation or suppression responses to binaural stimuli [168]. That is, contralateral activity is generally more vigorous, of lower threshold and of shorter latency than that evoked by equivalent ipsilateral stimuli. Binaural stimuli presented with zero time delay or at equal intensities may evoke no more activity than the contralateral stimulus alone [7]. Moreover, the temporal auditory regions are known to be anatomically asymmetric: on the right the posterior regions of the Sylvian fissure arise higher, and the postcentral segments and planum temporale are smaller than on the left [169]. These anatomical asymmetries evidently explain some hemispheric differences in AEFs, though they strongly depend on the subject and the simulation characteristics, because neurons in the auditory cortex respond to the intensive, spectral and temporal characteristics of sounds. In general, the auditory cortex demonstrates tonotopy [7, 170, 168], namely, the existence of an orderly projection of frequencies onto the human auditory cortex. Sources for the AEFs are systematically increased in depth beneath the scalp with increasing frequency of the stimuli, and the tonotopic progression has a logarithmic dependance with distance along the direction at maximum change [170, 171, 60]. Moreover, the human auditory cortex demonstrates an "amplitopic" organization [172]. A neuromagnetic study for frequency and amplitude modulations of a continuous tone in the human auditory cortex was reported in [173].

An auditory stimulus activates various areas of the human brain. The specific audi-
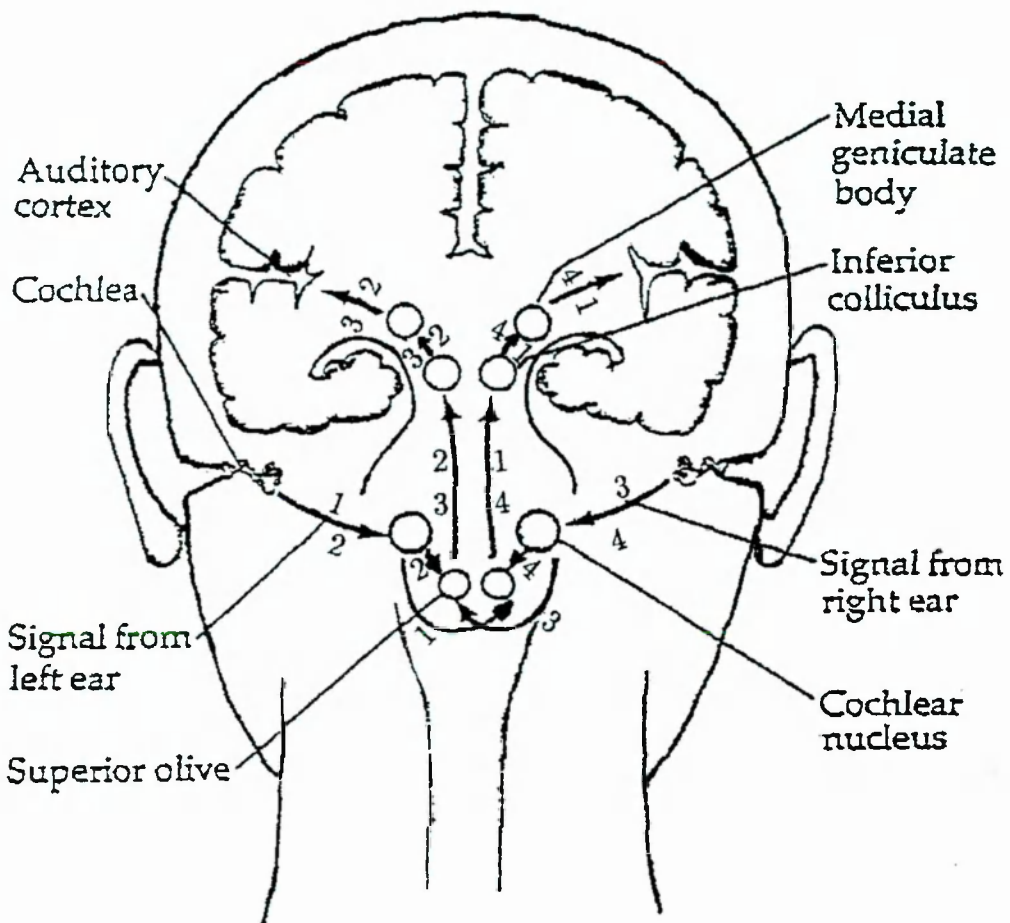
Figure 8.1 A simplified sketch of the auditory pathways: the auditory system is bilateral above the level of the cochlear nucleus, i.e., each side of the brain has input from both ears. There are several relay nuclei in the auditory pathways, but the major pathway is from the cochlear nucleus to the inferior colliculus in the midbrain, then to the medial geniculate body nucleus in the thalamus, and finally to the auditory region of the cerebral cortex. The pathway includes four possibilities, as shown in the figure, with the numbers denoting how signals (stimuli) reach the auditory cortex from both ears. Modified from [167].

tory areas are widely distributed at the temporal lobe extending from the supratemporal plane and the superior temporal gyrus to the parietal operculum and to the inferior parietal lobule [174]. In addition, very few stimuli can activate brain areas involving in the genesis of the orienting reaction, e.g., frontal cortex and hippocampus [168]. It is worth noting that auditory cortical units also fire spontaneously, in the absence of acoustic stimulation [7] (also refer to Chapter 7). On the other hand, evoked responses of the human auditory cortex may be enhanced by preceding stimuli, specially when preceded by a different tone (the adaption activity in the auditory cortex) [60, 175], and auditory attention modifies cortical activity [176, 177].

Typical auditory responses (AEFs) for the first 100 ms following the onset of the stimulus can be divided into short-latency (< 12 ms), middle-latency ($12 - 50$ ms), and long-latency (> 50 ms) responses. Short-latency responses are regarded as brainstem auditory responses and have become an indispensable, powerful diagnostic tool in both audiology and neurology [70, 178], though most AEF studies have concentrated on the large-amplitude late responses. Middle-latency responses (MLR) are characterized by several components, namely Na (mean latency 19 ms), Pa (mean latency 30 ms), Nb (mean latency 38 ms) and $P1$ (mean latency 50 ms). These components are reliable and constant in normal subjects, their origins however remain controversial [179]. A MLR study suggested that the MLR sequence may consist in part of an evoked rhythmicity with a center frequency in the range of 30-50 Hz [180]. Long-latency responses, featured by a prominent component N100m, have both stimulus-specific and nonspecific sources [181], though controversy still exists regarding the generators of the N100m [182, 179].

In this chapter, emphasis is placed on the study of interhemispheric interplays and differences. It has been long suggested that activity in the auditory cortex is the result of intrinsic cortical synaptic circuitry interacting with continuous feedback and feedforward activity of thalamo-cortical loops [7, 183]. With the advent of multichannel MEG systems (more than 100 channels), it is possible to map the responses from the whole head simultaneously and the studies of these auditory evoked responses provoke substantial interest [179, 184]. For the following discussions, we use auditory evoked measurements obtained from the two multichannel MEG systems as examples, to extract estimates of where the generators are located, responsible for the different deflections of the AEFs complex. The combination of MEG and MRI shows that the N100m is generated at or near the primary auditory

cortex, including the posterior auditory area. The ultimate goal of the analysis is to provide hints of how the left and right hemisphere interact with each other in space and time, by correlating the different activation areas in both hemispheres. In this chapter we also compare directly single trials recorded from the left and right hemisphere. To begin with, we provide the description of the experiment set-ups and source space definitions for the MFT analysis, and then proceed with the MFT analysis of the averaged and unaveraged data, including data obtained from each hemisphere at different placements and simultaneously.

8.2. Experiments

Three different sets of auditory evoked MEG measurements taken from two subjects from two MEG systems are used for the MFT analysis in this chapter. The auditory stimuli were the same for the three experiments, i.e., a simple 600 ms long, 1 kHz tone was delivered monaurally to the ear (left ear in one session and to the right ear in another session). The first experiment was carried out to measure the ipsilateral and contralateral auditory response of the left and right cortices of subject KS using the KRENIKON 37-channel MEG system [124]. During the whole recording of the 8 sensor placements, subject KS's eyes remained either open or closed (see Table 6.3). The same experiment was repeated with the same MEG system for another subject AI (a normal right-handed male; the second experiment). The third experiment was conducted to measure the bi-hemispheric auditory responses simultaneously for subject AI using the BTi twin MAGNES probe (2×37 channels). The second and third experiments were conducted in such a way as to allow a study (not described here) of the spurious effects related to eye movements (the artifacts listed in Section 3.1). To this end, subject AI's eyes were closed for a long period first (e.g 175 seconds) and then the eyes were open and closed deliberately for a short period (e.g. 45 seconds), finally the subject closed his eyes again until the end of the experiments. For ease of reference, the three experiments are labelled as (KS,ERL), (AI,ERL) and (AI,BTi) respectively.

The average signals for experiment (KS,ERL) were obtained from averaging all the artifact free epochs for the 8 sensor placements respectively (see Table 6.3), while for experiment (AI,ERL) and (AI,BTi), we will use the average signals calculated from the single trials recorded with the subject's eyes closed before the rapid eye movements, namely, the first 20 and 30 single trials for (AI,ERL) and (AI,BTi) re-

spectively.

The hemispherical source space for the MFT analysis for the experiment (KS,ERL) has been described fully in Section 6.2. Similar hemispherical source spaces are defined for subject AI in the second and third experiment, as shown in Figure 8.2. Both source spaces are divided by 9 levels for the purpose of inspection of generators obtained from the MFT analysis, and the left and right source space are overlapped at their bottom level (level 1). The relative positions of the sensors are also displayed in the figure, by comparing the experiment set-ups for experiment (KS,ERL) (refer to Section 6.2), it can be seen that the sensors were not placed as closely as those in (KS,ERL), especially for the sensor array over the left hemisphere. The sensor placements in each of the three experiments covered areas around the primary auditory cortex in each temporal region. We have retained the coordinate system used in association with each biomagnetic probe.

8.3. MFT Analysis of Averaged Data

This section aims at the analysis of auditory responses in the three sets of experiments, for the first 100 ms following the onset of the stimuli, when the source areas change slightly as a function of time. We emphasize that the MFT estimates from single trials are not expected to be too accurate in each timeslice, because of the likely influence of noise and activity from other brain areas, and specifically strong deep generators. All we wish to do for the purposes of this thesis is to compare the average and single trial MFT estimates with each other and with the known auditory pathway.

Table 8.1 lists the comparison of the average signals, V_3 and MFT estimates for the N100m generator for the 8 sensor placements in experiment (KS,ERL). The results from the table show three things – first, the average signals, V_3 and MFT estimates for the N100m response agree with each other in terms of time, position and direction. Secondly, eyes open or closed does not make significant difference for the N100m response. Thirdly, contralateral N100m responses activate generally earlier by 7-14 ms than the ipsilateral N100m, but the ipsilateral N100m takes longer latency (by 3-11 ms) to reach the peak magnitude from the appearance than the contralateral N100m. The reason for this latency difference is not known; the

(a)

(b)

(c)
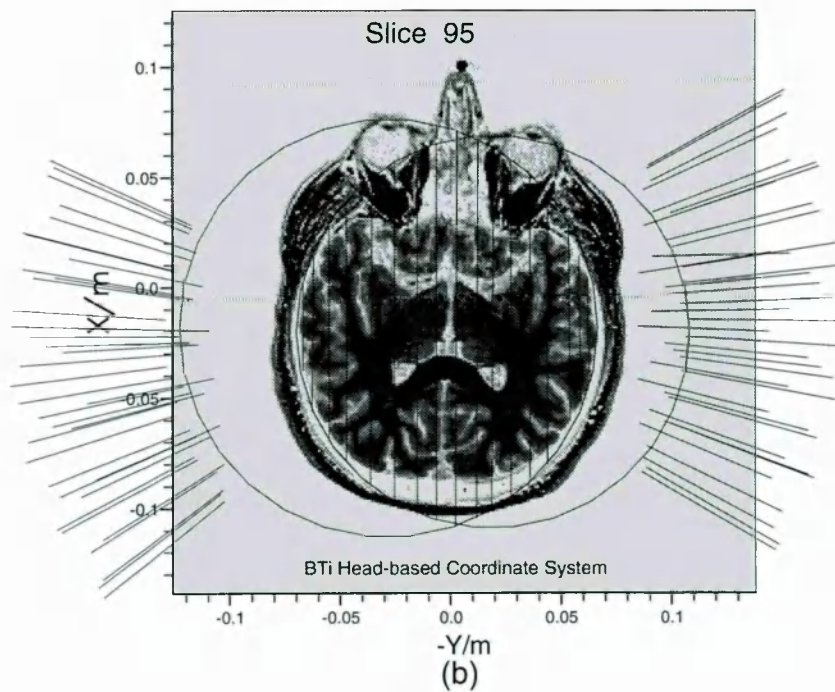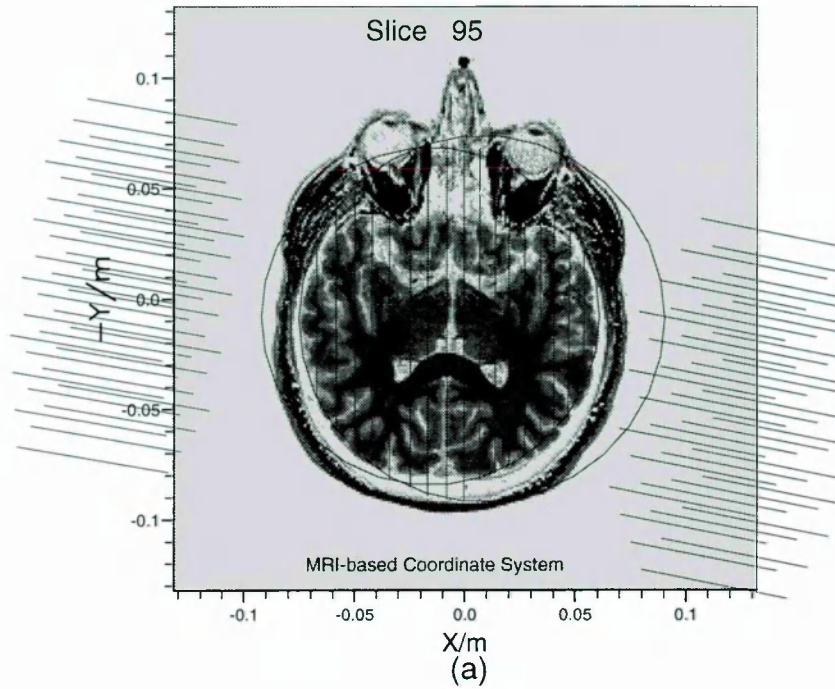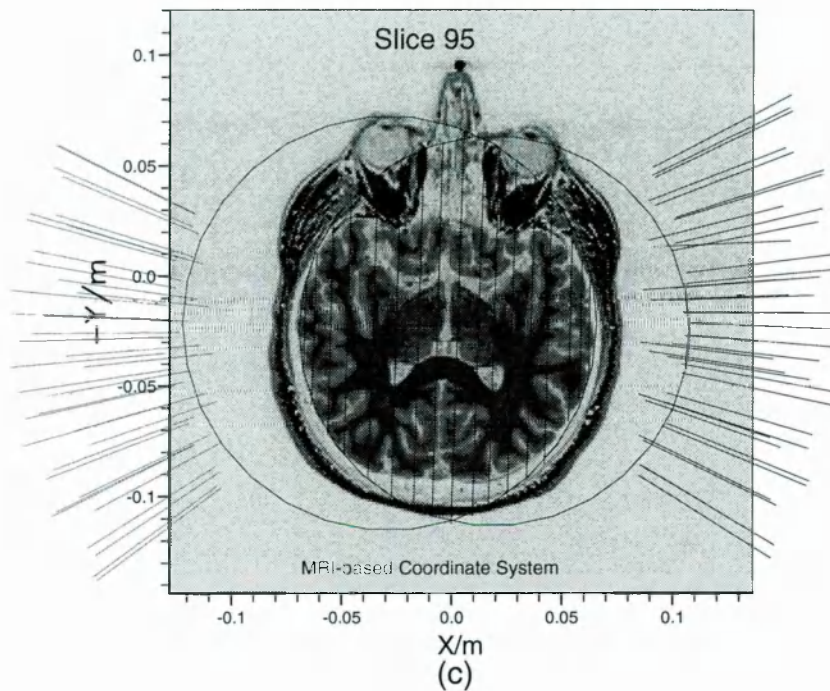
Figure 8.2 Axial view of the hemispherical source space for subject AI in two auditory evoked experiments obtained from (a) the KRENIKON 37-channel system; (b) and (c) the BTi twin MAGNES probe (2 × 37 channels). For the ease of comparison between the results from the two experiments for the same subject AI, the experiment set-up in the BTi head-based coordinate system as shown in (b) is also transformed to the MRI-based coordinate system as shown in (c).

ipsilateral response may be transferred either through ipsilateral pathways or via the contralateral auditory cortex through collosal connections [168]. Moreover, the magnitude difference between the contralateral N100m and the ipsilateral N100m in the experiment is not obvious enough to allow a definite conclusion. Thirdly, there exists a hemispheric difference for the N100m response, the generator in the left hemisphere is more posterior (1.5-2.5 cm) and lower (0.5-1.7 cm) than that in the right hemisphere, though the generators in both hemispheres are at or near the primary auditory cortex and may include posterior auditory area, and point from the back towards the front of the head. This hemispheric difference can be explained by the anatomical asymmetry of the auditory regions, as discussed earlier in this chapter. The above observations are also valid for another subject AI in the two experiments (AI,ERL) and (AI,BTI). Table 8.2 and 8.3 show the N100m response obtained from subject AI (eyes closed) with the KRENIKON 37-channel system and the BTi twin MAGNES probe (2×37 channels). As mentioned earlier, the sensors in these two experiments were not placed as close to the auditory cortex as those in the first experiment, especially for the left hemisphere. As a result, the signal-to-noise ratio is necessarily higher, e.g., V_3 estimates for the generator may not be as accurate as in the first experiment, because V_3 offers crude estimation of superficial sources below the sensors, in this case, the closer the sensors to the sources, the better results yield from V_3 (see Chapter 6). In addition, the results are not so uniform as shown in Table 8.1, e.g., the direction of the N100m does not always point towards the front of the head, it may point towards the neck.

To examine the MFT estimates in space, the estimates are superimposed on the subject's 3D MRI slices. For experiment (KS,ERL), with a view to covering all the placements in the experiment, we chose to display the results: (i) in axial view using the stimulus delivered to the left ear with the subject's eyes closed (see Figure 8.3) and the stimulus delivered to the right ear with the subject's eyes open (see Figure 8.4), and (ii) in coronal view, using the the stimulus delivered to the left ear with the subject's eyes open (see Figure 8.5). Though the MFT estimates are well capable of revealing the brain activity millisecond by millisecond, we choose to display the estimates integrated over 5 ms to eliminate small, probably noisy variations. All the display is from the onset of the stimulus to 90 ms onward, by a step of 5 ms, hence covering the short-, middle- and long-latency responses. Each icon consists of separate left and right axial MRI semi-slices (i.e., Lmri and Rmri), each selected automatically by the software to include the MFT maxima of the corresponding

		Ipsilateral		Contralateral	
		open	closed	open	closed
Left Hemisphere					
Signal	Tmax(ms)	89	92	79	76
	ch.(no)	11	11	18	18
	mag(pT)	49.3	50.9	56.6	53.4
V_3	Tmax(ms)	89	90	80	80
	pos.(cm)	-6.59, 7.30, 2.48	-6.59, 7.30, 2.48	-6.47, 7.73, 2.77	-6.47, 7.74, 2.77
	dire.(x,y)	-0.18, -0.98	-0.16, -0.99	-0.15, -0.99	-0.14, -0.99
	mag(10^{-12}fT/m)	75.4	70.5	83.1	77.9
MFT	Tmax(ms)	89	89	80	78
	pos.(cm)	-6.04, 7.50, 3.52	-6.04, 7.50, 3.52	-6.04, 8.55, 2.47	-6.04, 8.55, 2.47
	dire.(x,y,z)	-0.20, -0.98, -0.08	-0.14, -0.99, -0.10	-0.36, -0.93, 0.10	-0.35, -0.93, 0.09
	Jmag(a.u.)	0.931	0.921	0.476	0.462
Right Hemisphere					
Signal	Tmax(ms)	96	90	89	77
	ch.(no)	8	12	8	12
	mag(pT)	48.3	45.3	44.2	50.6
V_3	Tmax(ms)	97	84	86	85
	pos.(cm)	6.89, 5.13, 1.47	6.89, 5.13, 1.47	6.89, 5.14, 1.47	6.89, 5.13, 1.47
	dire.(x,y)	0.49, -0.87	0.66, -0.75	0.62, -0.79	0.53, -0.85
	mag(10^{-12}fT/m)	64.7	70.1	57.4	69.0
MFT	Tmax(ms)	87	88	80	74
	pos.(cm)	5.96, 6.27, 1.89	5.96, 6.27, 1.83	5.96, 5.20, 1.95	5.96, 6.27, 1.89
	dire.(x,y,z)	0.34, -0.94, 0.04	0.11, -0.99, 0.12	0.66, -0.74, -0.08	0.49, -0.87, 0.05
	Jmag(a.u.)	0.503	0.528	0.451	0.495

Table 8.1 Comparison of the average signals, V_3 and MFT estimates for the N100m generator for the 8 sensor placements in experiment (KS,ERL). The MFT estimates are given in the MRI-based coordinate system (refer to Figure 6.6). The unit of *Jmag* is arbitrary (a.u.).

		Ipsilateral		Contralateral	
		Left Hemi.	Right Hemi.	Left Hemi.	Right Hemi.
Signal	Tmax(ms)	102	94	40	83
	ch.(no)	23	20	18	18
	mag(fT)	32.4	46.4	47.1	75.1
V_3	Tmax(ms)	92	93	78	82
	pos.(cm)	-6.74, 2.35, 0.02	5.80, 1.58, -0.39	-6.37, 2.13, 0.23	5.62, 1.88, -0.16
	dire.(x,y)	0.28, -0.96	-0.18, -0.98	0.82, 0.57	-0.18, -0.98
	mag(10^{-12}fT/m)	30.0	69.3	54.2	10.0
MFT	Tmax(ms)	93	93	85	83
	pos.(cm)	-6.69, 2.87, 0.37	5.41, 2.11, -0.61	-6.69, 2.14, 0.37	5.41, 1.81, -0.61
	dire.(x,y,z)	0.85, -0.38, 0.37	-0.38, -0.91, 0.18	-0.97, -0.24, -0.05	-0.29, -0.93, 0.21
	Jmag(a.u.)	1.405	1.273	1.003	1.625

Table 8.2 Comparison of the average signals, V_3 and MFT estimates for the N100m generator for experiment (AI,ERL) with the subject's eyes closed. The MFT estimates are given in the MRI-based coordinate system (refer to Figure 8.2(a)).

		Ipsilateral		Contralateral	
		Left Hemi.	Right Hemi.	Left Hemi.	Right Hemi.
Signal	Tmax(ms)	69	97	96	98
	ch.(no)	12	5	22	5
	mag(fT)	20.9	41.4	23.0	61.3
MFT	Tmax(ms)	87	97	89	79
	posA.(cm)	-2.20, 6.28, 7.93	1.29, -6.35, 6.96	-2.20, 6.28, 7.94	1.29, -6.37, 8.10
	posB.(cm)	-6.30, 2.40, 0.23	6.11, 1.35, -0.46	-6.31, 2.38, 0.34	6.19, 1.37, -0.70
	dire.(x,y,z)	0.12, -0.29, -0.97	-0.42, -0.27, 0.85	0.83, -0.06, -0.55	-0.86, -0.30, 0.41
	Jmag(a.u.)	0.225	0.281	0.255	0.462

Table 8.3 Comparison of the average signals and MFT estimates for the N100m generator for experiment (AI,BTI) with the subject's eyes closed. For easy comparison with experiment (AI,ERL), the MFT estimates are given in the BTI head-based coordinate system (posA.) and the MRI-based coordinate system (posB.) by co-registrating the two coordinate systems (refer to Figure 8.2(b) and (c)).

experiment.

Figure 8.3 and Figure 8.4 are the axial view of the MFT estimates superimposed on the actual MRI slice outlines of the left and right hemisphere. The MRI slices are numbered from 1 to 93, pointing from the head to the foot, where slice 1 is through the crown of the head at a z value of -4.53 cm. The figures show: for the short-latency response (< 12 ms), for the ipsilateral side of the stimuli, there is a very short period of lateral activity followed by the central and low activity (i.e. slice 58-71), while the contralateral side activates at higher positions (i.e. slice 21-28). The activities observed in this latency range in general are of small amplitude in comparison with later deflections in the signal, hence sophisticated experimental techniques are necessary for reliable signal detection. This is in good accordance with the short-latency AEFs study in [178], in which these AEFs were referred to as brainstem auditory responses and mainly generated in the central area of the brain. For the middle-latency response (12 – 50 ms), activities are seen more towards the lateral side, especially for the contralateral side of the stimuli, i.e., a trend towards the lateral auditory cortex: the deflection at about 30 ms is seen at the inside edge of the auditory cortex. This observation is also in agreement with the middle-latency auditory response study in EEG [179] and in MEG [184]. It is worthy of note that during the middle-latency response, in comparison with Figure 7.11, a striking similarity between these two figures (for the left hemisphere) can be seen, indicating that 40-Hz activity observed in the average may correspond to resetting of an ongoing spontaneous process. For the long-latency response, based on the discussion of the N100m response in the previous section, focus is placed on the trace and pin-point the source(s) for the N100m. From the two figures, two things are clearly seen, first is the activities in both hemispheres reach the peak amplitude for each hemisphere within 90 ms following the onset of the stimulus, and second, the contralateral N100m appears and focuses in space earlier than the ipsilateral N100m. The location of N100m is very similar to the P30m, only is more lateral and slightly posterior in the auditory cortex, similar to the studies in [182, 179, 184]. It is interesting to note that before the main deflection in the signal occurs (e.g, at about 65 ms, when the prominent N100m starts to appear), the comparative activity strength for the left and right hemisphere is reversed with each other. Take Figure 8.3 for instance. Before t =65 ms, $Lmag$ is smaller than $Rmag$, however afterwards, $Lmag$ changes into the bigger one. This is also true for Figure 8.4. Therefore, it is not necessary true that the contralateral activity is stronger than the ipsilateral activity.

To make comparison easier with the auditory pathways shown in Figure 8.1, especially the link between the left and right hemisphere, we superimpose one case of the experiment (KS,ERL) on the coronal outline of the brain, as shown in Figure 8.5. Unfortunately, we can not superimpose the MFT estimates on the actual coronal outlines of the brain, because only the axial MRI slices have been taken for the subjects and at the time of writing, the facility of interpolating MRI slices in 3D is not available yet at the Open University. Hence, we can only superimpose the MFT estimates on the coronal outline of the brain at a fixed slice (obtained from interpolation of an axial slice). The coronal MRI slices are assumed to start from slice 1 to 256, beginning from the front and moving to the back of the head with increasing index and slice 127 roughly at the origin of the MRI-based coordinate system (see Appendix A). Therefore, the bigger slice number referred to in Figure 8.5, corresponds to the more posterior part of the brain. With this definition, the fixed MRI slice for the coronal outline is slice 191 at a y value of 6.6 cm, roughly the intersection slice between the yz plane and the activation position of the N100m in the primary auditory cortex on the left side (refer to Figure 6.6). There is no doubt that the superimposition on a fixed outline is not so accurate as on actual coronal outlines, it is however appropriate provided that the actual slices of the activation areas are not too far away from the fixed slice, e.g., 4 cm on the either side of slice 191 (about 40 slices, inter-slice distance is 1.0 mm in y direction). Figure 8.5 shows the organization of the auditory pathways on broad agreement with those proposed in [7]: shortly after the onset of the stimulus, much deep and central activity observed on the ipsilateral side of the stimulus (left in this case). Then this activity crosses to the right hemisphere as well (t =30-35 ms) and both hemispheres activate simultaneously in depth and lower part of the brain (brainstem). The left hemisphere continues to show activity in the similar area, while the right hemisphere extends its activity from the central area to more lateral area (t =35-40 ms) and then activates at the auditory cortex. Only when the N100m starts to appear (t =65 ms), the activity of the left hemisphere focuses on the auditory cortex. During the first 100 ms auditory responses, the deep and central part of the left hemisphere activates as though it is the origin of the sequence of activities occurring in the left and right hemispheres. This observation is also valid for the stimulus delivered to the right ear, as indicated in Figure 8.6, showing the MFT estimate as a depth function over time for four sensor placements in experiment (KS,ERL). The strength of the activity is indicated by the grey level of the plot. From the figure, it can be seen that

Figure 8.3 MFT estimates superimposed on the actual MRI slice outlines of the left and right hemisphere for experiment (KS,ERL) with the stimulus delivered to the left ear and the subject's eyes closed: the square represents the intersection of a box containing the hemispherical source space with the half axial slice displayed.
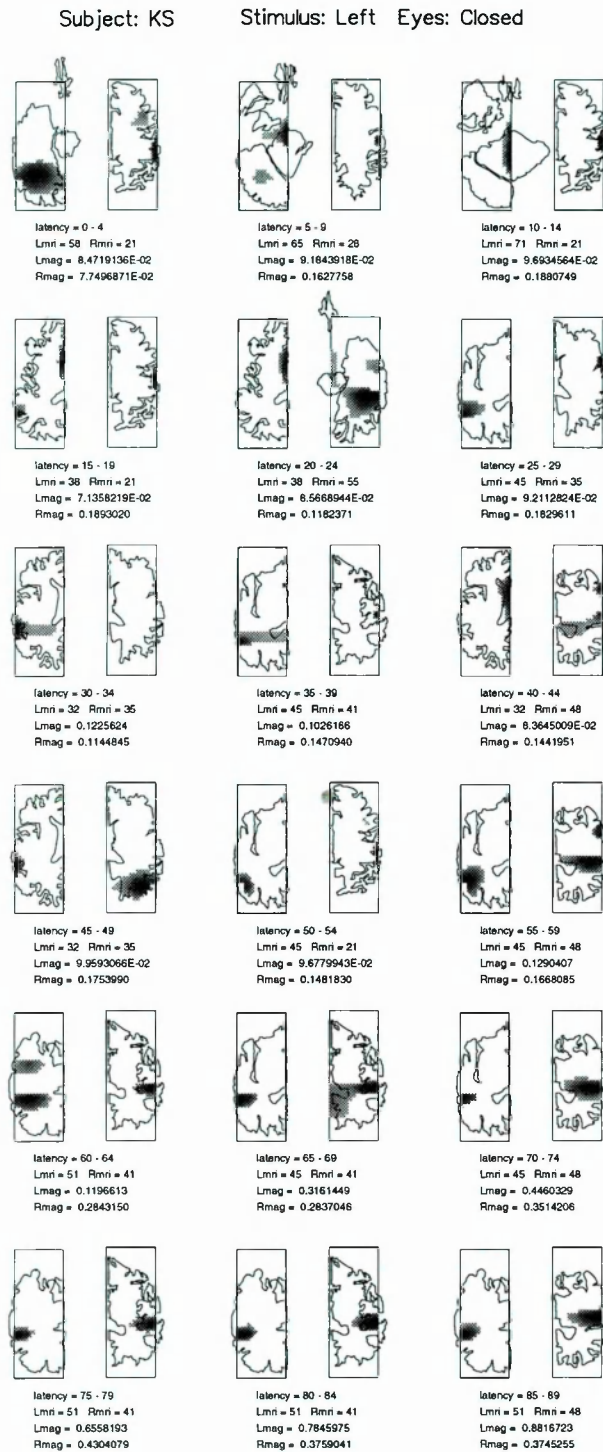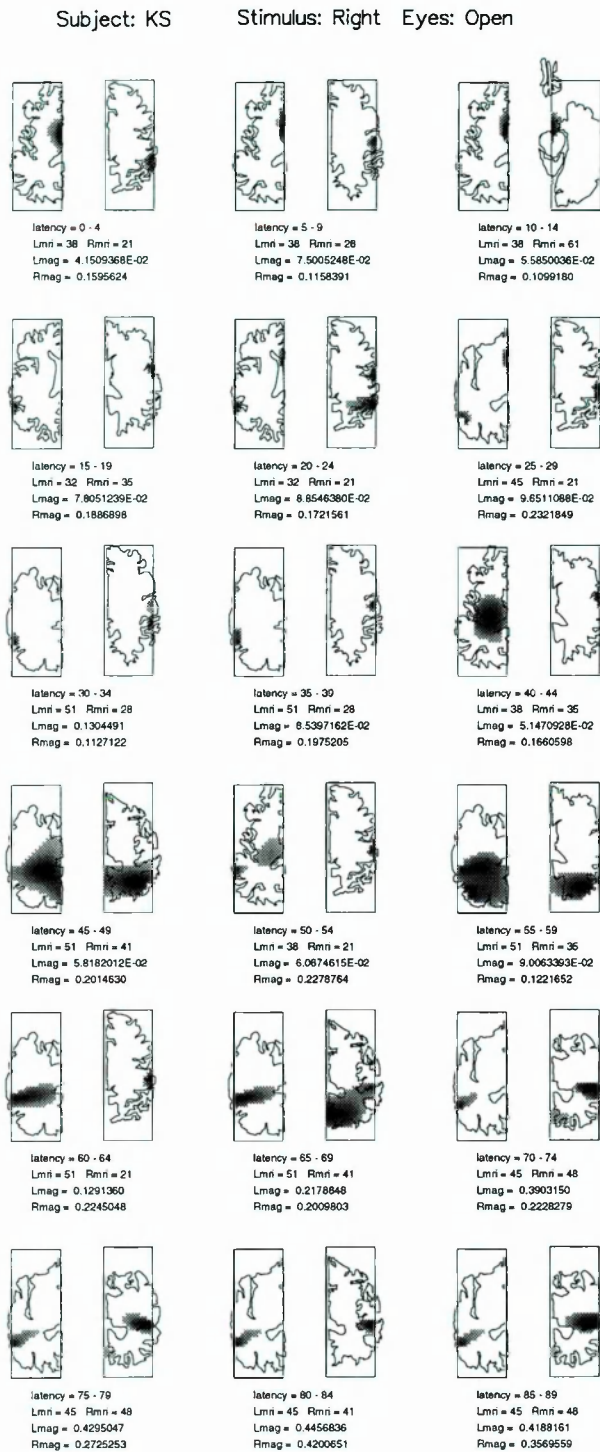
Figure 8.4 MFT estimates superimposed on the actual MRI slice outlines of the left and right hemispheres for experiment (KS,ERL) with the stimulus delivered to the right ear and the subject's eyes open: the square represents the intersection of a box containing the hemispherical source space with the half axial slice displayed.

deep activity appears first in the hemisphere of the stimulus side soon after the onset of the stimulus, followed by the simultaneous deep activities at the center of both hemispheres, and finally the strong and superficial nature of the N100m response is evident.

In order to testify the generality of the above conclusions made from the experiment (KS,ERL) and to investigate the inter-subject differences, we superimpose the MFT estimates for the very similar experiment conducted for another subject (AI,ERL) on the actual axial MRI outlines, as shown in Figure 8.7. The axial MRI slices are numbered from 44 to 136, pointing from the head to the foot, with slice 44 through the crown of the head at a z value of -4.53 cm. In comparison with Figure 8.3, in general the observations seen in Figure 8.3 are also valid for Figure 8.7, except that the activities for subject AI are in slightly higher positions and more frontal activities are seen in the left hemisphere, within the known inter-subject variability, e.g., right or left handed, long or round face, male or female and so on [182]. Additionally, the sensors were placed in a much frontal place in experiment (AI,ERL) than (KS,ERL) (see Figure 6.9 and Figure 8.2), especially for the left hemisphere, hence more frontal activities may be picked up by the sensors, while more posterior ones missed.

The above two experiments (KS,ERL) and (AI,ERL) were conducted with the KRENIKON 37-channel system, which can only cover one side at a time of the head for each placement. The only way to study the relationship between left and right hemisphere activity is to record simultaneously over each hemisphere; we have therefore used the BTi twin 37-channel MAGNES probe and recorded the bi-hemispheric auditory response simultaneously, i.e., experiment (AI,BTi). The experiment was conducted as an addition to a scheduled set of measurements under less than optimal conditions. In particular, the head shape outline was only recorded once, and the dewar position prevented us from recording all five points required by the BTi software for later co-registration with MRI. The net effect was that the co-registration accuracy is limited and we therefore do not show the MFT solutions in the background of MRIs, but only in relation to the sensors (which of course we know accurately) and an estimate of the head outline. Our interest in this thesis is the relationship between distant areas across the midline, which is not greatly influenced by the unfortunate limitation in co-registration accuracy. Figure 8.8 shows the MFT estimates superimposed on the axial headshape outline for the
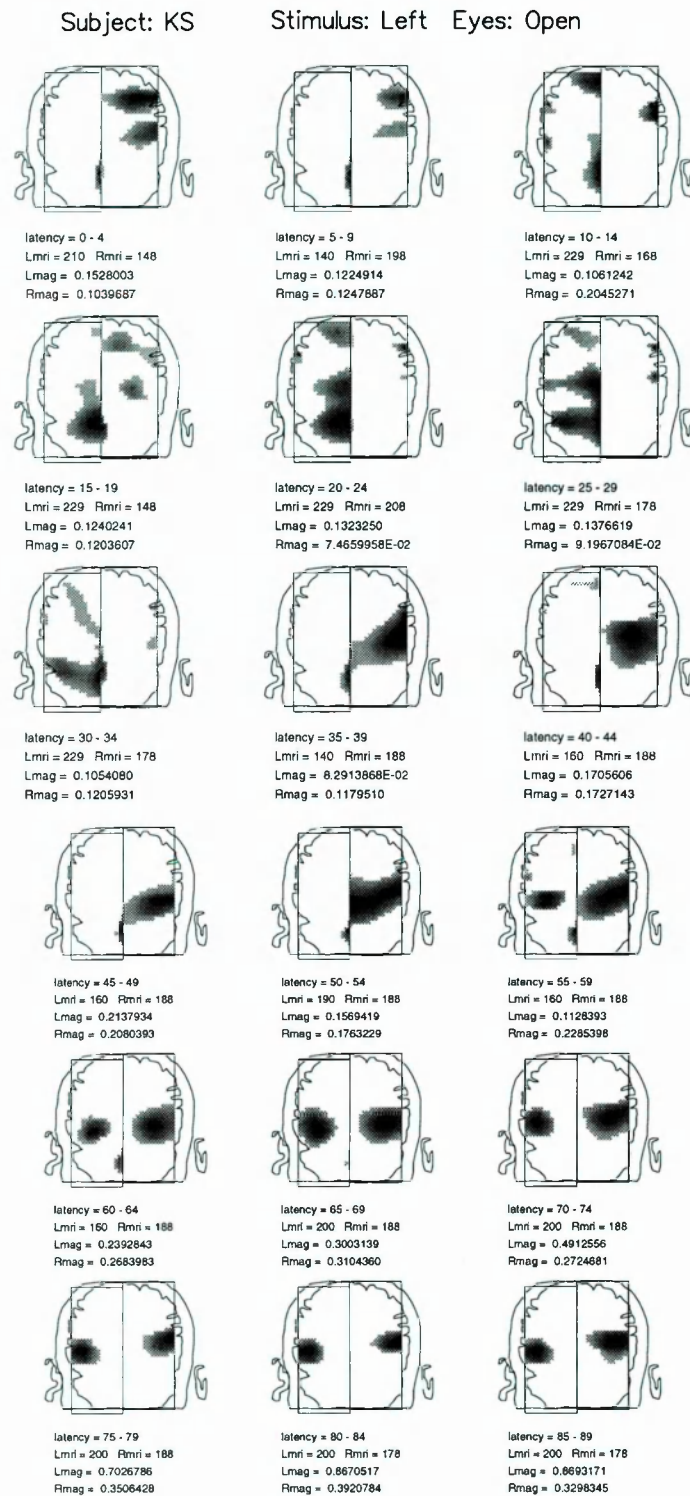
Figure 8.5 MFT estimates superimposed on a fixed coronal MRI slice outline for experiment (KS,ERL) with the stimulus delivered to the left ear and the subject's eyes open: the square represents the intersection of a box containing the hemispherical source space with the half coronal slice displayed.
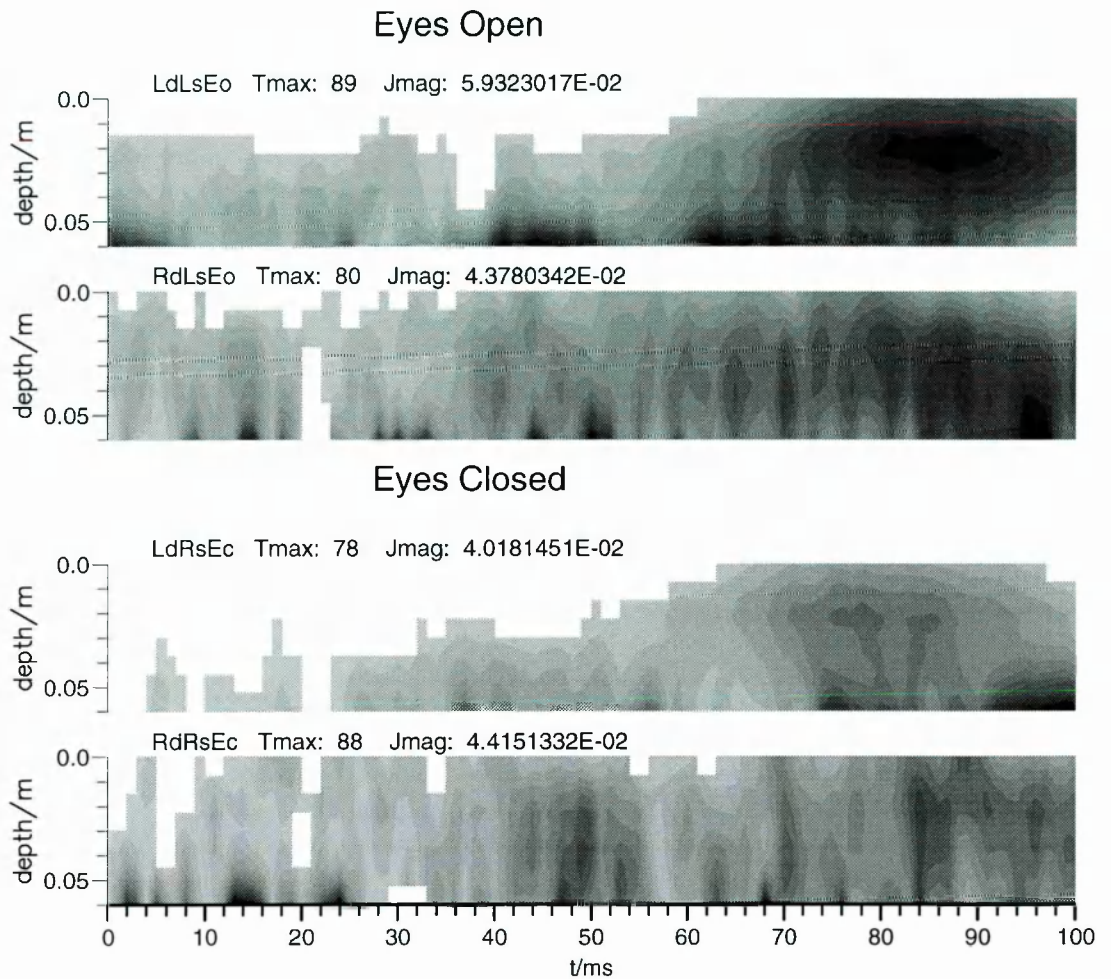
Figure 8.6 MFT estimates plotted as a depth function over time for four sensor placements in experiment (KS,ERL): the depth indicates the distance from the superficial level (level 9). The dewar side, stimulus side, and eyes condition are suffixed by the small letter d, s and o/c respectively. Notice the deep activity at the ipsilateral side of the stimuli first, followed by the simultaneous deep activities at both hemispheres, and finally the strong and superficial N100m response.

Figure 8.7 MFT estimates superimposed on the actual MRI slice outlines of the left and right hemispheres for experiment (AI,ERL) with the stimulus delivered to the left ear and the subject's eyes closed: the square represents the intersection of a box containing the hemispherical source space with the half axial slice displayed.
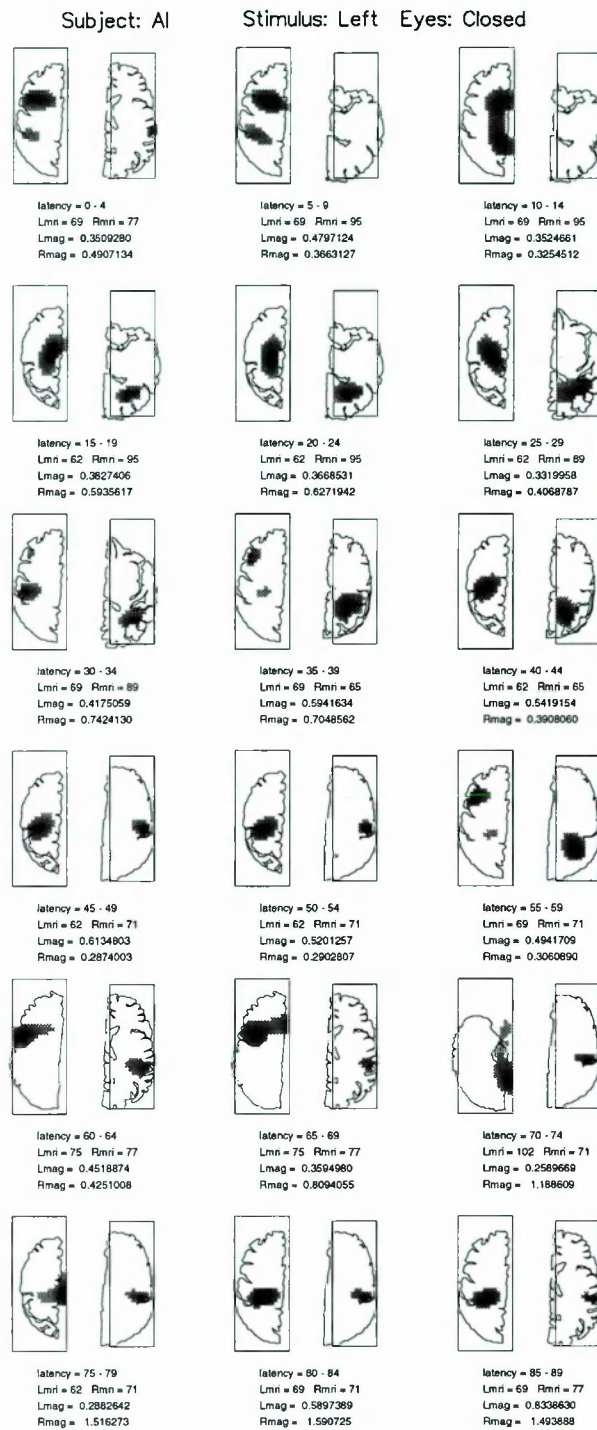
stimulus delivered to the left ear and the subject's eyes closed. The slice number quoted in the figure is based on the MRI numbering system in experiment (AI,ERL). The results in the figure are in broad agreement with the observations made from the first two experiments. In addition it provides direct evidence concerning the hemispheric interplays and differences: deep and central activities are first seen in the left hemisphere, then these activities extends to the central part of the right hemisphere, followed by the prominent N100m responses at the lateral and superficial level of both hemispheres, and finally both hemispheres activate at the central areas again.

8.4. MFT Analysis of Unaveraged Data

In this section the single epoch analysis is extended to the unaveraged data without any digital bandpass filtering obtained from the last two experiments (AI,ERL) and (AI,BTi). The analysis aims at establishing the connection between the average and single trial signals, and the link between the left and right hemisphere in space and time by correlating the sequence of activations in both hemispheres. Since the uncertainty in depth is considerably higher, we will focus on descriptions of superficial activation.

Figure 8.9 shows the MFT estimates for experiment (AI,ERL): integrals of intensity over 12 ms and transitions ms by ms for the first 100 ms following the onset of the stimulus, for superficial sagittal slices at the level of the right auditory cortices, with the stimulus delivered to the right ear. The first row show the MFT estimates extracted from the average signal, while the other six rows are for the single epochs. Darker shades represent stronger activity, with the relative normalization factors, computed for all the signals and timeslices, printed in each window. Two main activation areas, A_1 where $y = 2$cm, $z = 0$cm and A_2 where $y = 4$cm, $z = 4$cm are identified in both the average and single trials. It is interesting to note that for the average during the first 50 ms, the main activation area is A_2 and then switches to A_1 for the next 50 ms: another evidence for the different sources for P30m and N100m. As pointed out in Section 7.3, it is the order and precise time of activation area that counts for the correlation between the average and single trial signals. From the figure, it can be seen that for each integration period, there is at least one single epoch behaving similarly to the average (consistent with the 5-10% figure found earlier), i.e., in different intervals different epochs are similar to the average; however the

Subject: AI   Stimulus: Left   Eyes: Closed
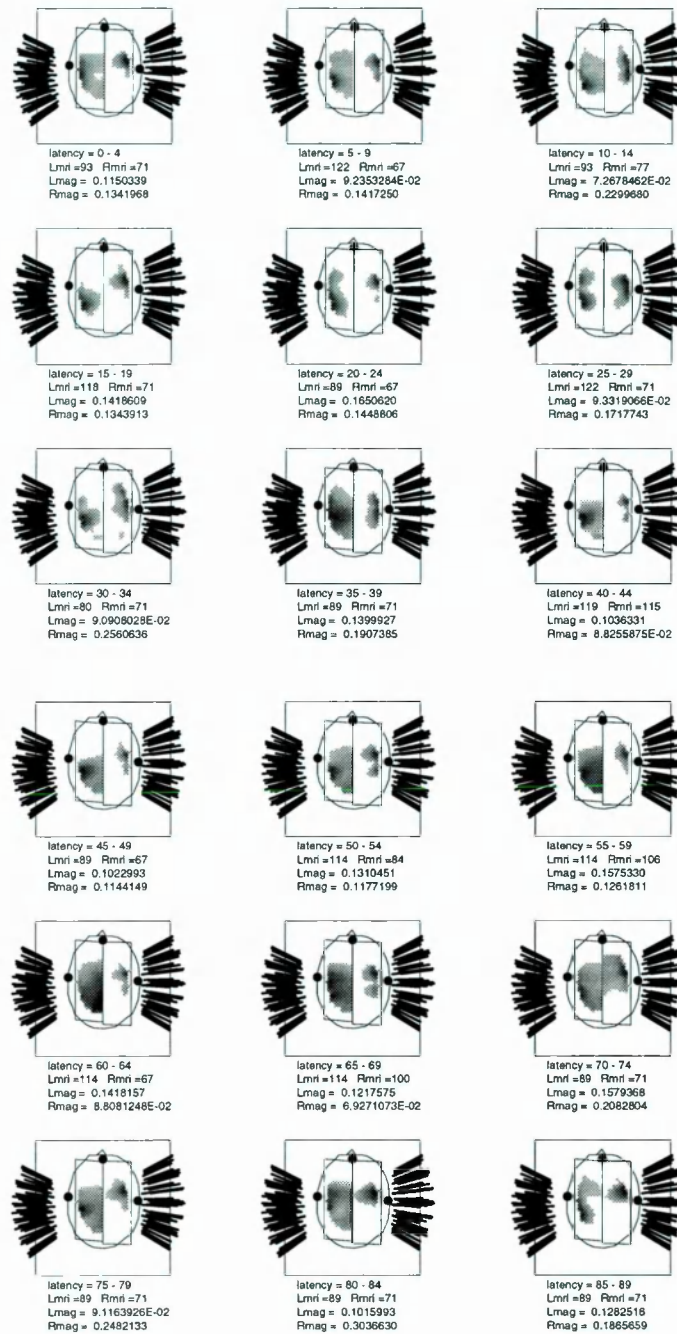
Figure 8.8 MFT estimates superimposed on the axial headshape outline for experiment (AI,BTi) with the stimulus delivered to the left ear and the subject's eyes closed: the dark dots represent the left periauricular point, nasion, right periauricular point in clockwise and the thick lines indicate the sensor positions and orientations; the square represents the intersection of a box containing the hemispherical source space with the head shape outline displayed.

single trial signals also show high variability, i.e., the difference between the average
and single epochs, and among the single epochs confirms the observation made from
Figure 7.8, that is, integrals over short period show high variability, especially when
the integration period is less than 25 ms. As the integration period increases, the
agreement between the average and the single trials tends to more prevailing. This
is demonstrated by the following two integrals of intensity for the MFT estimates for
experiment (AI,BTi) over 30 ms (Figure 8.10) and 100 ms (Figure 8.11) respectively,
which also show the interhemispheric difference. Both figures are shown in a similar
way as Figure 8.9, except that the relative normalization factors are computed sep-
arately for each hemisphere and the stimulus was delivered to the left ear. Figure
8.10 shows the integrals of intensity over 30 ms and transitions every 10 ms for the
first 120 ms following the onset of the stimulus, and Figure 8.11 shows the integrals
of intensity over 100 ms and transitions every 50 ms for the first 400 ms following
the onset of the stimulus. By comparing these two figures with Figure 8.9, it is clear
that the agreement between the average and single trial signals increases with the
integration period; and when the intensity is integrated over 100 ms, the agreement
is excellent, though the shifts in activity are similar but not identical, because a
small but definite variability is evident from trial to trial. The above observations
strongly suggest that the "sequence of events" in the average is not identical to that
in single trials and hence the average can only represent the evolution of events in
single trials in a statistical way.

Comparing the interhemispheric differences in the integrals of intensity over long
periods, as shown in Figure 8.10 and Figure 8.11, it can be seen that for the cortical
auditory activity, the main activation area in the left is slightly posterior than that
in the right hemisphere, by 2-3 cm. The activity in the right hemisphere tends to
be more focused than the left one when the integration is over 50 ms. In order
to obtain better understanding of how the left and right hemisphere interacts with
each other and the how the different parts of the brain correlate with each other in
the sequence of event extracted from the MFT estimates, we need to investigate the
MFT estimates level by level.

Figure 8.12 is a contour cylinder plot showing how the activity in the left and right
hemisphere changes at the 3 superficial levels of the hemispherical source space over
the first 50 ms following the onset of the stimulus delivered to the left ear: the first 3
rows are for the left hemisphere and the rest of the 3 rows are for the right one; the

Figure 8.9 Intensity integrals over 12 ms for MFT estimates of the average and single trial signals without any digital filtering in experiment (AI,ERL). The stimulus was delivered to the right ear and the dewar was over the right temporal area with the eyes closed: viewed from outside the brain with the head up and the nose medial, and the circle delineating the intersection of the hemispherical source space. Notice the high variability of the single epochs.
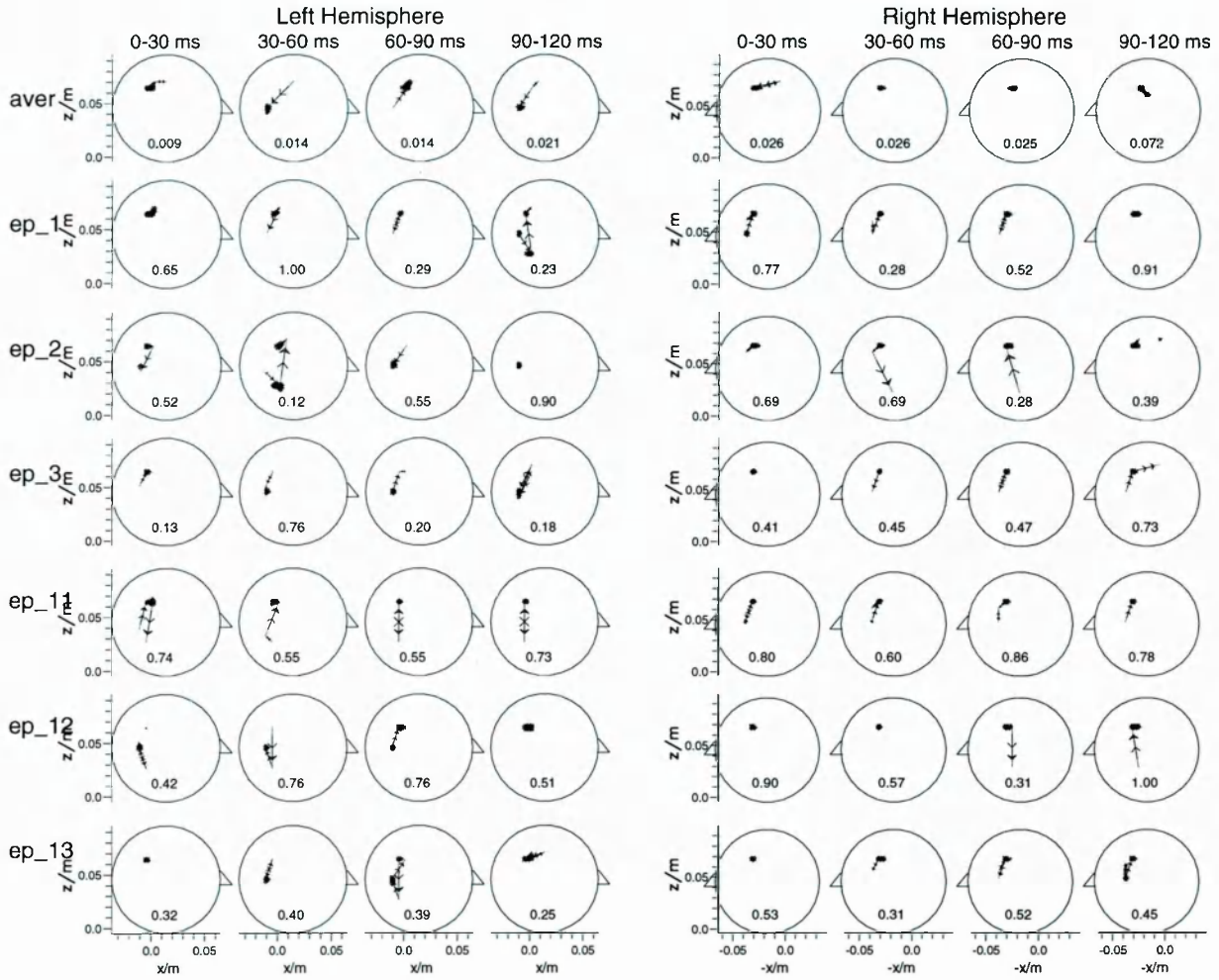
Figure 8.10 Intensity integrals over 30 ms for MFT estimates of the average and single trial signals without any digital filtering in experiment (AI,BTi). The stimulus was delivered to the left ear with the eyes closed: viewed from inside the brain with the head up and the nose medial, and the circle delineating the intersection of the hemispherical source space. Notice the improved agreement between the average and single trials.
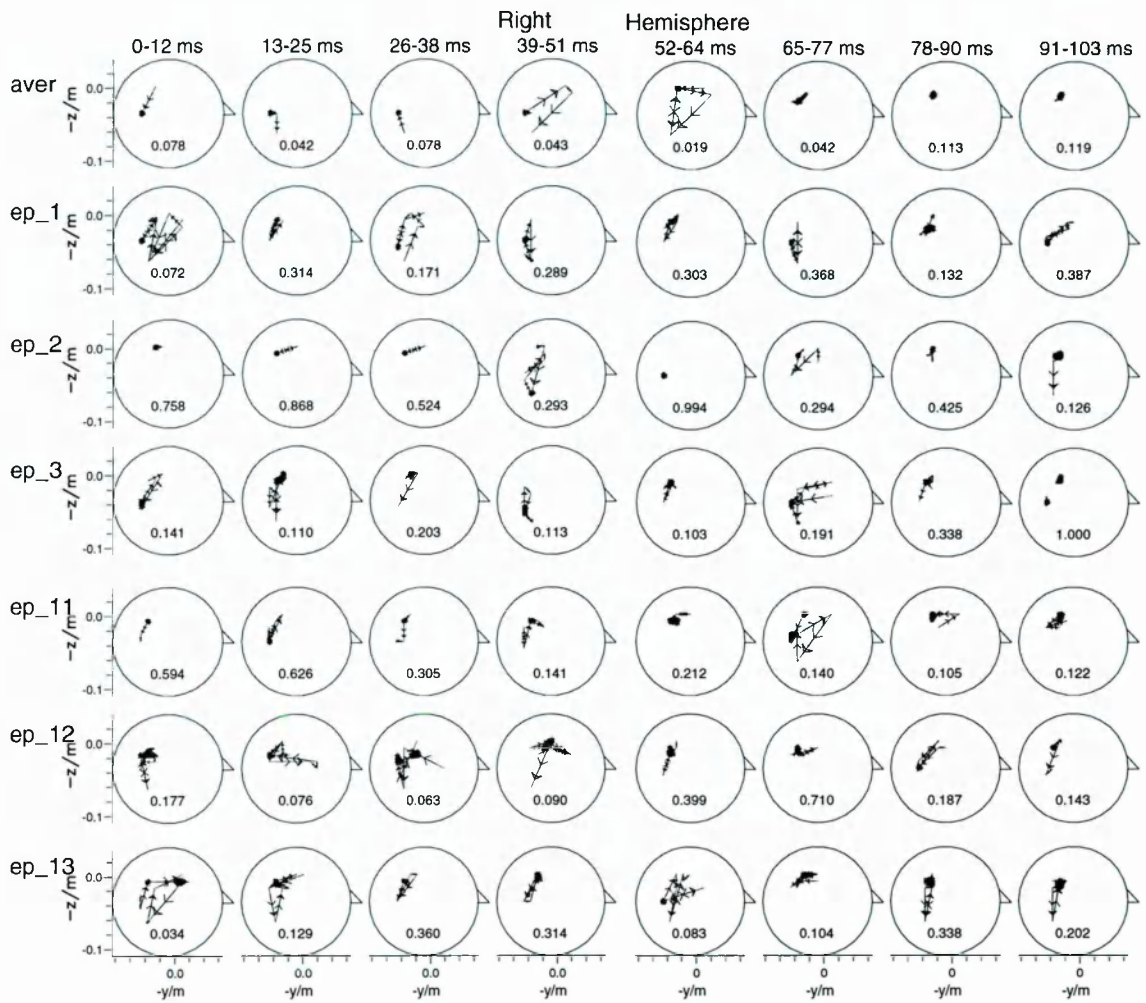
Figure 8.11 Intensity Integrals over 100 ms for the MFT estimates of the average and single trial signals without any digital filtering in experiment (AI,BTi). The stimulus was delivered to the left ear with the eyes closed: viewed from inside the brain with the head up and the nose medial, and the circle delineating the intersection of the hemispherical source space. Notice the good agreement between the average and single trials.
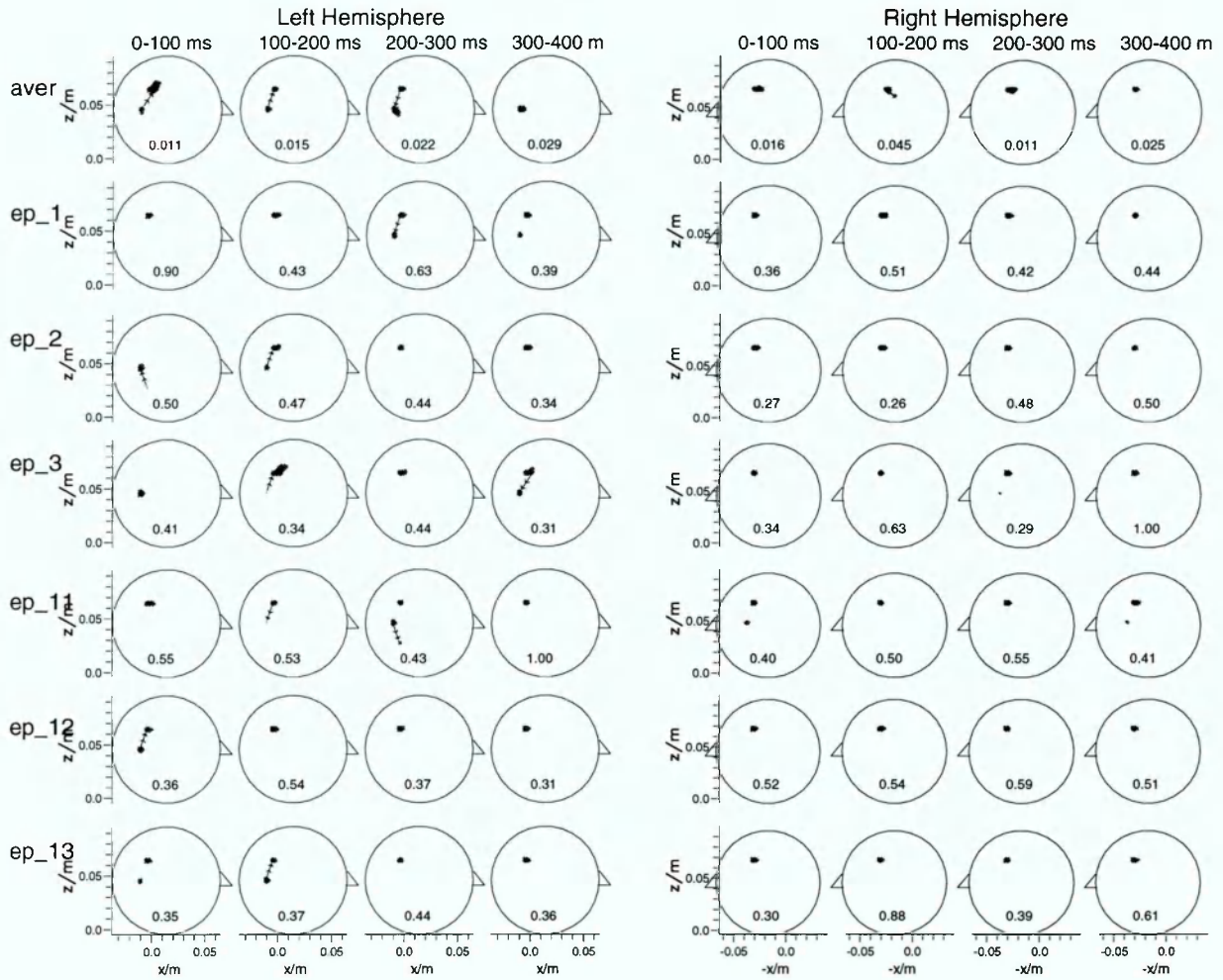
first column is for the average signal, while the rest of the 6 columns are for the 6 single trial signals. From the figure, it can be seen that at each level, there exists at least one main common activation area for both the average and single trial signals; and the area is changed with the level. Therefore, if we single out these main activation areas at each level for both the average and single trial signals, then we can trace how the activity in these areas changes over time. For level 9 (the top level), as shown in Figure 8.13, the main activation area is marked by a square, which is about 1 cm^2 in area (the radius of the intersection of the hemispherical source space at level 9 is 3.63 cm). Similar plot for level 7 is shown in Figure 8.14, where the area is about 3 cm^2 (the radius at level 7 is 5.99 cm). Hence, the main activation areas of these two superficial levels by our selection are rather focused. For the following tracing of how the activity in the left and right hemisphere changes over time and correlate different activation areas in time and space, we choose to display the MFT estimates for 4 levels, namely, level 9 and 7 within each main area ($area1$ and $area2$), and level 8 and 1 (the bottom level) within each whole intersection area ($area4$).

Figures 8.15 to 8.18 are the activation curves for integrals of intensity over the specific areas at 4 levels for the average and 3 single trial signals in experiment (AI,BTi) when the stimulus was delivered to the left ear. In each figure, the first 4 rows are for the left hemisphere (ipsilateral), while the rest of the 4 rows are for the right hemisphere (contralateral). For each hemisphere, the integrals of intensity over the $area1$, $area2$, $area4$ and $area4$ for level 9, 7, 8, and 1 are displayed respectively from 200 ms before to 500 ms after the onset of the stimulus. From Figure 8.15, it shows that at level 9, for the average in the left hemisphere, the integrated activity in the selected area is rather irregular, i.e., there does not exist a distinct interval(s) when the MFT estimates shows dramatic activity in $area1$; similar observation can be made for level 7, except at around 300 ms following the onset of stimulus, substantial activity occurs in $area2$, which might be related to the well known P300m activity. For level 8 and 1, when the integrals are over the whole area ($area4$), distinct intervals are seen in the figure, around 300 ms for level 8, 100 and 300 ms for level 1. It is interesting to note that activities at these two levels appear nearly simultaneously. Moreover, a noticeable double hump is seen at level 1 around 300 ms. In comparison, for the right hemisphere, at level 9 and 8, a distinct hump is seen at about 100 ms; a similar but with much smaller amplitude hump is also seen at level 7 at about 100 ms, while this hump is barely visible at level 1.
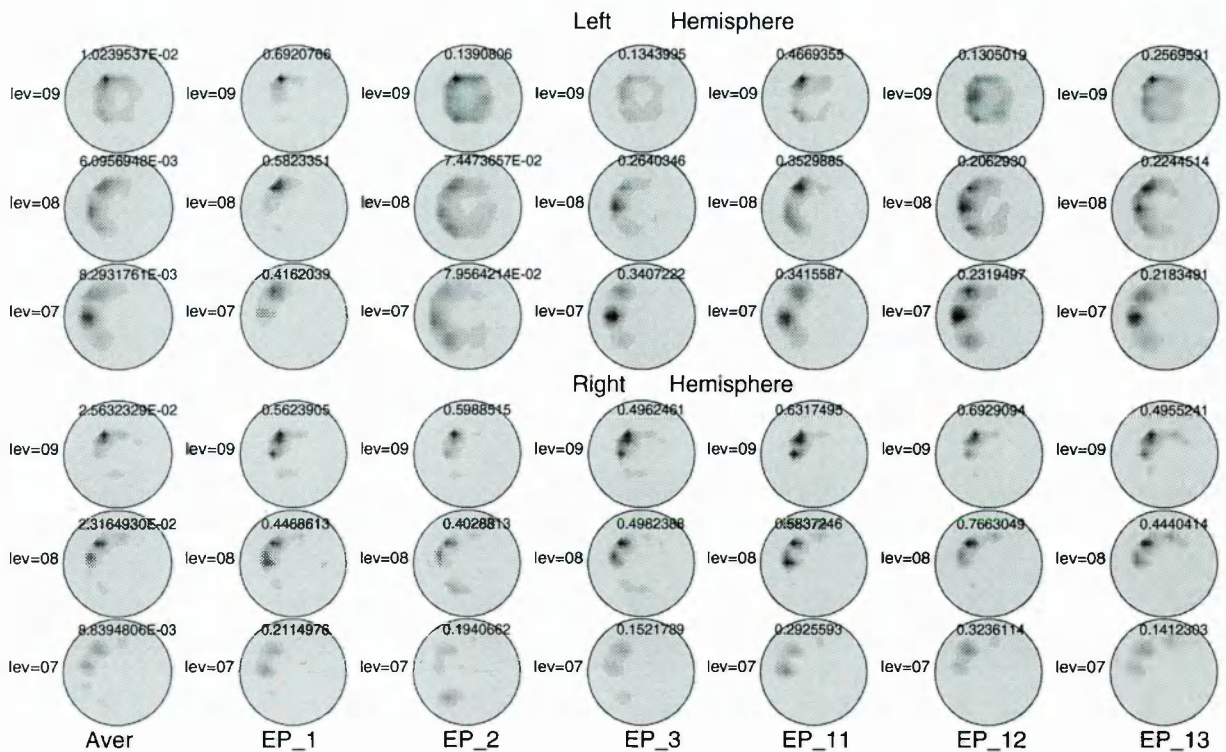
Figure 8.12 A contour cylinder plot for integrals of intensity for the MFT estimates at the 3 superficial levels of the hemispherical source space over the first 50 ms following the onset of stimulus to the left ear: viewed from inside the brain with the head up, and the circle delineating the intersection of the hemispherical source space at that level. Notice the existence of main common activation area for both the average and single trial signals at each level.
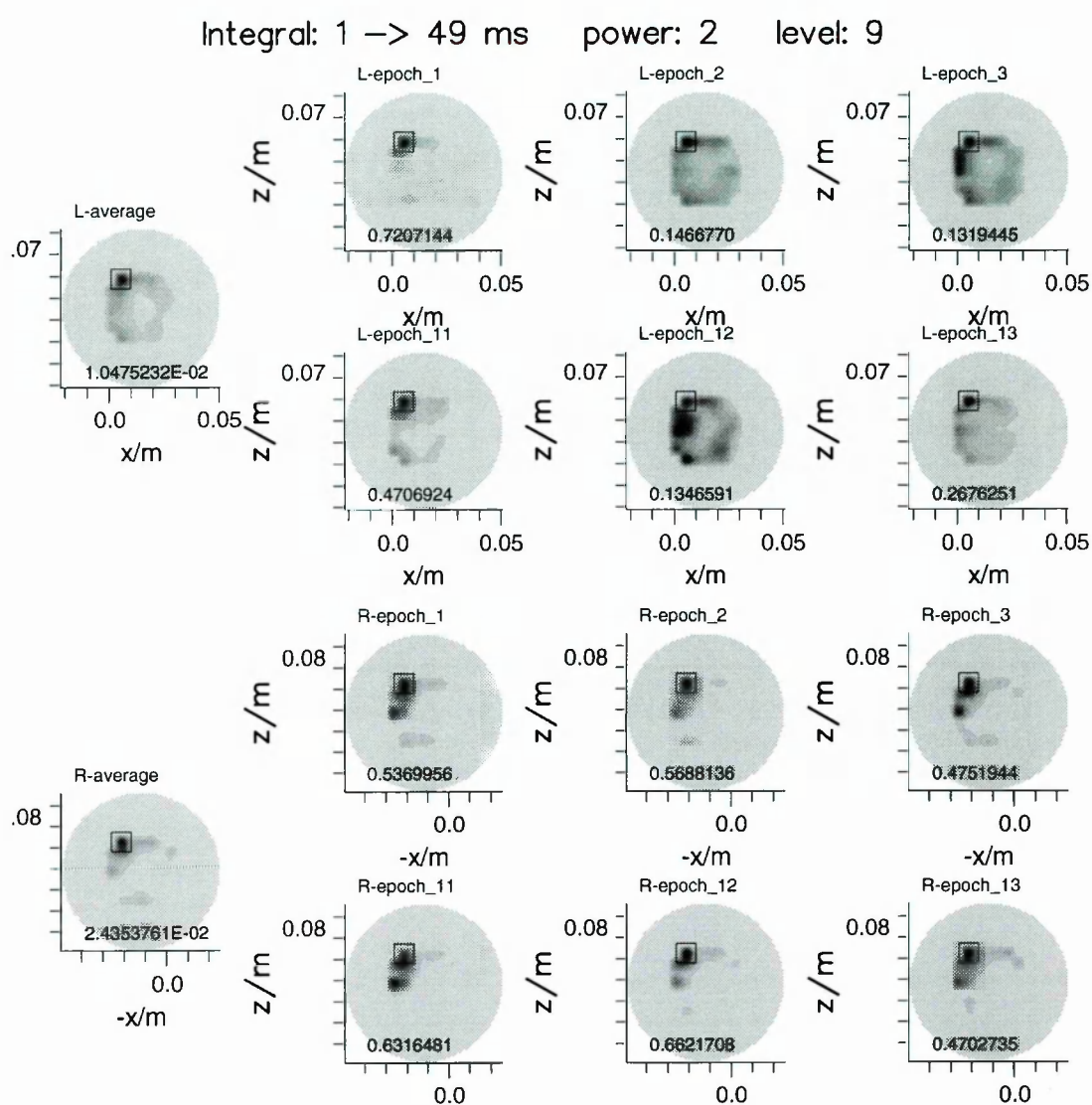
Figure 8.13 The MFT estimates at level 9 showing the main common activation area within the small square, for the average and 6 single trial signals recorded simultaneously from both hemispheres (experiment (AI,BTi)).
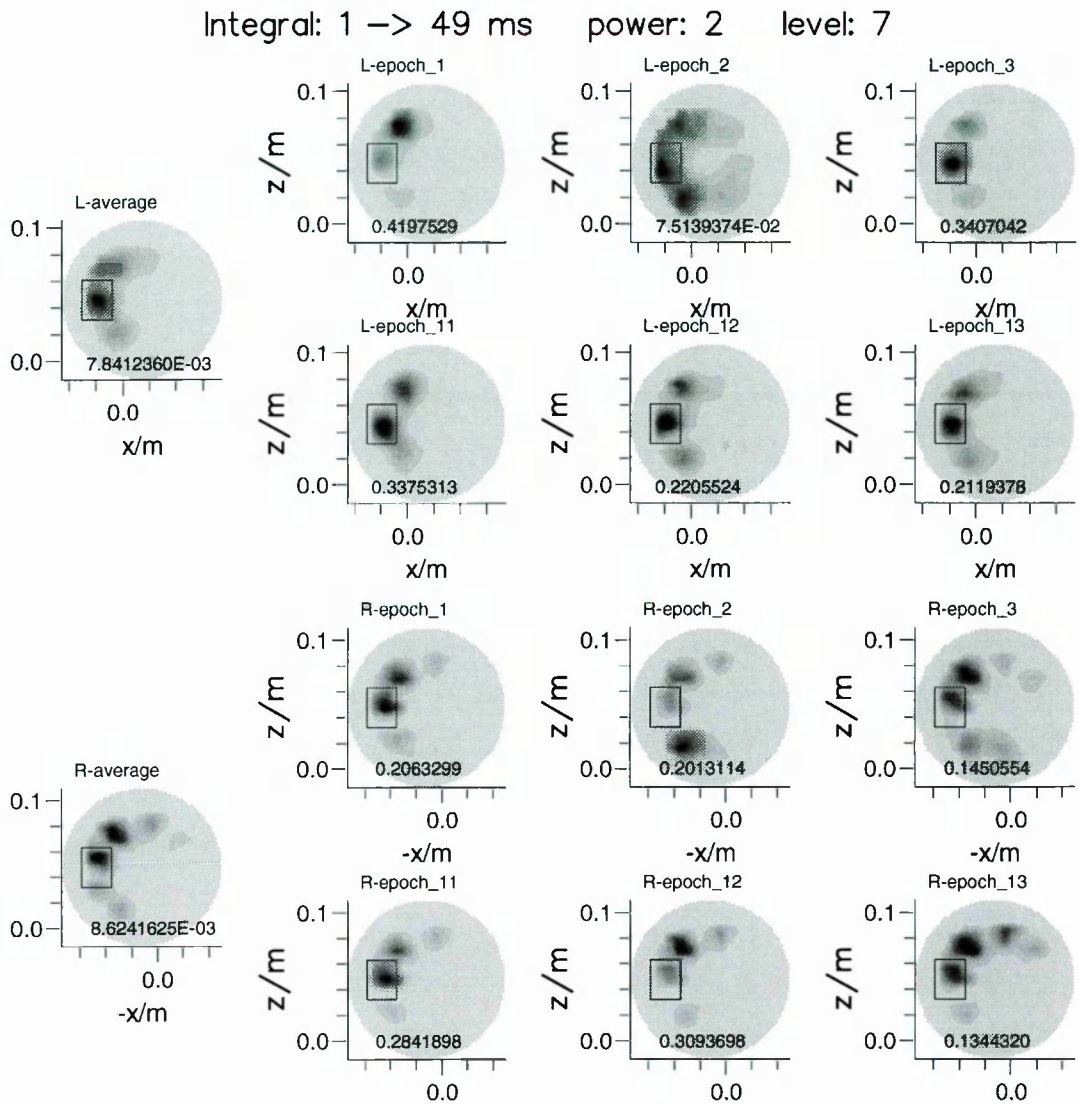
Figure 8.14 The MFT estimates at level 7 showing the main common activation area within the small square, for the average and 6 single trial signals recorded simultaneously from both hemispheres (experiment (AI,BTi)).

Hence, at about 100 ms, superficial activities dominate the right hemisphere; while at about 300 ms, both the sharp cortical and extended deep activity are seen in the right hemisphere. The above observations are based on the study the left and right hemisphere separately, and it is of importance to establish a connection between the activities in the left and the right hemisphere, which is one of the advantages offered by the twin MEG system. Hence, a summary of the activities in the left and right hemisphere in the MFT estimates for the average signal can be made as follows: following the onset of the stimulus, before 100 ms, deep activity originates in the ipsilateral side of the stimulus (left), while superficial activities are seen in the contralateral side. This activity pattern continues and is shown most distinctly at around 100 ms for 20 ms. At around 260 ms, deep activity starts to reappear in the left hemisphere and peaks at 276 ms; this peak extends to the right hemisphere after 12 ms. Follow on this peak, the deep activity in the left hemisphere was decreasing gradually until zero (at 300 ms), forming the first hump, but soon a similar second hump follows; and the deep activity in the right hemisphere is more or less sustained. Meanwhile, when the left reaches its peak for the second time, substantial activities are seen at the superficial levels in the left hemisphere. Hence, at around 300 ms, a redistribution of activity across levels is evident: the activity appears first in the left at depth, extends to the right at depth later, then swing back to the left at depth and finally to the left superficial levels. Furthermore, the above conclusions are also applicable to the single trials, as shown in the Figures 8.16 to 8.18, corresponding to epoch 1, 2 and 12. As pointed out earlier, one of the differences between the average and the single trials lies in the temporal organization, i.e., in different intervals different epochs are similar to the average. This conclusion is verified here again, e.g., the double hump seen in the average is also present in the single epochs, only at different interval, around 400 ms, -150 ms, and -100 ms for epoch 1, 2 and 12 respectively. Finally, it is worthy of mention that the double hump in the left hemisphere and a hump in the right hemisphere at depth is also seen in the similar plot for the stimulus delivered to the right ear, and it is the left hemisphere that activates earlier than the right hemisphere, from which we may draw a very tentative conclusion that the activities at depth originate in the left then extends to the right, regardless of the side of the ear where the stimulus has been delivered.

The comparison between the average and the single trials in Figures 8.15 to 8.18 shows similar features to the properties of the earlier comparison between the average

and the single trials for the 40-Hz activity in Section 7.3. It is tempting to interpret the dominant features observed in the average, e.g. the peak at 100 ms and 300 ms, as a contribution of a subset of epochs. Unfortunately, neither V_3 was available for the MAGNES probe nor a full MFT analysis for all the epochs. Clearly this must be the subject of further investigation; preferably with an experiment of a more demanding task and a feedback measure so that a behaviour response can be obtained from every single trial.

Figure 8.15 Activation curves for integrals of intensity over the specific areas for the MFT estimates of the average signal at 4 levels: (a) left, (b) right hemisphere. Notice the activity within the arrow pointed period.

Figure 8.16 Activation curves for integrals of intensity over the specific areas for the MFT estimates of single trial 1 at 4 levels: (a) left, (b) right hemisphere. Notice the activity within the arrow pointed period.

Figure 8.17 Activation curves for integrals of intensity over the specific areas for the MFT estimates of single trial 2 at 4 levels: (a) left, (b) right hemisphere. Notice the activity within the arrow pointed period.
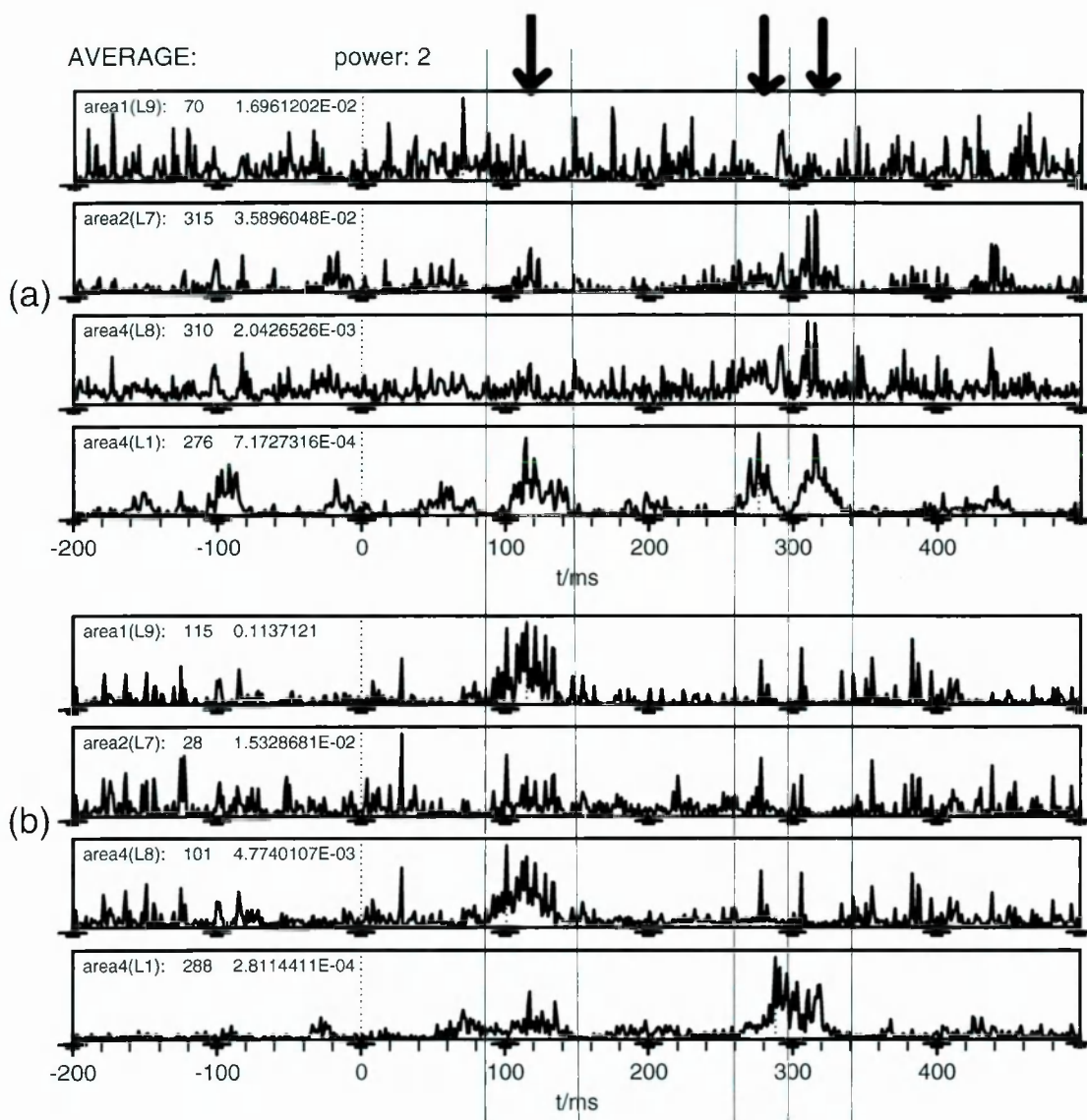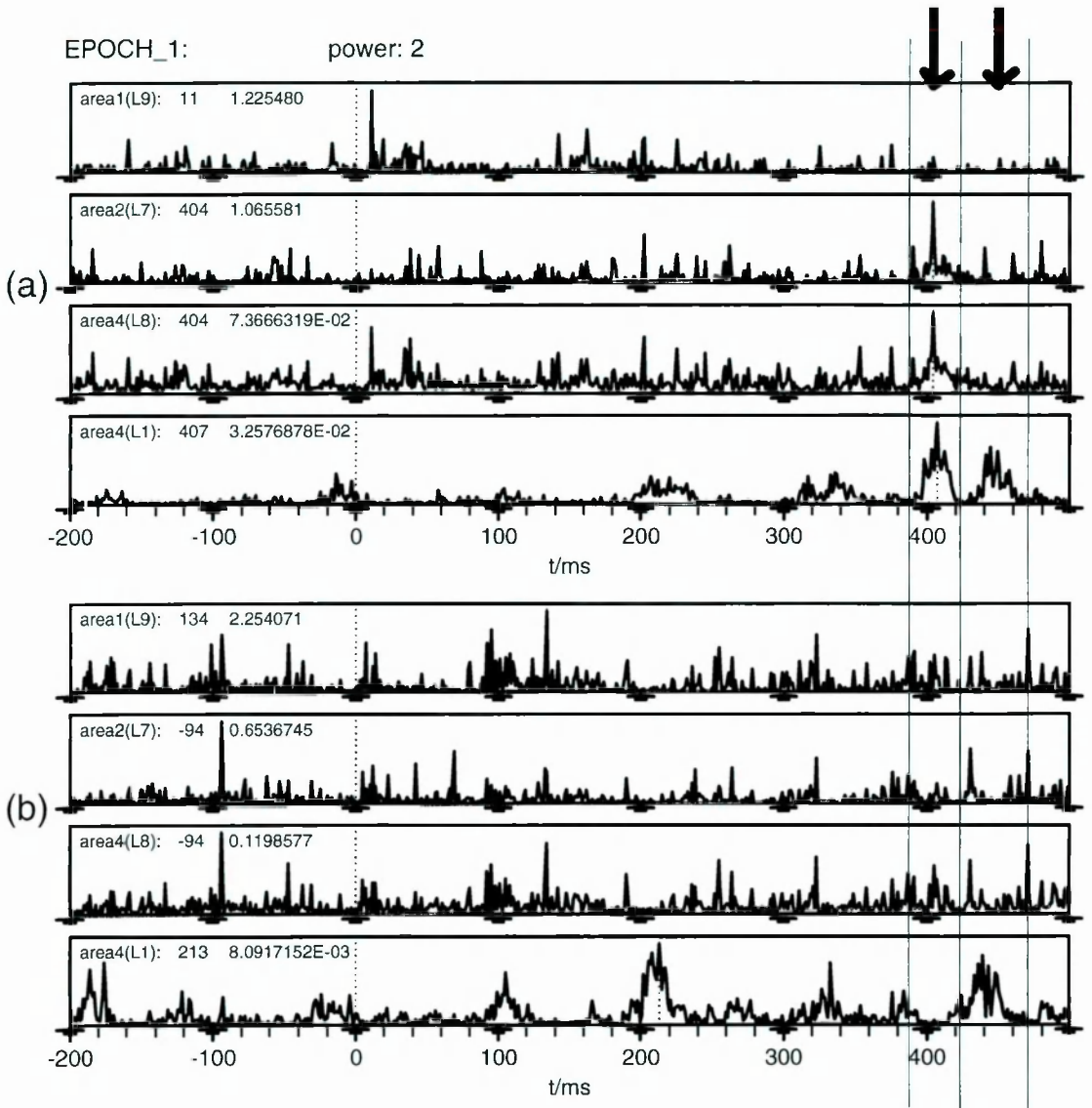
Figure 8.18 Activation curves for integrals of intensity over the specific areas for the MFT estimates of single trial 12 at 4 levels: (a) left, (b) right hemisphere. Notice the activity within the arrow pointed period.
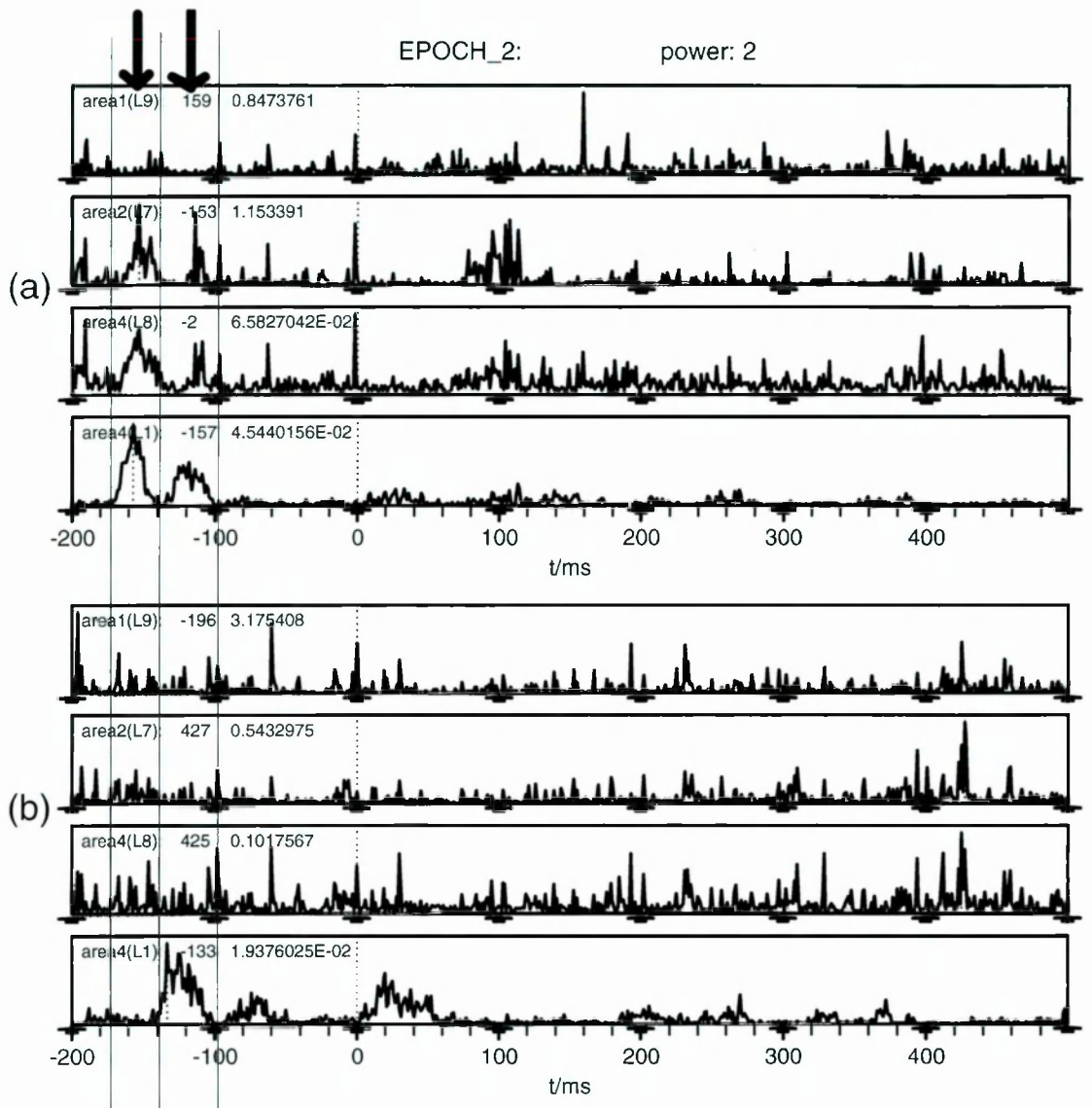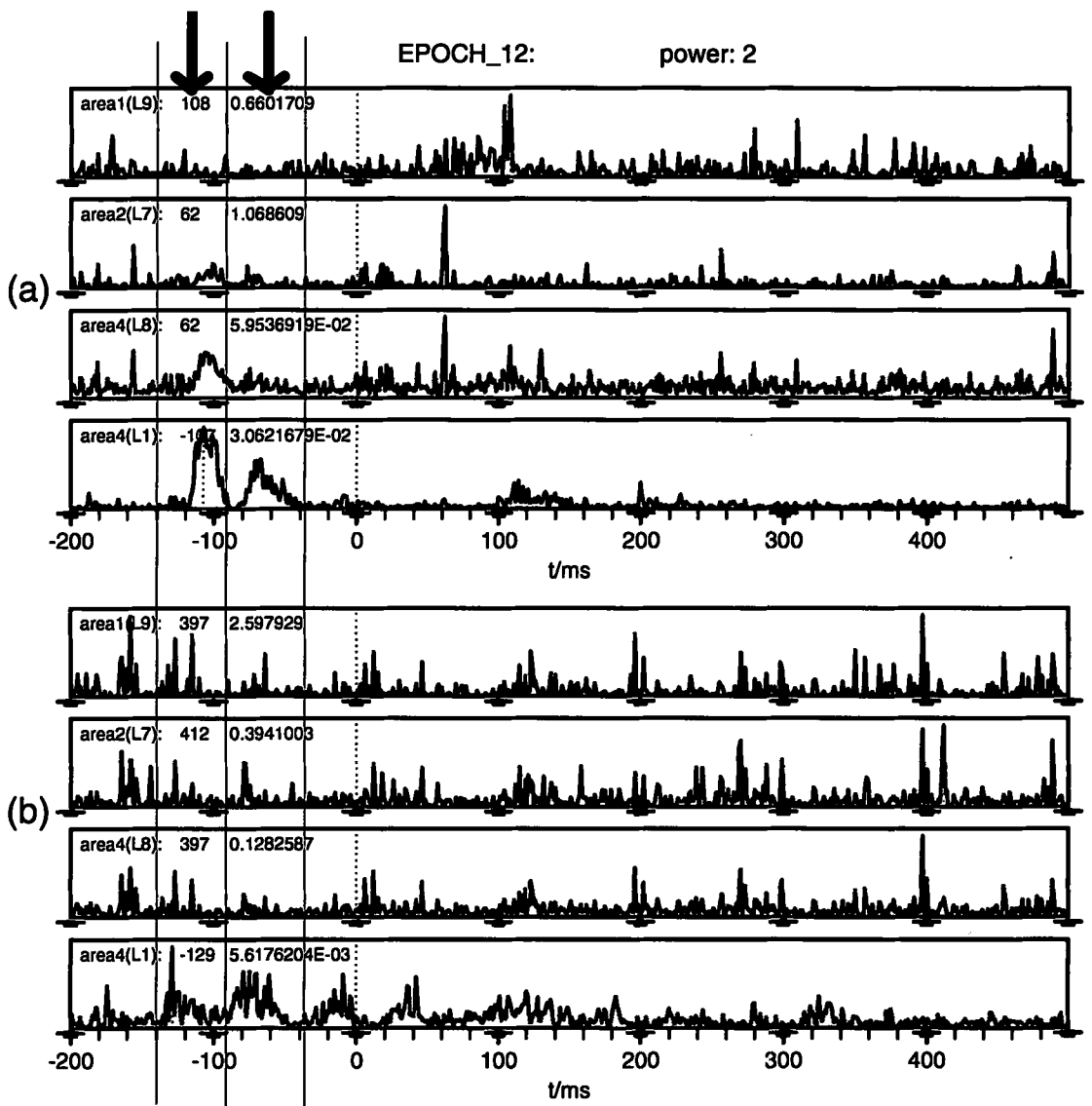
CHAPTER 9.

CONCLUSIONS AND FUTURE WORK

In this chapter, the main results of the research are summarized and possible future work based on the work done in this thesis is proposed.

9.1. Summary of the Research and Contributions

The main objective of this project has been to develop the simple vector signal transformation V_3 into a useful tool for the analysis of MEG signals, particularly for studying single trials. Chapter 6 describes V_3 fully and provides tests with computer generated data and a set of auditory evoked measurements, showing that V_3 identifies superficial sources correctly and efficiently. The application of V_3 to both the average signal and single trials is taken up in Chapter 7, which discusses in some detail the 40-Hz (or gamma band) auditory response. Using the V_3, we found that in single epochs similar patterns of high frequency activity are observed in the area around the auditory cortex well before, close to, and well after stimulus onset. Together with the MFT distributed source analysis in Chapter 8, we established the connection between the average signal and the single trials, namely, in different intervals different epochs are similar to the average; when the intensity is integrated over time, agreement between the average and single trials is evident, provided that the integration period is long, typically 50 ms or more. Therefore, the sequence of events observed in the average can only represent the evolution of events in single trials in a statistical way. Furthermore, we also studied the bi-hemisphere differences and interplays using the MEG signals recorded from both hemispheres at different placements and simultaneously: we studied the bi-hemisphere auditory response for the first 100 ms following the onset of the stimulus by combining the MFT estimates for generators with structural information provided by MRI, and we demonstrated the auditory response changes over time in a way which is consistent with the known auditory pathway. Our results suggest that deep and central areas of the brain may

be the seeds for the main deflections (e.g. at 30 ms, 50 ms and 100 ms) observed in the auditory responses. This however needs further investigation and confirmation from experiments using many subjects.

The main contribution of the work done in this thesis is the implementation of the signal transformation, and the demonstration of how efficiently it highlights nearby sources. It could become a routine tool of basic and crude estimation of (superficial) generators of MEG signals without running the resource demanding inversion first.

The single epoch analysis in this thesis has produced evidence against the traditional view of the impropriety and impossibility of using single trial records in the MEG signal analysis, due to the noise which dominates the raw signals. This is thanks to the recent advent of huge multi-channel MEG systems with whole-head coverage allowing us to record brain activity in real time. Moreover, it provides hints of the relationship between the average and single trials and emphasizes the importance and necessity of the MEG signal analysis epoch by epoch for investigating the spontaneous brain activity. Going beyond the initial aim of this thesis was too tempting; we have thus provided the first study of single trial bi-hemisphere auditory responses. Though the results need further confirmation, it is, we believe, a useful first attempt of furthering our understanding of how inter-hemisphere differences and interplays contribute to normal brain processes.

9.2. Future Work

There are several lines of pursuit which appear important to develop further:

1. The V_3 we have used for much of the work done in the thesis is initially specific to the MEG signals taken from the KRENIKON 37-channel system, which has a flat-bottomed dewar, therefore the implementation of the V_3 is based on the two-dimensional signal transformation. In order to realize the goal of making V_3 a routine tool of providing somewhat crude but quick estimates of superficial generators directly from the MEG signals, further development for the V_3 is needed, aiming at the application of V_3 to any MEG systems, especially for the MEG systems with a curved bottom, such as the BTi 37-channel systems. This has already been carried out at Jülich.

2. By projecting the 2D V_3 distribution onto the brain surface (e.g., extracted from MRI), a dynamic quasi-3D display can be obtained by joining in animation successive timeslices. We have so far only produced animations of V_3 in the measurement plane using the transputer. We need software to extract the brain surface and project V_3 onto it; we need to make this into a systematic and efficient package.

3. The correlation method developed in this work has complemented the distributed source analysis which allows us to scan through each and every single trial and identify each cortical activation similar to the ones picked out in the average by using the V_3. We have applied the method to the simplest possible example (i.e., a set of auditory evoked measurements) for building up our understanding of the relationship between the average and single trials. To progress further, clearly a more complex experiment, with more demanding tasks and feed-back measures, is needed for tracing the behaviour response extracted from every single trial. The design and plan of such an experiment has been under discussion and will be carried out at Jülich in the near future.

4. The distributed sources models need to be refined and tested more fully; they are more realistic models of physiological events than is the single-dipole model. Improvements can be made in the development of an objective procedure, mainly employing statistical techniques, to carry out the task of choosing optimal parameters. The definition of the source space in the MFT distributed source analysis can also be refined further with improvements in localization at cortical and deep regions, probably through additional constraints. A more powerful method applying the principle of cross-entropy minimization has been discussed in [185] and will be implemented on the transputer at the Open University. The new algorithm is particularly useful when partial information about the location and/or direction of some of the generators is known.

5. Because of the non-uniqueness of the inverse problem, it is necessary to combine MEG data with supplementary information, e.g. structural information given by MRI, metabolic blood flow data provided by PET and functional MRI [186, 187]. A successful clinical case was reported in [186], in which a tumor was accurately located and related to the sensorimotor cortex by combining the somatosensory evoked magnetic field with the functional MRI. The improvement in localization from such a treatment may justify the increased resources in terms of computer time necessary to utilize such techniques on a

broad scale.

6. It is also quite important to attempt to utilize the information from both MEG and EEG together. Simplistic approaches such as independent localization utilizing each technique with subsequent averaging of estimated dipole locations are clearly suboptimal [35]. A three-step approach has been suggested by Cohen and Cuffin [188] in which the MEG map is used in an inverse way to estimate dipole parameters of the tangential dipole; then a forward solution is subtracted from EEG map to give a residual EEG map (presumably reflecting predominantly components of radial sources). An inverse solution is then performed on this EEG map to localize the radial sources. In principle, measurements of EEG and MEG give independent information about the electrical activity of the brain [40, 14], and techniques which make optimal use of the differences need to be further developed.

7. Another area in which work needs to be pursued is in making use of the information available in the time dependencies of the signals. The signals from moment to moment must have some order, and this information may be useful in visualizing changes in source currents which may, in turn, improve our understanding of cerebral activity. In essence, what can be done is to incorporate some feedback into the inference algorithm. That is, the physiological state is as much a result of the previous state as it is of the input [189]. It will be important to incorporate this physiologically vital feature into future models.

8. Furthermore, digital filtering methods for the estimation of signal wave forms from noisy data need to be refined. Much more care and emphasis must also be put on the development of techniques for handling signals that arise from a multitude of simultaneous sources.

Appendix A.

Co-registration

After the generators for the magnetic measurements from the head surface are obtained, in order to provide insight into the functioning and pathology of the brain, it is essential to superimpose the solutions onto the anatomy, as revealed for example by MRI slices. The process is often referred to as *co-registration*. An accurate co-registration is a prerequisite of localization. In general, the measurements (the sensors) are taken in a different co-ordinate system from that the MRI slices (the brain structure) are taken. Hence, the task of the co-registration is to link these two different systems together and express them in a common system [190]. In the analyses and examples used in this thesis, two coordinate systems to co-registrate between the sensors and the head are adopted, namely, MRI- and head- based coordinate system.

A.1. MRI-based Coordinate System

MRI-based coordinate system is based on the axial MRI slices. As an example, the MRI slices obtained from Magnetom SP (Siemens, Germany) has a precision of 264 mm (x axis) × 264 mm (y axis) on a field of view of 256 times × 256 times in the frequency- and phase-encoding directions, and the thickness (z axis) was 1.563 mm. Distances in MRI were measured by the number of voxels. Small capsules of liposoluble vitamin were placed at some key points, such as the nasion (the deepest point of the nasal bone between the eyes), the middle and tip of the nose, the left and right periauricular points and so on. Serial transverse sections of the brain were obtained generally from the top to the bottom.

The origin of the system is defined just behind above the nasion, with the centre of each axial image at $x = 0$ and $y = 0$, and the z component corresponds to the MRI slice on a fixed xy plane, i.e. the SP number for the MRI slice. The direction of

the x axis corresponds to the left ear to the right ear, the y axis is from the front to the back of the head, while the z axis points from the head to the foot. Fixed points or tubes containing water (appearing as 'water marks' on the MRIs) are used to define a transformation matrix which is stored in a file termed as a PAB file. In our studies with the KRENIKON 37-channel system in Erlangen, we have made use of the PAB file, and separately checked the co-registration with inhouse software [190, 191]. In general, there are two PAB files for each experiment; differences in the transformation parameters signify movement of the head during the experiment.

A.2. The BTi Head-based Coordinate System

Biomagnetic Technologies Inc. has developed a different system which relates directly to large scale features on the head. It uses Cartesian coordinates with centre and axes defined entirely in terms of the nasion and periauricular points. The origin of this system is defined to be exactly midway between the periauricular points. The x-axis of the Cartesian system is a line that extends from this origin through the nasion. The z-axis is defined as the line that extends upward from the origin, oriented perpendicular to the plane defined by the x-axis and the line passing through the periauricular points (the Cz point of EEG). The z-axis emerges from the scalp in the general vicinity of the vertex. The y-axis is defined as the line that extends towards the left from the origin, oriented perpendicular to the plane defined by the x-axis and z-axis. The y-axis emerges from the scalp in the general vicinity of the left periauricular point. Note that the y-axis in general is not exactly parallel to the line between periauricular points. The system serves to reference both the position and orientation of each magnetic sensor being used, and was first used by BTi in the dinosaur age of single channel probes [77] very early on and it is now used by many groups especially in North America (e.g. CTF system ect.) as well as Phillips system in Germany. It has been proved to be an efficient coordinate system in terms of providing an easy general reference of areas in the brain. The use of the minimum necessary points for co-registration is however dangerous, and the use of more points is advisable so that redundancy can be used to minimize the error in co-registration.

For the analysis of MEG data obtained from the BTi twin 37-channel system, all the MEG measurements were taken under the head-based coordinate system defined as above. However, the MRI slices of the subject were obtained from the Magnetom SP in Erlangen, which were expressed in the MRI-based coordinate system. To min-

imize the computing demand for co-registration, the unit vector of the three axes of the MRI-based system is defined the same as the head-based coordinate system, i.e., from back to front, from right to left and from foot to head respectively. However, the origin of the MRI-based system is defined the same as above. The difference between these two coordinate system is rather substantial, especially in terms of orientation (see Figure A.1(a)). To superimpose the solutions onto the MRI slices, we need to bridge these two systems, e.g., transfer the MRI slices in the MRI-based system to the head-based system. To achieve this, one can take some points from the head outline in both systems and develop some mathematic methods to transfer these points from its own 'local' system to the target 'global' system. For instance, collect some points of the head outline in the head-based system and gather the corresponding points from the MRI slices by clicking the head outline in the MRI-based system. The selection of points can be as simple as taking the coordinates of the vitamin pills, or as complicated as taking the points of the head outline slice by slice. After these two data-sets are obtained, one just needs to calculate the transformation by matching the corresponding points in both systems. The calculation mainly involves in solving a number of linear equations [191]. Figure A.1(b) shows the the head outline from the MRI slices after the transformation, superimposed onto the head outline in the head-based system. Tests have shown that the co-registration error between the two systems is less than 0.5 cm. However, the actual error between the MEG (probe definition) and the MRI system could be considerably larger (1-2 cm).
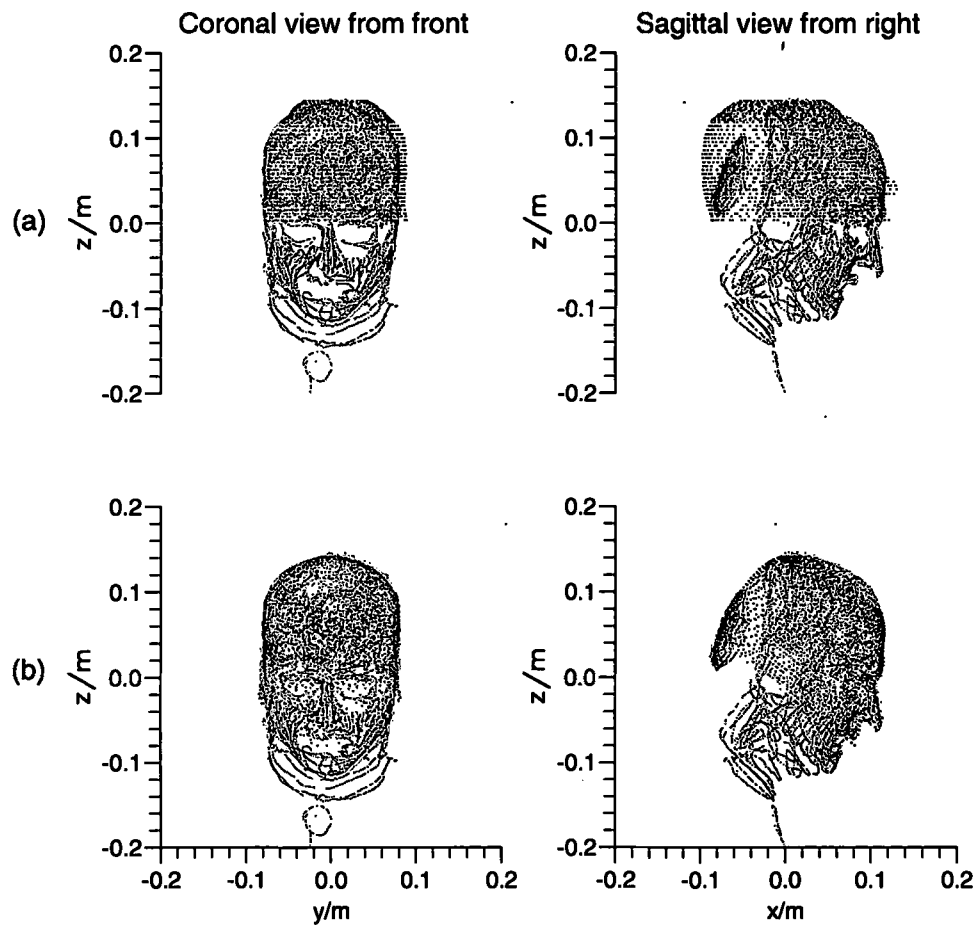
Figure A.1 Co-registration between the MRI- and head-based coordinate system: (a) before and (b) after the co-registration. The bigger and darker dots are for the head outline from the MRI slices, while the smaller and lighter dots stands for the headline collected and expressed in the head-based system, which definition is as shown in the figures.

BIBLIOGRAPHY

[1] R.J. Ilmoniemi, M.S. Hämäläinen, and J. Knuutila. 'The Forward and Inverse Problems in the Spherical Model'. In H. Weinberg, G. Stroink, and T. Katila, editors, *'Biomagnetism: Applications and Theory'*, pages 278–282. Pergamon Press, New York, 1985.

[2] E. Başar, C. Başar-Eroglu, J. Röschke, and Schütt. 'The EEG is a Quasi-deterministic Signal Anticipating Sensory-Cognitive Tasks'. In E. Başar and T.H. Bullock, editors, *'Brain Dynamics'*, pages 43–71. Springer-Verlag Berlin Heidelberg, 1989.

[3] A.A. Ioannides. 'Estimates of Brain Activity using Magnetic Field Tomography and Large Scale Communication within the Brain'. In M.W. Ho, F.A. Popp, and U. Warnke, editors, *'Bioelectrodynamics and Biocommunication'*. World Scientific, Singapore, 1994.

[4] D. Robinson, editor. *'Biology: Brain & Behaviour'*, volume 2, chapter 2-4. The Open University (U.K.), 1992.

[5] R.F. Thompson. *'The Brain: An Introduction to Neuroscience'*. W.H. Freeman and Company, New York, 1985.

[6] A.C. Scott. 'The Electrophysics of a Nerve Fiber'. *Rev. Mod. Phys.*, 47:487–533, 1975.

[7] L. Aitkin. *'The Auditory Cortex'*. Chapman and Hall, 1990.

[8] I.S. Grant and W.R. Phillips. *'Eletromagnetism'*. John Wiley & Sons, 1990.

[9] S.J. Williamson and L. Kaufman. 'Therory of Neuroelectric and Neuromagnetic Field'. In F. Grandori, M. Hoke, and G.L. Romani, editors, *'Auditory Evoked Magnetic Fields and Electric Potentials, Vol. 6 of Advances of Audiology'*, pages 1–9. Basel:Karger, 1990.

[10] M.S. Hämäläinen, R. Hari, R.J. Ilmoniemi, J. Knuutila, and O.V. Lounasmaa. 'Magnetoencephalography – Theory, Instrumentation, and Applications

to Noninvasive Studies of the Working Human Brain'. *Reviews of Modern Physics*, 65(2):413–497, 1993.

[11] S.J. Williamson and L. Kaufman. 'Magnetic Fields of the Cerebral Cortex'. In S.N. Erné, H.D. Hahlbohm, and H. Lubbig, editors, *'Biomagnetism'*, pages 352–402. Walter de Gruyter, Berlin, 1981.

[12] R. Plonsey. *'Biomagnetic Phenomena'*. NewYork: McGraw-Hill, 1969.

[13] J.P. Wikswo. 'Cellular Action Currents'. In S.J. Williamson, G.L. Romani, L. Kaufman, and I. Modena, editors, *'Biomagnetism: An Interdisciplinary Approach'*, chapter 8, pages 173–207. Plenum Press, New York, 1983.

[14] R. Hari and R.J. Ilmoniemi. 'Cerebral Magnetic Fields'. *CRC Critical Rev Biomed Eng*, 14:93–126, 1986.

[15] D.C. Barber. 'Electrical Impedance Tomography'. Private notes for Biomagnetism Sciences Society meeting at Aston University, Birmingham, England, June 26, 1992.

[16] D.C. Barber and A.D. Seagar. 'Fast Reconstruction of Impedance Images'. *Clin. Phys. Physiol. Meas.*, 8 Suppl. A:47–54, 1987.

[17] B.H. Brown and A.D. Seagar. 'The Sheffield Data Collection System'. *Clin. Phys. Physiol. Meas.*, 8 Suppl. A:91–98, 1987.

[18] D.S. Holder. 'Cerebral Impedance Changes in Epilepsy'. Private notes for Biomagnetism Sciences Society meeting at Aston University, Birmingham, England, June 26, 1992.

[19] D.S. Holder. 'Detection of Cerebral Ischaemia in the Anaesthetised Rat by Impedance Measurement with Scalp Electrodes: Implications for Non-invasive Imaging of Stroke by Electrical Impedance Tomography'. *Clin. Phys. Physiol. Meas.*, 13:63–75, 1992.

[20] D.S. Holder. 'Detection of Cortical Spreading Depression in the Anaesthetised Rat by Impedance Measurement with Scalp Electrodes: Implications for Non-invasive Imaging of the Brain with Electrical Impedance Tomography'. *Clin. Phys. Physiol. Meas.*, 13:77–86, 1992.

[21] P.T. Fox, M.E. Raichle, and W.T. Thach. 'Functional Mapping of the Human Cerebellum with Positron Emission Tomography'. *Proc. Natl. Acad. Sci.*, USA 82:7462–7466, 1985.

[22] P.T. Fox and M.A. Mintum. 'Noninvasive Functional Brain Mapping by Change-Distribution Analysis of Averaged PET Images of $H_2^{15}O$ tissue activity'. *J. Nucl. Med.*, 30:141–149, 1989.

[23] R.S.J. Frackowiak and K.J. Friston. 'Functional Neuroanatomy of the Human Brain: Positron Emission Tomography – a new Neuroanatomical Technique'. *J. Anat.*, 184:211–225, 1994.

[24] J.C. Mazziotta, S.C. Huang, M.E. Phelps, R.E. Carson, N.S. MacDonald, and K. Mahoney. 'A Noninvasive Positron Computed Tomography Technique Using Oxygen-15 – Labeled Water for the Evaluation of Neurobehavioral Task Batteries'. *J. Cereb. Blood Flow Metab*, 5:70–78, 1985.

[25] G.F. Knoll. 'Single-photon Emission Computed Tomography'. *Proc. IEEE*, 71:320–329, 1983.

[26] R.S.J. Frackowiak and K.J. Friston. 'Functional Neuroanatomy of the Human Brain: Positron Emission Tomography – A New Neuroanatonical Technique'. *J. Anat.*, 184:211–225, 1994.

[27] P. Morris. *'NMR in Medicine and Biology'*. Oxford University Press, Oxford, 1986.

[28] K.K. Kwong, J.W. Belliveau, D.A. Chesler, and et al. 'Dynamic Magnetic Resonance Imaging of Human Brain Activity during Primary Sensory Simulation'. *Proc Natl Acad Sci*, USA 89:5675–5679, 1992.

[29] J.R. Binder, S.M. Rao, T.A. Hammeke, F.Z. Yetkin, A. Jesmanowicz, P.A. Bandettini, E.C. Wong, and et al. 'Functional Magnetic Resonance Imaging of Human Auditory Cortex'. *Ann Neurol*, 35:662–672, 1994.

[30] J.W. Belliveau, D.N. Kennedy, R.C. McKinstry, B.R. Buchbinder, R.M. Weisskoff, M.S. Cohen, and et al. 'Functional Mapping of the Human Visual Cortex by Magnetic Resonance Imaging'. *Science*, 254:716–719, 1991.

[31] R.W. Thatcher and et al. *'Functional Neuroimaging: Technical Foundations'*. Academic Press, Orlando, 1993.

[32] O. Creutzfeldt and J. Houchin. 'Neuronal Basis of EEG Waves'. In A. Redmond, editor, *'Handbook of Electroencephalography and Clinical Neurophysiology'*, volume 2 (part C), pages 5–55. Amsterdam: Elsevier, 1974.

[33] P. Gloor. 'Contributions of Electroencephalography and Electrocorticography to the Neurosurgical Treatment of the Epilepsies'. In D.P. Purpura,

J.K. Penry, and R.D. Walter, editors, *'Advances in Neurology'*, pages 59–105. NewYork: Raven Press, 1975.

[34] H. Petsche, H. Pockberger, and P. Rappelsberger. 'On the Search for the Sources of the Electroencephalogram'. *Neuroscience*, 11:1–27, 1984.

[35] C.J. Stok. *'The Inverse Problem in EEG and MEG with Application to Visual Evoked Response'*. PhD thesis, Leiden University, 1986.

[36] C.J. Stok, J.W.H. Meijs, and M.J. Peter. 'Inverse Solutions Based on MEG and EEG Applied to Volume Conductor Analysis'. *Phys. Med. Biol.*, 32:99–104, 1987.

[37] P.L. Nunez. *'Eletrical Fields of the Brain: the Neurophysics of EEG'*. NewYork: Oxford University Press, 1981.

[38] B. Hjorth. 'An On-line Transformation of EEG Scalp Potentials into Orthogonal Source Derivations'. *Electroencephalogr Clin Neurophy*, 39:526–530, 1975.

[39] M.S. Hämälainen and J. Sarvas. 'Feasibility of the Homogeneous Head Model in the Interpretation of Neuromagnetic Fields'. *Phys. Med. Biol.*, 32:91–97, 1987.

[40] D. Cohen and B.N. Cuffin. 'Demonstration of Useful Differences between Magnetoencephalogram and Electroencephalogram'. *Electroencephalogr Clin Neurophy*, 56:38–51, 1983.

[41] T. Fieseler, H. Nowak, and A.A. Ioannides. 'Model Studies of the Accuracy of the Conducting Sphere Model in Magnetoencephalography Using the Spheroid'. In *'Proceedings of the BIOMAG'93 Conference in Vienna'*. Elsevier Science Publishers, Amstemdam, 1993. In press.

[42] D.F. Rose, S. Sato, P.D. Smith, R.J. Porter, W.H. Theodore, W. Friauf, R. Bonner, and B. Jabbari. 'Localization of Magnetic Interictal Discharges in Temporal Lobe Epilepsy'. *Ann Neurol*, 22:348–354, 1987.

[43] R. Hari, K Aittoniemi, M.L. Jarvinen, T. Katila, and T. Varpula. 'Auditory Evoked Transient and Sustained Magnetic Fields of Human Brain: Localization of Neural Generators'. *Exp Brain Res*, 40:237–240, 1980.

[44] G. Anogianakis, J.M. Badier, G. Barrett, and et al. 'A Consensus Statement on Relative Merits of EEG and MEG'. *Electroencephalogr Clin Neurophy*, 82:317–319, 1992.

[45] R. Hari, K. Reinikainen, E. Kaukoranta, M. Hämäläinen, R. Ilmoniemi, A. Penttinen, J. Salminen, and D. Teszner. 'Somatosensoty Evoked Cerebral Magnetic Fields from SI and SII in Man'. *Electroencephalogr Clin Neurophy*, 57:254–263, 1984.

[46] T.T. Yang, C.C. Gallen, B.J. Schwartz, and F.E. Bloom. 'Noninvasive Somatosensory Homunculus Mapping in Humans by Using a Large-array Biomagnetometer'. *Proc Natn Acad Sci*, USA 90:3098–3102, 1993.

[47] D. Cohen, B.N. Cuffin, K. Yunokuchi, R. Maniewski, C. Purcell, G.R. Cosgrove, J. Ives, J.G. Kennedy, and D.L. Schomer. 'MEG versus EEG Localization Test using Implanted Sources in the Human Brain'. *Ann. Neurol.*, 28:811–817, 1990.

[48] S.J. Williamson. 'MEG versus EEG Localization Test (Letter to the Editor)'. *Ann. Neurol.*, 30:222, 1991.

[49] R. Hari, M. Hämäläinen, R. Ilmoniemi, and O. Lounasmaa. 'MEG versus EEG Localization Test (Letter to the Editor)'. *Ann. Neurol.*, 30:222–223, 1991.

[50] N. Nakasato, M.F. Levesque, D.S. Barth, C. Baumgartner, R.L. Rogers, and W.W. Sutherling. 'Comparisons of MEG, EEG, and ECoG Source Localization in Neocortical Partial Epilepsy in Humans'. *Electroencephalogr Clin Neurophy*, 171:171–178, 1994.

[51] J. Sarvas. 'Basic Mathematical and Electromagnetic Concepts of the Biomagnetic Inverse Problem'. *Phys. Med. Biol.*, 32(1):11–22, 1987.

[52] J.H. Tripp. 'Physical Concepts and Mathematical Models'. In S.J. Williamson, G.L. Romani, L. Kaufman, and I. Modena, editors, *'Biomagnetism: An Interdisciplinary Approach'*, chapter 6, pages 101–139. Plenum Press, New York, 1983.

[53] R.M. Arthur and D.B. Geselowitz. 'Effect of Inhomogeneities on the Apparent Location and Magnitude of a Cardiac Current Dipole Source'. *IEEE Transactions on Biomedical Engineering*, BME-17:141–146, 1970.

[54] T.M. Darcey. PhD thesis, California Institute of Technology, 1979.

[55] B.N. Cuffin and D. Cohen. 'Magnetic Fields of a Dipole in Special Volume Conductor Shapes'. *IEEE Transactions on Biomedical Engineering*, BME-24:372–381, 1977.

[56] M.S. Hämäläinen and J. Sarvas. 'Realistic Conductivity Geometry Model of the Human Head for Interpretation of Neuromagnetic Data'. *IEEE Transactions on Biomedical Engineering*, BME-36:165–171, 1989.

[57] J.W.H. Meijs, F.G.C. Bosch, M.J. Peters, and F.H. Lopes da Silva. 'On the Magnetic Field Distribution Generalized by a Dipolar Current Source Situated in a Ralistically Shaped Compartment Model of the Head'. *Electroencephalogr Clin Neurophy*, 64:286–298, 1987.

[58] J.W.H. Meijs and M.J. Peters. 'The EEG and MEG, Using a Model of Eccentric Spheres to Describe the Head'. *IEEE Transactions on Biomedical Engineering*, BME-34:913–920, 1987.

[59] D.S. Barth, W.W. Sutherling, J. Broffman, and J. Beatty. 'Magnetic Localization of a Dipolar Current Source Implanted in a Sphere and a Human Cranium'. *Electroencephalogr Clin Neurophy*, 63:260–273, 1986.

[60] T. Yamamoto, S.J. Williamson, L. Kaufman, C. Nicholson, and R. Llinás. 'Magnetic Localization of Neuronal Activity in the Human Brain'. *Proc Natn Acad Sci*, USA 85:8732–8736, 1988.

[61] E. Ducla-Soares. 'Volume Current Effects on MEG and Modeling'. In S.J. Williamson, M. Hoke, G. Stroink, and M. Kotani, editors, *'Advances in Biomagnetism'*, pages 533–538. Plenum Press, New York, 1990.

[62] A.C. Barnard, I.M. Duck, M.S. Lynn, and W.P. Timlake. 'The Application of Electromagnetic Theory to Electrocardiology'. *Biophy. J.*, 7:463–491, 1967.

[63] G.L. Romani, S.J. Williamson, and L. Kaufman. 'Biomagnetic Instrumentation'. *Rev. Sci. Instrum.*, 53(12):1815–1845, 1982.

[64] S.N. Erné and G.L. Romani. 'Performances of Higher Order Planar Gradiometers for Biomagnetic Source Localization'. In H.D. Hahlbohm and H. Lubbig, editors, *'SQUID 85: Superconducting Quantum Interference Devices and their Applications'*, pages 951–961. Berlin: Walter de Gruyter, 1985.

[65] J. Knuutila, A.I. Ahonen, M.S. Hämäläinen, R.J. Ilmoniemi, and M.J. Kajola. 'Design Consideration for Multichannel SQUID Magnetometers'. In H.D. Hahlbohm and H. Lubbig, editors, *'SQUID 85: Superconducting Quantum Interference Devices and their Applications'*, pages 939–944. Berlin: Walter de Gruyter, 1985.

[66] P. Carelli and R. Leoni. 'Localization of Biological Sources with Arrays of Superconducting Gradiometers'. *J Appl Phys*, 56:645–650, 1986.

[67] R.J.P. Bain, A.E. Jones, and G.B. Donaldson. 'Design of High-order Super-conducting Planar Gradiometers with Shaped Asymmetric Near-source Response'. *IEEE Trans Magn*, MAG-23:1146–1149, 1987.

[68] J.E. Desmedt, E. Brunko, J. Debecker, and J. Carmeliet. 'The System Band-pass Required to Avoid Distortion of Early Components when Averaging Somatosensory Evoked Potentials'. *Electroencephalogr Clin Neurophy*, 37:407–410, 1974.

[69] O. Bertrand, J. Bohorquez, and J. Pernier. 'Technical Requirements for Evoked Potential Monitoring in the Intensive Care Unit'. In P.M. Rosini and F. Mauguiere, editors, *'New Trends and Advanced Techniques in Clinical Neurophysiology'*, pages 51–70. Elsevier, Amsterdam, 1990.

[70] E.J. Moore. *'Bases of Auditory Brain-Stem Evoked Response'*. Grune & Stratton, Inc., NewYork, 1983.

[71] M. Hoke, B. Ross, R. Wickesberg, and B. Lütkenhöner. 'Weighted Averaging – Theory and Application to Electric Response Audiometry'. *Electroencephalogr Clin Neurophy*, 57:484–489, 1984.

[72] B. Lütkenhöner, M. Hoke, and C. Pantev. 'Possibilities and Limitations of Weighted Averaging'. *Biol Cybern*, 52:409–416, 1985.

[73] S.J. Swithenby. 'Biomedical Engineering - SQUID Magnetometers in Clinical Measurement'. An Entry in the 1987 Yearbook of Science and Technology 1989, McGraw Hill Inc., New York (1988).

[74] D.S. Buchanan, D.N. Paulson, G.A. Klemic, and S.J. Williamson. 'Development of a Hybrid Gifford-McMahon Joule-Thomson Based SQUID Gradiometer'. In P. Lindquist and A. Johnson, editors, *'Proceedings of the International Cryocooler Conference'*, 1988.

[75] G.L. Romani and R. Leoni. 'Localization of Cerebral Source by Neuromagnetic Measurement'. In *'Biomagnetism: Application and Theory'*, pages 205–220, 1984.

[76] S.N. Erné, L. Narici, V. Pizzella, and G.L. Romani. 'The Positioning Problem in Biomagnetic Measurements: a Solution for Arrays of Superconducting Sensors'. *IEEE Trans. Mag.*, MAG-23:1319–1322, 1987.

[77] 'Coming Together with the BTI System'. Biomagnetic Technologies Inc. 4174 Sorrento Valley Blvd, San Diego, CA.

[78] S. Cerutti, D. Baselli, D. Liberati, and G. Pavesi. 'Single Sweep Analysis of Visual Evoked Potentials Through a Model of Parametric Identification'. *Biol Cybern*, 56:111–120, 1987.

[79] H.E. Hoenig, G.M. Daalmans, L. Bär, F. Bömmel, A. Paulus, D. Uhl, H.J. Weisse, and et al. 'Multichannel DC SQUID Sensor Array for Biomagnetic Applications'. *IEEE Transactions on Magnetics*, 27:2777–2785, 1991.

[80] A.I. Ahonen, M.S. Hämäläinen, M.J. Kajola, J.E. Knuutila, P.L. Laine, O.V. Lounasmaa, and et al. 'A 122-channel Magnetometer Covering the Whole Head'. In A. Dittmar and J.C. Froment, editors, *'Proceedings of the Satellite Symposium on Neuroscience and Technology, 14th Annual International Conference of the IEEE Engineering in Medicine and Biology Society'*, pages 16–20. IEEE Engineering and Medicine and Biology Society, Lyon, France, Nov. 1992.

[81] J. Vrba, K. Betts, M. Burbank, T. Cheung, A.A. Fife, and et al. 'Whole Cortex, 64 Channel SQUID Biomagnetometer System'. *IEEE Transactions on Superconductivity*, 3:1878–1882, 1993.

[82] D.F. Rose, S. Sato, P.D. Smith, and J. White. 'Modeling the Temporal Region in Patients with Temporal Lobe Epilepsy'. *Phys Med Biol*, 32:59–63, 1987.

[83] J.C. de Munck and M.J. Peters. 'Mathematical Aspects of Biomagnetic and Bioelectric Modeling'. In M Hoke and et al., editors, *'Biomagnetism: Clinical Aspects'*, pages 13–21. Elsevier Science Publishers B.V., 1992.

[84] J.W.H. Meijs, H.B.K. Boom, M.J. Peters, and A. Oosterom. 'Application of the Richardson Extrapolation in Simulation Studies of EEGs'. *Med Biol Eng Comput*, 25:222–226, 1987.

[85] T.R. Tuomisto, R. Hari, T. Katila, T. Poutanen, and T. Varpula. 'Studies of Auditory Evoked Magnetic and Electric Responses: Modality Specificity and Modeling'. *Nuovo Cimento D 2*, pages 471–483, 1983.

[86] E. Kaukoranta, M. Hämäläinen, J. Sarvas, and R. Hari. 'Mixed and Sensory Nerve Simulations Activate Different Cytoarchitechtonic Areas in the Human Primary Somatosensory Cortex SI'. *Exp. Brain Res.*, 63:60–66, 1986.

[87] S. Supek and C.J. Aine. 'Model Order Determination and Limits of Source Resolution for Multi-Source Neuromagnetic Data: Simulation Studies'. *IEEE Transactions on Biomedical Engineering*, 1993. In Press.

[88] Y.C. Okada, R. Tanenbaum, S.J. Williamson, and L. Kaufman. 'Somatotopic Organization of the Human Somatosensory Cortex Revealed by Neuromagnetic Measurements'. *Exp. Brain Res.*, 56:197–205, 1984.

[89] M.S. Hämäläinen, H. Haario, and M.S. Lehtinen. 'Inferences about Sources of Neuromagnetic Fields Using Bayesian Parameter Estimation'. Helsinki University of Technology, Finland, Technical Report TKK-F-A620.

[90] C.J. Stok. 'The Influence of Model Parameters on EEG/MEG Single Dipole Source Estimation'. *IEEE Transactions on Biomedical Engineering*, BME-34:289–296, 1987.

[91] R. Hari, S.L. Joutsiniemi, and J. Sarvas. 'Spatial Resolution of Neuromagnetic Records: Theoretical Calculations in a Spherical Model'. *Electroencephalogr Clin Neurophy*, 71:64–72, 1988.

[92] Y. Okada. 'Discrimination of Localized and Distributed Current Dipole Sources and Localized Single and Multiple Sources'. In H. Weinberg, G. Stroink, and T. Katila, editors, *'Biomagnetism: Applications and Theory'*, pages 266–272. Pergamon Press, New York, 1985.

[93] B.N. Cuffin. 'A Comparison of Moving Dipole Inverse Solutions Using EEG's and MEG's'. *IEEE Transactions on Biomedical Engineering*, BME-32:905–910, 1985.

[94] P.L. Nunez. 'The Brain's Magnetic Field: Some Effects of Multiple Sources on Localization Methods'. *Electroencephalogr Clin Neurophy*, 63:75–82, 1986.

[95] D.S. Barth, C. Baumgartner, and W.W. Sutherling. 'Neuromagnetic Field Modeling of Multiple Brain Regions Producing Interical Spikes in Human Epilepsy'. *Electroencephalogr Clin Neurophy*, 73:389–402, 1989.

[96] M. Scherg. 'Fundamentals of Dipole Source Potential Analysis'. In F. Grandori, M. Hoke, and G.L. Romani, editors, *'Auditory Evoked Magnetic Fields and Electric Potentials, Vol. 6 of Advances of Audiology'*, pages 40–69. Basel:Karger, 1990.

[97] M. Scherg, R. Hari, and M. Hämäläinen. 'Frequency-specific Sources of the Auditory N19-P30-P50 Response Detected by a Multiple Source Analysis of Evoked Magnetic Fields and Potentials'. In S.J. Williamson, M. Hoke, G. Stroink, and M. Kotani, editors, *'Advances in Biomagnetism'*, pages 97–100. Plenum Press, New York, 1990.

[98] M.S. Hämäläinen. 'Multidipole Models in MEG'. Lecture notes for Comett II course on Biomagnetic localization and 3D modelling, Sjökulla, May 28, 1991.

[99] J.C. Mosher, P.S. Lewis, and R. Leahy. 'Multiple Dipole Modeling and Localization from Spatio-Temporal MEG Data'. *IEEE Transactions on Biomedical Engineering*, BME-39:541–557, 1992.

[100] J.C. Mosher, P.S. Lewis, R. Leahy, and M. Singh. 'Multiple Dipole Modeling of Spatio-Temporal MEG Data'. In A.F. Gmitro, P.S. Idell, and I.J. La-Haie, editors, *'Digital Image Synthesis and Inverse Optics, Proc. SPIE 1351'*, pages 364–375. SPIE International Society for Optical Engineering, Bellingham, 1990.

[101] P. Stoica and A. Nehorai. 'MUSIC, Maximum Likelihood, and Cramer-Rao Bound'. *IEEE Transactions on Acoustics, Speech, and Signal Processing*, 37:720–741, 1989.

[102] R.O. Schmit. 'Multiple Emitter Location and Signal Parameter Estimation'. *IEEE Trans. Antennas propag.*, AP-34:276–280, 1986.

[103] M. Singh, D. Doria, V. Henderson, G. Huth, and J. Beatty. 'Reconstruction of Images from Neuromagnetic Fields'. *IEEE Transactions on Nuclear Science*, NS-31:585–589, 1984.

[104] B. Jeffs, R. Leahy, and M. Singh. 'An Evaluation of Methods for Neuromagnetic Image Reconstruction'. *IEEE Transactions on Biomedical Engineering*, BME-34(6):713, Sep. 1987.

[105] Y.S. Shim and Z.H. Cho. 'SVD Pseudoinversion Image Reconstruction'. *IEEE Transactions on Acoustics, Speech, and Signal Processing*, ASSP-29(4):904, Aug. 1981.

[106] S.N. Erné, L. Trahms, and Z. Trontelj. 'Current Multipoles as Sources of Biomagnetic Fields'. In K. Atsumi, M. Kotani, S. Ueno, T. Katila, and S.J. Williamson, editors, *'Biomagnetism 87'*, pages 302–305. Tokyo Denki University Press, 1988.

[107] V. Jazbinsek, Z. Trontelj, S.N. Erné, and L. Trahms. 'Influence of the Finite Pickup Coil Size on the Localization of Current Sources with Quadrupolar Components'. In S.J. Williamson, M. Hoke, G. Stroink, and M. Kotani, editors, *'Advances in Biomagnetism'*, pages 559–562. Plenum Press, New York, 1990.

[108] G.C.K. Yeh, J. Martinek, and H. deBeaumont. 'Multipole Representations of Current Generators in a Volume Conductor'. *Bull Math Biophys*, 20:203–216, 1958.

[109] T. Katila and P. Karp. 'Magnetocardiography: Morphology and Multipole Presentations'. In S.J. Williamson, G.L. Romani, L. Kaufman, and I. Modena, editors, *'Biomagnetism: An Interdisciplinary Approach'*, pages 237–263. Plenum Press, New York, 1983.

[110] L.I. Titomir and P. Kneppo. 'Simultaneous Analysis of Cardiac Electric and Magnetic Fields using the Scalar Multipole Expansion'. *Bull Math Biol*, 47:123–143, 1985.

[111] G. Stroink, F. Brauer, C. Purcell, and P. Krieger. 'An Inverse Solution in Magnetoencephalography'. In H. Weinberg, G. Stroink, and T. Katila, editors, *'Biomagnetism: Applications and Theory'*, pages 406–410. Pergamon Press, New York, 1985.

[112] J.P. Wikswo and K.R. Swinney. 'A Comparison of Scalar Multipole Expansions'. *J Appl Phys*, 56:3039–3049, 1984.

[113] S.A. Ferguson and D. Durand. 'Magnetic Fields of Current Monopoles'. In S.J. Williamson, M. Hoke, G. Stroink, and M. Kotani, editors, *'Advances in Biomagnetism'*, pages 583–586. Plenum Press, New York, 1990.

[114] A.A. Ioannides, J.P.R. Bolton, R. Hasson, and C.J.S. Clarke. 'Localised and Distributed Source Solutions for the Biomagetic Inverse Problem II'. In S.J. Williamson, M. Hoke, G. Stroink, and M. Kotani, editors, *'Advances in Biomagnetism'*, pages 591–594. Plenum Press, New York, 1990.

[115] M.J. Liu, R. Hasson, and A.A. Ioannides. 'A Transputer-based System for Magnetic Field Tomography'. In R. Grebe, J. Hektor, S.C. Hilton, M. Jane, and P.H. Welch, editors, 'Transputer Applications and Systems'93', volume 2, pages 1290–1297. IOS Press, Amsterdam, 1993.

[116] H. Kado, S. Kashiwaya, M. Higuchi, and H. Miura. 'Direct Approach to an Inverse Problem: a Trial to Describe Signal Sources by Current Elements Distribution'. In S.J. Williamson, M. Hoke, G. Stroink, and M. Kotani, editors, *'Advances in Biomagnetism'*, pages 579–582. Plenum Press, New York, 1990.

[117] C.W. Crowley, R.E. Greenblatt, and I. Khalil. 'Minimum Norm Estimation of Current Distributions in Realistic Geometries'. In S.J. Williamson, M. Hoke,

G. Stroink, and M. Kotani, editors, *'Advances in Biomagnetism'*, pages 603–606. Plenum Press, New York, 1990.

[118] W.H. Kullmann. 'A Linear Estimation Approach to Biomagnetic Imaging'. In S.J. Williamson, M. Hoke, G. Stroink, and M. Kotani, editors, *'Advances in Biomagnetism'*, pages 571–574. Plenum Press, New York, 1990.

[119] C.J. Clarke, A.A. Ioannides, and J.P.R. Bolton. 'Localised and Distributed Source Solutions for the Biomagetic Inverse Problem I'. In S.J. Williamson, M. Hoke, G. Stroink, and M. Kotani, editors, *'Advances in Biomagnetism'*, pages 587–590. Plenum Press, New York, 1990.

[120] R.E. Greenblatt, C.W. Crowley, and I. Khalil. 'Source Activity Mapping from Biomagnetic Data by Minimum Norm Estimation'. In L. Kaufman and S.J. Williamson, editors, *'Digest of the 7th International Conference on Biomagnetism'*, pages 93–94. New York: New York University, 1989.

[121] A.A. Ioannides, J.P.R. Bolton, and C.J.S. Clarke. 'Continuous Probabilistic Solutions to the Biomagnetic Inverse Problem'. *Inverse Problem 6*, pages 523–542, 1990.

[122] A.A. Ioannides. 'Estimates of 3D Brain Activity ms by ms from Biomagnetic Signals: Method (MFT), Results and their Significance'. In E. Eiselt, U. Zwiener, and H. Witte, editors, *'Quantitative and Topological EEG and MEG Analysis'*. Universitätsverlag Druckhaus-Maayer GmbH, Jena, 1994.

[123] A.A. Ioannides, K.D. Singh, R. Hasson, S.B. Baumann, R.L. Rogers, F.C. Guinto, and A.C. Papanicolaou. 'Comparison of Current Dipole and Magnetic Field Tomography Analyses of the Cortical Response to Auditory Stimuli'. *Brain Topograghy*, 6:27–34, 1993.

[124] K.D. Singh, A.A. Ioannides, N. Gray, H. Kober, H. Pongratz, A. Daun, P. Grummich, and J. Vieth. 'Distributed Current Analyses of Bi-hemispheric Magnetic N1m Responses to Ipsi/Contralateral Monaural Stimulus from a Single Subject'. *Electroencephalogr Clin Neurophy*, 92:365–368, 1994.

[125] U. Ribary, A.A. Ioannides, K.D. Singh, R. Hasson, J.P.R. Bolton, F. Lado, A. Mogilner, and R. Llinás. 'Magnetic Field Tomography (MFT) of Coherent Thalamo-Cortical 40 Hz Oscillations in Humans'. *Proc. Natl. Acad. Sci.*, USA 88:11037–11041, 1991.

[126] F.B.C. Fenwick, A.A. Ioannides, G.W. Fenton, J. Lumsden, P. Grummich, H. Kober, A. Daun, and J. Vieth. 'Estimates of Brain Activity using Magnetic

Field Tomography in a GO/NOGO Avoidance Paradigm'. *Brain Topograghy*, 5:275–282, 1993.

[127] A.A. Ioannides, K.M. Stephan, P.B.C. Fenwick, J. Lumsden, G.W. Fenton, M.J. Liu, J. Vieth, K.C. Squires, D. Lawson, R. Myers, G.R. Fink, and R.S.J. Frackowiak. 'Analysis of MEG Signals from a GO/NOGO Avoidance Paradigm and Comparison of Estimates of Brain Activity using PET'. In *'Proceedings of the BIOMAG'93 Conference in Vienna'*. Elsevier Science Publishers, Amstemdam, 1993. In press.

[128] A.A. Ioannides, P.B.C. Fenwick, J. Lumsden, M.J. Liu, P.D. Bamidis, K.C. Squires, D. Lawson, and G.W. Fenton. 'Activation of Discrete Brain Areas during Cognitive Processes: Results from Magnetic Field Tomography'. *Electroencephalogr Clin Neurophy*, 1994. In Press.

[129] A.A. Ioannides, E. Hellstrand, and K. Abraham-Fuchs. 'Point and Distribted Current Density Analysis of Interictal Epileptic Actvity Recorded by Magnetoencephalography'. *Physiological Measurements*, 14:121–130, 1993.

[130] C.J.S. Clarke and B.S. Janday. 'The Solution of the Biomagnetic Inverse Problem by Maximum Statistical Entropy'. *Inverse Problem 5*, pages 483–500, 1989.

[131] M.J. Liu and A.A. Ioannides. 'Choice of Source Space for Magnetic Field Tomography'. In *'Proceedings of the BIOMAG'93 Conference in Vienna'*. Elsevier Science Publishers, Amstemdam, 1993. In press.

[132] O. Josephs, K. Fiaschi, K. Singh, and S. Swithenby. 'A Multichannel Tangential-Field Gradiometer System'. In *'Proceedings of the BIOMAG'93 Conference in Vienna'*. Elsevier Science Publishers, Amstemdam, 1993. In press.

[133] A.A. Ioannides. 'Graphical Solutions and Representations for the Biomagnetic Inverse Problem'. In P.C. Sabatier, editor, *'Advances in Electronics and Electron Physics Supplement 19, Inverse Problems: an Interdisciplinary Study'*, pages 205–216. Academic press, Orlando, 1987.

[134] A.A. Ioannides, R. Hasson, and G.J. Miseldine. 'Model-dependent Noise Elimination and Distributed Source Solutions for the Biomagnetic Inverse Problem'. In A.F. Gmitro and et al., editors, *'Digital Image Synthesis and Inverse Optics'*, pages 471–481. *Proc. SPIE 1351*, 1990.

[135] L.C. Liu and A.A. Ioannides. 'Single Epoch Analysis of MEG Signals'. In *'Proceedings of the BIOMAG'93 Conference in Vienna'*. Elsevier Science Publishers, Amstemdam, 1993. In press.

[136] S.L. Bressler. 'The Gamma Wave: a Cortical Information Carrier ?'. *Trends Neurosci.*, 13:161–162, 1990.

[137] R.M. Chapman, R.J. Ilmoniemi, S. Barbanera, and G.L. Romani. 'Selective Localization of Alpha Brain Activity with Neuromagnetic Measurements'. *Electroencephalogr Clin Neurophy*, 58:569–572, 1984.

[138] M. Schürmann, C. Başar-Eroglu, E. Rahn, M. Braasch, O. Dössel, M. Fuchs, and E. Başar. 'A Comparative Study of Alpha Responses in Human MEG Temporo-parietal and Occipital Recordings and Cat Intracranial EEG Recordings'. In A. Dittmar and J.C. Froment, editors, *'Proceedings of the Satellite Symposium on Neuroscience and Technology, 14th Annual International Conference of the IEEE Engineering in Medicine and Biology Society'*, pages 132–137. IEEE Engineering and Medicine and Biology Society, Lyon, France, Nov. 1992.

[139] E. John, editor. *'Machinery of the Mind'*, chapter 25, pages 479–511. Birkhaeuser, Boston, 1990.

[140] J.A.S. Kelso, S.L. Bressler, S. Buchanan, G.C. DeGuzman, M. Ding, A. Fuchs, and T. Holroyd. 'Cooperative and Critical Phenomena in the Human Brain Revealed by Multiple SQUIDs'. In D. Duke and W. Pritchard, editors, *'Chaos in the Human Brain'*. World Scientific, Teaneck, New Jersey, 1991.

[141] H. Berger. 'About the EEG in Human'. *Arch Psychiat*, 106:165–187, 1937.

[142] W. Freeman. *'Mass Action in the Nervous System'*. Academic Press, New York, 1975.

[143] J. Suk, U. Ribary, J. Capell, T. Yamamoto, and R. Llinás. 'Anatomical Localization Revealed by MEG Recordings of the Human Somatosensory System'. *Electroencephalogr Clin Neurophy*, 78:185–196, 1991.

[144] W.J. Freeman. 'The Physiology of Perception'. *Scientif Am*, 264(2):34–41, 1991.

[145] D.E. Sheer. 'Sensory and Cognitive 40-Hz Event-Related Potentials: Behavioural Correlates, Brain Function, and Clinical Application'. In E. Başar and T.H. Bullock, editors, *'Brain Dynamics'*, pages 339–374. Springer-Verlag Berlin Heidelberg, 1989.

[146] B.W. Johnson, H. Weinberg, Ribary U., D.O. Cheyne, and R. Ancil. 'Topographic Distribution of the 40 Hz Auditory Evoked-Related Potential in Normal and Aged Subjects'. *Brain Topograghy*, 1:117–121, 1988.

[147] C. Pantev, S. Makeig, M. Hoke, R. Galambos, S. Hampson, and C. Gallen. 'Human Auditory Evoked Gamma-band Magnetic Fields'. *Proc. Natl. Acad. Sci.*, USA 88:8996–9000, 1991.

[148] F. Crick and C. Koch. 'Towards a Neurobiological Theory of Consciousness'. *Semin. Neurosci.*, 2:263–275, 1990.

[149] W.J. Freeman. 'Development of a New Science of Brain Dynamics with Guidance from the Theory of Nonlinear Dynamics and Choas'. In M. Hoke and et al., editors, *'Biomagnetism: Clinical Aspects'*, pages 3–11. Elsevier Science Publishers B.V., 1992.

[150] W.J. Freeman and B.W. van Dijk. 'Spatial Patterns of Visual Cortical Fast EEG During Conditioned Reflex in a Rhesus Monkey'. *Brain Res.*, 422:267–276, 1987.

[151] W.J. Freeman and J.M. Barrie. 'Chaotic Oscillations and the Genesis of Meaning in Cerebral Cortex'. In G. Buzsáki and et al., editors, *'Temporal Coding in the Brain'*, pages 13–37. Spring-Varlag Berlin Heidelberg, 1994.

[152] M. Abeles, Y. Prut, H. Bergman, and E. Vaadia. 'Synchronization in Neuronal Transmission and Its Importance for Information Processing'. In G. Buzsáki and et al., editors, *'Temporal Coding in the Brain'*, pages 40–50. Spring-Varlag Berlin Heidelberg, 1994.

[153] W. Singer. 'Time as Coding Space in Neocortical Processing: A Hypothesis'. In G. Buzsáki and et al., editors, *'Temporal Coding in the Brain'*, pages 51–79. Spring-Varlag Berlin Heidelberg, 1994.

[154] W.J. Freeman and G. Viana Di Prisco. 'EEG Spatial Pattern Differences with Discriminated Odors Manifest Chaotic and Limited Cycle Attractors in Olfactory Bulb of Rabbits'. In G. Palm and A. Aertsen, editors, *'Brain Theory'*, pages 97–119. Springer, Berlin, 1986.

[155] A.K. Engel. 'Temporal Coding in the Visual Cortex: New Vistas on Integration in the Nervous System'. *Trends Neurosci.*, 15:218–226, 1992.

[156] C. Tallon, O. Bertrand, P. Bouchet, and J. Pernier. '40-Hz Visual Evoked Response Correlates with Stimulus Coherency in Human'. In *'1st Congress*

of the European Federation of Psychophysiology Societies: Abstracts Book', pages 70–P, Barcelona, April 7th -10th, 1994.

[157] C.M. Gray, P. König, A.K. Engel, and W. Singer. 'Oscillation Responses in Cat Visual Cortex Exhibit Inter-Columnar Synchronization which Reflects Global Stimulus Properties'. *Nature*, 338:334–337, 1989.

[158] R. Llinás, U. Ribary, M. Joliot, and X.J. Wang. 'Content and Context in Temporal Thalamocortical Binding'. In G. Buzsáki and et al., editors, *'Temporal Coding in the Brain'*, pages 251–272. Spring-Varlag Berlin Heidelberg, 1994.

[159] M. Joliot, U. Ribary, and R. Llinás. 'Human Oscillatory Brain Activity near 40 Hz Coexists with Cognitive Temporal Binding'. *Proc. Natl. Acad. Sci.*, USA 91:11748–11751, 1994.

[160] R. Llinás and U. Ribary. 'Coherent 40-Hz Oscillation Characterizes Dream State in Humans'. *Proc. Natl. Acad. Sci.*, USA 90:2078–2081, 1993.

[161] R. Galambos, S. Makeig, and P.J. Talmachoff. 'A 40-Hz Auditory Potential Recorded from the Human Scalp'. *Proc. Natl. Acad. Sci.*, USA 78:2643–2647, 1981.

[162] R. Llinás and U. Ribary. 'Rostrocaudal Scan in Human Brain: A Global Characteristic of the 40-Hz Response During Sensory Input'. In E. Başar and T.H. Bullock, editors, *'Induced Rhythms in the Brain'*, pages 147–154. Birkhauser, Boston, 1992.

[163] U. Ribary, R. Llinás, A. Kluger, J. Suk, and S.H. Ferris. 'Neuropathological Dynamics of Magnetic, Auditory Steady-State Responses in Alzheimer's Disease'. In S.J. Williamson, M. Hoke, G. Stroink, and M. Kotani, editors, *'Advances in Biomagnetism'*, pages 311–314. Plenum Press, New York, 1990.

[164] T. Demiralp, J. Yordanova, and V. Kolev. 'The Effect of Cognitive Variables on the Evoked Gamma-band Activity'. In *'1st Congress of the European Federation of Psychophysiology Societies: Abstracts Book'*, pages 60–P, Barcelona, April 7th -10th, 1994.

[165] H. Tiitinen, J. Sinkkonen, K. Reinikainen, K. Alho, J. Lavikainen, and R. Näätänen. 'Selective Attention Enhances the Auditory 40-Hz Transient Response in Humans'. *Nature*, 364:59–60, 1993.

[166] A.A. Ioannides, M.J. Liu, L.C. Liu, P.D. Bamidis, E. Hellstrand, and K.M. Stephan. 'Magnetic Field Tomography of Cortical and Deep Processes: Ex-

amples of "Real-Time Mapping" of Averaged and Single Trial MEG Signals'. submitted to *International Journal of Psychophysiology*.

[167] P.H. Lindsay and D.A. Norman. *'Human Information Processing: An Introduction to Psychology'*. New York: Academic Press, 2nd edition, 1977.

[168] R. Hari. 'The Neuromagnetic Method in the Study of the Human Auditory Cortex'. In F. Grandori, M. Hoke, and G.L. Romani, editors, *'Auditory Evoked Magnetic Fields and Electric Potentials, Vol. 6 of Advances of Audiology'*, pages 222–282. Basel:Karger, 1990.

[169] A.B. Rubens, M.V. Mahowals, and J.T. Hutton. 'Asymmetry of the Lateral (Sylvian) fissures in Man'. *Neurology*, 26:620–624, 1976.

[170] C. Pantev, M. Hoke, K. Lehnertz, B. Lütkenhöner, G. Anogianakis, and W. Wittkowski. 'Topotopic Organization of the Human Auditory Cortex Revealed by Transient Auditory Evoked Magnetic Fields'. *Electroencephalogr Clin Neurophy*, 69:160–170, 1987.

[171] G.L. Romani, S.J. Williamson, and L. Kaufman. 'Tonotopic Organization of the Human Auditory Cortex'. *Science*, 216:1339–1340, 1982.

[172] C. Pantev, M. Hoke, K. Lehnertz, and B. Lütkenhöner. 'Neuromagnetic Evidence of an Amplitopic Organization of the Human Auditory Cortex'. *Electroencephalogr Clin Neurophy*, 72:225–231, 1989.

[173] J.P. Mäkelä, R. Hari, and A. Linnankivi. 'Differet Analysis of Frequency and Amplitude Modulations of a Continuous Tone in the Human Auditory Cortex'. *Hearing Research*, 27:257–264, 1987.

[174] A. Galaburda and F. Sanides. 'Cytoarchitectonic Organization of the Human Auditory Cortex'. *J. comp. Neurol.*, 190:597–610, 1980.

[175] N. Loveless, R. Hari, M. Hämäläinen, and J. Tiihonen. 'Evoked Responses of Human Auditory Cortex may be Enhanced by Preceding Stimuli'. *Electroencephalogr Clin Neurophy*, 74:217–227, 1989.

[176] D.L. Arthur, P.S. Lewis, P.A. Medvick, and E.R. Flynn. 'A Neuromagnetic Study of Selective Auditory Attention'. *Electroencephalogr Clin Neurophy*, 78:348–360, 1991.

[177] J. Rif, R. Hari, M. Hämäläinen, and M. Sams. 'Auditory Attention Affects two Different Areas in the Human Supratemporal Cortex'. *Electroencephalogr Clin Neurophy*, 79:464–472, 1991.

[178] S.N. Erné and M. Hoke. 'Short-Latency Evoked Magnetic Fields from the Human Auditory Brainstem'. In S. Sato, editor, *'Advances in Neurology'*, pages 167–176. Raven Press, New York, 1990.

[179] C. Liégeois-Chauvel, A. Musolino, J.M. Badier, P. Marquis, and P. Chauvel. 'Evoked Potentials Recorded from the Auditory Cortex in Man: Evaluation and topography of the Middle Latency Components'. *Electroencephalogr Clin Neurophy*, 92:204–214, 1994.

[180] S. Makeig. 'A Dramatic Increase in the Auditory Middle Latency Response at very Low Rates'. In C. Brunia and et al., editors, *'Psychophysiological Brain Research'*, pages 60–64. Netherlands Tilburg Univ. Press, 1990.

[181] R. Hari. 'On Brain's Magnetic Responses to Sensory Stimuli'. *Electroencephalogr Clin Neurophy*, 8(2):157–169, 1991.

[182] J.P. Mäkelä and R. Hari. 'Long-Latency Auditory Evoked Magnetic Fields'. In S. Sato, editor, *'Advances in Neurology'*, pages 177–191. Raven Press, New York, 1990.

[183] H.T. Chang. 'The Repetitive Discharges of Corticothalamic Reverberating Circuits'. *Journal of Neurophysiology*, 13:235–257, 1950.

[184] J.P. Mäkelä, M.S. Hämäläinen, R. Hari, and L. McEvoy. 'Whole-head Mapping of Middle-latency Auditory Evoked Magnetic Fields'. *Electroencephalogr Clin Neurophy*, 92:414–421, 1994.

[185] F.N. Alavi, J.G. Taylor, and A.A. Ioannides. 'Estimates of Current Density Distributions, Applying the Principle of Cross-Entropy Minimisation to Electrographic Recordings'. *Inverse Problem 9*, pages 623–639, 1993.

[186] K. Kamada, F. Takeuchi, S. Kuriki, O. Oshiro, K. Houkin, and H. Abe. 'Functional Neurosurgical Simulation with Brain Surface Magnetic Resonance Images and Magnetoencephalography'. *Neurosurgery*, 33:269–273, 1993.

[187] C. Pantev, M. Hoke, K. Lehnertz, B. Lütkenhöner, G. Fahrendorf, and U. Stöber. 'Identification of Sources of Brain Neuronal Activity with High Spatiotemporal Resolution through Combination of Neuromagnetic Source Location (NMSL) and Magnetic Resonance Imaging (MRI)'. *Electroencephalogr Clin Neurophy*, 75:173–184, 1990.

[188] D. Cohen and B.N. Cuffin. 'A Method for Combining MEG and EEG to Determine the Sources'. *Phys Med Biol*, 32:85–89, 1987.

[189] E. Harth. 'Order and Chaos in Neural Systems: an Approach to the Dynamics of Higher Brain Functions'. *IEEE Trans Systems Man Cybernet*, SMC-13:782–789, 1983.

[190] P.D. Bamidis and A.A. Ioannides. 'Relating Function (MEG) to Structure (MRI)'. In *'BIOMAG'93 Vienna: Abstracts'*, pages 241–242, 1993.

[191] P.D. Bamidis, E. Hellstrand, and A.A. Ioannides. 'Spatio-Temporal Evolution of Epileptic Activity as Revealed from Unaveraged Interictal Multichannel MEG Recordings'. In *'IPSM & BES: 1st Joint Annual Scientific Conference and Exhibition, Scientific Programme & Abstracts'*, page 160. University of Keele, 1994.